

# Radiation Transport Around Kerr Black Holes

by

Jeremy David Schnittman

B. A. Physics

Harvard University (1999)

Submitted to the Department of Physics  
in partial fulfillment of the requirements for the degree of

Doctor of Philosophy

at the

MASSACHUSETTS INSTITUTE OF TECHNOLOGY

February 2005

© Jeremy David Schnittman, MMV. All rights reserved.

The author hereby grants to MIT permission to reproduce and  
distribute publicly paper and electronic copies of this thesis document  
in whole or in part.

Author .....  
Department of Physics  
January 20, 2005

Certified by .....  
Edmund Bertschinger  
Professor of Physics  
Thesis Supervisor

Accepted by .....  
Thomas J. Greytak  
Professor of Physics  
Associate Department Head for Education



# Radiation Transport Around Kerr Black Holes

by

Jeremy David Schnittman

Submitted to the Department of Physics  
on January 20, 2005, in partial fulfillment of the  
requirements for the degree of  
Doctor of Philosophy

## Abstract

This Thesis describes the basic framework of a relativistic ray-tracing code for analyzing accretion processes around Kerr black holes. We begin in Chapter 1 with a brief historical summary of the major advances in black hole astrophysics over the past few decades and outline some of the important questions still open today. In Chapter 2 we present a detailed description of the ray-tracing code, which integrates the geodesic equations of motion for massless particles, tabulating the position and momentum along each photon trajectory. Coupled with an independent model for the emission and absorption at each point in spacetime, time-dependent images and spectra can be produced by integrating the radiative transfer equation along these geodesic photon paths. This approach can be used to calculate the transfer function between the plane of the accretion disk and the detector plane, an important tool for modeling relativistically broadened emission lines.

Observations from the *Rossi X-Ray Timing Explorer* have shown the existence of high frequency quasi-periodic oscillations (HFQPOs) in a growing number of black hole binary systems. In Chapter 3, we employ a simple “hot spot” model to explain the position and amplitude of these HFQPO peaks. Using the exact geodesic equations of motion for the Kerr metric, we calculate the trajectories of massive test particles, which are treated as isotropic, monochromatic emitters in their rest frames, imaged with the ray-tracing code described above. The power spectrum of the periodic X-ray light curve consists of multiple peaks located at integral combinations of the black hole coordinate frequencies. Additionally, we model the effects of shearing the hot spot in the disk, producing an arc of emission that also follows a geodesic orbit. By including non-planar orbits that experience Lense-Thirring precession, we investigate the possible connection between high and low frequency QPOs.

In Chapter 4, we introduce additional features to the hot spot model to explain the broadening of the QPO peaks as well as the damping of higher frequency harmonics in the power spectrum. We present a number of analytic results that agree closely with more detailed numerical calculations. Three primary pieces are developed: the addition of multiple hot spots with random phases, a finite width in the distribution of geodesic orbits, and the scattering of photons from the hot spot through a corona

around the black hole. The complete model is used to fit the observed power spectra of both type A and type B QPOs seen in XTE J1550–564, giving confidence limits on each of the model parameters. We also include a discussion of higher-order statistics and the use of the bicoherence to distinguish between competing QPO models.

To gain more insight into the overall accretion geometry, in Chapter 5 we follow the formulation of Novikov & Thorne (1973) for describing the structure of a relativistic  $\alpha$ -disk around a Kerr black hole. The resulting equations of vertical structure can be integrated at each radius to give the complete density and temperature profile of the steady-state disk. Inside of the ISCO, the gas is propagated along a plunging geodesic trajectory, evolving according to one-dimensional classical hydrodynamics in the local inertial frame of the fluid. Given the surface temperature of the disk everywhere outside of the horizon, the observed spectrum is calculated using the transfer function mentioned above. The features of this modified thermal spectrum may be used to infer the physical properties of the accretion disk and the central black hole.

As an extension of the simple scattering model presented in Chapter 4, in Chapter 6 we develop a Monte Carlo code to calculate the detailed propagation of photons from a hot spot emitter scattering through a high-temperature, low-density corona surrounding the black hole. Each photon is followed until it is either captured by the black hole or is “detected” by a distant observer. The coronal scattering has two major observable effects: the inverse-Compton process alters the photon spectrum by adding a high energy power-law tail, and the random scattering of each photon effectively damps out the highest frequency modulations in the X-ray light curve. We present simulated photon spectra and light curves and compare with *RXTE* data, concluding with the implications for the hot spot model of HFQPOs.

Thesis Supervisor: Edmund Bertschinger  
Title: Professor of Physics

## Acknowledgments

*Gravity can not be held responsible for people falling in love.*

*No, this trick won't work...How on earth are you ever going to explain in terms of chemistry and physics so important a biological phenomenon as first love?*

-Albert Einstein

*For Nomi*

*The love of my life, my closest friend, my foundation, my joy, my  $\alpha$  and my  $\Omega$ .  
And sometimes even my  $v$ .*

This work is the cumulative result of so many people and so much effort that I am almost certain to omit important names, places, and events. My apologies in advance.

In roughly chronological order, I would like to thank the following: The Almighty, the Creator, for making a world so beautiful and full of wonder. Albert Einstein, my childhood hero, who only gained in stature and esteem as I grew older and was fortunate enough to learn more about his unequalled accomplishments. He was a Giant standing on the shoulders of giants, seeing farther than anyone else has before or since. My parents, Michael and Suzanne Schnittman, for giving me a lifetime full of love and encouragement, and always reminding me to get back to work. Thank you dad for teaching me the value of a sense of humor. Thank you mom for teaching me the value of an education, whether formal or informal. My brother Aaron for keeping me in my place and always giving me someone to look up to. My superb teachers and classmates at Wilson Magnet High School, for igniting my passion for science and mathematics. Steve Craxton, my first research advisor, who introduced me to scientific computing, proper writing style (may he forgive me for the pages to come), ray-tracing and radiation transport, and the world of professional physics research.

Rabbis Blau, Brovender, Ebner, Kilimnick, Schrader, and Walk, for teaching me about what is really important in this life. And my MIT office-mates, for distracting me with what is really unimportant in life. From the early days in 37-644, Tesla Jeltema, Josh Winn, and Jon Miller; from the mezzanine clubhouse, Jamie Portsmouth, Nick Morgan, Josh Faber, and John Fregeau; from 37-638, Adrienne Juett, Ed Boyce, Alex Shirokov, Kristin Burgess, Dave Pooley, and Adam Bolton; from the silly putty foosball madhouse, Matt Muterspaugh, Jake Hartman, Eric Pfahl, and my replacements Allyn Dullighan and Will Farr; from the antechamber, Justin Kasper, Miriam Krauss, Judd Bowman, Molly Swanson, and Bobby Cohan. Thanks to the D. Samuel Gottesman Library of the Albert Einstein College of Medicine, for being my office away from home.

Thank you to Paul Schechter, who took me under his wing my first day on the job; Fred Rasio, who introduced me to black holes and general relativity; Jack Wisdom, who trained me in the art of chaotic dynamics; Scott Hughes, whose office was always wide open for me to come in and bounce ideas off the white board; Jackie Hewitt, for offering an outsider's point of view and fitting me into her crazy schedule. Arlyn Hertz for fitting me into Jackie's schedule and helping make the defense run so smoothly. Martha Bezzat for answering all my random questions and requests for help with the mail, fax machine, and MIT bureaucratic regulations, always promptly and with a smile. And of course, many many thanks to my advisor, Ed Bertschinger, who provided the inspiration and direction for much of this work. His careful, critical eye kept me in line, and his encouragement this past year brought the final product to completion. Much of this work was supported by his NASA ATP grant NAG5-13306.

Again, the biggest accolades are for my wife Nomi, for putting up with me and supporting me, especially these past few months. I couldn't have done it without you.

השמים מספרים כבוד א-ל, ומעשה ידיו מגיד הרקיע -- תהלים יט:ב

The heavens proclaim the glory of God; the sky declares His handiwork

— Psalms 19:2

חכם אינו מדבר לפני מי שגדול ממנו בחכמה, ואינו נכנס לתוך דברי חברו, ואינו נבהל להשיב, שואל כענין ומשיב כהלכה, ואומר על ראשון ראשון ועל אחרון אחרון, ועל מה שלא שמע אומר לא שמעתי, ומודה על האמת -- פרקי אבות ה:ט

The wise man does not speak in the presence of one who is greater than he in wisdom; he does not interrupt the speech of his companion; he is not hasty to answer; he questions and answers properly, to the point; he speaks on the first point first, and on the last point last; regarding that which he has not learned he says: "I have not learned"; and he acknowledges the truth.

— Ethics of the Fathers 5:9

# Contents

<b>1</b>	<b>Introduction and Outline</b>	<b>15</b>
1.1	Motivation . . . . .	16
1.2	Historical Background . . . . .	17
1.2.1	Theory . . . . .	17
1.2.2	Observations . . . . .	20
1.3	Outline of Methods and Results . . . . .	22
1.3.1	Ray-tracing in the Kerr Metric . . . . .	22
1.3.2	The Hot Spot Model . . . . .	25
1.3.3	Steady-state Disks . . . . .	27
1.3.4	Electron Scattering . . . . .	30
1.4	Alternative QPO Models . . . . .	31
<b>2</b>	<b>Ray-Tracing in the Kerr Metric</b>	<b>35</b>
2.1	Equations of Motion . . . . .	35
2.1.1	Boyer-Lindquist Coordinates . . . . .	38
2.1.2	Doran Coordinates . . . . .	40
2.1.3	Analytic Methods . . . . .	42
2.2	Geodesic Ray-tracing . . . . .	44
2.2.1	Tetrads . . . . .	48
2.2.2	The Radiative Transfer Equation . . . . .	51
2.3	Numerical Methods . . . . .	57
2.4	Broadened Emission Lines from Thin Disks . . . . .	59
2.4.1	Transfer Function . . . . .	59
2.4.2	Observations of Iron Emission Lines . . . . .	63
<b>3</b>	<b>The Geodesic Hot Spot Model</b>	<b>69</b>
3.1	Hot Spot Emission . . . . .	69
3.1.1	Overbrightness and QPO Amplitudes . . . . .	71
3.1.2	Harmonic Dependence on Inclination and Spin . . . . .	73
3.2	Non-circular Orbits . . . . .	77
3.3	Non-planar Orbits . . . . .	87
3.4	Summary . . . . .	90

<b>4</b>	<b>Features of the QPO Spectrum</b>	<b>93</b>
4.1	Introduction . . . . .	93
4.2	Parameters for the Basic Hot Spot Model . . . . .	95
4.3	Peak Broadening from Hot Spots with Finite Lifetimes . . . . .	96
4.4	Distribution of Coordinate Frequencies . . . . .	100
4.5	Electron Scattering in the Corona . . . . .	107
4.6	Fitting QPO Data from XTE J1550–564 . . . . .	112
4.7	Higher Order Statistics . . . . .	117
4.7.1	The Bispectrum and Bicoherence . . . . .	117
4.7.2	The Bicoherence of the Simulated Data . . . . .	118
4.7.3	Simulations with Poisson Noise . . . . .	122
4.8	Summary . . . . .	124
<b>5</b>	<b>Steady-state <math>\alpha</math>-disks</b>	<b>127</b>
5.1	Steady-state Disks Outside the ISCO . . . . .	127
5.1.1	Radial Structure . . . . .	128
5.1.2	Vertical Structure . . . . .	131
5.1.3	Revised Eddington Limit . . . . .	138
5.2	Geodesic Plunge Inside the ISCO . . . . .	139
5.3	Numerical Implementation . . . . .	143
5.4	Observed Spectrum of the Disk . . . . .	148
<b>6</b>	<b>Electron Scattering</b>	<b>157</b>
6.1	Physics of Scattering . . . . .	157
6.1.1	Classical Electron Scattering . . . . .	157
6.1.2	General Relativistic Implementation . . . . .	161
6.2	Effect on Spectra . . . . .	167
6.3	Effect on Light Curves . . . . .	172
6.4	Implications for QPO Models . . . . .	178
<b>7</b>	<b>Conclusions and Future Work</b>	<b>181</b>
7.1	Summary of Results . . . . .	181
7.1.1	Ray-tracing . . . . .	181
7.1.2	The Hot Spot Model . . . . .	182
7.1.3	Steady-state Disks . . . . .	183
7.1.4	Electron Scattering . . . . .	184
7.2	Caveats . . . . .	185
7.3	New Applications of Current Code . . . . .	187
7.4	New Features for Code . . . . .	189
7.5	Development of New Models . . . . .	190



<i>CONTENTS</i>	9
<b>A Formulae for Hamiltonian Equations of Motion</b>	<b>193</b>
<b>B Summing Periodic Functions with Random Phases</b>	<b>197</b>



# List of Figures

1-1	Sample of observations from black holes with QPOs . . . . .	23
1-2	Power spectrum from hot spot model and data from <i>RXTE</i> . . . . .	28
2-1	Schematic picture of ray-tracing method . . . . .	45
2-2	Projection of image plane onto disk plane . . . . .	46
2-3	Relativistic transformation of an absorbing medium . . . . .	53
2-4	Schematic of photon path for radiative transfer equation . . . . .	54
2-5	Redshift transfer function for flat disks . . . . .	61
2-6	Line broadening as a function of inclination . . . . .	62
2-7	Line broadening as a function of spin; constant emission . . . . .	63
2-8	Observations of broad iron emission lines . . . . .	64
2-9	Observational evidence for the Blandford-Znajek process . . . . .	66
2-10	Line broadening as a function of spin; power-law emission . . . . .	67
3-1	Spectrogram of hot spot on circular orbit . . . . .	71
3-2	Required hot spot overbrightness for 1% rms modulation . . . . .	73
3-3	Light curves for a variety of inclinations . . . . .	74
3-4	Light curve and power spectrum for circular hot spot orbit . . . . .	75
3-5	Fourier amplitude $a_n(\text{rms})$ as a function of inclination and hot spot size	76
3-6	Spectrograms for a variety of spins, $i = 30^\circ$ . . . . .	77
3-7	Spectrograms for a variety of spins, $i = 75^\circ$ . . . . .	78
3-8	Fourier amplitude $a_n(\text{rms})$ as a function of inclination for $a/M = 0.9$	79
3-9	Radius of orbits with commensurate frequencies as a function of spin	80
3-10	Trajectory of hot spot with closed rosette orbit . . . . .	81
3-11	Light curve and power spectrum for eccentric hot spot orbit . . . . .	82
3-12	Harmonic power in beat modes as a function of inclination . . . . .	83
3-13	Harmonic power in beat modes as a function of eccentricity . . . . .	84
3-14	Power spectra for sheared hot spot arcs . . . . .	86
3-15	Matching LFQPOs and HFQPOs as a function of spin . . . . .	88

4-1	Power spectrum of multiple hot spots with random phases and finite lifetimes . . . . .	99
4-2	Geodesic coordinate frequencies as a function of radius . . . . .	102
4-3	Power spectrum of multiple hot spots at different radii . . . . .	105
4-4	QPO peak widths due to finite resonance width . . . . .	106
4-5	Schematic diagram for coronal scattering . . . . .	108
4-6	Power spectrum from a single hot spot, including coronal scattering .	111
4-7	Comparison of model spectrum with data from XTE J1550–564 . . .	115
4-8	Simulated bicoherence for ideal detector . . . . .	120
4-9	Analytic model for bicoherence of hot spot model . . . . .	121
4-10	Simulated bicoherence for next-generation X-ray timing mission . . .	123
5-1	Hydrodynamic fluid variables for an $\alpha$ -disk with $a/M = 0$ . . . . .	136
5-2	Hydrodynamic fluid variables for an $\alpha$ -disk with $a/M = 0.9$ . . . . .	137
5-3	2-D density and temperature profiles of $\alpha$ -disk with $a/M = 0$ . . . . .	149
5-4	2-D density and temperature profiles of $\alpha$ -disk with $a/M = 0.9$ . . . . .	150
5-5	Spectra of thermal steady-state $\alpha$ -disks . . . . .	154
6-1	Dipole scattering of linearly polarized radiation . . . . .	159
6-2	Dipole scattering of unpolarized radiation . . . . .	160
6-3	Photons traced from isotropic emitter at ISCO . . . . .	164
6-4	Coordinate transformations for electron scattering . . . . .	166
6-5	Scattering distribution for an ADAF corona . . . . .	170
6-6	Spectra of a thermal source scattering through a hot corona . . . . .	171
6-7	Spectrograms of hot spot emission including scattering, $i = 45^\circ$ . . . . .	173
6-8	Spectrograms of hot spot emission including scattering, $i = 75^\circ$ . . . . .	175
6-9	Integrated light curves for a range of optical depths . . . . .	177
6-10	Harmonic power as a function of optical depth . . . . .	178
6-11	Light curves in different <i>RXTE</i> energy bands . . . . .	179

# List of Tables

3.1	Black hole parameters, matching LFQPOs and HFQPOs to geodesic frequencies . . . . .	89
3.2	QPO amplitudes of the hot spot/arc model for XTE J1550–564 . . .	90
4.1	Widths of QPO peaks due to finite distribution of radii . . . . .	104
4.2	Best-fit model parameters for QPOs from XTE J1550–564 . . . . .	114
4.3	Amplitudes and widths of QPO peaks from XTE J1550-564 . . . . .	116
5.1	Accretion efficiency for torqued and non-torqued disks . . . . .	142
5.2	Ratio of $E_{\text{cut}}/E_{\text{max}}$ for steady-state disks . . . . .	153
6.1	Amplitudes and phase shifts of scattered light curves . . . . .	176



# Chapter 1

## Introduction and Outline

*I want to know God's thoughts; the rest are details.*

*My religion consists of a humble admiration of the illimitable superior Spirit who reveals Himself in the slight details we are able to perceive with our frail and feeble mind.*

-Albert Einstein

For nearly a century now, Einstein's special and general theories of relativity (SR/GR) have helped form our understanding of the universe. Yet still many of Einstein's most fundamental predictions have not been proven (or disproved, to be fair). Central among these predictions are the laws governing matter and radiation in the strong gravitational fields around neutron stars and black holes. As our observational and theoretical capabilities continue to advance, the ability to probe these strong field regions steadily improves. Some of the most recent of these impressive advances are the spatial and spectral resolution attainable with the *Chandra* and *XMM-Newton* observatories and the timing resolution of the *Rossi X-ray Timing Explorer (RXTE)*. The equally important developments in large-scale parallel processing have made cost-effective computing widely available for accurate, high-resolution astrophysical modeling.

However, the technological marvels of space observatories and the impressive simulations of massive supercomputers are limited in their ability to independently explain the laws of physics around black holes. Unfortunately, many of the data analysis tools used today to fit observations are lacking important fundamental physics. At the same time, many theoretical models for accretion disks do not include emission mechanisms that would allow us to compare them directly to observations. It is

within this context that we present a framework that works towards bridging the gap between theory and observations of black hole accretion disks.

The central foundation of this Thesis is a ray-tracing code for the Kerr metric, the basis of a more generalized analysis tool for relativistic accretion disk models. Often referred to as a “post-processor,” this tool could be used to analyze the raw output data from an independent simulation that models the dynamic behavior of accreting gas around the black hole. The ultimate goal for this tool is to allow direct comparison of a variety of simulations with spectral and timing observations of black hole binaries as well as active galactic nuclei (AGN). In the following chapters, we will describe the physics packages included in this analysis code and apply it to a number of simple models. In doing so, we hope to gain some insight into a number of observational features, such as the broad iron emission line, quasi-periodic oscillations (QPOs) in the X-ray light curves, and the shape of the continuum photon energy spectra from black hole systems.

## 1.1 Motivation

In the past decade, observations of X-ray emission from accreting neutron stars and black holes have introduced new possibilities for astrophysical tests of fundamental physics. Recent discoveries made by satellites such as *ASCA*, *BeppoSAX*, *RXTE*, *Chandra*, and *XMM-Newton* provide direct evidence for strong-field gravitational effects in compact binary systems and AGN. These results include Doppler-broadened iron  $K\alpha$  fluorescent emission from microquasars and millisecond variability of the X-ray flux from black holes in low-mass X-ray binaries [see McClintock & Remillard (2004) for an excellent review]. These measurements give the exciting prospect for determining a black hole’s mass and spin, as well as tests of general relativity in the strong-field regime.

The strong gravitational fields near a black hole introduce significant deviations from Newtonian physics, including the existence of an inner-most stable circular orbit (ISCO), a feature absent in the classical Kepler problem. Since accreting gas can efficiently lose energy and angular momentum only outside of the ISCO, the hydrodynamic and radiative behavior of the inner accretion disk should be strongly dependent on the structure of the spacetime metric near the ISCO. The famous “no hair” theorem states that the only observable features of a stationary, electrically neutral black hole are functions of its mass  $M$  and specific angular momentum  $a \equiv J/M$ .

Yet the spin is a much more difficult quantity to measure, since the leading order curvature terms scale as  $\sim M/r^3$  for the mass and  $\sim a/r^4$  for the spin contributions [see, e.g. Bardeen, Press, & Teukolsky (1972)], analogous to the relative scaling of monopole and dipole fields in electromagnetism. Thus any observable that is sensitive



to the spin parameter will presumably originate from the regions closest to the black hole. As with most observations in astrophysics, the most difficult ones are also the most rewarding. While mass is also the most important ingredient in Newtonian gravity, the spin is a fundamentally relativistic feature, so is one of the ideal means of probing strong gravity. By understanding the behavior of matter near the ISCO, we can determine the mass and angular momentum, and thus completely describe the black hole.

While all of the current observations of GR in the weak field regime are consistent with Einstein's theory [see Will (2001) for a review], it is still conceivable that GR may break down in the strong gravity limit. Alternatively, the black hole spacetime may not be strictly described by the Kerr metric, but possibly a perturbed version of the stationary "no-hair" case (Collins & Hughes, 2004). If this is the case, the proof of such a deviation would require precision measurements of the behavior of space time around black holes (De Deo & Psaltis, 2004; Psaltis, 2004a). We are actually nearing that level of precision with the present state of X-ray observations, but are still severely lacking in our theoretical understanding of the accretion and radiation physics that produce the X-ray emission. Until the theory is advanced significantly further, these phenomenal observations will not be able to either prove or disprove general relativity.

## 1.2 Historical Background

Much of the early history presented in this section is based on the excellent narrative in the book *Black Holes and Time Warps* by Kip Thorne (1994), a thoroughly satisfying read for both astrophysicists and non-scientists alike.

### 1.2.1 Theory

Unlike many of the other fundamental physics developments of the 20<sup>th</sup> century (e.g. quantum theory; standard model of particle physics), black holes were conceived of in theory long before any observational evidence pointed us in their direction. The original idea of a black hole was in fact the natural consequence for Newtonian gravity and a finite speed of light. First proposed by John Michell in 1783, a "dark star" was one for which the escape velocity from the surface was equal to or greater than the speed of light. In fact, for a given mass, this classical critical surface is identical to the event horizon for a Schwarzschild black hole. With the advent of the wave theory of light, Michell's thought experiment based on light corpuscles was not quite so compelling.

Only with the formulation of Einstein's general theory of relativity as a geometric

theory (in which even massless light waves would be affected by gravity's pull) did the question of dark stars resurface. Mere months after Einstein's original publication on GR, Karl Schwarzschild successfully derived the complete spacetime metric for the inside and outside of a spherically symmetric star, including the prediction of an event horizon from which even light could not escape (Schwarzschild, 1916a,b). Despite the elegance of the Schwarzschild solution, most physicists, including Einstein, resisted the idea of a black hole for many years, based largely on an aesthetic distaste for spacetime singularities where all known laws of physics would fail. Not until the 1960s was the theoretical astrophysics community more or less in consensus that dark stars were in fact physically possible and perhaps even "compulsory." Then in 1967, John Wheeler first coined the term *black hole* (Wheeler, 1968), and they passed from the realm of curious oddity to scientific reality.

Thorne refers to the decade extending roughly from the mid-sixties to the mid-seventies as the *Golden Age* of black hole research, when black holes evolved from a scientific reality to an entire field of intense theoretical and observational research. Some of the most important results to come out of this golden age were the "no hair" conjecture (Ginzburg, 1964; Israel, 1967; Price, 1972), the Kerr metric for spinning black holes (Kerr, 1963; Carter, 1966; Boyer & Lindquist, 1967), the Penrose process (Penrose, 1969), black hole thermodynamics (Hawking & Ellis, 1973; Bekenstein, 1973; Hawking, 1974, 1975; Bekenstein, 1975), and black hole perturbation theory (Teukolsky, 1972). During the same period, the seminal papers were written on accretion theory for compact objects (Lynden-Bell, 1969; Pringle & Rees, 1972; Shakura & Sunyaev, 1973; Novikov & Thorne, 1973; Page & Thorne, 1974). And finally, it was during this period that the GR Bible, often referred to simply as MTW, was "canonized" (Misner, Thorne, & Wheeler, 1973).

For the purposes of this Thesis, we are interested primarily in the astrophysically observable characteristics of black holes, which generally are the product of the accretion of hot gas and its emission of radiation. Many authors have approached the problem of accretion in compact binaries with a variety of different methods, both analytic and computational. One of the earliest is that of Bondi & Hoyle (1944), who consider spherically symmetric accretion. Surely the most popular theoretical paper on the physics of accretion disks is Shakura & Sunyaev (1973), which derives the basic structure and observational appearance of a steady-state thin accretion disk. Novikov & Thorne (1973) promptly extended this model to include full relativistic effects in the Kerr metric, which we will explore in greater detail in Chapter 5. Shapiro, Lightman, & Eardley (1976) brought these results closer in line with observations of hard photon spectra from Cygnus X-1 by including a hot corona around the disk, which is now a widely accepted feature of the accretion geometry (Paczynski, 1978; Haardt & Maraschi, 1993). An early theory for the coupling of magnetic fields between the

disk and the black hole was proposed by Blandford & Znajek (1977) and is still one of the leading explanations for the formation of relativistic jets. The application of accretion disk theory to neutron stars was spear-headed by Ghosh & Lamb (1978) with the addition of magnetic field effects in the inner disk.

In addition to the classical slim disk geometry, a number of thick disk and pseudo-spherical solutions have also been developed, most notably the advection-dominated accretion flows [ADAF; see Narayan & Yi (1994)], convection-dominated accretion flows [CDAF; see Narayan, Igumenshchev, & Abramowicz (2000)], the advection-dominated inflow-outflow solution [ADIOS; see Blandford & Begelman (1999)], and the disk + corona geometry mentioned above.

As the X-ray observations grew steadily more sensitive throughout the 1980s and 1990s (see Section 1.2.2 below), the focus of theoretical work shifted towards better understanding the data, much like the trend of most other branches of physics in the 20<sup>th</sup> century. Some approaches have simplified the hydrodynamics in favor of a flat, thin, steady-state disk and a more detailed treatment of general relativistic effects (George & Fabian, 1991; Laor, 1991; Karas, Vokrouhlicky, & Polnarev, 1992; Reynolds & Begelman, 1997; Dovciak, Karas, & Yaqoob, 2004). This approach focuses on calculating the *transfer function* of radiation from a flat disk to a distant observer, described below in Section 2.4.1, and most often applied to observations of broad iron emission lines and studies of photon polarization. More detailed spectra from finite thickness  $\alpha$ -disk models have been simulated in a series of papers by Hubeny et al., who include non-LTE (local thermodynamic equilibrium) radiation transport and the detailed vertical structure of the disk (Hubeny & Hubeny, 1997, 1998; Hubeny et al., 2000, 2001; Davis et al., 2004). Emission and absorption lines of many other atomic species have been studied in great detail by Jimenez-Garate et al. (2001) and applied successfully to high-resolution *XMM-Newton* observations (Jimenez-Garate et al., 2002).

To include dynamic effects, essential for modeling QPOs, others have included magnetohydrodynamics [MHD; Hawley & Krolik (2001); Armitage, Reynolds, & Chiang (2001)] in a pseudo-Newtonian potential (Paczynski & Wiita, 1980). These MHD calculations are in turn based on detailed local simulations of the magneto-rotational instability (Balbus & Hawley, 1991; Hawley, Gammie, & Balbus, 1995, 1996; Stone et al., 1996). Another relatively simple approach is through the use of smoothed particle hydrodynamics (Lanzafame, Molteni, & Chakrabarti, 1998; Lee & Ramirez-Ruiz, 2002), but this is a method that has yet to gain full acceptance in the astrophysical community, largely due to the difficulty in achieving convergent solutions with different codes. At the same time, it has the distinct advantage of being able to handle arbitrary accretion geometries in three dimensions with relative ease.

More recently, with the ever-increasing power of parallel computing, fully relativistic-

tic global MHD codes have been developed and tested (Gammie, McKinney, & Toth, 2003; De Villiers & Hawley, 2003; De Villiers, Hawley, & Krolik, 2003), yet as of this writing, they do not include the effects of radiation transport or emission, certainly an important ingredient in accretion disk physics. Furthermore, no MHD calculation to date has yet predicted the existence of QPOs at any particular frequency, much less those that have been observed. Again we face the disconnect between theory and experiment- even in the most sophisticated simulations, there remains no mechanism for producing spectra and light curves with real physical units with which to compare observations. We hope that the work presented in this Thesis will help bridge that gap.

### 1.2.2 Observations

As mentioned above in the previous section, theoretical predictions of the existence of black holes far preceded any observational evidence of them. As late as the 1960s, when most of the theoretical community was convinced at least of the possibility of their existence, there was still no known observation of such an object. Led by the theories of Zel'dovich and Novikov, a search began for bright X-ray sources produced by accreting black holes. The first major success in that search was the discovery of the accreting neutron star Sco X-1 by Riccardo Giacconi in 1962 (Giacconi et al., 1962) and later Cyg X-1 (Bowyer et al., 1965). The identification of Cyg X-1 as a black hole candidate was not proposed until after the launch of *Uhuru*, which also discovered periodic pulsations in the X-ray light curve (Giacconi et al., 1971; Webster & Murdin, 1972; Bolton, 1972).

Despite the excitement from the steady early successes of X-ray astronomy, in reality it was the radio astronomers who really discovered the first black holes, in the form of quasi-stellar objects, or *quasars*, a few years earlier. It was the identification of these compact radio sources with optical point sources (from which a redshift could be measured) that led to the realization that they were extremely luminous objects, orders of magnitude brighter than any known star (Schmidt, 1963; Greenstein & Matthews, 1963; Matthews & Sandage, 1963). The intrinsic luminosity of the quasar 3C273 is roughly equal to the Eddington limit (see Section 5.1.2 below) for a mass of  $6 \times 10^7 M_{\odot}$ , and thus the first evidence for supermassive black holes was found. The association of such objects with extended radio jets led to the likely possibility that these supermassive black holes were also rapidly spinning.

The birth of X-ray timing astronomy came with a series of satellites launched during the 1970s that discovered a large number of X-ray pulsars, attributed to magnetized, spinning, accreting neutron stars [for a review, see Rappaport & Joss (1983)]. *Einstein*, the first X-ray telescope with real imaging capabilities, was launched in 1978 and discovered the remarkable precessing jets of SS-433 and measured its spec-

tral properties (Seaquist et al., 1982; Watson et al., 1983). The subsequent missions of *EXOSAT*, *Tenma*, *Ginga*, *ROSAT*, *BeppoSAX*, and *ASCA* steadily improved in imaging and spectral resolution, sensitivity, and energy range.

The current generation of X-ray observatories is comprised of the three major satellites mentioned above: *RXTE*, *Chandra*, and *XMM-Newton*, as well as the recently launched *INTEGRAL* for high-energy observations, and the upcoming launch of *Astro-E2*, which will provide even higher resolution spectroscopy. An excellent review of the observations of black hole binaries is given by McClintock & Remillard (2004), and is the motivation for much of the work in this thesis. A few of the highlights of the last twenty years are outlined below:

- Application of the multicolor disk (MCD) model to explain the thermal spectra observed from accreting low-mass X-ray binaries (LMXBs) (Mitsuda et al., 1984). Determined disk temperatures in the range 1 – 2 keV.
- Broad iron emission lines were detected in a large variety of sources: Cyg X-1 with *EXOSTAT* (Barr, White, & Page, 1985), V404 Cyg with *Ginga* (Zycki, Done, & Smith, 1999a,b), the Seyfert 1 galaxy MCG–6-15-30 with *ASCA* (Tanaka et al., 1995), V4641 Sgr with *BeppoSAX* (Miller et al., 2002b), and XTE J1650-500 with *XMM-Newton* (Miller et al., 2002a).
- Esin, McClintock, & Narayan (1997) performed a comprehensive classification of multiple spectral states as a function of the total mass accretion rate (scaled to Eddington units).
- The discovery of ultraluminous X-ray sources (ULXs) that exceed the Eddington luminosity for a typical  $10M_{\odot}$  black hole (Fabbiano, 1989; Makishima et al., 2000; Fabbiano, Zezas, & Murray, 2001; Humphrey et al., 2003). One popular explanation for these ULXs is that they are accreting, intermediate-mass black holes with  $100 \lesssim M/M_{\odot} \lesssim 1000$  (Miller, Fabian, & Miller, 2004). Alternatively, they may be “normal” black holes that are exhibiting super-Eddington luminosities due either to relativistic beaming or very high mass-transfer rates for short periods when the system is not in hydrostatic equilibrium (Rappaport, Podsiadlowski, & Pfahl, 2004).
- By analyzing the orbits of stars in the galactic center, Ghez et al. (2003) and Schodel et al. (2003) have determined the radio source Sgr A\* to be a super-massive black hole with mass in the range  $(3 - 4) \times 10^6 M_{\odot}$ .
- Rapid X-ray flares from Sgr A\* with time scales less than an hour suggest the existence of hot gas near the inner-most stable circular orbit of the galactic center black hole (Baganoff et al., 2001). There is even some evidence that

the X-ray light curve of this source has QPO variability in the power spectrum (Aschenbach et al., 2004).

- Shortly after the launch of *RXTE* at the end of 1995, Strohmayer et al. (1996) discovered a pair of high frequency QPOs (HFQPOs) in neutron star binary system. Remillard et al. (1996) found a broader, weaker HFQPO in the black hole binary GRO J1655–40, soon followed by similar features in the power spectra of 4U 1543–47, XTE J1858+226, and XTE J1550–564 (Remillard & Morgan, 1998; Markwardt, Swank, & Taam, 1999; Remillard et al., 1999; Homan et al., 2001).
- McClintock & Remillard (2004) compiled a representative sample of photon energy spectra and light curve power spectra for many of these black hole systems, reproduced here in Figure 1-1. The QPOs typically are seen in the “Very High” or “Steep Power Law” spectral state, described in more detail later in this Thesis.
- Miller et al. (2001) first identified the 3:2 ratio of HFQPO pairs in XTE J1550–564, followed by identical ratios in GRO J1655–40, GRS 1915+105, and H1743–322 (Remillard et al., 2002; Homan et al., 2004; Remillard et al., 2004). Recently, similar ratios have been reported in intermediate-mass and even super-massive black holes (Abramowicz et al., 2004; Fiorito & Titarchuk, 2004; Aschenbach et al., 2004; Aschenbach, 2004; Torok, 2004), but these results are still quite preliminary and widely open to other interpretations.
- Miller & Homan (2005) have recently found evidence linking the phase of a low frequency QPO with the shape of the iron emission line in GRS 1915+105, giving a promising connection between the two leading methods of probing strong field gravity.

## 1.3 Outline of Methods and Results

### 1.3.1 Ray-tracing in the Kerr Metric

The central framework on which the results in this Thesis are based is a relativistic ray-tracing code that calculates the trajectories of photons in the Kerr spacetime of a spinning black hole. By tracing the photons from either the emitter to the observer or backwards in time from the observer to the emitter, we can reconstruct time-dependent images and spectra of the accretion region. When starting at the observer, the image plane is divided into pixels of equal solid angle, each corresponding to a

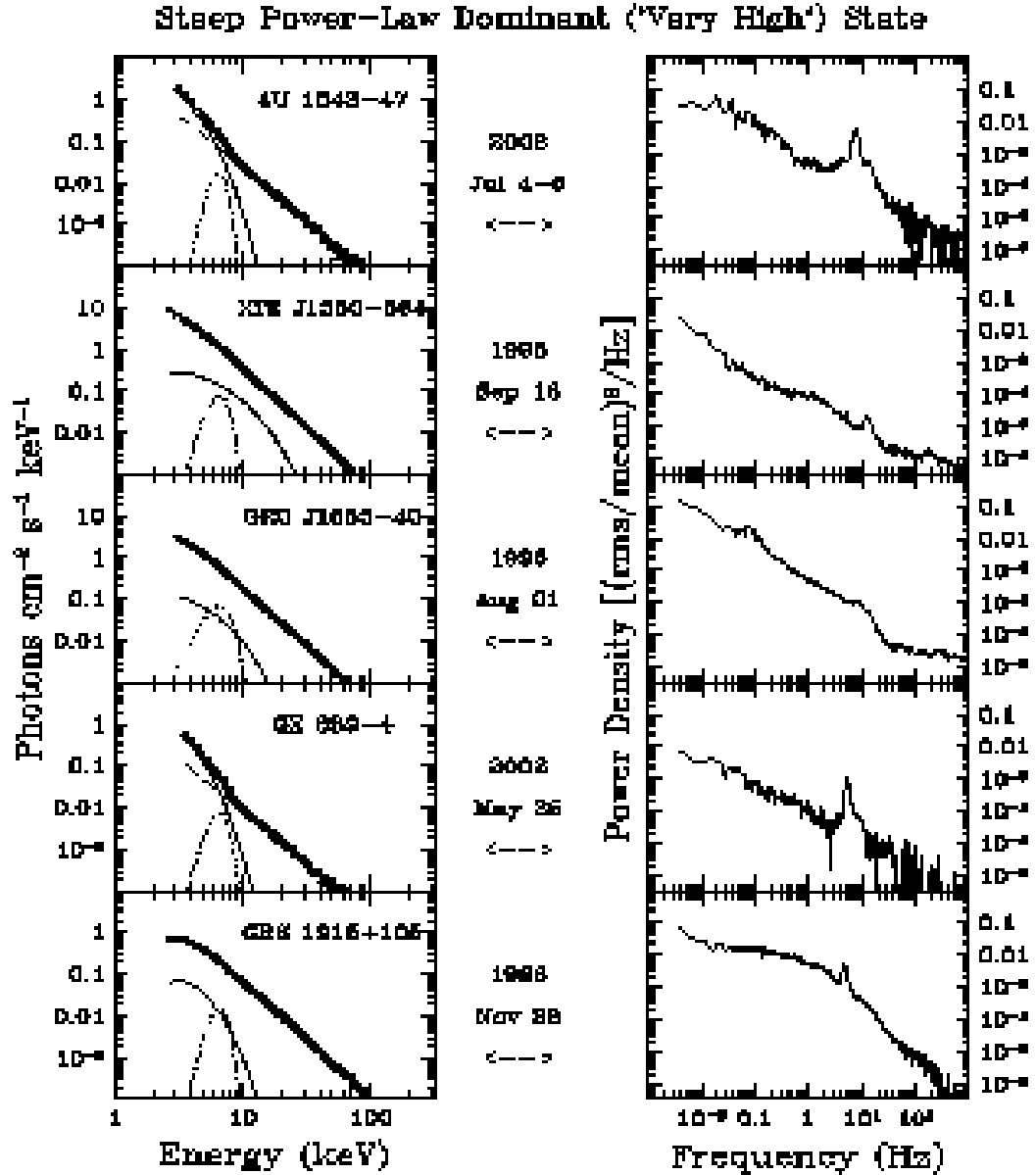


Figure 1-1: On the left is shown a collection of *RXTE* photon energy spectra from black hole binaries in the “Very High” state, characterized by a dominant steep power-law (dashed curve), a weaker thermal component (solid), and a faint broad iron emission line (dotted). On the right, *RXTE* power spectra from X-ray timing observations of the same sources show the presence of QPOs from  $\sim 5 - 500$  Hz. [Reproduced from McClintock & Remillard (2004) with permission]

single ray pointing in a slightly different direction, not unlike a classical telescope. Following the sample rays backward in time, we tabulate the spacetime position and momentum at multiple points on the trajectory, which are then used in conjunction with an emission model to solve the radiative transfer equation along the photon path. The gravitational lensing and magnification by the black hole is performed automatically by the geodesic integration of these evenly spaced photon trajectories, so that high magnification occurs in regions where nearby points in the disk are projected to points with large separation in the image plane.

In Chapter 2 we describe in detail the Hamiltonian methods used to numerically integrate the photon trajectories. The code primarily uses Boyer-Lindquist coordinates, but we also include a discussion of the Doran coordinate system and their relative benefits and drawbacks. Similarly, while we employ an adaptive-step Runge-Kutta integrator, Section 2.1.3 describes some of the alternative analytic methods for calculating trajectories with separable equations of motion.

To calculate physical processes such as emission, absorption, and scattering along the photon path, it is convenient to define locally orthonormal reference frames called “tetrads” at each point in coordinate space. Then the transformation from any tetrad basis to another defined at the same point can be carried out by a special relativistic Lorentz transformation, as described in Section 2.2.1. The Zero Angular Momentum Observer (ZAMO) tetrad is particularly useful in the Kerr metric, since unlike the Boyer-Lindquist coordinate basis, the ZAMO time coordinate is in fact time-like even inside the static limit (ergosphere). Based on the special relativistic discussion in Rybicki & Lightman (1979), Section 2.2.2 describes how we solve the classical radiative transfer equation numerically in general relativity by using the tetrad formalism. By combining these results with an independent hydrodynamic calculation of the accretion disk, we can in principle use the ray-tracing code as a post-processor analysis tool that allows direct comparison of simulations and observations.

Section 2.3 presents a description of the numerical techniques used to integrate the Hamiltonian equations of motion, both for photons and also massive test particles. Most of the results presented in this thesis are based on relatively benign computations, easily carried out in a few minutes on a personal computer. For the more time-intensive calculations, a parallel version of the code was developed to run on the Astrophysics Beowulf Cluster at MIT. Since the light rays can be treated as non-interacting, the problem can be split up trivially into multiple processes and thus scales extremely well with the number of processors.

Chapter 2 concludes with the application of the ray-tracing code to a flat disk made up of test particles on circular orbits in the plane normal to the black hole spin axis. Assuming each particle is a monochromatic, isotropic emitter in its rest frame, we calculate the “transfer function” from the disk to the observer. This function is



a measure of how the disk emission is relativistically redshifted, beamed, and lensed, and is a classic means of simulating the shape of broadened iron emission lines seen by many X-ray observations. We show how the transfer function is sensitive to the disk inclination, but not the black hole spin. Only when truncating the disk at the ISCO *and* scaling the emission by a power law (e.g.  $g(r) \sim r^{-\alpha}$ ), thus giving more weight to the inner regions, are the line profiles noticeably different for different spin values. However, since both the ISCO-truncation and  $r^{-\alpha}$  scaling are only conjectures as of this writing, the broadened emission lines do not seem to be an unambiguous means for measuring black hole spin. Hence we turn our attention in the direction of timing observations and QPOs.

### 1.3.2 The Hot Spot Model

Recent observations of commensurate integer ratios in the high-frequency QPOs of black hole accretion disks (Miller et al., 2001; Remillard et al., 2002), as well as the longstanding puzzles of the frequency variability of low-frequency QPO peaks and their correlations with X-ray flux and energy, motivate more detailed study of the QPO phenomenon as a means to determining the black hole parameters [for reviews, see Lamb (2003) and Psaltis (2004b)]. We have developed a model that is a combination of many of the above approaches (see Section 1.2.1), in which additional physics ingredients can be added incrementally to a framework grounded in general relativity. The model does not currently include radiation pressure, magnetic fields, or hydrodynamic forces, instead treating the emission region as a collection of cold test particles radiating isotropically in their respective rest frames. The dynamic model uses the geodesic trajectory of a massive particle as a guiding center for a small region of excess emission, a “hot spot,” that creates a time-varying X-ray signal, in addition to the steady-state background flux from the disk.

An early prototype of the hot spot model was originally proposed by Sunyaev (1972) as a means for identifying the black hole horizon (as opposed to a NS surface) as the emitter spirals in towards the horizon and then fades away to infinity. Bao (1992) calculated light curves and power spectra for a collection of random hot spots in an AGN disk to model the variability seen on time scales of hours or days. Our version of the hot spot model described in Chapter 3 is motivated by the similarity between the QPO frequencies and the black hole (or neutron star) coordinate frequencies near the ISCO (Stella & Vietri, 1998, 1999) as well as the suggestion of a resonance leading to 3:2 integer commensurabilities between these coordinate frequencies (Abramowicz & Kluzniak, 2001, 2003; Kluzniak & Abramowicz, 2001; Rebusco, 2004; Horak, 2004). Stella & Vietri (1999) investigated primarily the QPO frequency pairs found in low-mass X-ray binaries (LMXBs) with a neutron star (NS) accretor, but their basic methods can be applied to black hole systems as well. Both NS and BH binaries

also show strong low frequency QPOs (LFQPOs;  $\nu \approx 5 - 10$  Hz) at frequencies that vary between observations. One critical difference between these systems is the variability of the HFQPOs ( $\nu > 50$ Hz) in NS systems as opposed to the generally constant frequencies of the black hole HFQPOs (McClintock & Remillard, 2004). If anything, it seems more appropriate to apply the geodesic hot spot model to the black hole systems since they lack the complications of magnetic fields and X-ray emission from the rotating neutron star surface, which confuse the interpretation of coordinate frequencies. In fact, the QPOs from the two different types of compact binaries may be caused by two completely different physical mechanisms.

Markovic & Lamb (2000) have presented a thorough analysis of this hot spot model for a collection of NS binaries for which pairs of QPOs have been observed. Based on a number of observational and theoretical arguments, they conclude that the geodesic hot spot model is not a physically viable explanation for the observed neutron star QPOs. For low to moderate eccentricity orbits, the coordinate frequencies simply do not agree with the QPO data. For highly eccentric geodesics, they argue that the relative power in the different frequency modes are qualitatively at odds with the observations. Furthermore, they show that hydrodynamic considerations place strong constraints on the possible size, luminosity, coherency, and trajectories of the hot spots.

Many of these points are addressed in our version of the hot spot model. Also, by including full three-dimensional (3D) relativistic ray-tracing, we can quantitatively predict how much QPO power will be produced by a hot spot of a given size and emissivity moving along a geodesic orbit near the ISCO. In Section 3.1.1 we compute the hot spot overbrightness necessary to produce a given amplitude modulation in the light curve, as a function of disk inclination and black hole spin. Along with the special relativistic beaming of the emitted radiation, we find that strong gravitational lensing can cause high-amplitude modulations in the light curves, even for relatively small hot spots. To match the observed 3:2 frequency ratios, we used closed rosette orbits with  $\nu_\phi = 3\nu_r$  to give Fourier power at the beat modes  $\nu_\phi \pm \nu_r$ , and in Section 3.2 show the dependence of this power on the orbital eccentricity. The issues of differential rotation and shearing of the emission region as well as the possible connection to LFQPOs are addressed in Section 3.3 when we consider the generalization of the hot spot model to include arcs and non-planar geometries.

Perhaps the most powerful feature of the hot spot model is the facility with which it can be developed and extended to more general accretion disk geometries. In addition to providing a possible explanation for the commensurate HFQPOs in at least three systems (XTE J1550–564, GRO J1655–40, and H1743–322), the hot spot model with full general relativistic ray-tracing is a useful building block toward any other viable model of a dynamic 3D accretion disk. Within the computational framework of the

Kerr metric, we can investigate many different emission models and compare their predicted X-ray spectra and light curves with observations.

Chapter 4 introduces the first simple extension of the hot spot model, moving from a single periodic hot spot orbiting the black hole indefinitely at a single radius, to a collection of hot spots each with a finite lifetime, distributed over a range of radii and random phases. The corresponding power spectrum changes from the set of delta-functions described in Chapter 3 to a set of broad peaks characteristic of a *quasi*-periodic oscillation. We present a number of analytic models for the amplitudes and widths of the different peaks and confirm these results with direct ray-tracing calculations of multiple hot spots. In particular, we show how the addition of many hot spots with random phases will broaden every peak in the power spectrum by the same amount, while a distribution of geodesic orbits with a range of coordinate frequencies will broaden different peaks by different amounts. This “differential peak broadening” turns out to be a promising method for probing the spacetime structure near the ISCO, testing the assumptions of the hot spot model, and ultimately measuring the black hole spin.

In Section 4.5 we present a simplified model for electron scattering in a uniform density corona around the black hole. By giving a random added path length (and thus time delay) to each ray, the light curve gets smoothed out in time as each photon is assigned to a different time bin. This process does not contribute to broadening the QPO peaks, but can significantly damp out the higher harmonic modes in the power spectrum, much like the effect of shearing the hot spot into an arc. Finally, all the pieces of the model are brought together in Section 4.6 and used to interpret the power spectra from a number of observations of XTE J1550–564. Figure 1-2 shows the remarkable success this simple hot spot model has in fitting the *RXTE* data with only a few free parameters.

Based on a recent paper by Maccarone & Schnittman (2005), Section 4.7 introduces the use of higher-order statistics as an observational tool for distinguishing between the various peak broadening mechanisms. We apply these statistical methods to two different hot spot light curves that give similar power spectra: one broadened by random phases and one by a finite range of orbital frequencies. Not only can the bispectrum distinguish between these two models, but like the differential peak broadening method, it also can be used to map out the spacetime around the black hole.

### 1.3.3 Steady-state Disks

To gain more insight into the structure and continuum spectrum of the steady-state accretion flow, in Chapter 5 we develop a relativistic  $\alpha$ -disk model, based largely on the work of Shakura & Sunyaev (1973) and Novikov & Thorne (1973). Beginning

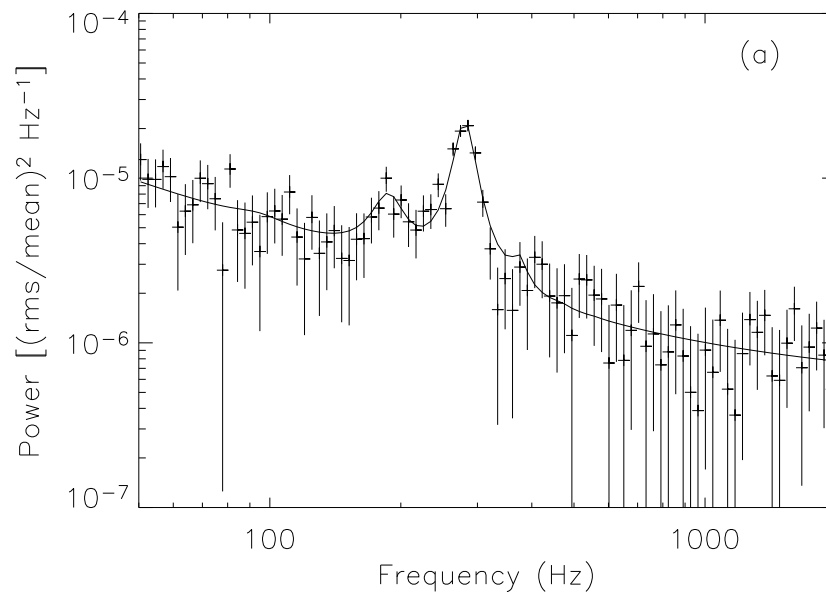


**Figure 1-2:** Comparison of hot spot model power spectrum (line) with data (crosses) from XTE J1550-564 [taken from Remillard et al. (2002)]. Details of the model are given in Chapters 3 and 4.

with the Novikov-Thorne equations for radial structure, we derive a set of boundary conditions for the vertical structure equations at each radius in the disk. These vertical structure equations for the density, temperature, pressure, and energy flux closely resemble the classical stellar structure equations for hydrostatic equilibrium (Hansen & Kawaler, 1994). The only difference is that here, the gravitational force is caused by the relativistic tidal force in the plane of the disk, and the thermal energy is generated not by nuclear fusion, but by turbulent viscosity. We also present an analytic “two-zone” model that gives the temperature and density at the mid-plane as well as the disk’s surface. With this analytic approach, we are able to derive a modified expression for the Eddington luminosity, giving an estimated upper limit to the accretion rate for the thin disk geometry.

To self-consistently model the torque on the inner edge of the disk, in Section 5.2 we show how the accreting gas expands along plunging geodesic trajectories inside of the ISCO. By matching the radial scale length of the plunge  $l_{\text{plunge}}$  to the turbulent scale length of the disk  $l_{\text{turb}} \approx h(R_{\text{ISCO}})$ , we can solve for the integrated stress at the ISCO, which in turn gives the initial conditions for the infalling radial velocity. Following a column of gas in the frame of the plunging particle, we can model the time-dependent vertical structure of the innermost disk with one-dimensional Lagrangian hydrodynamics. We find that the plunging disk temperature and density fall off rapidly inside the ISCO, contributing little to the thermal emission of the disk. However, we also show that even a small torque at the inner edge can significantly change the flux and surface temperature outside the ISCO, as well as the total accretion efficiency of the disk.

We outline the numerical methods used to solve for the disk structure in Section 5.3, both for inside and outside of the ISCO. The Lagrangian hydrodynamics is based on an implicit scheme described in Bowers & Wilson (1991). This implicit scheme is especially useful since the sound speed of the radiation pressure-dominated gas would otherwise demand an extremely small Courant step for an explicit approach. Given the temperature and scale height of the disk atmosphere, in Section 5.4 we use the relativistic ray-tracing code described above to calculate a “multi-colored” spectrum of the disk. This modified thermal spectrum is characterized by a slow rise with  $I_\nu \sim \nu$  at low energies, a broad peak around  $0.5 - 2$  keV, followed by a steep cutoff around 10 keV. The location of the thermal peak is a function of the black hole mass and accretion rate (and thus might ultimately be used to identify intermediate-mass black holes), while the cutoff frequency appears to be sensitive to the black hole spin and the inclination of the disk.

### 1.3.4 Electron Scattering

While the simple scattering model introduced in Section 4.5 ignored a number of important physical details, in Chapter 6 we revisit the topic of electron scattering with a Monte Carlo code including angular dependence, multiple scatterings, and relativistic effects. We begin with a derivation of electron scattering in the low-energy photon regime ( $h\nu \ll m_e c^2$ ), following the treatment of Rybicki & Lightman (1979). As with the treatment of the radiative transfer equation in Section 2.2.2, the classical results can easily be applied to a general relativistic model by transforming to a tetrad basis at the point of scattering. The major difference is that in Chapter 6 we trace the photons *forward* in time from the emitter to the observer. While conceptually simpler, this approach is computationally more intensive, but even that minor drawback can be somewhat mitigated, as will be explained in the main text.

The coronal electron density and temperature profiles can be approximated by a self-similar ADAF distribution (Narayan & Yi, 1994), which gives  $\rho_e \sim r^{-3/2}$  and  $T_e \sim r^{-1}$ . Thus most of the scattering events occur close to the hot spot emitter in the inner region of the disk/corona, where the scattering electrons are hottest. We assume an isotropic Maxwellian velocity distribution in the ZAMO frame, giving a random 4-velocity to each electron. Boosting from the ZAMO frame to the rest frame of the electron, we can use the Thomson differential cross section to determine the new photon momentum, which is then transformed back to the coordinate frame and then continues to propagate along its new geodesic path.

The electron scattering has two major observable effects: the thermal photon spectrum is modified by the inverse-Compton process [which can be approximated by solving the Kompaneets equation (Kompaneets, 1957)], giving a significant high energy power-law tail, and the integrated light curve is smoothed out in time, effectively damping the higher harmonic modes in the power spectrum. We also see some evidence of phase lags between different *RXTE* energy bands, since photons that experience more scattering events tend to have higher energy and a greater time delay to the observer (Galeev, Rosner, & Vaiana, 1979). Finally, in Section 6.4, we review the results of these scattering calculations in view of the observations and discuss the implications for various QPO models. Our tentative conclusion is that the HFQPO power is primarily produced by very *hot* hot spots with  $T_{\text{hs}} \gtrsim 5$  keV (as opposed to the relatively cool thermal disk at  $T_{\text{disk}} \sim 1$  keV), surrounded by a hot corona with moderate optical depth  $\tau_{\text{es}} \sim 1$  and temperature  $T_e \sim 100$  keV. As in Chapter 3, the higher harmonics are more likely damped by “arc-shearing,” and not repeated scatterings, which tend to damp out power in all harmonic modes of the light curve. Another possibility, which we have not yet thoroughly explored, is that the seed photons are not from a hot spot, but a more global, isotropic emitter like an oscillating torus. This would allow the electron corona to scatter the radiation field

isotropically yet still maintain significant amplitude modulations in time.

## 1.4 Alternative QPO Models

In this Thesis, we have focused primarily on the geodesic hot spot model for QPOs for a few reasons: (1) It is conceptually simple and not very computationally intensive to simulate spectra and light curves; (2) It is quite successful in fitting the data from *RXTE*, matching the QPO frequencies, peak widths, and amplitudes (or lack thereof); (3) It is easily expanded and can be used as a building block to construct more complex disk models. However, it also has its shortcomings: First and foremost, there is no clear physical explanation for how or why the hot spots should form around one special radius. Also, as we will see in Chapter 6, it is not clear why the QPOs should be more significant in the higher energy bands. Related to both of these questions is a marked lack of understanding of what the geometry of the accretion disk/corona is like in the Steep Power Law state, where most QPOs are seen.

Thus one of the major goals of this research is to develop a generalized analysis tool that can be applied to *any* disk model and compare simulations directly to observations. Here we give a brief summary of some of the more popular dynamic disk models in the literature today, along with a few representative references. In addition to the global GR-MHD simulations mentioned above (Gammie, McKinney, & Toth, 2003; De Villiers & Hawley, 2003; De Villiers, Hawley, & Krolik, 2003), there exist at least five basic concepts for producing the high frequency quasi-periodic oscillations seen from accreting black holes. In historical order (to the best of our limited knowledge), these are (1) magnetic flares (Galeev, Rosner, & Vaiana, 1979; Haardt, Maraschi, & Ghisellini, 1994; Stern et al., 1995b; Di Matteo, 1998; Beloborodov, 1999; Poutanen & Fabian, 1999), (2) diskoseismology (Okazaki, Kato, & Fukue, 1987; Nowak et al., 1997; Kato, Fukue, & Mineshige, 1998; Wagoner, 1999; Kato, 2001; Wagoner, Silbergleit, & Ortega-Rodriguez, 2001), (3) resonances at geodesic frequencies (Stella & Vietri, 1999; Stella, Vietri, & Morsink, 1999; Kluzniak & Abramowicz, 2001; Abramowicz et al., 2003; Rebusco, 2004; Horak, 2004), (4) oscillating axisymmetric tori (Lee & Ramirez-Ruiz, 2002; Rezzolla et al., 2003; Rezzolla, Yoshida, & Zanotti, 2003; Zanotti, Rezzolla, & Font, 2003; Lee, Abramowicz, & Kluzniak, 2004), and (5) Rayleigh-Taylor instabilities (Titarchuk, 2002, 2003; Li & Narayan, 2004). The hydrodynamic studies of Psaltis & Norman (2000) and Psaltis (2001a) combine the global MHD techniques with a semi-analytic treatment of the resonance frequencies of approach (3).

The magnetic flare model was introduced in the earliest days of X-ray timing astronomy to explain the high frequency variability of Cyg X-1 (Galeev, Rosner, & Vaiana, 1979). Similar to the magnetic flares in the solar atmosphere, they can produce short-lived, tightly confined regions of overbrightness on or above the accretion

disk surface. Magnetic flares are particularly promising for explaining the formation and subsequent destruction of hot spots, as well as the phase lags between soft and hard X-rays (Poutanen & Fabian, 1999), but at this point cannot explain the frequency locations of the QPO peaks or their integer commensurability.

The next model proposed was diskoseismology — the excitation of various trapped modes in an accretion disk [see Kato, Fukue, & Mineshige (1998); Wagoner (1999) for reviews]. This model seems not to be directly applicable to the data, at least for the cases where small integer ratios of frequencies exist; it would require considerable fine tuning in the different mass and spin values for the black holes to produce routinely a 3:2 frequency ratio. Global perturbations may also take the form of spiral density waves in the disk, much like the arms of the milky way (Gottlieb, 2002). However, like the classical diskoseismic modes, it may require fine tuning to produce the appropriate frequencies in the observed light curve.

Related to diskoseismology is the oscillating torus model of Rezzolla et al. (2003). This model also computes the frequencies of  $p$ -modes (i.e. sound waves), but in a geometrically thick, pressure supported torus (as expected at high accretion rates like those where the HFQPOs are seen), rather than in a geometrically thin, Keplerian accretion disk. In this case, the different overtones are found to be approximately in a series of integer ratios, starting from 2, so the model is compatible with existing data on high frequency QPOs in black holes. We have recently begun to apply the ray-tracing code to the torus model with mixed results. Assuming a simplified emission model and an optically thin torus, we can produce light curves with the output data from the hydrodynamic simulations. These light curves have significant modulation in the fundamental mode, but it seems very difficult to produce appreciable amplitude power in the overtones. Furthermore, the present version of the torus model is axisymmetric, but accretion flows have been shown to be susceptible to a number of hydrodynamic instabilities that would compromise this symmetry [see, e.g. Papaloizou & Pringle (1984, 1985); Hawley (2000)].

The model most recently applied to high frequency QPOs from black hole candidates is that of Rayleigh-Taylor instabilities, although the same basic idea had been applied earlier to QPOs from accreting neutron stars earlier (Titarchuk, 2002, 2003). In this picture, non-axisymmetric structures can grow unstably at the magnetospheric radius (presumed to exist also for black holes, as their accretion disks can become magnetically dominated) with frequencies of integer ratios of the angular frequency at that radius, though the lowest mode will be stable for relatively low gas pressures (Li & Narayan, 2004). Related to this model is that of Wang et al. (2003), who propose a magnetic coupling between the rotating black hole and the accretion disk as a means of producing high-frequency QPOs, analogous to the Blandford-Znajek process (Blandford & Znajek, 1977) sometimes used to explain the behavior of relativistic



jets.

After the first indications that small integer ratios between HFQPO frequencies were likely, it was noted by Abramowicz & Kluzniak (2001) that if the relativistic coordinate frequencies determined the frequencies of the quasi-periodic oscillations, then resonances between these different frequencies (e.g. vertical and radial epicyclic frequencies) might occur at locations in the accretion disk where these frequencies have small integer ratios. The excitation of these resonances could very well produce the regions of overdensity and overbrightness that we treat as geodesic hot spots.

In addition to these models for the high frequency QPOs, there are also a large number and variety of different models to describe the low frequency QPOs in black hole systems. Here too, global diskoseismic modes are used to explain the observed oscillations. These include the “normal disk” mode, where the entire disk is displaced by a small perturbation normal to the rotation plane (Titarchuk & Osherovich, 2000), and the “corrugation” or “c-mode” oscillations where the inner regions of an inclined disk precess at roughly the Lense-Thirring rate (Silbergleit, Wagoner, & Ortega-Rodriguez, 2001). A recent model by Tagger et al. (2004) employs “magnetic floods,” which in turn lead to the accretion-ejection instability (Tagger & Pellat, 1999), to explain the LFQPOs and also transfer energy from a cool disk to a hot corona. While this Thesis primarily focuses on HFQPOs, many of the techniques and models presented herein could easily be applied to observations and models of LFQPOs as well.



## Chapter 2

# Ray-Tracing in the Kerr Metric

*Do not worry about your difficulties in Mathematics.  
I can assure you mine are still greater.*

*God does not care about our mathematical difficulties.  
He integrates empirically.*

-Albert Einstein

The results presented in the next two chapters are based largely on the paper “The Harmonic Structure of High Frequency Quasi-periodic Oscillations in Accreting Black Holes,” by Schnittman & Bertschinger (2004), ApJ **606**, 1098.

### 2.1 Equations of Motion

To simulate the appearance of a distant black hole and surrounding accretion disk, we begin by dividing the image plane into regularly spaced “pixels” of equal solid angle in the observer’s frame, each corresponding to a single ray. Following the sample rays backward in time, we calculate the original position and direction that a photon emitted from the disk would require in order to arrive at the appropriate position in the detector. The gravitational lensing and magnification of emission from the plane of the accretion disk is performed automatically by the geodesic integration of these evenly spaced photon trajectories, so that high magnification occurs in regions where nearby points in the disk are projected to points with large separation in the image plane. To model the time-varying emission from the disk, each photon path is marked with the time delay along the path from the observer to the emission point in the

disk. Then coupled with a dynamic model for the accretion disk, we can reconstruct the observed X-ray “movies.”

To integrate the geodesic trajectories of photons or massive particles, we use a Hamiltonian formalism that takes advantage of certain conserved quantities in the dynamics (Bertschinger, 1999, 2001). The resulting equations of motion do not contain any sign ambiguities from turning points in the orbits, as are introduced by many classical treatments of the geodesic equations in the Kerr metric (see below, Section 2.1.3). We define a Hamiltonian function of eight phase space variables  $(x^\mu, p_\mu)$  and an integration variable (affine parameter)  $\lambda$  along the path length. For a general space-time metric  $g_{\mu\nu}(\mathbf{x})$  with inverse  $g^{\mu\nu}(\mathbf{x})$ , we can define a Hamiltonian  $H_2$  quadratic in the momenta as

$$H_2(x^\mu, p_\mu; \lambda) = \frac{1}{2}g^{\mu\nu}(\mathbf{x})p_\mu p_\nu = -\frac{1}{2}m^2, \quad (2.1)$$

where the rest mass  $m$  is a constant ( $m = 0$  for photons,  $m = 1$  for massive particles).

Applying Hamilton’s equations of motion from classical mechanics, we reproduce the geodesic equations:

$$\frac{dx^\mu}{d\lambda} = \frac{\partial H_2}{\partial p_\mu} = g^{\mu\nu}p_\nu = p^\mu, \quad (2.2a)$$

$$\frac{dp_\mu}{d\lambda} = -\frac{\partial H_2}{\partial x^\mu} = -\frac{1}{2}\frac{\partial g^{\alpha\beta}}{\partial x^\mu}p_\alpha p_\beta = g^{\gamma\beta}\Gamma_{\mu\gamma}^\alpha p_\alpha p_\beta. \quad (2.2b)$$

For any metric, the Hamiltonian  $H_2$  is independent of the affine parameter  $\lambda$ , allowing us to use one of the coordinates as the integration parameter and reduce the dimensionality of the phase space by two. We use the coordinate  $t = x^0$  as the independent time coordinate for the six dimensional phase space  $(x^i, p_i)$ . The corresponding Hamiltonian (now homogeneous of degree 1 in the momenta) is

$$H_1(x^i, p_i; t) \equiv -p_0 = \frac{g^{0i}p_i}{g^{00}} + \left[ \frac{g^{ij}p_i p_j + m^2}{-g^{00}} + \left( \frac{g^{0i}p_i}{g^{00}} \right)^2 \right]^{1/2} \quad (2.3)$$

with equations of motion

$$\frac{dx^i}{dt} = \frac{\partial H_1}{\partial p_i}, \quad (2.4a)$$

$$\frac{dp_i}{dt} = -\frac{\partial H_1}{\partial x^i}. \quad (2.4b)$$

We have thus reduced the phase space to the six-dimensional tangent bundle  $(x^i, p_i)$ . Moreover, because the Kerr metric is independent of  $t = x^0$  and  $\phi = x^3$ ,  $H_1 = -p_0$  and  $p_\phi$  are also integrals of motion. These two integrals of motion correspond to the

*Killing vectors*  $\xi_{(t)} = \partial_t$  and  $\xi_{(\phi)} = \partial_\phi$ . A Killing vector field  $\xi_\mu$  satisfies the equation

$$\nabla_\mu \xi_\nu + \nabla_\nu \xi_\mu = 0, \quad (2.5)$$

with  $\xi_\mu p^\mu = \text{const}$  along a geodesic trajectory (Misner, Thorne, & Wheeler, 1973).

Just as in classical mechanics, we can alternatively take the Lagrangian approach to the equations of motion, working with the coordinate velocities instead of the momenta [see e.g. Shapiro & Teukolsky (1983)]. In fact, one possible Lagrangian takes the same form as the original Hamiltonian in equation (2.1):

$$L_2(x^\mu, p^\nu; \lambda) = \frac{1}{2} g_{\mu\nu}(\mathbf{x}) p^\mu p^\nu = -\frac{1}{2} m^2. \quad (2.6)$$

The Euler-Lagrange equations of motion are

$$\frac{d}{d\lambda} \left( \frac{\partial L_2}{\partial p^\alpha} \right) - \frac{\partial L_2}{\partial x^\alpha} = 0. \quad (2.7)$$

Plugging equation (2.6) into (2.7) gives

$$\frac{d}{d\lambda} (g_{\alpha\nu} p^\nu) - \frac{1}{2} p^\mu p^\nu g_{\mu\nu,\alpha} = 0. \quad (2.8)$$

Writing

$$\frac{d}{d\lambda} g_{\alpha\nu} = \frac{\partial g_{\alpha\nu}}{\partial x^\mu} \frac{dx^\mu}{d\lambda}, \quad (2.9)$$

we get

$$g_{\alpha\nu} \frac{dp^\nu}{d\lambda} + \left( g_{\alpha\nu,\mu} - \frac{1}{2} g_{\mu\nu,\alpha} \right) p^\mu p^\nu = 0. \quad (2.10)$$

From symmetry in the indices, we can write

$$g_{\alpha\nu,\mu} p^\mu p^\nu = \frac{1}{2} (g_{\alpha\nu,\mu} + g_{\alpha\mu,\nu}) p^\mu p^\nu, \quad (2.11)$$

and then multiplying through by the inverse metric  $g^{\alpha\gamma}$  gives the Lagrangian geodesic equation:

$$\frac{d^2 x^\gamma}{d\lambda^2} + \Gamma_{\mu\nu}^\gamma p^\mu p^\nu = 0, \quad (2.12)$$

where  $\Gamma_{\mu\nu}^\gamma$  is the Christoffel symbol with its standard definition.

Despite the relative compactness of equation (2.12), the Lagrangian approach comes with the increased algebraic and computational cost of calculating all the Christoffel symbols (of which there are at least 20 different non-zero terms for the

Kerr metric). Recently Dovciak (2004) has compiled a complete list of the Christoffel terms in Kerr ingoing coordinates, as well as their first derivatives, which are necessary for integrating the geodesic deviation equation (Rauch & Blandford, 1994).

### 2.1.1 Boyer-Lindquist Coordinates

By far the most common implementation of the Kerr solution for a neutral, spinning black hole spacetime is the Boyer-Lindquist coordinate system (Boyer & Lindquist, 1967). In Boyer-Lindquist coordinates  $(t, r, \theta, \phi)$ , the Kerr metric may be written

$$g_{\mu\nu} = \begin{pmatrix} -\alpha^2 + \omega^2\varpi^2 & 0 & 0 & -\omega\varpi^2 \\ 0 & \rho^2/\Delta & 0 & 0 \\ 0 & 0 & \rho^2 & 0 \\ -\omega\varpi^2 & 0 & 0 & \varpi^2 \end{pmatrix}, \quad (2.13)$$

giving a line element

$$ds^2 = -\alpha^2 dt^2 + \varpi^2 (d\phi - \omega dt)^2 + \frac{\rho^2}{\Delta} dr^2 + \rho^2 d\theta^2. \quad (2.14)$$

This allows a relatively simple form of the inverse metric

$$g^{\mu\nu} = \begin{pmatrix} -1/\alpha^2 & 0 & 0 & -\omega/\alpha^2 \\ 0 & \Delta/\rho^2 & 0 & 0 \\ 0 & 0 & 1/\rho^2 & 0 \\ -\omega/\alpha^2 & 0 & 0 & 1/\varpi^2 - \omega^2/\alpha^2 \end{pmatrix}. \quad (2.15)$$

For a black hole of mass  $M$  and specific angular momentum  $a = J/M$ , we have defined (in geometrized units with  $G = c = 1$ )

$$\rho^2 \equiv r^2 + a^2 \cos^2 \theta \quad (2.16a)$$

$$\Delta \equiv r^2 - 2Mr + a^2 \quad (2.16b)$$

$$\alpha^2 \equiv \frac{\rho^2 \Delta}{\rho^2 \Delta + 2Mr(a^2 + r^2)} \quad (2.16c)$$

$$\omega \equiv \frac{2Mra}{\rho^2 \Delta + 2Mr(a^2 + r^2)} \quad (2.16d)$$

$$\varpi^2 \equiv \left[ \frac{\rho^2 \Delta + 2Mr(a^2 + r^2)}{\rho^2} \right] \sin^2 \theta. \quad (2.16e)$$

As a check, we see that equation (2.14) reduces to the well-known Schwarzschild metric in the limit  $a \rightarrow 0$ . In the limit  $M \rightarrow 0$  (holding  $a/M$  constant), it reduces to

flat spacetime with hyperbolic-elliptical coordinates.

The horizon can be defined as the surface where

$$r_{\pm} = M \pm \sqrt{M^2 - a^2}, \quad (2.17)$$

where, unlike the Schwarzschild solution, there are two distinct horizons, corresponding to the two roots of the equation  $\Delta(r) = 0$ . But as in the Schwarzschild case, no information or particles can escape once they cross the outer horizon, so we will define that as the effective surface of our black hole. From equation (2.17), it is also evident that the spin  $a$  must be less than or equal to  $M$ , or else the horizon will not exist and the result would be a “naked singularity.”

Another interesting feature of the Boyer-Lindquist coordinates is that the metric component  $g_{tt}$  can be greater than zero outside of the horizon. Solving the equation

$$g_{tt} = - \left( 1 - \frac{2Mr}{r^2 + a^2 \cos^2 \theta} \right) = 0 \quad (2.18)$$

gives us a formula for the surface of the “ergosphere”:

$$r_{\text{erg}} = M + \sqrt{M^2 - a^2 \cos^2 \theta}. \quad (2.19)$$

Inside of the ergosphere (where  $g_{tt} > 0$ ), there can exist no coordinate stationary observers, no matter how hard they fire their rockets. Thus the ergosphere is sometimes also referred to as the static limit. While it is always good to be cautiously skeptical about results based on the choice of coordinates in GR (the most common example is of course the coordinate singularity at the horizon of the Schwarzschild metric), this particular feature does have some physical significance. As shown by Penrose (1969), particles can exist inside the ergosphere with negative energy trajectories, get captured by the horizon, and effectively transfer angular momentum away from the black hole.

With the form of the metric given in equation (2.13), the Hamiltonian  $H_1$  can be written in Boyer-Lindquist coordinates

$$H_1(r, \theta, \phi, p_r, p_\theta, p_\phi; t) = \omega p_\phi + \alpha \left( \frac{\Delta}{\rho^2} p_r^2 + \frac{1}{\rho^2} p_\theta^2 + \frac{1}{\varpi^2} p_\phi^2 + m^2 \right)^{1/2}. \quad (2.20)$$

Since  $H_1$  is independent of  $t$ , it can be thought of as the conserved energy at infinity  $E_0 = H_1 = -p_t$ . This new Hamiltonian is also independent of  $\phi$  (azimuthally symmetric spacetime), giving the conjugate momentum  $p_\phi$  as the second integral of motion for  $H_1$ . We are now left with five coupled equations for  $(r, \theta, \phi, p_r, p_\theta)$ . The

third integral of motion, “Carter’s constant” (Carter, 1968a)

$$\mathcal{Q} \equiv p_\theta^2 + \cos^2 \theta [a^2(m^2 - p_0^2) + p_\phi^2 / \sin^2 \theta], \quad (2.21)$$

is used as an independent check of the accuracy of the numerical integration. In Appendix A, we include all the relevant derivatives and formulas for solving equations (2.4a, 2.4b, and 2.20).

## 2.1.2 Doran Coordinates

The Boyer-Lindquist coordinate system is relatively compact and easy to visualize in flat space, but shares with the Schwarzschild metric the problem of a coordinate singularity at the horizon. One way around this problem is presented by Doran (2000), who defines a new coordinate system in terms of observers freely falling from rest at infinity. This approach can be seen most clearly in the spherically symmetric Schwarzschild case, where the metric can be written

$$ds^2 = -d\tau^2 + \left[ dr + \left( \frac{2M}{r} \right)^{1/2} d\tau \right]^2 + r^2(d\theta^2 + \sin^2 \theta d\phi^2). \quad (2.22)$$

In these coordinates, the time  $d\tau$  is the same as the proper time measured by a free-falling observer, whose trajectory is given simply by

$$p^\mu = [1, -\sqrt{2M/r}, 0, 0] \quad (2.23a)$$

and

$$p_\mu = [-1, 0, 0, 0]. \quad (2.23b)$$

This solution is well-behaved at and inside the horizon, consistent with the fact that an observer crossing the horizon should feel nothing particularly special, which makes these coordinates especially useful for “flight simulators” that image the extreme gravitational lensing of observers falling into black holes (Hamilton, 2004). In fact, the trajectory defined by equation (2.23a) is consistent with the Newtonian law of gravity:

$$\frac{d^2 r}{d\tau^2} = -\frac{M}{r^2}. \quad (2.24)$$

Doran’s achievement was extending this approach to the Kerr metric, following the trajectories of free-falling observers as they get swept into the swirling spacetime around the black hole. This approach has recently been explained in detail with the *River Model* of Hamilton & Lisle (2004). Following Bertschinger (2001), it is



convenient to define

$$b \equiv (r^2 + a^2)^{1/2}, \quad c \equiv (2Mr)^{1/2}. \quad (2.25)$$

In Doran coordinates, the metric of a spinning black hole has the form

$$ds^2 = -d\tau^2 + \left[ \frac{\rho}{b} dr + \frac{c}{\rho} (d\tau - a \sin^2 \theta d\bar{\phi}) \right]^2 + \rho^2 d\theta^2 + b^2 \sin^2 \theta d\bar{\phi}^2, \quad (2.26)$$

where  $r$  and  $\theta$  have the same meaning as in the Boyer-Lindquist metric,  $\tau$  is the free-falling observer's proper time, and  $\bar{\phi}$  is defined by the trajectory of a free-falling particle with zero angular momentum at infinity. Thus, unlike the Boyer-Lindquist case, in Doran coordinates particles can fall in “radially” along paths of constant  $\theta$  and  $\bar{\phi}$ . The Boyer-Lindquist  $t$  and  $\phi$  can easily be recovered via the transformations

$$t = \tau + \int_r^\infty \frac{bc}{\Delta} dr \quad (2.27a)$$

and

$$\phi = \bar{\phi} + \int_r^\infty \frac{ac}{b\Delta} dr. \quad (2.27b)$$

As above, the equations of motion are perfectly well-behaved at the horizon, making it an attractive coordinate system for calculating physical processes there. Furthermore, the inverse metric also has a very convenient form:

$$g^{\mu\nu} = \begin{pmatrix} -1 & bc/\rho^2 & 0 & 0 \\ bc/\rho^2 & \Delta/\rho^2 & 0 & ac/b\rho^2 \\ 0 & 0 & 1/\rho^2 & 0 \\ 0 & ac/b\rho^2 & 0 & 1/b^2 \sin^2 \theta \end{pmatrix}. \quad (2.28)$$

The same Hamiltonian approach to the equations of motion works even better in Doran coordinates, since there are no imaginary roots in the Hamiltonian even inside the event horizon. Equation (2.3) can be expressed in the Doran metric as

$$H_1(r, \theta, \bar{\phi}, p_r, p_\theta, p_{\bar{\phi}}; \tau) = -\frac{bc}{\rho^2} p_r + D, \quad (2.29)$$

where the determinant  $D^2$  is given by

$$D^2 = \left( \frac{b^2}{\rho^2} + \frac{a^2 c^2 \sin^2 \theta}{\rho^4} \right) p_r^2 + \frac{2ac}{b\rho^2} p_r p_\theta + \frac{p_\theta^2}{\rho^2} + \frac{p_{\bar{\phi}}^2}{b^2 \sin^2 \theta} + m^2. \quad (2.30)$$

Since  $D^2 > 0$  for all  $r \geq 0$  and  $\rho > 0$ , it is particularly easy to parameterize trajectories (even inside the horizon) with the Doran time coordinate  $\tau$ . As we mentioned above, particles falling from rest at infinity will follow paths of constant  $\theta$  and  $\phi$ . Thus, like the Schwarzschild case, the geodesics can be defined by

$$p^\mu = [1, -bc/\rho^2, 0, 0] \quad (2.31a)$$

and

$$p_\mu = [-1, 0, 0, 0]. \quad (2.31b)$$

Despite the many attractive features of the Doran coordinates, for the majority of the calculations in this thesis, we will generally use the more traditional Boyer-Lindquist coordinate system. First, we will not be considering processes on or inside the horizon, so need not worry too much about the coordinate singularities there. Second, since for the most part we are interested in comparing theory with experiment, it is particularly convenient to use the Boyer-Lindquist  $t$  coordinate to parameterize trajectories, since  $t$  corresponds with the distant observer's proper time. Lastly, to a certain degree, we must be slaves to convention, especially when comparing with previously published results, and the Boyer-Lindquist coordinates are by far the predominant coordinates for modeling the Kerr metric in the literature.

### 2.1.3 Analytic Methods

The Hamiltonian equations of motion described above can be reduced from eight to five coupled, first-order differential equations by employing the symmetries in  $t$  and  $\phi$ . For ease of implementation, we have not employed Carter's constant  $\mathcal{Q}$  in the equations of motion, but rather use it as an independent check for the accuracy of our numerics. Many traditional schemes to calculate trajectories in the Kerr metric use this additional integral of motion to further reduce the dimensionality of the problem and even reduce the problem to one of quadrature integration [e.g. Rauch & Blandford (1994)]. While potentially increasing the speed of the computation, this approach also introduces significant complications in the form of arbitrary signs in the equations of motion corresponding to turning points in  $r$  and  $\theta$ .

As Carter (1968b) first showed, the Lagrangian equations of motion can be written

in separable form as [in Boyer-Lindquist coordinates, following Merloni et al. (1999)]:

$$\rho^2 \frac{dr}{d\lambda} = \pm \sqrt{R(r)} \quad (2.32a)$$

$$\rho^2 \frac{d\theta}{d\lambda} = \pm \sqrt{\Theta(\theta)} \quad (2.32b)$$

$$\rho^2 \frac{d\phi}{d\lambda} = \frac{p_\phi}{\sin^2 \theta} + ap_t + \frac{aP}{\Delta} \quad (2.32c)$$

$$\rho^2 \frac{dt}{d\lambda} = a(p_\phi + ap_t \sin^2 \theta) + (r^2 + a^2) \frac{P}{\Delta} \quad (2.32d)$$

where

$$\Theta(\theta) = \mathcal{Q} - \cos^2 \theta [a^2(1 - p_t^2) + p_\phi^2 / \sin^2 \theta] \quad (2.33a)$$

$$P(r) = -p_t(r^2 + a^2) - ap_\phi \quad (2.33b)$$

$$R(r) = P^2 - \Delta [m^2 r^2 + \mathcal{Q} + (p_\phi + ap_t)^2], \quad (2.33c)$$

with  $p_t$ ,  $p_\phi$ , and  $\mathcal{Q}$  constants of the motion as described above.

Now here is where things start to get complicated. A single trajectory can have both positive and negative signs in equations (2.32a) and (2.32b) along different segments of its path. So the first thing that needs to be done is solve for the turning points of  $R(r)$  and  $\Theta(\theta)$  at  $r_0$  and  $\theta_0$ , respectively. Then  $r$  and  $\theta$  can be solved parametrically by equating

$$\rho^2 = \frac{dr}{\pm \sqrt{R(r)}} = \frac{d\theta}{\pm \sqrt{\Theta(\theta)}}, \quad (2.34)$$

or

$$\int_{r_0}^r \frac{dr'}{\sqrt{R(r')}} = (\text{sgn}_r)(\text{sgn}_\theta) \int_{\theta_0}^\theta \frac{d\theta'}{\sqrt{\Theta(\theta')}}, \quad (2.35)$$

where the signs ( $\text{sgn}_r$ ) and ( $\text{sgn}_\theta$ ) are equal to  $\pm 1$  and change whenever a turning point is reached for either variable. Rauch & Blandford (1994) show how these solutions can be written in terms of elliptic integrals, further accelerating the speed of computation.

Once the values of  $r$  and  $\theta$  are known along the trajectory,  $\rho^2$  is known and then equations (2.32c) and (2.32d) can be computed directly, and the entire trajectory is known. The momentum components  $p_r$  and  $p_\theta$  can be reproduced trivially from  $p^\mu$  and the metric, as in the Lagrangian approach.

For equatorial orbits with  $\theta = \pi/2$  and  $p^\theta = 0$ , it is relatively straightforward to frame the equations of motion in terms of an effective potential, as is often done for Schwarzschild orbits. In this case, equations (2.32a-2.32b) reduce to (Shapiro &

Teukolsky, 1983)

$$\frac{dt}{d\lambda} = -\frac{1}{r^2\Delta}[(r^4 + a^2r^2 + 2Ma^2r)p_t + 2aMp_\phi r] \quad (2.36a)$$

$$\frac{d\phi}{d\lambda} = \frac{1}{r^2\Delta}[(r^2 - 2Mr)p_\phi - 2aMp_t] \quad (2.36b)$$

$$\left(\frac{dr}{d\lambda}\right)^2 = \frac{1}{r^4}R(r, p_t, p_\phi), \quad (2.36c)$$

with  $R(r, p_t, p_\phi)$  defined as in equation (2.33c). In equation (2.36c), the right hand side  $R/r^4$  can be thought of as an effective potential for radial motion in the equatorial plane. Stable circular orbits for massive particles exist when

$$R = 0; \quad \frac{\partial R}{\partial r} = 0; \quad \frac{\partial^2 R}{\partial r^2} \leq 0. \quad (2.37)$$

The inner-most stable circular orbit (ISCO) occurs at the smallest possible  $r$  where a solution to equations (2.37) exists. From Bardeen, Press, & Teukolsky (1972), this radius is given by

$$r_{\text{ISCO}}/M = 3 + Z_2 \mp [(3 - Z_1)(3 + Z_1 + 2Z_2)]^{1/2}, \quad (2.38)$$

where

$$Z_1 \equiv 1 + \left(1 - \frac{a^2}{M^2}\right)^{1/3} \left[\left(1 + \frac{a}{M}\right)^{1/3} + \left(1 - \frac{a}{M}\right)^{1/3}\right] \quad (2.39a)$$

and

$$Z_2 \equiv \left(3\frac{a^2}{M^2} + Z_1^2\right)^{1/2}. \quad (2.39b)$$

Here the upper signs refer to prograde orbits (particles orbiting in the same direction as the black hole angular momentum) and the lower signs correspond to retrograde orbits. For the Schwarzschild case with  $a/M = 0$ , the ISCO is located at  $r = 6M$ , while for a maximally spinning Kerr black hole with  $a/M = 1$ , the prograde ISCO is at  $r = M$  and the retrograde ISCO is at  $r = 9M$  [ $R_{\text{ISCO}}(a/M)$  for prograde orbits is plotted as a dashed line in Fig. 3-9 below].

## 2.2 Geodesic Ray-tracing

The initial conditions for the photon or particle geodesics are determined in the local orthonormal frame of a “Zero Angular Momentum Observer” (ZAMO). The ZAMO

basis is defined such that the spatial axes are aligned with the coordinate axes and then the time axis is determined by orthogonality (see Section 2.2.1).

At a point far away from the black hole, the spacetime is nearly flat so Euclidean spherical geometry gives the spatial direction of the photon  $n^{\hat{i}}\mathbf{e}_{\hat{i}}$ , from which the initial momentum in the coordinate basis is calculated:

$$p_t = -E_{\text{obs}}(\omega\varpi n^{\hat{\phi}} + \alpha) \quad (2.40a)$$

$$p_r = E_{\text{obs}}\sqrt{\frac{\rho^2}{\Delta}} n^{\hat{r}} \quad (2.40b)$$

$$p_\theta = E_{\text{obs}}\sqrt{\rho^2} n^{\hat{\theta}} \quad (2.40c)$$

$$p_\phi = E_{\text{obs}}\sqrt{\varpi^2} n^{\hat{\phi}}, \quad (2.40d)$$

where the photon energy measured by the distant ZAMO is  $E_{\text{obs}}$ .

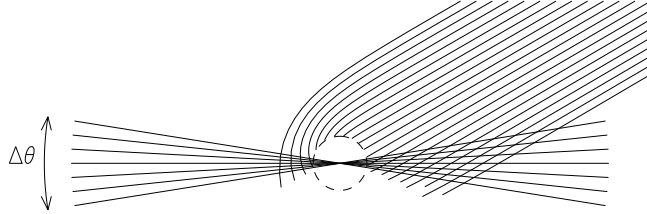


**Figure 2-1:** Schematic picture of ray-tracing method from distant observer through a disk of angular thickness  $\Delta\theta$ . The rays either terminate at the black hole horizon (dashed circle) or pass through the disk, with each point of intersection labeled with the photon position and momentum  $(x^\mu, p_\mu)$ .

The photon trajectories are integrated backward in time from the image plane oriented at some inclination angle  $i$  with respect to the axis of rotation for the black hole, where  $i = 0^\circ$  corresponds to a face-on view of the disk and  $i = 90^\circ$  is an edge-on view. The accretion disk is confined to a finite region of latitude with angular thickness

$\Delta\theta$ , oriented normal to the rotation axis. The photons terminate either at the event horizon or pass through the surfaces of colatitude ( $\theta = \text{const}$ ), as shown in Figure 2-1. As trajectories pass through the disk, the photon's position and momentum ( $x^\mu, p_\mu$ ) are recorded at each plane intersection in order to later reconstruct an image of the disk.

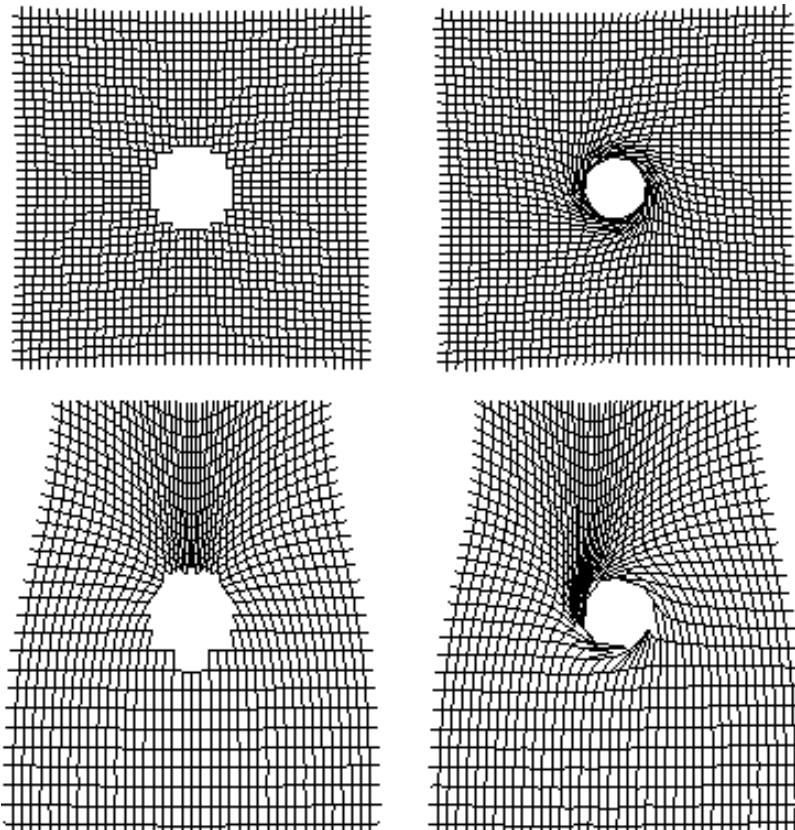


**Figure 2-2:** Projection of a uniform Cartesian grid in the image plane onto the source plane of the accretion disk ( $\theta = \pi/2$ ). Inclination angles are  $i = 0^\circ$  (*top*) and  $i = 60^\circ$  (*bottom*) and spin parameters are  $a/M = 0$  (*left*) and  $a/M = 0.95$  (*right*). The region inside the horizon is cut out from each picture.

For an infinitely thin disk ( $\Delta\theta \rightarrow 0$ ), it is easy to show how the image plane maps onto the source plane. Taking an evenly spaced grid of initial photon directions, Figure 2-2 plots the positions of intersection with the source plane, in pseudo-Cartesian

coordinates defined by

$$x = \sqrt{r^2 + a^2} \cos \phi \quad (2.41a)$$

$$y = \sqrt{r^2 + a^2} \sin \phi. \quad (2.41b)$$

Photons that cross the black hole event horizon before intersecting the plane are not shown. For  $i > 0^\circ$ , as the rays are deflected by the black hole, they tend to be focused on the far side, giving a strong magnification by mapping a large area in the image plane onto a small area of the source plane, as seen here by a higher density of lattice grid points. For the flat disk geometry, rays are not allowed to pass through the plane defined by  $\theta = 0$ , so we do not see multiple images of sources “behind” the black hole, as is often observed in the strong gravitational lensing of distant quasars by intervening galaxies (Hewitt et al., 1988). However, for sufficiently high inclinations and spin values, single points in the equatorial plane can be mapped to different regions of the image plane, creating multiple images of certain regions of the disk. This effect is seen in the folding of the image map onto itself near the horizon in the bottom right of Figure 2-2.

The disk itself is modeled as a collection of mass elements moving along geodesic orbits around the black hole, emitting isotropic, monochromatic light with energy  $E_{\text{em}}$  in the emitter’s rest frame. For each photon with 4-momentum  $p_\mu(\mathbf{x}_{\text{em}})$  intersecting a particle trajectory with 4-velocity  $v^\mu(\mathbf{x}_{\text{em}})$ , the measured redshift at the observer is given by

$$\frac{E_{\text{obs}}}{E_{\text{em}}} = \frac{p_\mu(\mathbf{x}_{\text{obs}})v^\mu(\mathbf{x}_{\text{obs}})}{p_\mu(\mathbf{x}_{\text{em}})v^\mu(\mathbf{x}_{\text{em}})}, \quad (2.42)$$

where for a distant observer at  $r \rightarrow \infty$ , we take  $v^\mu(\mathbf{x}_{\text{obs}}) = [1, 0, 0, 0]$ .

For disk models with finite thickness, the radiative transfer equation can be solved as the ray passes through the disk. While the classical transfer equation is applicable in the locally flat frame of the emitting gas, the spectral intensity at a given frequency also evolves as the photons are gravitationally red-shifted through the spacetime around the black hole, maintaining the Lorentz invariance of  $I_\nu/\nu^3$ . This Lorentz factor also accounts for the special relativistic beaming that is especially important in the hot spot model. The coupling of the geodesic ray-tracing and the radiation transfer equation is described in greater detail below in Section 2.2.2.

For most of the calculations presented in this Section, we are primarily concerned with radiation coming from a limited region of the disk, treated as a monochromatic source with zero opacity. When calculating the emission from a flat, steady-state disk, the plane defined by  $\cos \theta = 0$  is taken to be totally opaque so that rays cannot curve around and see the “underside” of the accretion disk. In the “thick disk” case, for each pixel  $(i, j)$  in the image plane, an observed photon bundle spectrum  $I_\nu(t_{\text{obs}}, i, j)$

is given for each time step  $t_{\text{obs}}$  by integrating the contribution of the hot spot and the disk through the computational grid. This collection of incident photons can then be summed to give time-dependent light curves, spectra, or spatially resolved images.

As mentioned above in the Introduction, one of the most promising applications of this approach is the ability to use the ray-tracing code as a post-processor to analyze other, more detailed simulations of the accretion disk. For example, we could take the tabulated output of a three-dimensional hydrodynamic calculation such as those by De Villiers, Hawley, & Krolik (2003) or Zanotti, Rezzolla, & Font (2003) and, with a given emission mechanism, produce simulated images and spectra. These simulations generally follow the hydrodynamic variables (e.g. density, temperature, velocity and magnetic fields) within a collection of volume elements. For the most part, these variables are defined with respect to an observer’s locally orthonormal reference frame. Such a frame is often referred to as a “tetrad,” and is an important tool for analyzing any physical process in general relativity.

### 2.2.1 Tetrads

One of the cornerstones of general relativity is the principle that, on small enough scales, spacetime can be treated as locally flat. In these locally Minkowski reference frames, physics appears (to first order) to follow the laws of special relativity. For much of the above discussion in this chapter, we have primarily used a global coordinate basis, which allows for a relatively straightforward metric and equations of motion for geodesic trajectories. Yet when modeling physical events such as photon-electron scattering or solving the radiative transfer equation (2.50), it is more convenient to define a locally flat, orthonormal coordinate basis, conventionally called a *tetrad*.

One of the simplest examples of such a tetrad is that of the *coordinate stationary observer* (CSO) in the Schwarzschild metric. This tetrad is exactly what it sounds like: an orthonormal basis fixed to an observer instantaneously at rest with coordinate 4-velocity  $v^\mu(\text{CSO}) \propto [1, 0, 0, 0]$ . The basis axes in such a tetrad are parallel to those of the coordinate basis, but normalized so that the metric appears to be locally



Minkowski. Denoting tetrad vectors by “hat” indices  $\hat{\mu}$ , the CSO tetrad  $\mathbf{e}_{\hat{\mu}}$  is

$$\mathbf{e}_{\hat{t}} = \left(1 - \frac{2M}{r}\right)^{-1/2} \mathbf{e}_t \quad (2.43a)$$

$$\mathbf{e}_{\hat{r}} = \left(1 - \frac{2M}{r}\right)^{1/2} \mathbf{e}_r \quad (2.43b)$$

$$\mathbf{e}_{\hat{\theta}} = \frac{1}{r} \mathbf{e}_\theta \quad (2.43c)$$

$$\mathbf{e}_{\hat{\phi}} = \frac{1}{r \sin \theta} \mathbf{e}_\phi. \quad (2.43d)$$

To transform between bases, we follow the approach employed in any standard vector analysis text: writing the invariant vector  $\mathbf{p}$  as a linear combination of basis vectors:

$$\mathbf{p} = \mathbf{e}_\mu p^\mu = \mathbf{e}_{\hat{\mu}} p^{\hat{\mu}}, \quad (2.44)$$

the transformation can be written as a matrix operation

$$p^\mu = E_{\hat{\mu}}^\mu p^{\hat{\mu}} \quad p^{\hat{\mu}} = E_{\mu}^{\hat{\mu}} p^\mu \quad (2.45)$$

with

$$E_{\hat{\mu}}^\mu = \begin{pmatrix} 1/\sqrt{1-2M/r} & 0 & 0 & 0 \\ 0 & \sqrt{1-2M/r} & 0 & 0 \\ 0 & 0 & 1/r & 0 \\ 0 & 0 & 0 & 1/r \sin \theta \end{pmatrix} \quad (2.46)$$

and

$$[E_{\mu}^{\hat{\mu}}] = [E_{\hat{\mu}}^\mu]^{-1}. \quad (2.47)$$

While it does not make a difference for diagonal or symmetric transformations, in general we will write matrix components with the lower index labeling the matrix row and the upper index labeling the column.

As mentioned above in Section 2.1.1, there is a region around a Kerr black hole called the ergosphere, where no coordinate stationary observers can exist. In other words, there is no physical acceleration that can give a time-like trajectory with  $v^\mu \propto [1, 0, 0, 0]$ . Since spacetime itself appears to be rotating faster than the speed of light, if we want to create a locally Minkowski coordinate basis, the only option is to “go with the flow.” In this approach, we consider the observer orbiting the black hole on a non-geodesic orbit at the frequency  $\omega$  as defined in equation (2.16d) (not to be confused with an actual massive particle orbiting on a circular orbit at the Kepler frequency  $\Omega_\phi$ ). Since this observer’s 4-momentum component in the  $\mathbf{e}_\phi$  direction is

$p_\phi = 0$ , it is called a “Zero Angular Momentum Observer,” or ZAMO. Due to the non-diagonal components of the Kerr metric, the ZAMO 4-velocity has  $p^\phi \neq 0$ , and is thus not a CSO.

The ZAMO tetrad  $\mathbf{e}_{\hat{\mu}}$  is derived in Bardeen, Press, & Teukolsky (1972) in Boyer-Lindquist coordinates:

$$\mathbf{e}_{\hat{t}} = \frac{1}{\alpha} \mathbf{e}_t + \frac{\omega}{\alpha} \mathbf{e}_\phi \quad (2.48a)$$

$$\mathbf{e}_{\hat{r}} = \sqrt{\frac{\Delta}{\rho^2}} \mathbf{e}_r \quad (2.48b)$$

$$\mathbf{e}_{\hat{\theta}} = \sqrt{\frac{1}{\rho^2}} \mathbf{e}_\theta \quad (2.48c)$$

$$\mathbf{e}_{\hat{\phi}} = \sqrt{\frac{1}{\varpi^2}} \mathbf{e}_\phi. \quad (2.48d)$$

The corresponding change of basis is given by

$$E_{\hat{\mu}}^\mu = \begin{pmatrix} 1/\alpha & 0 & 0 & \omega/\alpha \\ 0 & \sqrt{\Delta/\rho^2} & 0 & 0 \\ 0 & 0 & 1/\rho & 0 \\ 0 & 0 & 0 & 1/\varpi \end{pmatrix}. \quad (2.49)$$

As mentioned above, one advantage of the ZAMO basis is that the basis vector  $\mathbf{e}_{\hat{t}}$  is time-like ( $g_{\hat{t}\hat{t}} < 0$ ) everywhere outside of the horizon. For a coordinate stationary observer, on the other hand, the time basis vector  $\mathbf{e}_t$  becomes space-like ( $g_{tt} > 0$ ) inside the ergosphere. For sufficiently large values of the spin parameter  $a$ , the innermost stable circular orbit (often taken for the inner edge of the accretion disk) extends within the ergosphere, emphasizing the advantage of using the ZAMO basis.

Another useful feature of tetrads is that any tetrad basis with time-like  $\mathbf{e}_{\hat{t}}$  can be transformed to another tetrad through a Lorentz transformation (boost + rotation). By definition, this new basis will also have a time-like axis  $\mathbf{e}_{\hat{t}'}$ . In Chapter 6, we will use this feature to calculate scattering cross-sections and angles for Compton scattering of photons in the corona around the black hole. To do so requires first a transformation from the coordinate basis used for calculating geodesics to a ZAMO frame, then a Lorentz boost to the rest frame of the electron, where the scattering can be treated classically. After the scattering gives the photon a new direction in the electron frame, we do a boost back to the ZAMO frame, and finally an inverse transform to the coordinate basis, where the photon can continue along its new geodesic path until the next scattering event.

### 2.2.2 The Radiative Transfer Equation

Following the approach of Rybicki & Lightman (1979), we write the *radiative transfer equation* for the intensity  $I_\nu$  along a given ray's path length  $ds$ :

$$\frac{dI_\nu}{ds} = j_\nu - \alpha_\nu I_\nu, \quad (2.50)$$

where  $ds$  is the differential path length and  $I_\nu$ ,  $j_\nu$ , and  $\alpha_\nu$  are respectively the radiation intensity, the emissivity, and the absorption coefficient of the plasma at a frequency  $\nu$ . The absorption coefficient is related to the opacity  $\kappa_\nu$  through the density  $\rho$ :  $\alpha_\nu = \rho\kappa_\nu$ . In this form, basic emission and absorption is included, but not scattering, which involves more complicated angular terms and takes the form of an integrodifferential equation, which in general must be solved using more advanced numerical techniques (Rybicki & Lightman, 1979). In most of the results presented in this Thesis, we use extremely simple models for emission and do not include absorption. However, since the ultimate goal of this work is to produce a relativistic post-processor for any hydrodynamic simulation, in this Section we include both emission and absorption terms for generality.

We can rewrite the transfer equation by defining the optical depth  $\tau_\nu$

$$d\tau_\nu \equiv \alpha_\nu ds. \quad (2.51)$$

Now the transfer equation can be written as

$$\frac{dI_\nu}{d\tau_\nu} = S_\nu - I_\nu, \quad (2.52)$$

where  $S_\nu \equiv j_\nu/\alpha_\nu$  is called the *source function*, which is often more convenient to work with than the emissivity  $j_\nu$ . Over regions of constant source function  $S_\nu$ , equation (2.52) has the simple solution

$$I_\nu(\tau_\nu) = S_\nu + e^{-\tau_\nu}[I_\nu(0) - S_\nu]. \quad (2.53)$$

As mentioned above, the term  $I_\nu/\nu^3$  is a Lorentz invariant (in fact proportional to the photon phase space density  $f$ ). A simple proof of this invariance can be given as follows: Consider a small volume of particles in phase space  $dV = d^3\mathbf{x}d^3\mathbf{p}$  moving in the  $x$ -direction in the unprimed frame with velocity  $\beta = v_x/c$ . In the comoving frame, the proper volume is  $dV' = d^3\mathbf{x}'d^3\mathbf{p}'$ . Due to relativistic length contraction along the  $x$ -axis,  $dy = dy'$ ,  $dz = dz'$ , and  $dx = dx'/\gamma$ , giving

$$d^3\mathbf{x} = \gamma^{-1}d^3\mathbf{x}'. \quad (2.54)$$

The momentum components transform according to

$$dp_x = \gamma(dp'_x + \beta dp'_t), \quad (2.55a)$$

$$dp_y = dp'_y, \quad (2.55b)$$

$$dp_z = dp'_z, \quad (2.55c)$$

but to first order in the energy,  $dp'_t = 0$  in the fluid frame, giving

$$d^3\mathbf{p} = \gamma d^3\mathbf{p}' \quad (2.56)$$

and thus the invariant phase space volume

$$dV = dV' = \text{Lorentz invariant.} \quad (2.57)$$

Similarly, the phase space density  $f = dN/dV$  is invariant, since  $dN$  is simply a number and therefore also invariant. The angular spectral energy density  $U_\nu(\Omega) = I_\nu/c$  can be expressed in terms of the phase space density  $f$ :

$$U_\nu(\Omega)d\Omega d\nu = h\nu f d^3\mathbf{p} = h\nu f p^2 dp d\Omega. \quad (2.58)$$

Writing  $p = h\nu/c$ , we have

$$\frac{I_\nu}{\nu^3} = \frac{h^4}{c^2} f = \text{Lorentz invariant.} \quad (2.59)$$

Since the source function  $S_\nu$  appears in equations (2.52) and (2.53) as the difference  $I_\nu - S_\nu$ , it must have the same transformation properties as  $I_\nu$ , so we can write

$$\frac{S_\nu}{\nu^3} = \text{Lorentz invariant.} \quad (2.60)$$

Another Lorentz invariant is the optical depth, since the fraction of photons passing through a finite medium is given by  $e^{-\tau}$ , which is just a number, and thus the same in any reference frame. From this feature, we can calculate the absorption coefficient in a relativistic medium. Consider a small volume of matter flowing in the  $\mathbf{e}_{\hat{x}}$  direction with respect to the lab frame  $K$ , as in Figure 2-3. The temperature and density and thus the emissivity  $j'_\nu$  is typically given in the rest frame of the material  $K'$ . Since the motion is in the  $x$  direction, the slab thickness  $l$  is the same in both reference frames. The optical depth  $\tau_\nu$  can be written

$$\tau_\nu = \frac{l\alpha_\nu}{\sin\theta} = \frac{l}{\nu \sin\theta} \nu\alpha_\nu = \text{Lorentz invariant.} \quad (2.61)$$

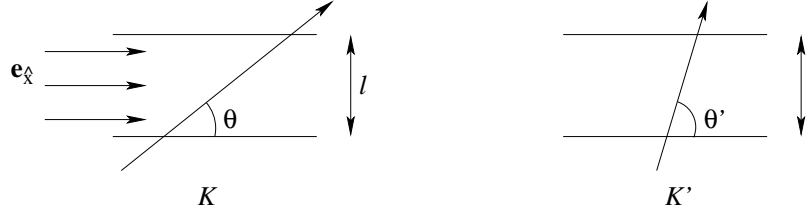


**Figure 2-3:** Two reference frames for a finite volume of matter flowing parallel to the  $x$ -axis. On the left is the “lab” frame  $K$ , and on the right is the material’s local rest frame  $K'$ . A ray propagates through the medium at respective angles  $\theta$  and  $\theta'$  in the two frames. Reproduced from Rybicki & Lightman (1979).

Since  $\nu \sin \theta$  is proportional to the  $p_y$  component of the photon 4-momentum, it must be the same in both frames because the boost is in a perpendicular direction. Thus  $\nu \sin \theta$  is another Lorentz invariant, and we find

$$\nu \alpha_\nu = \text{Lorentz invariant.} \quad (2.62)$$

Recalling the definition of the source function from  $j_\nu = \alpha_\nu S_\nu$ , we can combine equations (2.60) and (2.62) to find

$$\frac{j_\nu}{\nu^2} = \text{Lorentz invariant} \quad (2.63)$$

or

$$j_\nu = \left(\frac{\nu}{\nu'}\right)^2 j'_\nu. \quad (2.64)$$

Now we can proceed to solve the radiative transfer equation along a geodesic path through an arbitrary medium with emission and absorption. Earlier in this Section, we showed a schematic view (see Fig. 2-1) of the rays being traced through a fixed coordinate grid. That method is particularly well suited for thin, optically thick disks, where the photons cannot pass through the disk and will generally intersect each surface of constant  $\theta$  only once. For more general geometries and optically thin emission regions, it is more reasonable to tabulate the photon’s momentum and position at many points along its trajectory. Due to the adaptive step size used in integrating the equations of motion (see below, Section 2.3), the points of tabulation conveniently tend to be closer together in regions of higher curvature, which will also generally correspond to regions of higher density and temperature.

Denoting the photon’s spacetime position at step  $i$  by  $x_i^\mu$ , the differential vectors

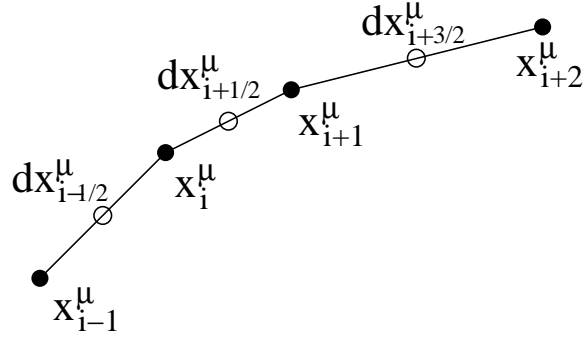


**Figure 2-4:** Photon positions and momenta are tabulated along its geodesic paths at coordinate points  $x_i^\mu$ . The calculation of the proper distances  $dl_i^2$  is described in the text.

between tabulated points are given by

$$dx_{i+1/2}^\mu = x_{i+1}^\mu - x_i^\mu. \quad (2.65)$$

These are the distances between solid circles in Figure 2-4. Then we can define a differential path length around  $x_i^\mu$  by the average

$$dx_i^\mu = \frac{1}{2}(dx_{i-1/2}^\mu + dx_{i+1/2}^\mu), \quad (2.66)$$

which is the distance between the empty circles in Figure 2-4.

Next, we transform from the coordinate basis to the ZAMO basis defined at  $x_i^\mu$ , giving the differential  $dx_i^\mu \rightarrow dx_i^{\hat{\mu}}$  and the momentum  $p_{\mu,i} \rightarrow p_{\hat{\mu},i}$ . In the ZAMO frame (here it can be thought of as the lab frame), the photon spatial path length is given by

$$ds_i^2 = \eta_{\hat{j}\hat{k}} dx_i^{\hat{j}} dx_i^{\hat{k}}. \quad (2.67)$$

In principle, we know the fluid velocity at a collection of fixed points in spacetime from another tabulated set of data produced by an independent hydrodynamics simulation. Using multi-linear extrapolation, the fluid variables (4-velocity, density, temperature) can be determined at the point  $x_i^\mu$ . The 4-velocity of the fluid in the ZAMO basis  $u_i^{\hat{\mu}}$  gives the angles  $\theta$  and  $\theta'$  from Figure 2-3, and the tabulated density and temperature (and thus absorption  $\alpha'_\nu$  and emissivity  $j'_\nu$ ) are typically given in the rest frame of the fluid.

To calculate the special relativistic redshift between the photons in the ZAMO frame and fluid frame, we define a null 4-vector parallel to the photon momentum in

the ZAMO frame:

$$n_{\hat{\mu}} = [-1, \vec{\mathbf{n}}], \quad (2.68)$$

where  $\vec{\mathbf{n}} = n_{\hat{j}}$  is a normalized 3-vector in standard Cartesian coordinates. Writing the fluid velocity

$$u^{\hat{\mu}} = [\gamma, \gamma\vec{\mathbf{v}}], \quad (2.69)$$

with  $\vec{\mathbf{v}} = v^{\hat{j}}$  having magnitude  $|\vec{\mathbf{v}}| = \beta = v/c$ , the frequency ratio is then given as

$$\frac{\nu}{\nu'} = \gamma(1 + \beta \cos \theta') = \frac{1}{\gamma(1 - \vec{\mathbf{v}} \cdot \vec{\mathbf{n}})}, \quad (2.70)$$

where  $\gamma \equiv 1/\sqrt{1 - \beta^2}$  as usual. Now we have enough information to solve the radiative transfer equation in a relativistic flow (Rybicki & Lightman, 1979):

$$\frac{dI_{\nu}}{ds} = \left(\frac{\nu}{\nu'}\right)^2 j'_{\nu} - \left(\frac{\nu'}{\nu}\right) \alpha'_{\nu} I_{\nu}. \quad (2.71)$$

In the first order finite difference form along the path  $dx_i^{\mu}$ , equation (2.71) can be written

$$I_{\nu,i+1} = I_{\nu,i} + ds_i \left[ \left(\frac{\nu}{\nu'}\right)_i^2 j'_{\nu,i} - \left(\frac{\nu'}{\nu}\right)_i \alpha'_{\nu,i} I_{\nu,i} \right], \quad (2.72)$$

where  $I_{\nu,i}$  is the spectrum of the photon beam entering the small volume around  $x_i^{\mu}$  and  $I_{\nu,i+1}$  is the spectrum of the beam upon leaving the volume element.

The above analysis, while quite useful for special relativistic flows in the ZAMO basis, ignores all general relativistic effects of curved spacetime around the black hole. To include these effects, we need only consider the invariant  $I_{\nu}/\nu^3$  along the geodesic path of the photons. This is particularly straightforward from a computational point of view, where the spectrum is stored as a finite array  $I^j$ , evaluated at the frequencies  $\nu^j$ . These frequencies are redshifted from one zone to the next due solely to gravitational effects. Since all the frequencies are shifted the same way, only a single fiducial redshift must be calculated. Let  $V_i^{\mu}$  be the coordinate 4-velocity of a ZAMO at position  $x_i^{\mu}$ . Then we can define the dot product with the photon 4-momentum as

$$\chi_i \equiv p_{\mu,i} V_i^{\mu}. \quad (2.73)$$

Then the array of frequencies is redshifted along the photon path according to

$$\nu_{i+1}^j = \nu_i^j \left( \frac{\chi_{i+1}}{\chi_i} \right). \quad (2.74)$$

Similarly, the spectral intensity defined at each frequency point scales as

$$I_{i+1}^j = I_i^j \left( \frac{\chi_{i+1}}{\chi_i} \right)^3. \quad (2.75)$$

While these methods are ideally suited for our implementation of the ray-tracing code, it should be noted that purely covariant approaches also exist for solving the radiative transfer equation in curved spacetime (Fuerst & Wu, 2004).

Because of this invariant scaling, a source with a blackbody spectrum will appear to a distant observer as a blackbody with temperature scaled as the redshift

$$(1+z)^{-1} = \frac{\nu_{\text{obs}}}{\nu_{\text{em}}}. \quad (2.76)$$

Since the differential frequency  $d\nu$  is also scaled by this factor, the total flux observed  $\int I_\nu d\nu$  will also scale as  $(1+z)^{-4}$ , just like a blackbody with temperature  $T_{\text{obs}} = T_{\text{em}}(1+z)^{-1}$ .

To summarize, the radiative transfer equation (2.50) is solved in full general relativity with the following steps:

- The geodesic photon trajectory is integrated backwards in time from a distant observer to the black hole, through the emission region, and is either captured by the horizon or escapes to infinity.
- At each point along the photon’s path, the spacetime position  $x_i^\mu$  and momentum  $p_i^\mu$  are tabulated.
- At the beginning (ray-tracing “end”) of the photon path, we set the spectrum  $I(\nu^j) = 0$  for all  $\nu^j$ .
- The spectrum  $I(\nu^j)$  and the frequencies  $\nu^j$  are transformed according to equations (2.74) and (2.75) from one tabulated position to the next.
- At each tabulated position in the emission region, after the spectrum is adjusted for general relativistic effects, the special relativistic radiative transfer equation (2.71) is used to update the spectrum  $I_i^j$ . The emission and absorption coefficients at that point are interpolated from another tabulated set of data (e.g. from a hydrodynamic simulation). The results presented in this Thesis generally treat the gas as an optically thin emitter with finite thickness and zero opacity or as flat disk of infinite opacity (Section 2.4.1).
- The spectrum is transformed to the next tabulated position, the transfer equation is applied again, and so on until the ray reaches the end-point at infinity (ray-tracing “start”), where the spectrum is observed.



- This entire procedure is done for each ray in the image plane and repeated for each time step of the simulation, creating a time-dependent spectrum and images of the accretion region.

## 2.3 Numerical Methods

The calculations as described so far can be divided into two major pieces (and in practice, they are carried out by two separate programs). The first, what we call “ray-tracing,” integrates the geodesic equations of motion in a vacuum, tabulating the position and momentum of each photon along its path. The second step, which is more accurately described as the “radiation transport” part of the calculation, requires an independent model for the disk emissivity at each point in the computational grid.

The ray-tracing calculation is carried out by numerically integrating equations (2.4a) and (2.4b) with a fifth-order Runge-Kutta algorithm with adaptive time stepping. This provides high accuracy over a large range of scales as the photon follows a long path through the relatively flat spacetime between the observer and the black hole, and then experiences strong curvature over a small region close to the horizon. The integrator was written from scratch, roughly following the methods described in Press et al. (1992). For completeness (and pedagogy), the basic algorithm is described here.

We begin with the classical fourth-order Runge-Kutta algorithm. Combining all position and momentum variables  $[x^\mu, p_\mu]$  into a single vector  $\mathbf{y}_n$ , the next iterative value for  $\mathbf{y}_{n+1}$  is given to first order by

$$\mathbf{y}_{n+1} = \mathbf{y}_n + h\mathbf{f}(\mathbf{y}_n). \quad (2.77)$$

Here  $\mathbf{f}(\mathbf{y})$  is the first derivative of the vector  $\mathbf{y}$  with respect to the independent variable  $\lambda$  (generally taken to be the coordinate time in our Hamiltonian approach), evaluated exactly according to equations (2.4a) and (2.4b). Equation (2.77) is only accurate to first order in  $h$  [i.e. the error term is  $\mathcal{O}(h^2)$ ], but by evaluating the function  $\mathbf{f}$  at a few points between  $\mathbf{y}_n$  and  $\mathbf{y}_{n+1}$ , we can achieve fourth order accuracy:

$$\begin{aligned} \mathbf{k}_1 &= h\mathbf{f}(\mathbf{y}_n) \\ \mathbf{k}_2 &= h\mathbf{f}\left(\mathbf{y}_n + \frac{1}{2}\mathbf{k}_1\right) \\ \mathbf{k}_3 &= h\mathbf{f}\left(\mathbf{y}_n + \frac{1}{2}\mathbf{k}_2\right) \\ \mathbf{k}_4 &= h\mathbf{f}(\mathbf{y}_n + \mathbf{k}_3) \\ \mathbf{y}_{n+1} &= \mathbf{y}_n + \frac{\mathbf{k}_1}{6} + \frac{\mathbf{k}_2}{3} + \frac{\mathbf{k}_3}{3} + \frac{\mathbf{k}_4}{6} \quad [+ \mathcal{O}(h^5)]. \end{aligned} \quad (2.78)$$

While we have written the error term as  $\mathcal{O}(h^5)$ , we can actually be a bit more precise and say that it is approximately  $h^5\phi$ , where  $\phi$  is proportional to the Taylor series expansion term  $\mathbf{y}^{(5)}/5!$ . Since  $\phi$  remains constant over the step size (at least to order  $h^5$ ), the error term in equation (2.78) scales directly as  $h^5$ . Thus if we compare two iterations, one with a single step of size  $2h$ , and one with two small steps  $h + h$ , the difference should give a quantitative value for  $\phi$ . By means of Richardson extrapolation, we can then arrive at a more accurate estimate for  $\mathbf{y}$ . The two solutions can be written

$$\begin{aligned}\mathbf{y}(\lambda + 2h) &= \mathbf{y}_1 + (2h)^5\phi + \mathcal{O}(h^6) \\ \mathbf{y}(\lambda + 2h) &= \mathbf{y}_2 + 2(h)^5\phi + \mathcal{O}(h^6),\end{aligned}\tag{2.79}$$

where  $\mathbf{y}(\lambda) = \mathbf{y}_0$ ,  $\mathbf{y}_1$  is the solution to equation (2.78) when taking a single step of size  $2h$ , and  $\mathbf{y}_2$  is the solution to taking two small steps, each of size  $h$ . Writing the difference as

$$\Delta = \mathbf{y}_2 - \mathbf{y}_1 = 30h^5\phi,\tag{2.80}$$

we can now derive a fifth-order estimate for  $\mathbf{y}(\lambda + 2h)$ :

$$\mathbf{y}(\lambda + 2h) = \mathbf{y}_2 + \frac{\Delta}{15} + \mathcal{O}(h^6).\tag{2.81}$$

Not only do we increase the order of the solution (and thus usually, but not always, increase the accuracy), but this approach also gives a good estimate for the absolute error in the solution, i.e. the difference between the exact solution for  $\mathbf{y}(\lambda)$  and the numerical approximation. Particularly for the problem of ray-tracing, where the photons encounter strongly curved space around the black hole and large regions of nearly flat space on their way to the observer, we would like to be able to take the largest steps possible while maintaining reasonable accuracy. In practice, the size of these steps will vary by many orders of magnitude along the photon path.

Let  $\epsilon$  be the desired fractional error for the numerical solution. Then the magnitude of the desired error should be, to leading order in  $h$ ,  $|\Delta_0| = \epsilon|\mathbf{y}|$ . Since  $\Delta$  scales as  $h^5$ , if a step size of  $h_1$  produces an error vector  $\Delta_1$ , then the step size  $h_0$  that would have given the desired error  $\Delta_0$  can be approximated as

$$h_0 \approx h_1 \left( \frac{|\Delta_0|}{|\Delta_1|} \right)^{1/5}.\tag{2.82}$$

If the error  $\Delta_1$  was too large, the step size will be adjusted accordingly in order to achieve the required accuracy. Similarly, if  $\Delta_1$  is smaller than the acceptable error, the step size will be increased in order to maximize efficiency.

Following Press et al. (1992), we actually use a slightly different prescription when the attempted step is too large, scaling the new step by an exponent of  $1/4$  instead of  $1/5$ . We also include a “safety factor”  $S$  to ensure that the estimate in equation (2.82) errs on the side of caution. It is much more computationally efficient to take steps that are  $\sim 10\%$  smaller than necessary, rather than trying to match exactly the target error, and thus going over half of the time, thus taking many steps that turn out to be wasted. So equation (2.82) is replaced by

$$h_0 = \begin{cases} Sh_1 \left( \frac{|\Delta_0|}{|\Delta_1|} \right)^{1/5} & |\Delta_0| \geq |\Delta_1| \\ Sh_1 \left( \frac{|\Delta_0|}{|\Delta_1|} \right)^{1/4} & |\Delta_0| < |\Delta_1| \end{cases}, \quad (2.83)$$

where the safety factor is typically  $S = 0.9 - 0.95$ .

We typically maintain an accuracy of one part in  $10^8 - 10^{10}$ , which can be independently confirmed by monitoring  $\mathcal{Q}$ , Carter’s constant from equation (2.21). The images and spectra are formed by ray-tracing a set of photon paths, usually of the order  $500 \times 500$  grid points in  $(i, j)$  with  $\sim 20$  latitudinal zones in  $\theta$  and spectral resolution of  $\nu/\Delta\nu \sim 200$ . When tracing photons originating at the emitter (see Chapter 6), only a fraction of the trajectories will actually end at the observer. Therefore, to get a comparable angular and energy resolution, a much larger number of rays must be traced, typically around  $10^8$ .

Fortunately, both methods of ray-tracing, whether from the observer to the source or vice versa, are quite suitable for parallelization. Since the photons are non-interacting, virtually no communication is necessary between different processors. Thus the problem is also extremely scalable and easily load-balanced. While the majority of the calculations in this thesis are small enough to carry out on a single-processor computer, some of the higher resolutions runs were performed on the MIT Astrophysics Beowulf cluster.

## 2.4 Broadened Emission Lines from Thin Disks

### 2.4.1 Transfer Function

There have been a number of calculations of the relativistic broadening of spectral lines from a steady-state accretion disk [Laor (1991); George & Fabian (1991); Reynolds & Begelman (1997); Bromley, Chen, & Miller (1997); Pariev, Bromley, & Miller (2001); for a detailed review, see Reynolds & Nowak (2003)]. As a check of the ray-tracing code and trajectories of massive particles, we have reproduced the results published in these papers for a variety of black hole spins and disk inclinations.

A steady-state disk can be made of a collection of massive particles moving in concentric planar circular orbits (in reality, these orbits will have a small inward radial velocity in order to satisfy mass conservation with a steady-state accretion flow; see Chapter 5 below). For orbits at a radius  $r$  in a plane orthogonal to the spin axis, a particle's specific energy and angular momentum are given analytically by Bardeen, Press, & Teukolsky (1972):

$$-p_0 = \frac{r^2 - 2Mr \pm a\sqrt{Mr}}{r(r^2 - 3Mr \pm 2a\sqrt{Mr})^{1/2}} \quad (2.84a)$$

and

$$p_\phi = \pm \frac{\sqrt{Mr}(r^2 \mp 2a\sqrt{Mr} + a^2)}{r(r^2 - 3Mr \pm 2a\sqrt{Mr})^{1/2}}. \quad (2.84b)$$

Here the top sign is taken for prograde orbits (particle angular momentum parallel to black hole angular momentum) and the bottom sign for retrograde orbits. Combining these equations gives the circular orbital frequency

$$\Omega_\phi \equiv \frac{p^\phi}{p^0} = \frac{g^{\mu\phi}p_\phi}{g^{\mu 0}p_0} = \frac{\pm\sqrt{M}}{r^{3/2} \pm a\sqrt{M}}. \quad (2.85)$$

For the large part of the disk, the orbits have nearly Keplerian frequencies, as measured in coordinate time  $t$ .

Inside the ISCO, the particles follow plunging trajectories with constant energy and angular momentum determined at the ISCO. Traditionally, when calculating emission from a steady-state disk, many approaches take the inner edge of the disk to be the ISCO radius  $R_{\text{ISCO}}$ . For larger values of  $a$ , the ISCO extends in closer to the event horizon, increasing the radiative area of the disk. However, due to the strong gravitational redshift in this inner region, the observed intensity is reduced by a significant factor of  $\nu_{\text{obs}}^3/\nu_{\text{em}}^3$ , resulting in a weak dependence on spin for disks with uniform emission.

Figure 2-5 shows a projection of the disk plane onto the image plane, color-coded by the observed redshift of an isotropic, monochromatic emitter. This projection is sometimes referred to as the transfer function, describing a map from the emission regions of the disk to the detector plane of the observer. The color scale in the lower left represents a logarithmic scale from  $\nu_{\text{obs}}/\nu_{\text{em}} = 0.1 \rightarrow 2$ . Contours of radius are also plotted as solid black lines, spaced at  $r/M = [3, 4, 6, 8, 10, 20]$ . Both Figures 2-5a and 2-5b correspond to an observer at inclination  $i = 70^\circ$  with respect to the disk axis, and the disk is rotating in a clockwise direction. Thus the blueshifted emission on the right side of the image is caused by gas moving towards the observer at roughly half the speed of light. The high redshift of the inner regions is caused by the deep

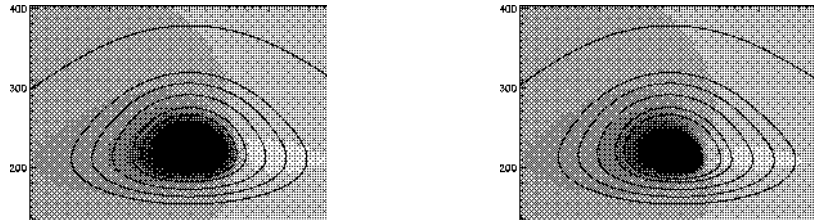


**Figure 2-5:** Projection of the accretion disk plane onto the plane of the observer. The color corresponds to a logarithmic scale of the redshift  $\nu_{\text{obs}}/\nu_{\text{em}} = 0.1 \rightarrow 2$ . On the left is a Schwarzschild black hole with  $a/M = 0$  and on the right is a Kerr black hole with  $a/M = 0.95$ . The contours correspond to constant values of  $r/M = [3, 4, 6, 8, 10, 20]$ . Both disks are seen from an observer inclination angle of  $i = 70^\circ$ .

gravitational potential well near the black hole.

On the left, Figure 2-5a shows the transfer function for a Schwarzschild black hole with  $a/M = 0$ . While the ISCO for such a black hole is at  $6M$ , it is clear that the emission extends continually all the way into the horizon at  $2M$ . On the right, Figure 2-5b is a black hole with near-maximal spin of  $a/M = 0.95$ . Qualitatively, the transfer function is nearly identical, right down to the inner-most regions of the disk, where the ISCO approaches the horizon at  $r/M \approx 1.3$ . For this reason, the observed spectra from these two disks are nearly identical.

For a disk made up of massive particles on circular orbits emitting isotropically from a region between  $R_{\text{in}}$  and  $R_{\text{out}}$ , the Doppler broadening of an emission line (typically iron  $K\alpha$  with  $E_{\text{em}} = 6.4$  keV) may be used to determine the inclination of the disk with respect to the observer. Disks at higher inclination will have an intense blue-shifted segment of the spectrum corresponding to the Doppler-boosted photons emitted from gas moving toward the observer. The higher intensity for the blue-shifted photons is caused by relativistic beaming, determined by the Lorentz invariance of  $I_\nu/\nu^3$  along a photon bundle:

$$I_\nu(\text{obs}) = I_\nu(\text{em}) \frac{\nu_{\text{obs}}^3}{\nu_{\text{em}}^3}. \quad (2.86)$$

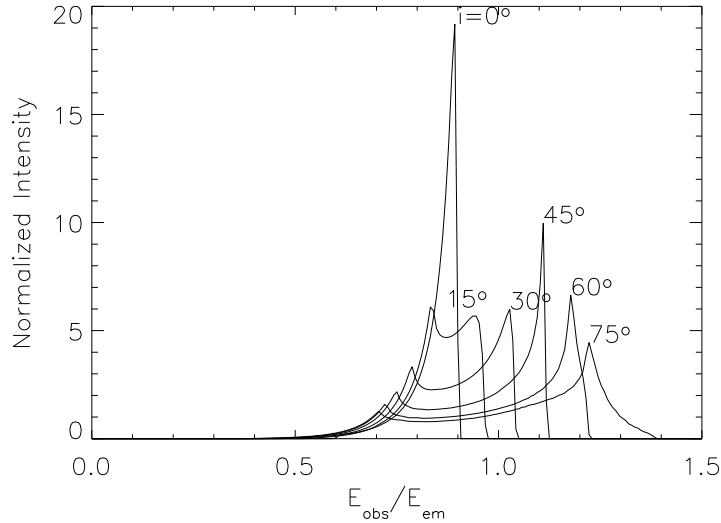


**Figure 2-6:** Normalized spectra of a monochromatic emission line from steady-state accretion disks of varying inclination. An inclination of  $i = 0^\circ$  corresponds to a face-on view of the disk while  $i = 90^\circ$  would be edge-on. The emissivity is taken to be uniform between  $R_{\text{in}} = R_{\text{ISCO}}$  and  $R_{\text{out}} = 15M$ . The spin is taken to be  $a/M = 0.5$  but the dependence on  $a$  is negligible for uniformly emitting disks.

Figure 2-6 shows the integrated spectra from a set of accretion disks with outer radius  $R_{\text{out}} = 15M$  and inner radius at  $R_{\text{in}} = R_{\text{ISCO}}$  for a spin parameter  $a/M = 0.5$ , normalized such that

$$\int I(E_{\text{obs}}/E_{\text{em}})d(E_{\text{obs}}/E_{\text{em}}) = 1. \quad (2.87)$$

All spectra are assumed to come from a flat, opaque disk with uniform emission (this is not quite physically accurate; below we include the likely possibility of increased emissivity in the inner disk). Repeating this calculation for a range of spin parameters (and thus a range of  $R_{\text{ISCO}}$ ), we find that the dependence on disk *inclination* is quite strong, while the dependence on black hole *spin* is almost insignificant, as shown in Figure 2-7 for an inclination of  $i = 30^\circ$  and various spins of  $a/m = [-0.99, -0.5, 0, 0.5, 0.99]$ . Figure 2-7a assumes constant emission all the way down to the horizon, while the emission in Figure 2-7b is cut off at the ISCO. Clearly, the different spectra are virtually indistinguishable, certainly for the present levels of observational sensitivity. This is reasonable because, except for very close to the horizon, the spin has little effect on the orbital velocity for circular orbits, as seen from equation (2.85). Furthermore, the emission from the innermost regions is weighted much less due to its significant

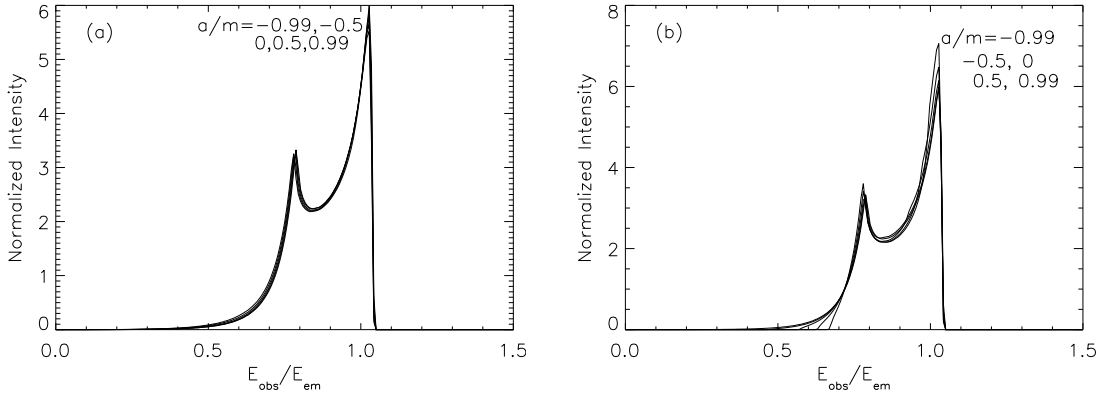


**Figure 2-7:** Normalized spectra of a monochromatic emission line from steady-state accretion disks with inclination  $i = 30^\circ$  and varying spin parameter  $a/M$  (negative spin values correspond to retrograde disk rotation). The emissivity is taken as constant between  $R_{\text{in}}$  and  $R_{\text{out}} = 15M$ . The disk extends all the way into the horizon in (a), with plunging trajectories inside of the ISCO, as described in the text. In (b), all emission is truncated inside of  $R_{\text{ISCO}}$ . For this uniform emission model, the various theoretical spectra are nearly indistinguishable, even when truncating the disk at the ISCO.

redshift and smaller area. However, as we will see below, many models predict a much higher emissivity in the inner disk, countering this redshift effect and in turn reviving the possibility of measuring black hole spin with relativistic line profiles.

### 2.4.2 Observations of Iron Emission Lines

As we mentioned in the Introduction, one of the most important astronomical measurements of strong field GR would be the successful determination of a black hole's spin. Since the leading order curvature terms scale as  $\sim M/r^3$  for the mass and  $\sim a/r^4$  for the spin contributions, any observable that is sensitive to the spin parameter will presumably originate from the regions closest to the black hole.

It is actually quite possible that such an observation has already been made, yet we currently lack the confidence in our theoretical models necessary to interpret the results as an unambiguous measurement of black hole spin. One of the most promising observations is that of the relativistically broadened Fe  $K\alpha$  emission line seen in both stellar-mass black holes and active galactic nuclei (AGN), easily seen with the remarkable spectral resolution and large collecting areas of *Chandra* and *XMM-Newton*. An example of such a line is shown in Figure 2-8a from the black hole

binary XTE J1650–500, reproduced from Miller et al. (2002a). Similar lines have been seen in the Seyfert 1 galaxy MCG–6–30–15 [Tanaka et al. (1995); Wilms et al. (2001); Lee et al. (2002); see Fig. 2-8b], and both have been interpreted as consistent with a near-maximal black hole spin ( $a/M = 0.998$ ).

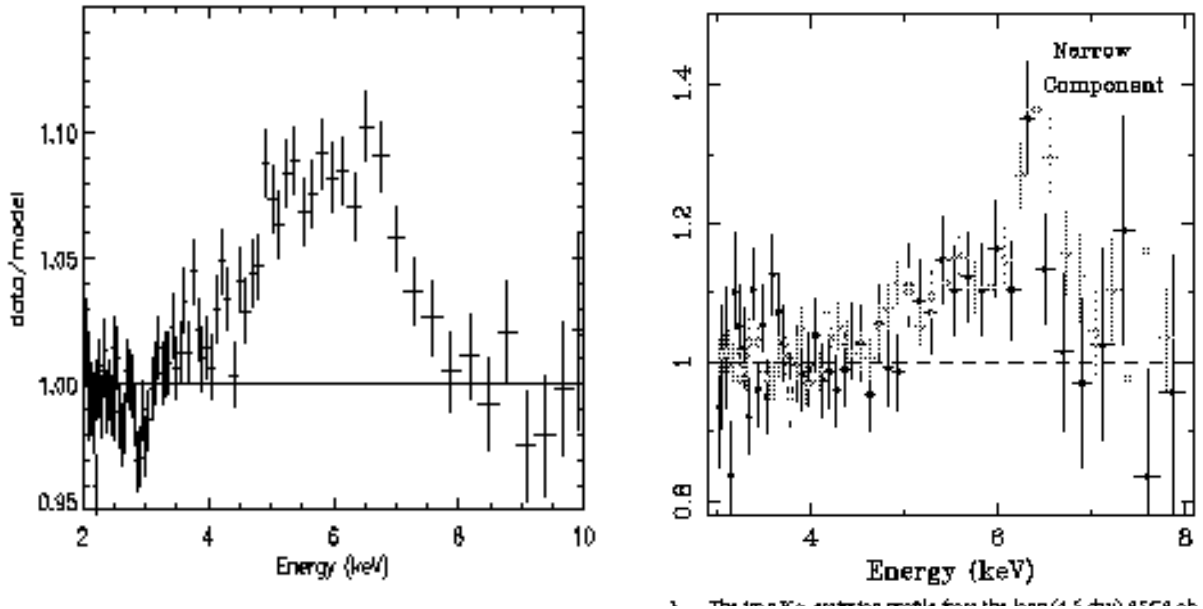


**Figure 2-8:** (left) A broadened Fe  $K\alpha$  line from the black hole binary XTE J1650–500, observed with *XMM-Newton*. (right) A similar line from the Seyfert 1 galaxy MCG–6–30–15, observed with *ASCA* (blue) and *Chandra* (black). Both plots show the excess emission with respect to a background model with blackbody and power-law components for a multicolor disk. The lines extend well below the rest energy of 6.4 keV, suggesting emission for highly relativistic regions of the inner accretion disk. [Reproduced from Miller et al. (2002a) and Lee et al. (2002) with permission]

This interpretation is heavily dependent on the assumption that the accretion disk has a relatively sharp edge at the inner-most stable circular orbit (ISCO). But many relativistic magnetohydrodynamic (MHD) simulations find no such cut-off (Gammie, McKinney, & Toth, 2003; De Villiers, Hawley, & Krolik, 2003), with significant pressure and density (and thus emission) all the way in to the horizon. This point has been made by Reynolds & Begelman (1997), but has unfortunately not been fully appreciated by much of the high-energy astrophysics community. Using simplified yet reasonable physical estimates (and without putting undue emphasis on the ISCO), Reynolds, Brenneman, & Garofalo (2004) are able to confirm some sort of spinning black hole in MCG–6–30–15 as well as the galactic black hole binary GX 339–4, but they still cannot provide a clear measurement of that spin.



In addition to the uncertainty around the treatment of the disk boundary conditions at the ISCO, there is also not an unambiguous illumination mechanism that would cause the disk to produce a high-energy emission line such as the Fe  $K\alpha$  at 6.4 keV. One likely possibility is that the iron emission is produced by hard X-rays from a hot electron corona reflecting off the relatively cool disk [see, e.g. McClintock & Remillard (2004)]. Another option is that it simply follows the intensity of the thermal emission from the disk itself (Agol & Krolik, 1999). If the line emission indeed tracks the total flux at each point in the disk, it may be possible to measure more exotic processes in the disk, including magnetic torques at the ISCO. In observations of MCG-6-30-15, Reynolds et al. (2004) claim to find evidence of a torque on the inner edge of the disk, presumably caused by some version of the Blandford-Znajek process, which provides a mechanism for extracting energy from the spin of a black hole through magnetic fields that thread the accretion disk as well as the black hole horizon (Blandford & Znajek, 1977). This effect can be seen in Figure 2-9, reproduced from Reynolds et al. (2004). The added stress on the inner disk puts a greater weight on the portions of the iron line spectrum produced there, generally highlighting the broader features caused by the strong relativistic effects near the ISCO.

For lack of a clear picture of the disk+corona geometry, many accretion disk models include an emissivity that simply scales as a power of the radius. Following Bromley, Chen, & Miller (1997), we apply an emissivity factor proportional to  $r^{-2}$ , giving an added weight to the inner, presumably hotter, regions. However, unlike the model of Reynolds et al. (2004), where the iron line emission traces that of the thermal disk, here we should note that the emission is coming essentially from the corona, but fluorescing off the much cooler disk. Thus, even though we will see in Chapter 5 that almost no *thermal* emission comes from inside of the ISCO, there is still enough matter in that region to reflect the high energy photons from the hot corona and contribute significantly to the iron emission line profile.

As can be seen in Figure 2-10, this extra emission from close to the black hole can serve to break the otherwise weak dependence on spin, but only if we assume all emission is truncated at the ISCO. For an inclination of  $i = 30^\circ$ , five different spin values are shown: ( $a/M = -0.99, -0.5, 0, 0.5, 0.99$ ), corresponding to inner disk boundaries at ( $R_{\text{ISCO}}/M = 8.97, 7.55, 6.0, 4.23, 1.45$ ). Since the sign of  $a$  is defined with respect to the angular momentum of the accretion disk, negative values of  $a$  imply retrograde orbits that do not survive as close to the black hole, plunging at larger values of  $R_{\text{ISCO}}$ . The disks that extend in closer produce more low-energy red-shifted photons, giving longer tails to the spectra at  $E_{\text{obs}}/E_{\text{em}} < 0.7$  and smaller relative peaks at  $E_{\text{obs}}/E_{\text{em}} \approx 1$ . These photon energy spectra closely reproduce previously published results; in particular compare with Figure 3 in Bromley, Chen, & Miller (1997).

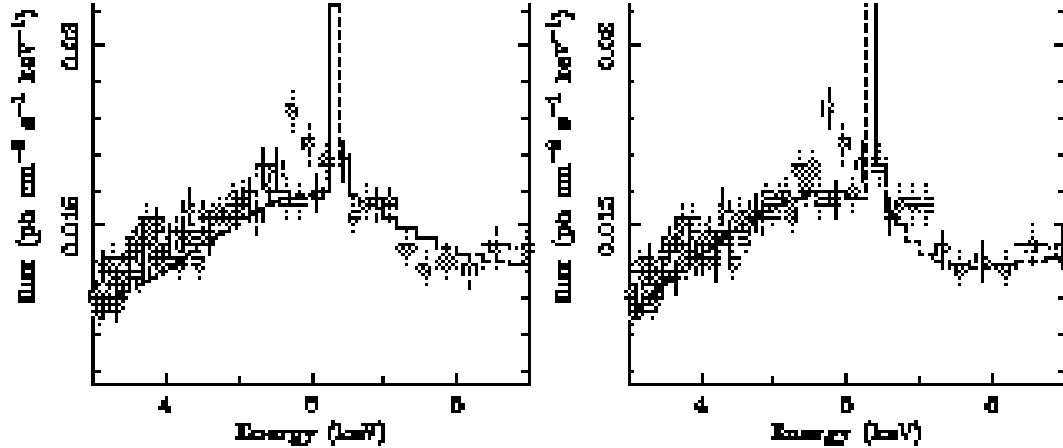
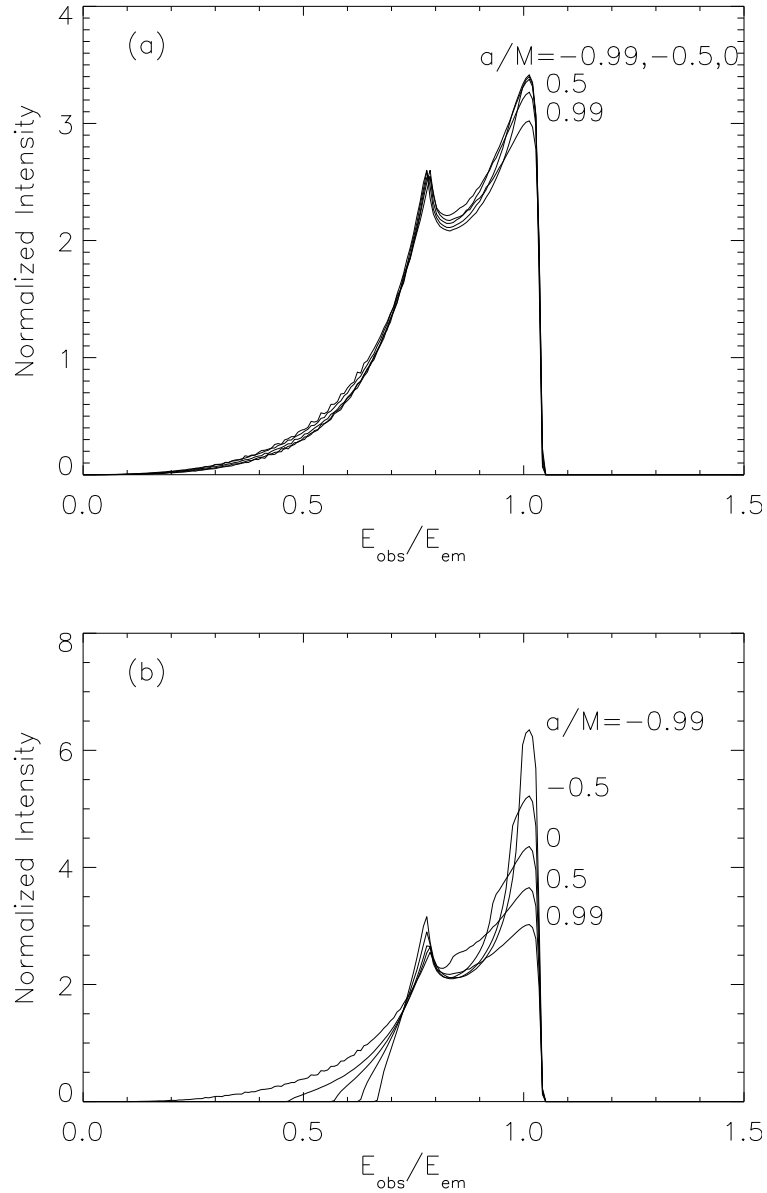


Figure 2-9. Broadened line fit assuming that the line emission tracks the underlying disk dissipation of (a) a standard (Novikov & Thorne 1974) accretion disk and (b) a model of Krolik (1999) torqued accretion disk. Modified from Reynolds et al.

**Figure 2-9:** *XMM-Newton* observation of the broadened Fe  $K\alpha$  line from the Seyfert 1 galaxy MCG-6-30-15. The theoretical fits assume that the line emission is proportional to the total local flux, as determined by a steady-state relativistic  $\alpha$ -disk model. On the left is the standard Novikov-Thorne model with near-maximal spin  $a/M = 0.998$  and zero torque (and thus zero emission) at the ISCO. On the right is a model with non-zero torque at the ISCO, as in Agol & Krolik (1999), which transfers significant energy into the inner disk, highlighting the iron emission there. [Reproduced from Reynolds et al. (2004) with permission]

Assuming the “best case scenario” where the disk *does* in fact get cut off at the ISCO, *and* if we can determine the inclination of the disk independently (e.g. through spectroscopic observations of the binary companion), the spin *might* be inferred from the broadening of an iron emission line. However, since the plane of the disk tends to align normal to the black hole spin axis close to the ISCO, the binary inclination may not coincide with the inclination of the inner disk. The problem of inclination and unknown illumination mechanisms, along with other complications, such as additional emission lines and other causes of scattering and line broadening, motivates us to look more closely at QPO power spectra as a method for determining black hole spin.



**Figure 2-10:** Normalized spectra of steady-state accretion disks with inclination  $i = 30^\circ$  and varying spin parameter  $a/M$  (negative spin values correspond to retrograde disk rotation). The emissivity is taken to be proportional to  $r^{-2}$  between  $R_{\text{in}}$  and  $R_{\text{out}} = 15M$ . The disk extends all the way into the horizon in (a), with plunging trajectories inside of the ISCO, as described in the text. In (b), all emission is truncated inside of  $R_{\text{ISCO}}$ . Black holes with higher values of  $a/M$  allow the inner disk to extend in closer to the horizon, giving a greater weight to the high-redshift radiation emitted there. Yet even with the added emission, for disks that are not truncated at the ISCO, the spectrum is quite insensitive to the black hole spin.



# Chapter 3

## The Geodesic Hot Spot Model

*Everything should be made as simple as possible, but not simpler.*

-Albert Einstein

### 3.1 Hot Spot Emission

Given the ray-tracing map from the accretion disk to the image plane, with each photon bundle labeled with a distinct 4-momentum and time delay, we can reconstruct time-dependent images of the disk based on time-varying emission models. The simplest model we consider is a single region of isotropic, monochromatic emission following a geodesic trajectory: the “hot spot” or “blob” model (Sunyaev, 1972; Bao, 1992; Stella & Vietri, 1998, 1999).

The hot spot is a small region with finite radius and emissivity  $j(x)$  chosen to have a Gaussian distribution in local Cartesian space:

$$j(\mathbf{x}) \propto \exp \left[ -\frac{|\tilde{\mathbf{x}} - \tilde{\mathbf{x}}_{\text{spot}}(t)|^2}{2R_{\text{spot}}^2} \right]. \quad (3.1)$$

The spatial position 3-vector  $\tilde{\mathbf{x}}$  is given in pseudo-Cartesian coordinates by the transformation defined by equations (2.41a,2.41b) and  $z = r \cos \theta$ . Outside a distance of  $4R_{\text{spot}}$  from the guiding geodesic trajectory, there is no emission. We typically take  $R_{\text{spot}} = 0.25 - 0.5M$ , but find the normalized light curves and QPO power spectra to be rather independent of spot size. We have also explored a few different hot spot shapes, ranging from spherical to an ellipsoid flattened in the  $\mathbf{e}_\theta$  direction and similarly find no significant dependence of the spectra on spot shape.

Because we assume all points in the hot spot have the same 4-velocity as the geodesic guiding trajectory, one must be careful not to use too large a spot or the point of emission  $\mathbf{x}_{\text{em}}$  can be spatially far enough away from the center  $\mathbf{x}_{\text{spot}}$  to render the inner product  $p_\mu(\mathbf{x}_{\text{em}})v^\mu(\mathbf{x}_{\text{spot}})$  unphysical. One way to quantify the size of this physical region is through the use of Riemann normal coordinates (Misner, Thorne, & Wheeler, 1973), where the metric is locally flat and the Cartesian dot product is well behaved. The quadratic deviations from flat space scale according to the local curvature scale, which is of order  $\mathcal{R} \sim 10M$  at the ISCO of a Schwarzschild black hole. Thus as long as the hot spot is within

$$\frac{|\tilde{\mathbf{x}} - \tilde{\mathbf{x}}_{\text{spot}}(t)|^2}{\mathcal{R}^2} \ll 1, \quad (3.2)$$

equation (3.1) should be reasonably well behaved.

After calculating and tabulating the hot spot trajectory as a function of coordinate time  $t$ , the ray-tracing map between the disk and the observer is used to construct a time-dependent light curve from the emission region. For each photon bundle intersection point there is a time delay  $\Delta t_{i,j,k}$  (where  $i, j$  are the coordinate indices in the image plane and  $k$  is the latitude index in the disk) so for the observer time  $t_{\text{obs}}$ , we first determine where the hot spot was at coordinate time  $(t_{\text{em}})_{i,j,k} = t_{\text{obs}} - \Delta t_{i,j,k}$ . If the spot centroid is close enough (within  $4R_{\text{spot}}$ ) to the disk intersection point  $(r, \theta, \phi)_{i,j,k}$ , then the redshifted emission is added to the pixel spectrum  $I_\nu(t_{\text{obs}}, i, j)$ , weighted by equation (3.1).

In this way, a movie can be produced that shows the blob orbiting the black hole, including all relativistic effects. Such a movie shows a few immediately apparent special relativistic effects such as the Doppler shift and beaming as the spot moves toward and then away from the observer. For a hot spot orbiting in the clockwise direction as seen from above ( $v^\phi < 0$  with  $\phi = 270^\circ$  toward the observer), the point of maximum blue shift actually occurs at a point where  $\phi > 0$  because of the gravitational lensing of the light, beamed in the forward direction of the emitter and then bent toward the observer by the black hole. Gravitational lensing also causes significant magnification of the emission region when it is on the far side of the black hole, spreading the image into an arc or even an Einstein ring for  $i \approx 90^\circ$ , much like distant quasars are distorted by intervening matter in galaxy clusters (Hewitt et al., 1988).

A simulated time-dependent spectrum or *spectrogram* for this hot spot model is shown in Figure 3-1, for an inclination  $i = 60^\circ$  and black hole spin  $a/M = 0$ . The horizontal axis measures time in the observer's frame, with  $t = 0$  corresponding to the time at which the spot center is moving most directly away from the observer ( $\phi = 180^\circ$ ). As mentioned above, this is *not* quite the same as the point of maximum

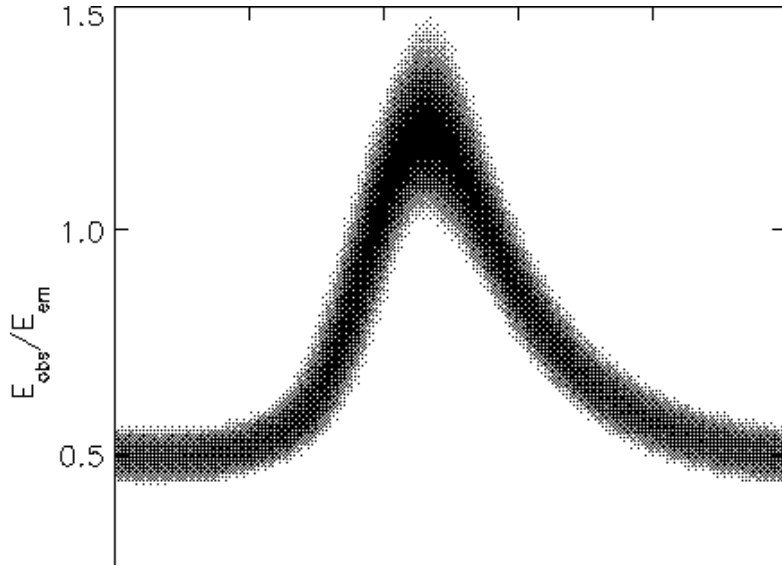


**Figure 3-1:** Spectrogram of a circular hot spot with radius  $R_{\text{spot}} = 0.5M$  orbiting a Schwarzschild black hole at the ISCO ( $R_{\text{ISCO}} = 6M$ ), viewed at an inclination of  $60^\circ$ . The spot is moving in the  $-\mathbf{e}_{\hat{\phi}}$  direction with  $\phi(t = 0) = 180^\circ$  and the observer at  $\phi = 270^\circ$ . The maximum redshift occurs when  $\phi \approx 160^\circ$  and the maximum blueshift occurs when  $\phi \approx 20^\circ$ .

redshift, which occurs closer to  $\phi = 160^\circ$  due to gravitational deflection of the emitted light.

### 3.1.1 Overbrightness and QPO Amplitudes

The spectrogram shown in Figure 3-1 can be integrated in time to give a spectrum similar to those shown in Figures 2-6 and 2-7, corresponding to something like a very narrow circular emitting region with  $R_{\text{out}} \approx R_{\text{in}} \approx R_{\text{ISCO}}$ . By integrating over photon energy, we get the total X-ray flux as a function of time, i.e. the light curve  $I(t)$ . This time-varying signal can be added to a background intensity coming from the inner regions of a steady state disk described below. By definition the hot spot will have a

higher temperature or density and thus greater emissivity than the background disk, adding a small modulation to the total flux. *RXTE* observations find the HFQPO X-ray modulations to have typical amplitudes of 1-5% of the mean flux during the outburst (Remillard et al., 2002; Remillard, 2004). Markovic & Lamb (2000) present a first-order argument that a 1% amplitude modulation requires a hot spot with 100% overbrightness extending over an area of 1% of the steady-state region of the disk. For  $R_{\text{out}} = 15M$ , this requires a hot spot with radius  $R_{\text{spot}} \approx 1.5M$ , which they argue is too large to survive the viscous shearing of the disk.

Hydrodynamic stability aside, this reasoning ignores the important effects of disk inclination, relativistic beaming and gravitational lensing of the hot spot emission. Assuming a Shakura-Sunyaev type disk with steady-state emissivity  $g(r) \propto r^{-2}$  and a similar scaling for the hot spot emission, we find that hot spots with significantly smaller size or overbrightness are capable of creating X-ray modulations on the order of 1% rms, defined by

$$\text{rms} \equiv \sqrt{\frac{\int [I(t) - \bar{I}]^2 dt}{\int I^2(t) dt}}. \quad (3.3)$$

Figure 3-2 shows the required overbrightness of a flattened Gaussian hot spot orbiting near the ISCO to produce a modulation with rms amplitude of 1% for a range of inclinations and black hole spin parameters. In the limit of a face-on accretion disk ( $i = 0^\circ$ ), even an infinitely bright spot on a circular orbit will not produce a time-varying light curve. As the inclination increases, the required overbrightness decreases, since the special relativistic beaming focuses radiation toward the observer from a smaller region of the disk, *increasing* the relative contribution from the hot spot. As the spin of the black hole increases, the ISCO moves in toward the horizon and the velocity of a trajectory near that radius increases, as does the gravitational lensing, further magnifying the contribution from the hot spot. This result seems to predict an observational preference for high-inclination, high-spin systems when detecting HFQPOs. As the number of black hole LMXB observations increases, the growing data set seems to confirm this prediction with regard to binary inclination and possibly spin as well [see McClintock & Remillard (2004) and references therein].

Understandably, the required overbrightness is inversely proportional to the area of the hot spot so we should expect

$$[\text{overbrightness}] * R_{\text{spot}}^2 = \text{const.} \quad (3.4)$$

For example, from Figure 3-2 we see that a black hole binary with inclination  $i = 60^\circ$  and spin  $a/M = 0.5$  would require a spot size of  $R_{\text{spot}} = 0.5M$  with 67% overbrightness (e.g. 14% temperature excess for blackbody emission) to produce a 1% rms modulation in the light curve. This is well within the range of the typical size and



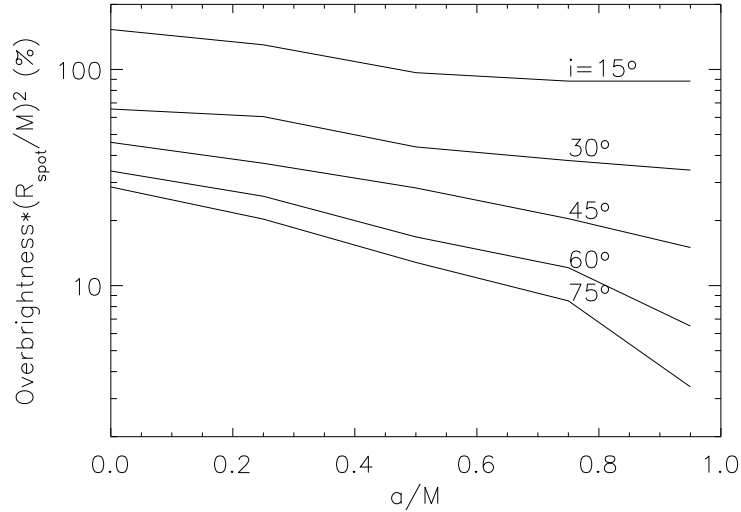


**Figure 3-2:** Overbrightness required of a hot spot on a circular orbit to produce a 1% rms modulation in X-ray flux when added to a steady-state disk with  $R_{\text{in}} = R_{\text{ISCO}}$ ,  $R_{\text{out}} = 15M$  and emissivity  $g(r) \propto r^{-2}$ . An overbrightness of 100% means the peak hot spot emissivity is twice that of the steady-state disk with no hot spot. The spot size  $R_{\text{spot}}$  is measured in gravitational radii  $M$ , so for a black hole with  $a/M = 0.5$  and  $i = 60^\circ$ , the required overbrightness for a hot spot with  $R_{\text{spot}} = 0.5M$  would be 67%.

magnitude of fluctuations predicted by MHD calculations of 3-dimensional accretion disks (Hawley & Krolik, 2001; De Villiers & Hawley, 2003). The hot spot model is well-suited for simplified calculations of the X-ray emission from these random fluctuations in the accretion disk. By adding the emission from small, coherent hot spots to the flux from a steady-state disk, we can interpret the amplitudes and positions of features in the QPO spectrum in terms of a model for the black hole mass, spin, and inclination.

### 3.1.2 Harmonic Dependence on Inclination and Spin

Considering the X-ray flux from the hot spot alone, the frequency-integrated light curves for a variety of inclinations are shown in Figure 3-3. All light curves are shown for one period of a hot spot orbiting a Schwarzschild black hole at the ISCO. As the inclination increases, the light curve goes from nearly sinusoidal to being sharply peaked by special relativistic beaming. Thus the shape of a hot spot light curve may

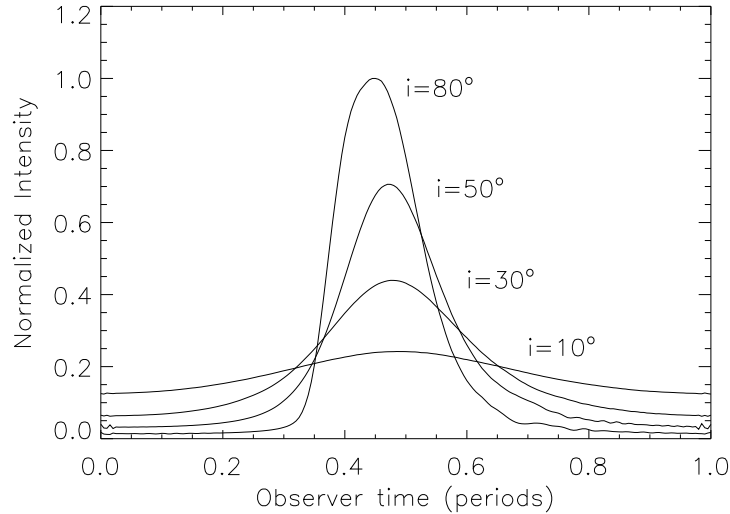


**Figure 3-3:** Frequency-integrated light curves of an orbiting hot spot at the ISCO of a Schwarzschild black hole for different disk inclination angles. The spot is moving in the  $-\mathbf{e}_{\hat{\phi}}$  direction as in Figure 3-1 with  $\phi(t = 0) = 180^\circ$ . For high inclination angles, the special relativistic beaming causes the light curve to become sharply peaked as the hot spot moves toward the observer.

be used to determine the disk inclination. With current observational capabilities, it is not possible even for the brightest sources to get a strong enough X-ray signal over individual periods as short as 3-5 msec to be able to differentiate between the light curves in Figure 3-3. Instead, the Fourier power spectrum can be used to identify the harmonic features of a periodic or quasi-periodic light curve over many orbits. Disks with higher inclinations will produce more power in the higher harmonic frequencies, due to the “lighthouse” effect, as the hot spot emits a high-power beam of photons toward the observer once per orbit, approximating a periodic delta-function in time.

Figure 3-4a shows a sample section of such a light curve, including only the X-ray flux from the hot spot, subtracting out the steady-state flux from the disk. The sharp peaks in the light curve, while unresolvable in the time domain, will give a characteristic amount of power in the higher harmonics, shown in Figure 3-4b. Here we have normalized the rms amplitudes to the background flux from the disk with a hot spot size  $R_{\text{spot}} = 0.5M$ , overbrightness of 100%, and inclination of  $60^\circ$ . For a

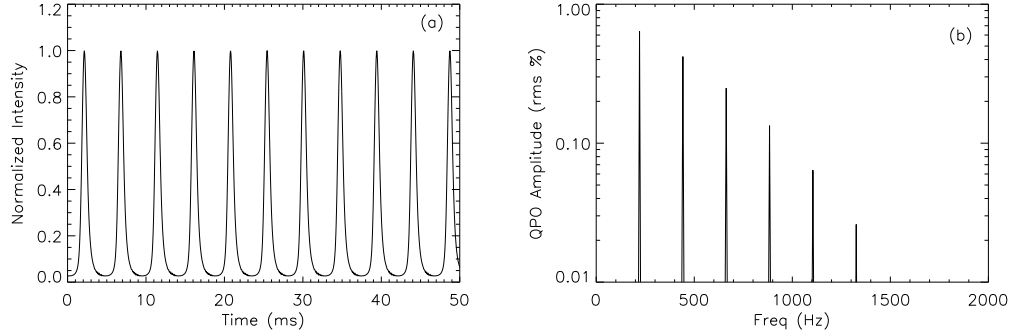


**Figure 3-4:** (a) X-ray light curve of an orbiting hot spot with same parameters as in Figure 3-1. (b) Fourier amplitude  $a_n(\text{rms})$  of the above light curve with over-brightness of unity, normalized to the flux from a steady-state disk as in equation (3.6), showing the fundamental Kepler frequency at 220 Hz for  $M = 10M_\odot$ . The non-sinusoidal shape of the light curve, due largely to beaming effects, is characterized by the declining power in the higher harmonic frequencies at  $n220$  Hz, where  $n > 1$  is an integer.

signal  $I(t)$  with Fourier components  $a_n$ :

$$I(t) = \sum_{n=0}^{\infty} a_n \cos(2\pi nt), \quad (3.5)$$

we define the rms amplitude  $a_n(\text{rms})$  in each mode  $n > 0$  as

$$a_n(\text{rms}) \equiv \frac{a_n}{\sqrt{2a_0}}. \quad (3.6)$$

With this normalization, the rms defined in equation (3.3) can be conveniently written

$$\text{rms} = \sqrt{\sum_{n>0} a_n^2(\text{rms})}. \quad (3.7)$$

In Figure 3-4b, the main peak at  $f = 220$  Hz corresponds to the azimuthal frequency for an orbit at the ISCO of a  $10M_\odot$  Schwarzschild black hole. In the limit where the light curve is a periodic delta-function in time, there should be an equal amount of power in all harmonic modes, because the Fourier transform of a periodic delta-function is a periodic delta-function. However, even in the case of edge-on inclination ( $i = 90^\circ$ ), unless the hot spot is infinitesimally small and ultra-relativistic, the

light curve will always be a continuous function with some finite width and non-zero minimum, thus contributing less and less power to the higher harmonics. The harmonic dependence on inclination for a hot spot orbiting a Schwarzschild black hole is shown in Figure 3-5a. Predictably, as the inclination increases, we see that both the absolute and relative amplitudes of the higher harmonics increase, almost to the limit of a periodic delta-function when  $i \rightarrow 90^\circ$ .

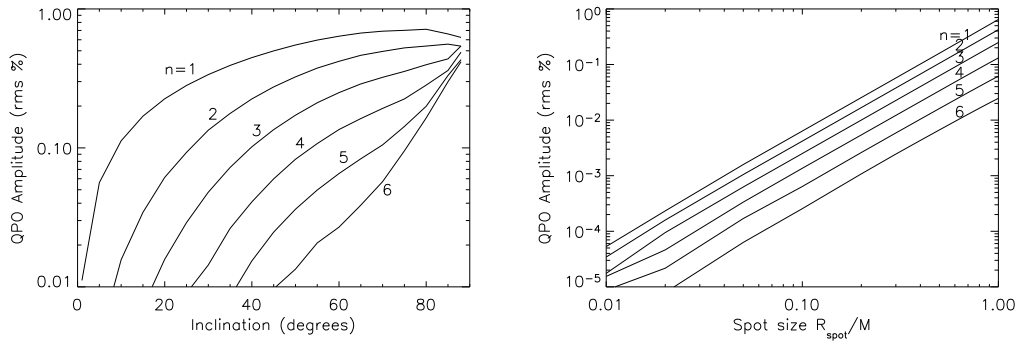


**Figure 3-5:** (a) Fourier amplitude  $a_n(\text{rms})$  in higher harmonic frequencies  $\nu_n = n\nu_\phi$  as a function of orbital inclination to the observer, normalized as in equation (3.6). The hot spot has size  $R_{\text{spot}} = 0.5M$ , an overbrightness factor of 100%, and is in a circular orbit at  $R_{\text{ISCO}}$  around a Schwarzschild black hole. (b) The same harmonic amplitude  $a_n(\text{rms})$  as a function of spot size  $R_{\text{spot}}$  with  $i = 60^\circ$  and a constant overbrightness factor of 100%. The harmonic amplitude scales directly with hot spot area  $a_n(\text{rms}) \propto R_{\text{spot}}^2$ .

Interestingly, we find very little dependence of the relative harmonic structure on hot spot size or shape. This emphasizes the robustness of the simple hot spot model in interpreting an X-ray power spectrum, without needing to include the detailed physics of the disk perturbations. To show clearly the independence of harmonic structure on spot size, Figure 3-5b plots the rms amplitude in each mode  $a_n(\text{rms})$ , defined as above. The overbrightness of 100% is held constant as the spot size varies. As expected, for constant overbrightness, the amplitude in each harmonic scales linearly with  $R_{\text{spot}}^2$ . Thus if the combination [overbrightness] \*  $R_{\text{spot}}^2$  is held constant, the rms amplitudes would also be constant. The small amount of numerical noise as  $R_{\text{spot}} \rightarrow 0$  is caused by the finite resolution of the ray-tracing grid; as the hot spot size approaches the grid size, it becomes more difficult to accurately calculate the light curve and associated power spectrum.

As the spin parameter increases for Kerr black holes, the ISCO moves closer to the horizon, increasing the circular velocities of particles on the ISCO and thus

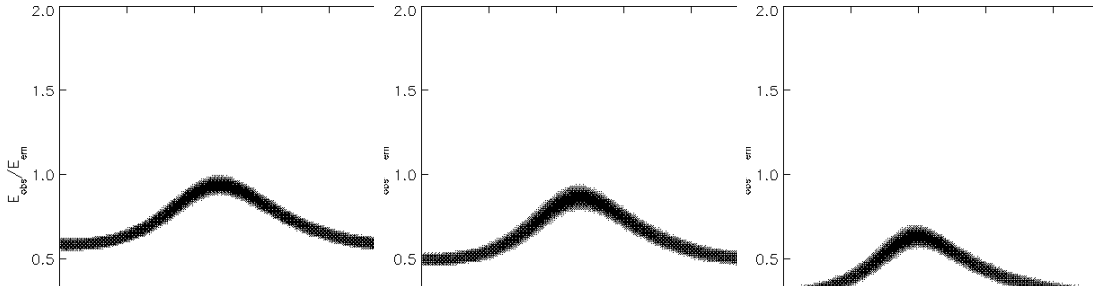


**Figure 3-6:** Spectrograms for hot spots on circular orbits at  $R_{\text{ISCO}}$  for  $i = 30^\circ$  and a variety of spins:  $a/M = 0, 0.5, 0.9$ . As the spin increases, the ISCO moves in towards the horizon, so the gravitational redshift is greater, lowering the observed frequency from a monochromatic emitter.

the Doppler shifts, giving broader photon energy spectra, as seen in Figure 2-10b. The phase lag in time of the peak blueshift with respect to angular phase of the hot spot is also amplified for these smaller values of  $R_{\text{ISCO}}$ , giving light curves that are asymmetric in time. Figure 3-6 shows spectrograms as in Figure 3-1, now for inclination of  $i = 30^\circ$  and spin values of  $a/M = 0, 0.5, 0.9$ . In each case the hot spot is on a circular orbit at the ISCO. Figure 3-7 repeats these results for a higher inclination of  $i = 75^\circ$ . Clearly the beaming and redshift effects increase for higher spin values. In Figure 3-8, we plot the harmonic power as a function of inclination for  $a/M = 0.9$ , as in Figure 3-5a. For the higher spin, the lighthouse effects are amplified, showing the high harmonic power affiliated with a periodic delta function.

## 3.2 Non-circular Orbits

One of the major unsolved puzzles motivating theoretical models of black hole QPOs is the observation of multiple peaks in the high frequency power spectrum (McClintock & Remillard, 2004). As discussed above, any non-sinusoidal light curve will contribute to Fourier power in harmonics at integer multiples of the fundamental orbital frequency. However, for at least three X-ray binary systems (XTE J1550–564, GRO J1655–40, and H1743–322; possibly also GRS 1915+105), peaks are found with rational (but non-integer) frequency ratios (Miller et al., 2001; Strohmayer, 2001b; Remillard et al., 2002, 2004; Homan et al., 2004). In these particular examples, significant power is measured around the frequencies (184, 276 Hz) for XTE J1550–564,

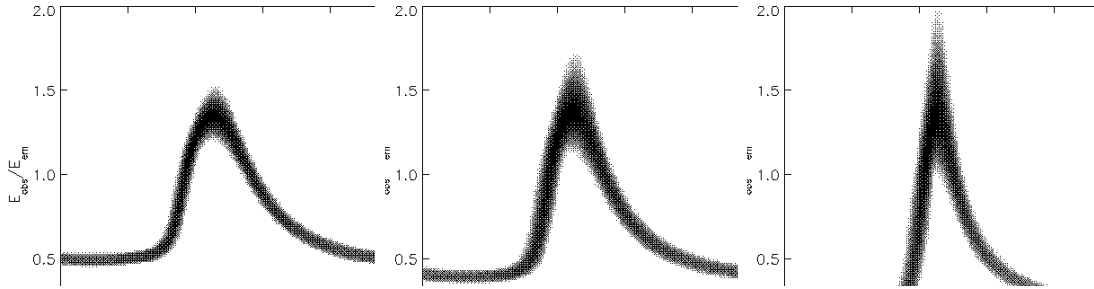


**Figure 3-7:** Spectrograms for hot spots on circular orbits at  $R_{\text{ISCO}}$  for  $i = 75^\circ$  and a variety of spins:  $a/M = 0, 0.5, 0.9$ . In addition to the increased gravitational redshift for higher spin, the orbital velocity increases, in turn increasing the relativistic beaming and blueshift as the hot spot moves towards the observer.

(160, 240 Hz) for H1743–322, and (300, 450 Hz) for GRO J1655–40, almost exactly a 2:3 commensurability in frequencies, while GRS 1915+105 has peaks at 40 and 67 Hz. Following the work of Merloni et al. (1999), we investigate the possibility of these commensurabilities coming from integral combinations of the radial and azimuthal coordinate frequencies of nearly circular geodesics around a Kerr black hole.

In a Newtonian point mass potential, the radial, azimuthal, and vertical (latitudinal) frequencies  $\nu_r$ ,  $\nu_\phi$ , and  $\nu_\theta$  are identical, giving closed planar elliptical orbits. For the Schwarzschild metric the vertical and azimuthal frequencies are identical, giving planar rosette orbits that are closed only for a discrete set of initial conditions. The Kerr metric allows three unique coordinate frequencies, so geodesic orbits in general can fill out a torus-shaped region around the black hole spin axis. When these coordinate frequencies are rational multiples of each other, the trajectories will close after a finite number of orbits.

While there is currently no clear physical explanation for why hot spots may tend toward such trajectories, some recent theoretical work suggests the possible existence of nonlinear resonances near geodesic orbits with integer commensurabilities (Abramowicz et al., 2003; Horak, 2004; Rebusco, 2004). Another important clue may come from the fact that these special orbits are closed, perhaps enhancing the stability of non-circular trajectories. The quasi-periodic nature of the oscillations suggest the continual formation and subsequent destruction of hot spots *near*, but not exactly at, the resonant orbits (see Chapter 4 below). For the purposes of this Thesis, we will take the apparent preference for such orbits as given and concern ourselves primarily

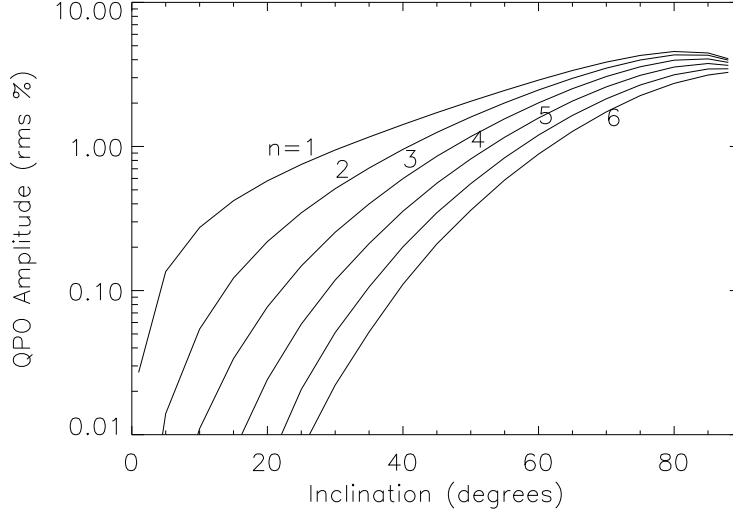


**Figure 3-8:** (a) Fourier amplitude  $a_n(\text{rms})$  in higher harmonic frequencies  $\nu_n = n\nu_\phi$  as a function of orbital inclination to the observer, normalized as in equation (3.6). The hot spot has size  $R_{\text{spot}} = 0.15M$ , an overbrightness factor of 100%, and is in a circular orbit at  $R_{\text{ISCO}}$  around a black hole with  $a/M = 0.9$ .

with calculating the resulting light curves and power spectra.

In geometrized units with  $G = c = M = 1$ , coordinate time is measured in units of  $4.9 \times 10^{-6} (M/M_\odot)$  sec. For example, an orbit with angular frequency  $\Omega_\phi = 2\pi\nu_\phi = 0.1$  around a  $10M_\odot$  black hole would have an observed period of 3.1 ms, whereas the analogous orbit around a supermassive black hole with mass  $10^9 M_\odot$  would have a period of 86 hours. In these units, the three fundamental coordinate frequencies for nearly circular orbits are given by Merloni et al. (1999) [following earlier work by Bardeen, Press, & Teukolsky (1972); Perez et al. (1997)]:

$$\Omega_\phi = 2\pi\nu_\phi = \frac{1}{r^{3/2} \pm a}, \quad (3.8a)$$

$$\Omega_\theta = 2\pi\nu_\theta = \Omega_\phi \left[ 1 \mp \frac{4a}{r^{3/2}} + \frac{3a^2}{r^2} \right]^{1/2}, \quad (3.8b)$$

and

$$\Omega_r = 2\pi\nu_r = \Omega_\phi \left[ 1 - \frac{6}{r} \pm \frac{8a}{r^{3/2}} - \frac{3a^2}{r^2} \right]^{1/2}, \quad (3.8c)$$

where the upper sign is taken for prograde orbits and the lower sign is taken for retrograde orbits. The radial frequency approaches zero at  $r \rightarrow R_{\text{ISCO}}$ , where geodesics can orbit the black hole many times with steadily decreasing  $r$ . In the limit of zero spin and large  $r$ , the coordinate frequencies reduce to the degenerate Keplerian case with  $\Omega_\phi = \Omega_\theta = \Omega_r = r^{-3/2}$ .

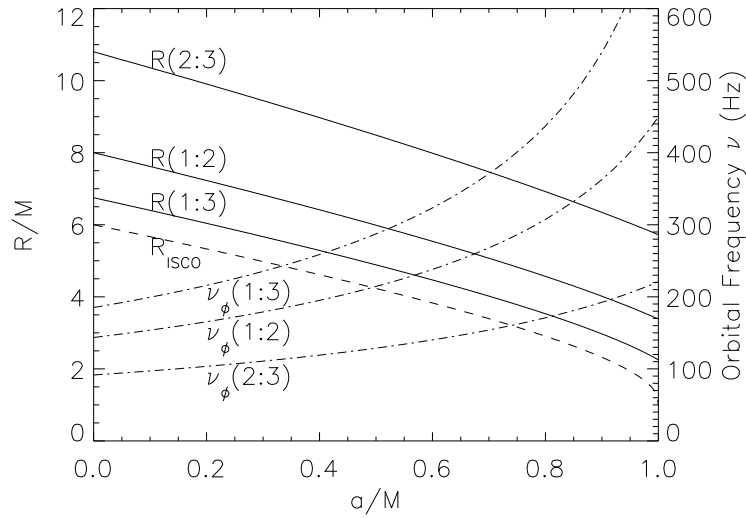


**Figure 3-9:** Radius of prograde orbits with commensurate frequencies  $\nu_r : \nu_\phi = (1:3, 1:2, 2:3)$  (solid lines) as a function of dimensionless spin parameter  $a/M$ . The ISCO (dashed line) corresponds to  $\nu_r : \nu_\phi = 1 : \infty$ . Also shown are the respective orbital frequencies  $\nu_\phi$  at these radii for a black hole with mass  $10M_\odot$  (dot-dashed lines).

To model the 2:3 frequency commensurability, we begin by looking for perturbed circular planar orbits where the radial frequency  $\nu_r$  is one-third the azimuthal frequency  $\nu_\phi$ . Since the orbits are nearly circular, the fundamental mode of the light curve should peak at the azimuthal frequency with additional power in beat modes at  $\nu_\phi \pm \nu_r$ . For  $\nu_r:\nu_\phi = 1:3$ , the power spectrum should have a triplet of peaks with frequency ratios 2:3:4. These commensurate orbits can be found easily from equations (3.8a) and (3.8c) and solving for  $r$ :

$$\left[ 1 - \left( \frac{\nu_r}{\nu_\phi} \right)^2 \right] r^2 - 6r \pm 8ar^{1/2} - 3a^2 = 0. \quad (3.9)$$

Figure 3-9 shows the radius (solid lines) of these special orbits as a function of spin



parameter. The orbital frequencies  $\nu_\phi$  are plotted against the right-hand axis (dot-dashed lines) for a black hole with mass  $10M_\odot$ . Also shown (dashed line) is the inner-most stable circular orbit for prograde trajectories. The position of the 1:3 commensurate orbits follows closely outside the ISCO, suggesting a connection between the high frequency QPOs and the black hole ISCO. However, other integer commensurabilities such as 1:2, 2:5, or 1:4 also closely follow the ISCO curves for varying  $a$ , so the proximity to the ISCO alone is probably not enough to explain the hot spot preference for these specific coordinate frequencies. It is important to note that any given black hole source will have a constant value of  $a/M$ , certainly over the lifetime of our observations. Thus, we may need to observe many more sources like XTE J1550–564 and GRO J1655–40 in order to better sample the parameter space of Figure 3-9 and thus the connection between certain preferred orbits and the black hole ISCO.

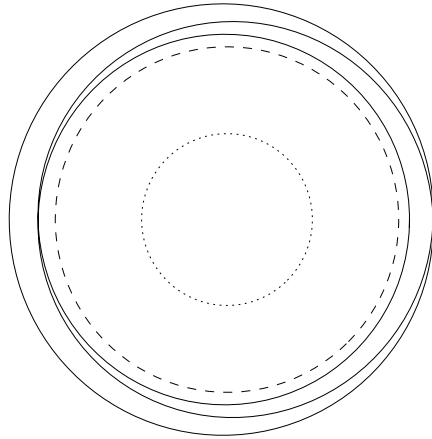


**Figure 3-10:** Overhead view ( $i = 0^\circ$ ) of hot spot trajectory with eccentricity  $e = 0.1$  and commensurate coordinate frequencies  $\nu_\phi = 3\nu_r$ , giving a closed rosette orbit where the hot spot circles the black hole three times between subsequent pericenter passages. The dotted and dashed lines are the horizon and ISCO, respectively, for a spin of  $a/M = 0.5$ .

A 1:3 commensurate trajectory moves through three revolutions in azimuth for each radial period, forming a closed rosette of three “layers.” For such rosettes, the

eccentricity can be defined as

$$e \equiv \frac{r_{max} - r_{min}}{r_{max} + r_{min}} = \frac{\Delta r}{r_0}. \quad (3.10)$$

A “birds-eye view” of such an orbit is shown in Figure 3-10 for  $a/M = 0.5$ , where the horizon is shown as a dotted line, the ISCO is a dashed line, and the commensurate rosette trajectory is plotted as a solid line.

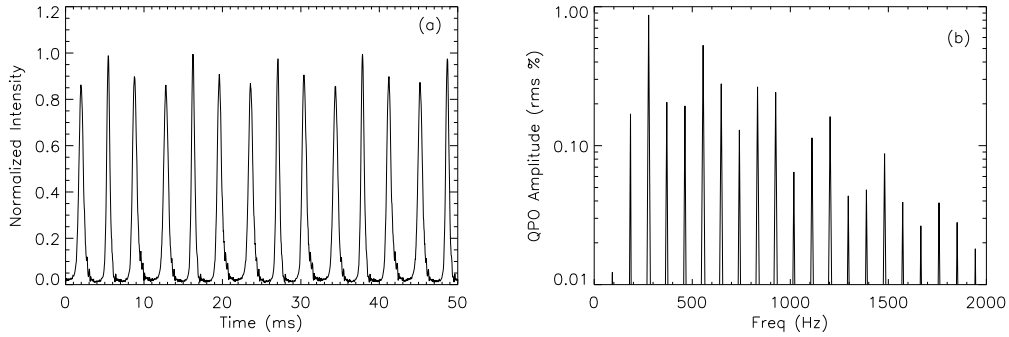


**Figure 3-11:** (a) X-ray light curve of a hot spot orbit with  $\nu_\phi = 3\nu_r$ ,  $e = 0.089$ ,  $M = 10M_\odot$ ,  $a/M = 0.5$ ,  $i = 60^\circ$ , and  $R_{\text{spot}} = 0.5M$ . (b) The Fourier amplitude  $a_n(\text{rms})$  of the above light curve, normalized as in Figure 3-4b, showing the fundamental Kepler frequency at  $\nu_\phi = 285$  Hz and beat modes at  $\nu = n\nu_\phi \pm \nu_r$ .

The time-dependent light curve for a prograde orbit with eccentricity  $e = 0.089$ , spin  $a/M = 0.5$ , and inclination  $i = 60^\circ$  is shown in Figure 3-11a. The time axis begins at the point when the hot spot is at apocenter, moving away from the observer. Thus the first and third peaks come from the hot spot moving toward the observer at a relatively larger radius, while the second, higher peak is caused by the emitter moving toward the observer through pericenter at a higher velocity, giving a larger blueshift and thus beaming factor. The combined Doppler beaming and gravitational lensing causes the peak following the pericenter peak to be slightly larger, as the emitter is moving away from the black hole yet the light is focused more toward the observer.

The power spectrum for this light curve is shown in Figure 3-11b, with the strongest peaks at the azimuthal frequency of  $\nu_\phi = 285$  Hz and its first harmonic at  $2\nu_\phi = 570$  Hz for  $M = 10M_\odot$ . Even for this modest deviation from circularity, there is significant power in the frequencies  $\nu_\phi \pm \nu_r$ . The beating of the fundamental  $\nu_\phi$  with the radial frequency  $\nu_r = (1/3)\nu_\phi = 95$  Hz gives the set of secondary peaks

at  $(2/3)\nu_\phi$  and  $(4/3)\nu_\phi$ . Additional peaks occur at beats of the harmonic frequencies  $n\nu_\phi \pm \nu_r$ .

It is interesting to note that there is not significant power in the radial mode at  $\nu = 95$  Hz, but only in the beats with the fundamental azimuthal frequency and its harmonics. However, in the limit of a face-on orientation ( $i \rightarrow 0^\circ$ ), the radial frequency should dominate the light curve variation as the gravitational and transverse Doppler redshift modulate the intensity as a function of the hot spot's radial coordinate. The radial mode should also be present in the limit of an edge-on orientation ( $i \rightarrow 90^\circ$ ), as gravitational lensing becomes more important, and the hot spot will experience more magnification when closer to the black hole. These two effects actually depend on the inclination in opposite ways. The gravitational redshift and transverse Doppler shift will make the light curve have a minimum at pericenter, where the gravitational lensing is stronger, giving a relative maximum.

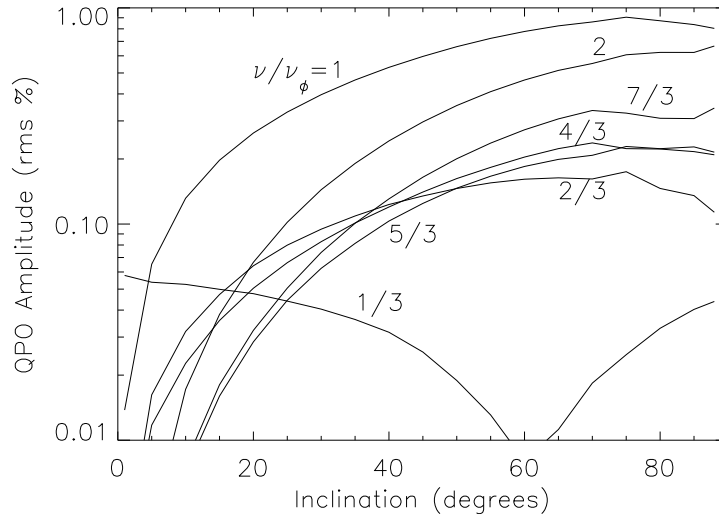


**Figure 3-12:** Power in low-order harmonics and beat modes with frequencies  $\nu = n\nu_\phi \pm \nu_r$ , as a function of disk inclination angle. The hot spot trajectory is the same as in Figure 3-11, with  $a_n(\text{rms})$  normalized as in Figure 3-5. The curves are labeled by the ratio  $\nu/\nu_\phi$ .

In Figure 3-12, which shows the dependence on inclination of the lower order harmonics and beat modes, these two competing effects are clearly evident in the power at  $\nu_r$ , canceling each other out and producing a net minimum for  $i \approx 60^\circ$ . At low inclinations, the radial frequency contributes significant power, while at higher inclinations, the first harmonic of the azimuthal mode begin to dominate with similar

behavior to the circular orbits shown in Figure 3-5a. Along with increasing power at  $2\nu_\phi$ , there is also increasing power in the radial beats of the first harmonic at  $2\nu_\phi \pm \nu_r = (5/3)\nu_\phi, (7/3)\nu_\phi$ . For a  $10M_\odot$  black hole, all these frequencies should be observable within the timing sensitivity of *RXTE*.

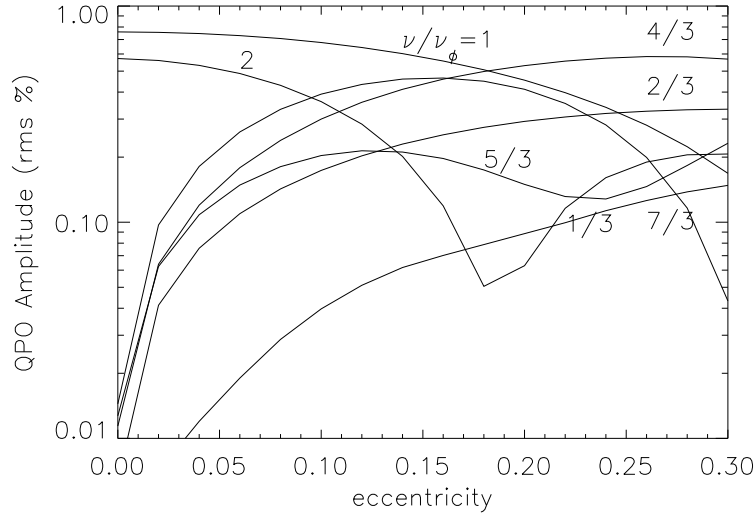


**Figure 3-13:** Power in low-order harmonics and beat modes with frequencies  $\nu = n\nu_\phi \pm \nu_r$ , as a function of orbital eccentricity. The power in each mode  $a_n(\text{rms})$  is normalized as in Figure 3-5. The curves are labeled by the ratio  $\nu/\nu_\phi$ .

To further explore the constraints of our model, we investigated the effect of orbital eccentricity on the QPO power. Maintaining a 3:1 commensurability between azimuthal and radial frequencies, we calculated the light curves for a range of eccentricities  $0 \leq e \leq 0.3$ , shown in Figure 3-13. As expected, the beat modes at  $\nu = \nu_\phi \pm \nu_r$  have more power for more eccentric orbits, as the radial variation of the emitter becomes larger. At the same time, the first harmonic at  $\nu = 2\nu_\phi$  provides relatively less power with increasing eccentricity. This is best understood as the “picket fence” character of the light curve becomes modulated in amplitude and frequency from peak to peak, i.e. for each 3-peak cycle, the time between peaks 1-2, 2-3, and 3-1 are not all the same, damping the harmonic overtone.

The Fourier power in the beat modes  $\nu_\phi \pm \nu_r$  appears to saturate at a moderate eccentricity of  $e \approx 0.15$ , while the fundamental power at  $\nu_\phi$  continues to decrease. One clear conclusion from this calculation is that without the full ray-tracing calculation, these results would be difficult if not impossible to derive by simple physical intuition. Since we still do not have a strong physical explanation for why hot spots might

form at this special commensurate radius  $r_0$ , we also do not have a clear means for determining the eccentricity of such orbits. One possibility is to limit the inner-most extent of the pericenter to the ISCO radius. With this approach, the maximum eccentricity for 3:1 orbits when  $a/M = 0.5$  would be

$$e_{\max} = 1 - \frac{r_{\text{ISCO}}}{r_0} \approx 0.13, \quad (3.11)$$

similar to the typical values used throughout this Thesis. Another limit on the eccentricity is given by the coordinate frequencies themselves. Equations (3.8a, 3.8b, and 3.8c) only apply for small deviations from circularity. As the eccentricity increases, the radius for which  $\nu_\phi = 3\nu_r$  changes slightly, as do the frequencies. Thus for a given black hole mass and spin, if the hot spot eccentricity grows too large, the 3:1 commensurable frequencies will no longer agree with the observed location of the QPO peaks.

While there is some evidence for higher frequency harmonic and beat modes in the QPO power spectrum of XTE J1550–564, the Fourier power is clearly dominated by the two frequencies 184 and 276 Hz (Remillard et al., 2002), corresponding to  $\nu_\phi - \nu_r$  and  $\nu_\phi$  in our model. What are the physical mechanisms that could damp out the higher frequency modes? One possible explanation is in the geometry of the hot spot. As explained in Section 3.1.1, in order to produce the power observed in QPOs, the total X-ray flux coming from the hot spot must be some finite fraction of that of the disk (typically  $10^{-3} - 10^{-2}$  for a QPO amplitude of 1–5%), so the hot spot must have some minimum size or it would not produce enough emission to be detected above the background disk. Yet if the hot spot is too large, it would be sheared by differential rotation in the accretion disk and not survive long enough to create the coherent X-ray oscillations that are observed. As mentioned above, we find that the relative QPO power in different modes is not sensitive to the size of the hot spot  $R_{\text{spot}}$ , as long as the hot spot remains roughly circular. Three-dimensional MHD simulations (Hawley & Krolik, 2001; De Villiers & Hawley, 2003) show a range of density and temperature fluctuations consistent with the hot spot size and overbrightness factor predicted by our model in conjunction with the observations.

It also appears from simulations that as the hot spot is formed in the disk, differential rotation will tend to shear a finite region of gas as it follows a geodesic orbit around the black hole, modifying the shape of the hot spot into an arc in azimuth. In the limit that the emission region could be sheared into a ring of arc length  $\Delta\phi = 360^\circ$ , the fundamental mode and its harmonics would be essentially removed, leaving power only in the radial modulation. Indeed, as shown in Figure 3-14a, for an arc length of  $\Delta\phi = 180^\circ$ , the higher frequency modes at  $\nu = 2\nu_\phi$  and  $\nu = 2\nu_\phi \pm \nu_r$  are strongly suppressed, while still maintaining a significant amount of power in the

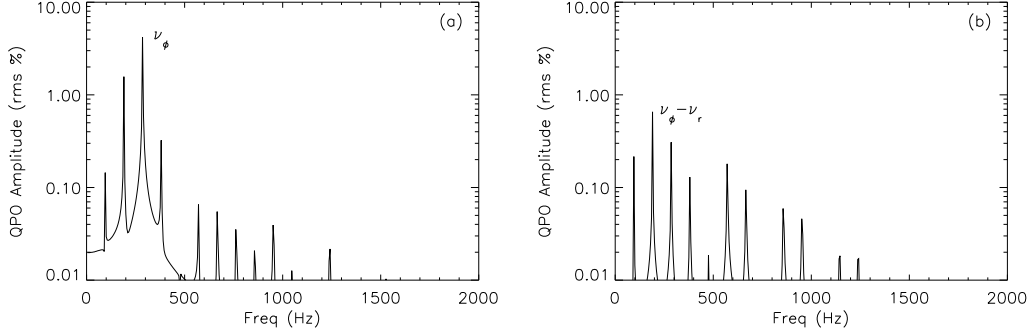


**Figure 3-14:** Power spectrum for a hot spot with same trajectory as in Figure 3-11, with the emission region sheared along the geodesic into an arc of length (a)  $180^\circ$  and (b)  $360^\circ$ . For the shorter arc (a), the power is still peaked at the fundamental frequency  $\nu_\phi = 285$  Hz, while the extended arc (b) produces more power in the beat frequency  $\nu_\phi - \nu_r = 190$  Hz.

fundamental beat modes  $\nu_\phi \pm \nu_r$ . The total QPO power also increases as the area of the emission region increases relative to the circular hot spot geometry.

However, when we allow the arc to be sheared into a ring with  $\Delta\phi = 360^\circ$ , the total QPO power is actually decreased as the differential beaming is essentially eliminated by the extended emission region: there is always some portion of the arc moving toward the observer. The resulting modulation is then more weighted to the first radial beat mode at  $\nu_\phi - \nu_r$ , as seen in Figure 3-14b. It is not intuitively obvious why the  $\nu_\phi - \nu_r$  mode is dominant while the  $\nu_\phi + \nu_r$  mode ( $\nu = 380$  Hz) is much weaker in the arc geometry. If anything, this is a strong argument for the necessity of a full ray-tracing calculation of the hot spot light curves when predicting QPO power spectra, as it clearly gives information unavailable to simple analysis of the geodesic coordinate frequencies. In Chapter 4 below, we will give a more physical explanation for why these lower frequency beat modes are amplified while the higher frequency modes are suppressed.

This behavior offers a plausible explanation for the two major types of QPOs described in Remillard et al. (2002), initially distinguished by the properties of their simultaneous LFQPOs. For XTE J1550–564, the type A power density spectra have more total power in the HFQPOs, with a major peak at 276 Hz and a minor peak at 184 Hz. Type B spectra have most of the QPO power around 184 Hz and a smaller peak around 276 Hz and less overall power in the high frequency region of the spectrum. Thus we propose that type A QPOs are coming from more localized hot spot/arc regions, while type B QPOs come from a more extended ring geometry.

### 3.3 Non-planar Orbits

In addition to the commensurate high-frequency QPOs observed in sources like XTE J1550–564, there are also strong low-frequency QPOs observed at the same time with frequencies in the range 5 – 15 Hz. There have been suggestions that these low-frequency QPOs may be caused by the Lense-Thirring precession of the disk near the ISCO, also known as “frame dragging” (Markovic & Lamb, 1998; Merloni et al., 1999; Abramowicz & Kluzniak, 2001; Remillard et al., 2002). For geodesic orbits out of the plane perpendicular to the black hole spin, the latitudinal frequency  $\Omega_\theta$  of massive particles is not equal to the azimuthal frequency  $\Omega_\phi$  [see eqs. (3.8b) and (2.85)], leading to a precession of the orbital plane with frequency

$$\Omega_{LT} \equiv |\Omega_\theta - \Omega_\phi|. \quad (3.12)$$

Figure 3-15 shows the bands of coordinate frequencies  $\nu_{LT}(r_0)$  and  $\nu_\phi(r_0)$  as a function of spin, for a small range of possible black hole masses for each of XTE J1550–564 and GRO J1655–40. Where the coordinate frequencies match the observed QPO frequencies, a possible solution for the spin exists. For black holes with the mass and spin used above ( $M = 10M_\odot$ ,  $a/M = 0.5$ ), the frame-dragging frequency, as calculated at the radius corresponding to the commensurability  $\nu_r:\nu_\phi=1:3$ , is somewhat higher than that observed in the low-frequency QPOs from XTE J1550–564. The type A QPO peaks at 12 and 276 Hz appear to be consistent with a black hole mass of  $8.9M_\odot$  and spin parameter of  $a/M = 0.35$  [Orosz et al. (2002) give a ( $1\sigma$ ) estimate of  $9.7 - 11.6M_\odot$ ], quite similar to the values used throughout much of this paper. For the BH binary GRO J1655–40, we can fit the QPOs at 18 and 450 Hz with a mass of  $5.1M_\odot$  and spin  $a/M = 0.28$ , also slightly less than the published mass range of  $5.5 - 7.9M_\odot$  (Shahbaz et al., 1999). These results are shown in Table 3.1.

If we relax the requirement of matching the LFQPOs and only fit the HFQPOs with a 1:3 coordinate frequency commensurability, there remains a 1-dimensional degeneracy in the mass-spin parameter space. Based solely on the HFQPOs, for XTE J1550–564 with  $9.5 < M/M_\odot < 11.5$ , the range of spin parameters would be  $0.42 < a/M < 0.6$ , and for GRO J1655–40, the spin would be in the range  $0.35 < a/M < 0.66$ .

To get a more quantitative feel for the effect of Lense-Thirring precession on the power spectrum, we investigated hot spot orbits with initial trajectories inclined to the plane of the disk:  $v^\theta \neq 0$ . This is much like changing the observer’s inclination with a period of  $2\pi/\Omega_{LT}$ . Thus we see additional modulation in the hot spot light curve at the “double-beat” modes  $\nu_\phi \pm \nu_r \pm \nu_{LT}$ . We find that, for modestly inclined hot spot orbits ( $i_0 = \pm 5^\circ$ ), the contribution to the power spectrum at Lense-Thirring frequencies is quite small ( $< 1\%$  of total power) for the basic circular hot spot geometry. This

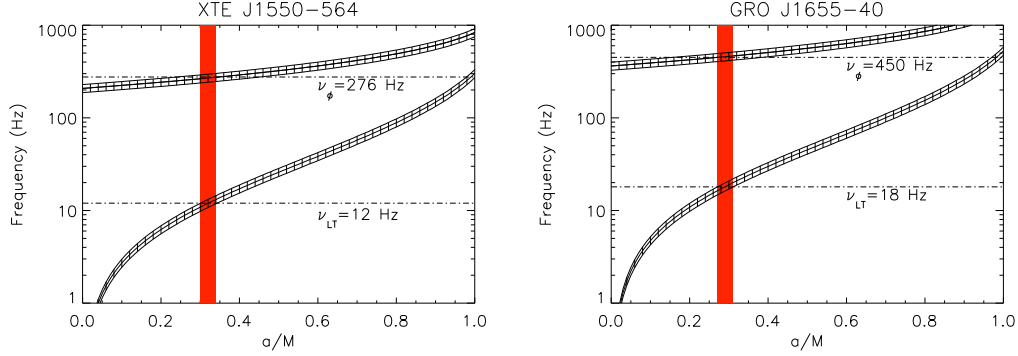


**Figure 3-15:** Coordinate frequencies  $\nu_{LT}$  and  $\nu_\phi$  as a function of spin for a small range of black hole masses (hashed bands), plotted over the observed low- and high-frequency QPO locations for XTE J1550-564 and GRO J1655-40. The orbital radius is picked such that  $\nu_\phi = 3\nu_r$ , and the spin is determined by the solution region marked by a vertical red band, corresponding to  $M = 8.9 \pm 0.9M_\odot$  for XTE J1550 and  $M = 5.1 \pm 0.5M_\odot$  for GRO J1655. [Compare with Figure 8 in Remillard et al. (2002)]

relative contribution increases with arc length as the spot becomes a ring precessing about the spin axis, consistent with the relative power in LFQPOs and HFQPOs in the type A (more high frequency power than low frequency) and type B (more low frequency power) sources described above.

Under the premise that the HFQPO commensurate frequencies are caused by the geodesic motion of a sheared, overbright region in the disk, in Table 3.2 we show the best fit parameters for the type A and type B power density spectra from XTE J1550-564 [cf. Table 1 in Remillard et al. (2002)]. Guided also by the (somewhat speculative) assumption that the LFQPOs come from the Lense-Thirring precession of the hot spot orbital plane, we predict a black hole mass and spin. Using a fixed inclination of  $70^\circ$ , we can match the frequencies and amplitudes of the observed HFQPO peaks (and, equally important, the lack of power at certain frequencies) for both type A and type B QPOs. Setting constant the eccentricity  $e = 0.1$ , geodesic inclination to the disk  $i_0 = 5^\circ$ , and the overbrightness to be a factor of unity, we fit the hot spot radius and arc length to match the observations. Being able to match the QPO rms amplitudes of the peaks (or lack thereof) at 92, 184, 276, and 368 Hz, for at least two different types of X-ray outburst, shows the robustness of our simple model in explaining these phenomena.

However, even with the sheared arc emission, many observations still show significantly more power in the LFQPOs (typically  $\sim 20\%$  rms) than can be explained



**Table 3.1:** Black hole parameters for the XTE J1550–564 and GRO J1655–40, matching low- and high-frequency QPOs to geodesic coordinate frequencies

Black Hole Parameters	XTE J1550–564	GRO J1655–40
BH Mass	$8.9M_{\odot}$	$5.1M_{\odot}$
BH Spin	$0.35M$	$0.28M$
$R_{\text{ISCO}}$	$4.8M$	$5.05M$
Inclination	$70^{\circ}$	$65^{\circ}$
<hr/> <hr/>		
Geodesic Frequencies		
$r_0$	$5.54M$	$5.77M$
$\nu_{\text{LT}}$	12 Hz	18 Hz
$\nu_r$	92 Hz	150 Hz
$\nu_{\phi}$	276 Hz	450 Hz

solely from the Lense-Thirring precession of a geodesic near the ISCO (Remillard, 2004). Coupled with the difficulty in simultaneously fitting the mass and spin to three coordinate frequencies in a manner consistent with spectroscopic mass predictions, it seems likely that the LFQPOs may be caused by some other mechanism in the disk that is related only indirectly to the high-frequency hot spot emission. Another likely possibility is that the thin, warped disk model breaks down near the ISCO, allowing more complicated emission geometries and thus amplifying the effects of Lense-Thirring precession (Markovic & Lamb, 1998).

A recent paper by Miller & Homan (2005) shows evidence for a correlation between the phase of the low-frequency QPO light curve (easily resolvable by *RXTE* for  $\nu \approx 1 - 2$  Hz) and the shape of the time-varying iron emission line in the black hole binary GRS 1915+105. One possible explanation for this behavior is a simple precessing ring made of geodesic particles orbiting out of the plane of the disk. For high observer inclinations, the total flux and the iron emission line will both be significantly modulated as the ring rotates due to Lense-Thirring precession. The edge-on disk gives a broader emission line, with a higher overall flux due to the greater relativistic beaming, while the face-on edge gives a minimum in the light curve, with a narrower emission line, just as reported by Miller & Homan (2005). Preliminary ray-tracing calculations of such a geometry suggest that the ring is centered around  $r \approx 10M$  with an inclination to the plane of  $\pm 20^{\circ}$ , with a black hole spin of  $a/M = 0.1 - 0.2$  and observer inclination  $i = 70^{\circ}$ .

**Table 3.2:** QPO amplitudes of the hot spot/arc model for XTE J1550–564

Parameter		Type A	Type B
$R_{\text{spot}}$		$0.3M$	$0.5M$
arc length		$200^\circ$	$320^\circ$
eccentricity		0.1	0.1
inclination to disk		$5^\circ$	$5^\circ$
overbrightness		100%	100%
Amplitude (mode)	Frequency (Hz)	rms(%)	rms(%)
$a(\nu_{\text{LT}})$	12	0.63	2.1
$a(\nu_r)$	92	0.48	0.89
$a(\nu_\phi - \nu_r)$	184	1.3	2.2
$a(\nu_\phi)$	276	3.2	0.42
$a(\nu_\phi + \nu_r)$	368	0.20	0.23

### 3.4 Summary

The hot spot model makes a number of general predictions of the Fourier power of the X-ray light curve as a function of inclination and black hole spin, and is also able to explain QPO observations from the black hole binaries XTE J1550–564 and GRO J1655–40. Simply by matching the locations of the low-frequency and high-frequency QPOs with the coordinate frequencies (under the condition  $\nu_\phi = 3\nu_r$ ), we can determine the black hole mass and spin. Relaxing the LFQPO constraint, the spin can still be determined uniquely for a given mass, which in turn could be measured independently with the inclination and radial velocity of the companion star.

By matching the amplitudes of various QPO peaks observed in XTE J1550–564, we have explored the model parameters such as the hot spot size, shape, and the overbrightness relative to a steady-state background disk. The predicted magnitude of these fluctuations are within the range predicted by 3D MHD calculations of the accretion disk. Future work will investigate the effect of multiple hot spots of various size, emissivity, and lifetime, as guided by MHD calculations. Observations of additional sources with commensurate frequency QPOs may help us further constrain the hot spot model and better understand the connection between the LFQPOs and HFQPOs.

Some of the physical problems with the original hot spot model have been raised by Markovic & Lamb (2000), as discussed above. Many of these points are addressed in our model. First, unlike Stella & Vietri (1998, 1999), we only attempt to explain a set of QPO data from *black hole* binaries, which differ qualitatively from neutron star

binaries in many ways, e.g. lacking strong global magnetic fields and thermonuclear activity. And perhaps most significant, black holes have no rotating surface to interact with the accreting matter and provide additional confusion to the QPO power spectrum. Our model produces light curves with power spectra consistent with black hole observations even with low eccentricity hot spot orbits.

Because they do not include ray tracing in their calculations, Markovic & Lamb (2000) are unable to model many relativistic effects, including the gravitational lensing of the hot spot source, which can be quite significant for systems with moderate to high inclination angles ( $i \geq 60^\circ$ ). Since we calculate the actual X-ray modulation from the orbiting hot spots, we predict both the location and amplitude of every peak in the light curve power spectrum, which cannot be done by analyzing the BH coordinate frequencies alone. By introducing a perturbation on circular orbits near the ISCO, additional peaks begin to appear in the power spectrum, caused by beats of the azimuthal and radial frequencies  $\nu_\phi$  and  $\nu_r$ . The dependence of the relative power in the different peaks on inclination and spin helps to constrain the details of the hot spot model in explaining the HFQPOs, particularly the 2:3 commensurability observed in the power spectra from XTE J1550–564 and GRO J1655–40.

As an additional parameter, we introduce a finite arc length for the emission region, motivated by the shearing of the hot spot by differential rotation in the disk. The spreading of the hot spot in azimuth leads to suppression of the higher QPO modes, in agreement with observations. We have also examined the possibility of Lense-Thirring precession for non-planar orbits as an explanation for the low-frequency QPOs that have been observed coincident with the HFQPOs yet often with even stronger Fourier power. The predicted power spectra from non-planar precessing arcs are consistent with observations of XTE J1550–564 if we associate type A QPOs with hot spot arcs of  $\Delta\phi \approx 180^\circ$  and type B QPOs with hot spot rings of  $\Delta\phi \approx 360^\circ$ . However, the difficulty in matching the LFQPOs amplitude and frequency with a single hot spot geodesic suggests the low-frequency modulations may be caused by a different mechanism or perhaps our disk geometry is too simplistic.

One major remaining issue with the hot spot model is the preferred location of the geodesic that gives rise to 1:3 coordinate frequencies. Why should the orbital frequencies favor integer ratios, and why should the preferred ratio be 1:3 and not 1:2 or 1:4? It is possible that detailed global radiation-MHD calculations with full general relativity will be required to answer this question. Perhaps the non-circular orbits can only survive along closed orbits such as these to somehow avoid destructive intersections (Abramowicz & Kluzniak, 2003). Or there may be magnetic interactions with the black hole itself, analogous to the Blandford-Znajek process, that lock the accreting gas into certain preferred trajectories (Wang et al., 2003). For now, we are forced to leave this as an open question unanswered by the geodesic hot spot model.

A less difficult problem is the explanation of the widths of the QPO peaks. As it stands, our hot spot model predicts purely periodic light curves and thus power spectra made up of delta functions. If there *is* some physical mechanism that preferentially focuses accreting material onto eccentric orbits at specific radii, then it is likely that these hot spots are forming and then being destroyed as a continual process. The superposition of many hot spots around the same orbit, all with slightly different initial trajectories, could explain the quasi-periodic nature of the power spectrum: the phase decoherence of the hot spots would cause a natural broadening of the strictly periodic signal from a single spot (Schnittman & Bertschinger, 2004b; Schnittman, 2005). With the computational framework in place, this question can be answered by modeling a whole collection of hot spots and arcs continually forming and evolving in shape and emissivity.

# Chapter 4

## Features of the QPO Spectrum

*As far as the laws of mathematics refer to reality, they are not certain, as far as they are certain, they do not refer to reality.*

*If the facts don't fit the theory, change the facts.*

-Albert Einstein

The results presented in this Chapter are based on the extension of the hot spot model, as described in the papers “Interpreting the High Frequency QPO Power Spectra of Accreting Black holes,” (Schnittman, 2005) and “The Bicoherence as a Diagnostic for Models of High Frequency QPOs,” (Maccarone & Schnittman, 2005).

### 4.1 Introduction

One of the most exciting results from the *Rossi X-Ray Timing Explorer (RXTE)* has been the discovery of high frequency quasi-periodic oscillations (HFQPOs) from neutron star and black hole binaries [Strohmayer et al. (1996); van der Klis et al. (1996); Strohmayer (2001a); see Lamb (2003) for a review]. For black hole systems, these HFQPOs are observed repeatedly at more or less constant frequencies, and in a few cases with integer ratios (Miller et al., 2001; Remillard et al., 2002; Homan et al., 2004; Remillard et al., 2004). These discoveries give the exciting prospect of determining a black hole’s mass and spin, as well as testing general relativity in the strong-field regime [see e.g. Kluzniak, Michelson, & Wagoner (1990); De Deo & Psaltis (2004); Psaltis (2004b)].

To understand these observations more quantitatively, we have developed a ray-tracing code to model the X-ray light curve from a collection of “hot spots,” small

regions of excess emission moving on geodesic orbits (Schnittman & Bertschinger, 2004a,b). Similar ray-tracing models of multiple hot spots with a range of geodesic orbits in a Schwarzschild metric have been proposed by Karas, Vokrouhlicky, & Polnarev (1992) and Karas (1999), and used to produce theoretical light curves and power spectra. The hot spot model is largely motivated by the similarity between the QPO frequencies and the black hole coordinate frequencies near the inner-most stable circular orbit (ISCO) (Stella & Vietri, 1998, 1999), as well as the suggestion of a resonance leading to integer commensurabilities between these coordinate frequencies (Abramowicz & Kluzniak, 2001, 2003; Rebusco, 2004). Stella & Vietri (1999) investigated primarily the QPO frequency pairs found in accreting neutron star binary systems, but their approach can be applied to black hole systems as well. The hot spots themselves could be formed and destroyed in any number of ways, including magnetic flare avalanches (Poutanen & Fabian, 1999; Zycki, 2002), vortices and flux tubes (Abramowicz et al., 1992), or magnetic instabilities (Balbus & Hawley, 1991).

The basic geodesic hot spot model (see above, Chapter 3) is characterized by the black hole mass and spin, the disk inclination angle, and the hot spot size, shape, and overbrightness. Motivated by the 3:2 frequency commensurabilities observed in QPOs from XTE J1550–564, GRO J1655–40, and H1743–322 (Remillard et al., 2002; Homan et al., 2004; Remillard et al., 2004), we pick a radius for the geodesic orbits such that the coordinate frequencies  $\nu_\phi$  and  $\nu_r$  will have a 3:1 ratio. Thus the 3:2 commensurability is interpreted as the fundamental orbital frequency  $\nu_\phi$  and its beat mode with the radial frequency at  $\nu_\phi - \nu_r$ . Conversely, when the orbital and radial frequencies have a 3:2 ratio, the corresponding power spectrum shows the strongest peaks at  $\nu_\phi:(\nu_\phi - \nu_r) = 3:1$ , in disagreement with the data. For this reason, in the discussion below, we will focus primarily on the 3:1 coordinate frequency resonance proposed by Abramowicz & Kluzniak (2001, 2003). Furthermore, we relax the low frequency QPO criterion, described above in Section 3.3, leaving a one-dimensional degeneracy in the mass-spin parameter space which can be broken by an independent determination of the binary system’s inclination and radial velocity measurements of the low-mass companion star [see e.g., Orosz et al. (2002, 2004)].

Given the black hole mass, spin, inclination, and the radius of the geodesic orbit, the parameters of the hot spot model (i.e. the hot spot size, shape, and overbrightness, and the orbital eccentricity) are determined by fitting to the amplitudes of the peaks in the observed power spectrum (Schnittman & Bertschinger, 2004a). However, the model as described so far produces a perfectly periodic X-ray light curve as a single hot spot orbits the black hole indefinitely. Such a periodic light curve will give a power spectrum composed solely of delta-function peaks, unlike the broad features seen in the observations.

In this Chapter we introduce two simple physical models to account for this broad-

ening of the QPO peaks. The models are based on analytic results, then tested and confirmed by comparison with three-dimensional ray-tracing calculations of multiple hot spots (Schnittman & Bertschinger, 2004b). We find the power spectrum can be accurately modeled by a superposition of Lorentzian peaks, consistent with the standard analysis of QPO data from neutron stars and black holes (Olive et al., 1998; Nowak, 2000; Belloni et al., 2002). Many of the methods and results presented here are equally valid for other QPO models such as diskoseismology (Wagoner, 1999), vertically-integrated disk oscillations (Zanotti, Rezzolla, & Font, 2003; Rezzolla et al., 2003; Rezzolla, Yoshida, & Zanotti, 2003), toroidal perturbations (Lee & Ramirez-Ruiz, 2002; Lee, Abramowicz, & Kluzniak, 2004), and magnetic resonances (Wang et al., 2003).

The previous Chapters outlined most of the general features of the basic hot spot model and the ray-tracing code used to produce periodic light curves. The specific parameters used in this Chapter are briefly summarized in Section 4.2. In Section 4.3 we explain the effect of summing the light curves from multiple hot spots with random phases and different lifetimes to give Lorentz-broadened peaks in the power spectrum. Section 4.4 shows how a finite width in the radii of the geodesic orbits produces a corresponding broadening of the QPO peaks. In Section 4.5 we develop a simple model for photon scattering in the corona, which affects other features of the power spectrum such as the continuum noise and the damping of high frequency harmonics, but does not contribute to the broadening of the QPO peaks. Finally, all the pieces of the model are brought together in Section 4.6 and used to interpret the power spectra from a number of observations of XTE J1550–564. Section 4.7 introduces the use of higher-order statistics as an observational tool for distinguishing between the various peak broadening mechanisms.

## 4.2 Parameters for the Basic Hot Spot Model

In Schnittman & Bertschinger (2004a) we developed a geodesic hot spot model (see Chapters 2 and 3 above) to explain the 3:2 frequency commensurabilities seen in the QPO power spectra of XTE J1550–564, GRO J1655–40, and H1743–322. The results of this extended model are based on the fully relativistic ray-tracing framework described in that paper. Starting from a distant observer, a collection of photon trajectories are integrated backwards in time to a fixed coordinate grid surrounding the black hole. With the spacetime position and momentum recorded at each point in the computational grid, time-dependent images of the dynamic disk can be created with ease. While this technique is quite general and can be used to analyze various QPO models, for simplicity we restrict our discussion in this Chapter to the geodesic hot spot model.

The hot spots are treated as monochromatic, isotropic emitters in their rest frames, moving along the geodesic orbits of massive test particles. For the Kerr geometry, these orbits generally have three non-degenerate frequencies (azimuthal, radial, and vertical). As explained above in Section 4.1, we focus our analysis on closed orbits with  $\nu_\phi = 3\nu_r$ , giving the strongest peaks in the power spectrum at the fundamental orbital frequency  $\nu_\phi$  and the beat mode  $\nu_\phi - \nu_r$ . The relative damping of the upper beat mode at  $\nu_\phi + \nu_r$  is explained below in Section 4.5.

For a given black hole mass, the spin is determined uniquely by matching the coordinate frequencies to the observed QPO peaks. As shown in Schnittman & Bertschinger (2004a), the rms amplitudes of the various peaks are determined by the hot spot's orbital inclination, eccentricity, and overbrightness relative to the steady-state emission from the disk. For the fiducial example used in much of this Chapter, the black hole has mass  $M = 10M_\odot$  and spin  $a/M = 0.5$  with a disk inclination of  $i = 70^\circ$ . Each hot spot is on a planar orbit around a radius of  $r_0 = 4.89M$  with  $\nu_\phi = 285$  Hz,  $\nu_r = 95$  Hz, and a moderate eccentricity of  $e = 0.1$ . These figures are similar, but not identical to the best-fit parameters for observations of XTE J1550–564 presented in Section 4.6.

For a single hot spot on a geodesic trajectory, the resulting light curve will be purely periodic, corresponding to a power spectrum made up of multiple delta-functions. These delta-function peaks will be located at linear combinations of the coordinate frequencies, with their relative amplitudes determined by the orbital parameters via the ray-tracing calculation. But unlike these periodic features, the actual data shows broad peaks in the observed power spectra, hence the term *quasi*-periodic oscillations. In Schnittman & Bertschinger (2004b) we showed how the superposition of many hot spots with finite lifetimes and random phases could give a natural explanation for this broadening, as we will explain in greater detail below.

### 4.3 Peak Broadening from Hot Spots with Finite Lifetimes

While the basic model presented above takes as given the existence of hot spots on certain special orbits, we can also gain some physical intuition about these hot spots from more detailed calculations. Three-dimensional magnetohydrodynamic simulations of accretion disks suggest that in general such hot spots are continually being formed and destroyed with random phases, with a range of lifetimes, amplitudes, and orbital frequencies (Hawley & Krolik, 2001; De Villiers, Hawley, & Krolik, 2003).

For now, we consider the contribution from identical hot spots, assuming that each one forms around the same radius with similar size and overbrightness and



survives for some finite time before being destroyed. Over this lifetime, the hot spot produces a coherent periodic light curve as in the single spot model. Analogous to radioactive decay processes, we assume that during each time step  $dt$ , the probability of the hot spot dissolving is  $dt/T_l$ , where  $T_l$  is the characteristic lifetime of the hot spots. As derived in Appendix B, if each coherent segment is a purely sinusoidal function  $f(t) = A \sin(2\pi\nu_0 t + \phi)$ , the corresponding power spectrum is a Lorentzian peak centered around  $\nu = \nu_0$  with a characteristic width given by

$$\Delta\nu = \frac{1}{2\pi T_l}. \quad (4.1)$$

If this model is a qualitatively accurate description of how hot spots form and dissolve in the disk, one immediate conclusion is that the oscillator quality factor  $Q \equiv \nu_0/\text{FWHM}$  can be fairly high even for relatively short coherence times:

$$Q = \pi T_l \nu_0 = \pi \times \langle \# \text{ of orbits} \rangle. \quad (4.2)$$

If, on the other hand, every hot spot has a lifetime of *exactly* four orbits ( $T_l = 4/\nu_0$ ), the central peak of the power spectrum  $G^2(\nu, T_l)$  has coherence  $Q \approx 4.5$ , about what one would expect from a first-order estimate. However, after integrating over the exponential lifetime distribution to get the Lorentzian profile of equation (B.10), the resulting quality factor is  $Q \approx 12.6$ , roughly a factor of three higher. Remillard et al. (2002) observe quality values of  $Q \sim 5 - 10$  for the HFQPOs seen in XTE J1550-564, corresponding to typical hot spot lifetimes of only 2-3 orbits.

While this result is based on a boxcar sampling function for the hot spots (i.e. instantaneous creation and destruction of each hot spot, with constant brightness over its lifetime), these results are quite general for other window functions as well. In Appendix B we show that, for any set of self-similar sampling functions  $w(t; T)$  [and its Fourier pair  $W(\nu; T)$ ], the exponential lifetime distribution has the effect of narrowing the peak of the net power spectrum compared with that of a single segment of the light curve with length  $T_l$ . This smaller width can be understood by considering the distribution of hot spot lifetimes and their relative contribution to the total power spectrum [see eqns. (B.7) and (B.9)]. While there are actually more segments with individual lifetimes shorter than  $T_l$ , the few long-lived segments of the light curves add significantly more weight to the QPO peaks since  $W(\nu = 0; T) \propto T$  while  $\Delta\nu \propto 1/T$ .

In addition to the boxcar function, another physically reasonable model for the hot spot evolution is that of a sharp rise followed by an exponential decay, perhaps caused by magnetic reconnection in the disk (Poutanen & Fabian, 1999; Zycki, 2002). In this case, the light curve would behave like a damped harmonic oscillator, for which the

power spectrum is also given by a Lorentzian [see van der Klis (1989), where this result is presented in the context of an exponential shot model]. Interestingly, the shape and width of the resulting QPO peak is exactly the same, whether we use a collection of boxcar functions with an exponential lifetime distribution, or if we use a set of exponential sampling functions, each with the same decay time. In the discussion below and when doing the actual light curve simulations, we will assume a boxcar sampling function and an exponential lifetime distribution, with its corresponding Lorentzian power spectrum. This approach also facilitates a direct comparison with observations and other theoretical models, where the QPO data is often fit by a collection of Lorentzian peaks (Nowak, 2000; Belloni et al., 2002).

Due to the linear properties of the Fourier transform, equation (4.1) and the analysis of Appendix B, while derived assuming a purely sinusoidal signal with a single frequency  $\nu_0$ , can be applied equally well to any periodic light curve with an arbitrary shape. If each coherent section of the light curve is written as

$$f(t) = \sum_j A_j \sin(2\pi\nu_j t + \phi_j), \quad (4.3)$$

then the total power spectrum (integrating over a distribution of coherent segments with random phase) is simply the sum of the Lorentz-broadened peaks from equation (B.10):

$$\tilde{I}^2(\nu) = 2N_{\text{spot}} A_j^2 \frac{T_l}{T_f} \sum_j \frac{1}{1 + 4\pi^2 T_l^2 (\nu - \nu_j)^2}, \quad (4.4)$$

where on average there are  $N_{\text{spot}}$  hot spots in existence at any given time and the light curve is integrated over a total time of  $T_f$ . Note that every peak in the power spectrum  $\tilde{I}^2(\nu)$  has the same characteristic width  $\Delta\nu = 1/(2\pi T_l)$ .

The sum in equation (4.3) can be generalized to a Fourier integral so that equation (4.4) becomes the convolution (denoted by the symbol  $\star$ ) of the segment power spectrum  $F^2(\nu)$  with a normalized Lorentzian  $\mathcal{L}(0, \Delta\nu)$  centered on  $\nu = 0$  with width  $\Delta\nu$ :

$$\tilde{I}^2(\nu) = \frac{1}{\pi\Delta\nu} \int_{-\infty}^{\infty} \frac{F^2(\nu') d\nu'}{1 + \left(\frac{\nu - \nu'}{\Delta\nu}\right)^2} = [F^2 \star \mathcal{L}(0, \Delta\nu)](\nu). \quad (4.5)$$

Now we can apply our results to the light curves as calculated by the original ray-tracing code for a single geodesic hot spot. First, the X-ray light curve over one complete period is calculated to give the Fourier components  $A_j$  in equation (4.3). For geodesic orbits in the Kerr metric, the power spectrum  $F^2(\nu)$  is concentrated at integer combinations of the black hole coordinate frequencies  $\nu_\phi$ ,  $\nu_r$ , and  $\nu_\theta$ . Given these frequencies  $\nu_j$ , amplitudes  $A_j$ , and a characteristic hot spot lifetime  $T_l$ , the integrated power spectrum follows directly from equation (4.4).

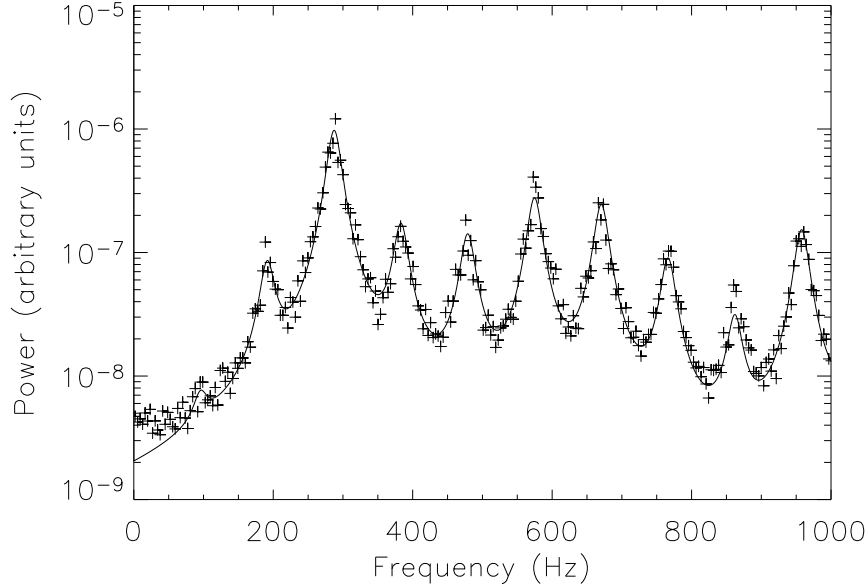


**Figure 4-1:** Simulated power spectrum (crosses) from a ray-tracing calculation of many hot spots on geodesic orbits with random phases and different lifetimes, along with an analytic model (solid line) of that power spectrum. The black hole has mass  $M = 10M_{\odot}$  and spin  $a/M = 0.5$ , giving  $\nu_r = 95$  Hz and  $\nu_{\phi} = 285$  Hz. The hot spot orbit has an eccentricity of 0.1 around a radius of  $r_0 = 4.89M$  and an inclination of  $70^{\circ}$ . The peaks have Lorentzian profiles with  $\Delta\nu \approx 11$  Hz, corresponding to a characteristic hot spot lifetime of four orbits.

Using the same ray-tracing code, we can also directly simulate the extended light curve and corresponding power spectrum produced by many hot spots orbiting with random phases, continually formed and destroyed over each time step with probability  $dt/T_l$  (Schnittman & Bertschinger, 2004b). The power spectrum of such a simulation is shown in Figure 4-1 (crosses), along with the analytic model (solid curve). The orbital parameters for each individual hot spot are the same as those outlined in Section 4.2. The characteristic lifetime  $T_l$  is four orbits (about 14 msec), corresponding to a Lorentzian width of  $\Delta\nu \approx 11$  Hz. We should stress that this curve is *not a fit to the simulated data*, but an independent result calculated using the model described above.

The defining characteristic of QPO peaks broadened by the summation of hot spots with finite lifetimes and random phases is the uniform width of the individual peaks. For a power spectrum with multiple harmonics and beat modes, each peak

is broadened by exactly the same amount, determined by the average lifetime of the individual hot spots. Thus if we can measure the widths of multiple QPO peaks in the data, the hot spot lifetime can be determined redundantly with a high level of confidence.

## 4.4 Distribution of Coordinate Frequencies

In the previous Section, we assumed a single radius for all the hot spot orbits. This ensures identical geodesic coordinate frequencies for different hot spots with different phases and lifetimes. However, this assumption betrays one of the major weaknesses of the geodesic hot spot model: there still does not exist a strong physical argument for why these hot spots should form at one special radius or why that radius should have coordinate frequencies with integer commensurabilities. For now, we will be forced to leave that question unanswered, but we can make progress by drawing on intuition gained from other fields of physics. If there does exist some physical resonance in the system that favors these orbits, causing excess matter to “pile up” at certain radii (Abramowicz & Kluzniak, 2001, 2003), then just like any other resonance, there should be some finite width in phase space over which the resonant behavior is important. The integer commensurability of the QPO peaks suggests that closed orbits may be playing an important role in the hot spot formation. If this is so, then some hot spots should also form along orbits that *almost* close, i.e. geodesics with nearly commensurate coordinate frequencies. These orbits will have guiding center radii similar to the critical radius  $r_0$  for which the geodesics form closed curves.

Motivated by other processes in nature such as damped harmonic oscillators and atomic transitions, we model the resonance strength as a function of radius with a Lorentzian of characteristic width  $\Delta r$ . Then the probability of a hot spot forming at a given radius is proportional to the strength of the resonance there, giving a distribution of orbits according to

$$P(r)dr = \frac{dr/(\pi\Delta r)}{1 + \left(\frac{r-r_0}{\Delta r}\right)^2}. \quad (4.6)$$

For a relatively small resonance width  $\Delta r$ , we can linearize the coordinate frequencies  $\nu_j(r)$  around  $r = r_0$  with a simple Taylor expansion:

$$\nu_j(r) \approx \nu_{j0} + (r - r_0) \left. \frac{d\nu_j}{dr} \right|_{r_0}, \quad (4.7)$$

in which case the probability distribution in frequency space is also a Lorentzian:

$$P(\nu_j)d\nu_j = \frac{d\nu_j/(\pi\Delta\nu_j)}{1 + \left(\frac{\nu_j - \nu_{j0}}{\Delta\nu_j}\right)^2}. \quad (4.8)$$

Here  $\nu_j = \nu_\phi, \nu_\theta, \nu_r$  are the azimuthal, vertical, and radial coordinate frequencies and  $\nu_{j0} = \nu_j(r_0)$  are those frequencies at the resonance center.

For nearly circular orbits, the coordinate frequencies (using geometrized units with  $G = c = M = 1$ ) are given by Merloni et al. (1999), as quoted above in Section 3.2

$$\nu_\phi = \frac{1}{2\pi(r^{3/2} \pm a)}, \quad (4.9a)$$

$$\nu_\theta = \nu_\phi \left[ 1 \mp \frac{4a}{r^{3/2}} + \frac{3a^2}{r^2} \right]^{1/2}, \quad (4.9b)$$

and

$$\nu_r = \nu_\phi \left[ 1 - \frac{6}{r} \pm \frac{8a}{r^{3/2}} - \frac{3a^2}{r^2} \right]^{1/2}, \quad (4.9c)$$

where the upper sign is taken for prograde orbits and the lower sign is taken for retrograde orbits (the results below assume prograde orbits, but the analysis for retrograde orbits is essentially the same). These frequencies are plotted in Figure 4-2 as a function of  $r$  for a representative black hole with mass  $10M_\odot$  and spin  $a/M = 0.5$ . The radial frequency approaches zero at the ISCO, where geodesics can orbit the black hole many times with steadily decreasing  $r$ . In the limit of zero spin and large  $r$ , the coordinate frequencies reduce to the degenerate Keplerian case with  $\nu_\phi = \nu_\theta = \nu_r = 1/(2\pi r^{3/2})$ .

Generally, the power spectrum of the periodic light curve from a single hot spot orbiting at  $r_0$  will be made up of delta-functions located at the harmonics of the fundamental  $\nu_\phi$  and the beat modes with  $\nu_r$  and  $\nu_\theta$ . Considering for the moment only planar orbits, the power will be concentrated at the frequencies  $\nu = n\nu_\phi \pm \nu_r$ , where  $n$  is some positive integer. In fact, there will be additional peaks at  $\nu = n\nu_\phi \pm 2\nu_r$  and even higher beat-harmonic combinations, but for coordinate frequencies with  $\nu_\phi = 3\nu_r$ , these higher modes are degenerate, e.g.  $\nu_\phi + 2\nu_r = 2\nu_\phi - \nu_r$ . A careful treatment can distinguish between these degenerate modes, but in practice we find the power in the radial double- and triple-beats to be insignificant compared to the single-beat modes at  $n\nu_\phi \pm \nu_r$ , so we limit our analysis to these frequencies.

From equations (4.7) and (4.8), we see that a QPO peak centered around  $\nu =$

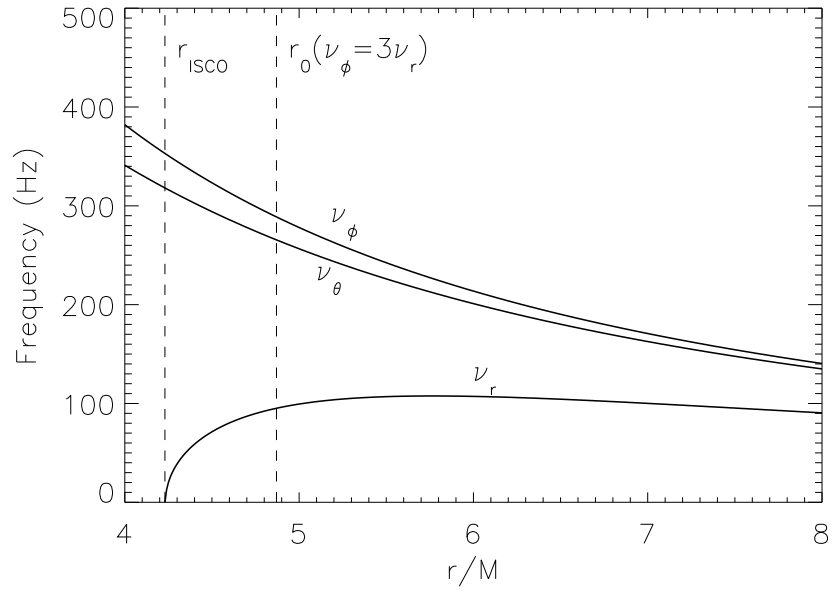


**Figure 4-2:** Geodesic coordinate frequencies as a function of radius for a black hole with mass  $M = 10M_\odot$  and spin  $a/M = 0.5$ . The radius of the inner-most stable circular orbit  $r_{\text{ISCO}}$  is where  $\nu_r \rightarrow 0$ . The commensurate radius  $r_0$  is where the ratio of azimuthal to radial coordinate frequencies is 3:1.

$n\nu_\phi \pm \nu_r$  will be a Lorentzian of width

$$\Delta\nu = \Delta r \left( n \frac{d\nu_\phi}{dr} \pm \frac{d\nu_r}{dr} \right)_{r_0}. \quad (4.10)$$

Unlike in the previous section where the finite lifetimes gave a single width for every QPO peak, now each peak in the power spectrum will be broadened by a different but predictable amount. Note in particular how the peaks at the higher harmonics with  $n > 1$  will be significantly broader (and thus lower in amplitude) than the fundamental. Another important feature evident from Figure 4-2 and equation (4.10) is that, due to the opposite-signed slopes of  $\nu_r(r)$  and  $\nu_\phi(r)$  around  $r_0$ , the beat mode at  $\nu_\phi + \nu_r$  remains very narrow, while the peak at  $\nu_\phi - \nu_r$  is quite broad. These features should play a key role in using the power spectrum as an observable in understanding the behavior of geodesic hot spots.

As in Section 4.3, the first step in producing the theoretical power spectrum is to calculate the Fourier amplitude in each mode with the full three-dimensional ray-tracing calculation of emission from a single periodic hot spot at  $r_0$ . Again, the linear properties of the problem allow us simply to sum a series of Lorentzians, each with a different amplitude, width, and location (peak frequency), to get the total power spectrum. The peak amplitudes  $A_j$  are given by the ray-tracing calculations, the locations  $\nu_j$  from the geodesic coordinate frequencies and their harmonics, and the widths  $\Delta\nu_j$  from equation (4.10).

Since the QPO peak broadening is most likely caused by a combination of factors including the hot spots' finite lifetimes as well as their finite radial distribution, the simulated power spectrum should incorporate both features in a single model. Now the computational convenience of Lorentzian peak profiles is clearly evident, since the net broadening is given by the convolution of both effects and the convolution of two Lorentzians is a Lorentzian:

$$[\mathcal{L}(\nu_1, \Delta\nu_1) \star \mathcal{L}(\nu_2, \Delta\nu_2)](\nu) = \mathcal{L}(\nu_{\text{tot}}, \Delta\nu_{\text{tot}})(\nu), \quad (4.11)$$

where the peak centers and widths simply add:  $\nu_{\text{tot}} = \nu_1 + \nu_2$  and  $\Delta\nu_{\text{tot}} = \Delta\nu_1 + \Delta\nu_2$ . In the case where one or both of the Lorentzians is *not* normalized, the amplitude of the convolved function is given as a function of the individual peak amplitudes and widths:

$$A_{\text{tot}} = \pi \frac{A_1 A_2 \Delta\nu_1 \Delta\nu_2}{\Delta\nu_1 + \Delta\nu_2}, \quad (4.12)$$

where  $A_1$  and  $A_2$  are the peak amplitudes of the respective Lorentzians [ $A_j = 1/(\pi\Delta\nu_j)$  corresponds to a normalized function.]

Figure 4-3 shows the power spectrum for a collection of hot spots orbiting near

**Table 4.1:** Widths of QPO peaks around coordinate frequency modes  $n\nu_\phi \pm \nu_r$ , due to a radial distribution of hot spots with  $\Delta r = 0.05M$ , as determined by equation (4.10). For relatively narrow resonance regions, the QPO peak widths are linearly proportional to  $\Delta r$ . The basic black hole and hot spot model parameters are the same as in Figures 4-1 and 4-3.

Mode	Frequency (Hz)	FWHM (Hz)
$\nu_r$	95	3.6
$\nu_\phi - \nu_r$	190	12.2
$\nu_\phi$	285	8.4
$\nu_\phi + \nu_r$	380	4.8
$2\nu_\phi - \nu_r$	475	20.6
$2\nu_\phi$	570	16.8
$2\nu_\phi + \nu_r$	665	13.2

the commensurate radius  $r_0 = 4.89M$  with a distribution width of  $\Delta r = 0.05M$ . All other black hole and orbital parameters are identical to those in Figure 4-1. Both the random phase broadening described in Section 4.3 and the effects of a finite resonance width are included in the model. Again, we should stress that the solid line is not a fit to the simulated data, but rather an independent analytic model constructed from the sum of Lorentzian profiles as described above. In this example, the hot spots have a typical lifetime of 30 orbits, so the random phase broadening contributes only  $\Delta\nu \approx 1.5$  Hz for each peak. While this is rather longer than the expected hot spot lifetime, it allows us to focus on the effect that a finite resonance width has on the behavior of the QPO peaks at the coordinate frequencies and their various beat harmonics. For a resonance width of  $\Delta r = 0.05M$ , the peak widths due only to coordinate frequency broadening are shown in Table 4.1.

The narrow peak at  $\nu_\phi + \nu_r = 380$  Hz and the neighboring broad peak at  $2\nu_\phi - \nu_r = 475$  Hz are clearly visible in the simulated data of Figure 4-3. Precise measurements of each peak's amplitude and width may not come until a next generation X-ray timing mission, but the qualitative behavior shown here should be detectable with the current observational capabilities of *RXTE*. Combining equations (4.1) and (4.10) gives a system of linear equations that can be solved for the hot spot lifetime  $T_l$  and the resonance width  $\Delta r$  as a function of the QPO peak widths  $\Delta\nu_j$ . If we could accurately measure the widths of only two peaks, both  $T_l$  and  $\Delta r$  could be determined with reasonable significance. More peaks would give tighter constraints and thus serve to either support or challenge the assumptions of the hot spot model.

If the hot spot paradigm is accurate, then by measuring multiple peak widths we



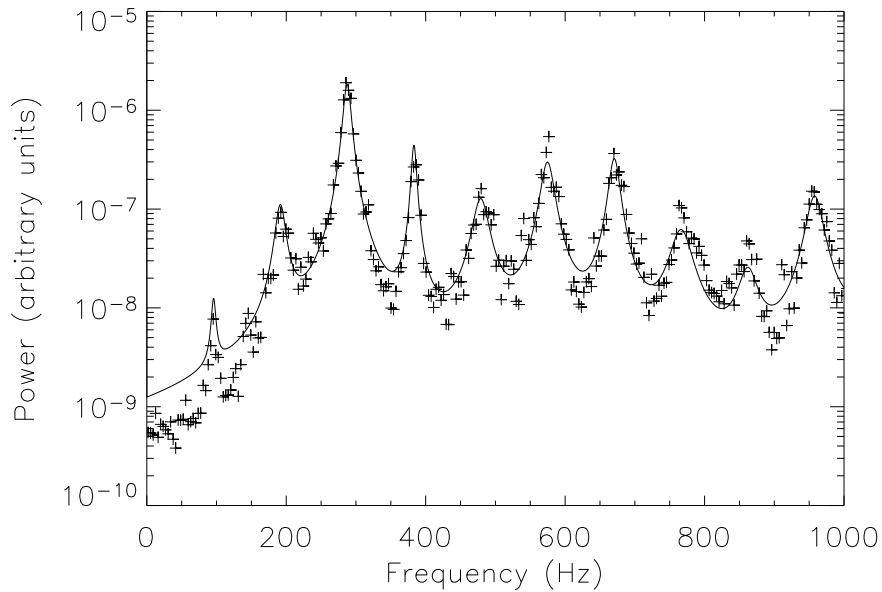


**Figure 4-3:** Simulated power spectrum (crosses) from a ray-tracing calculation of many hot spots on geodesic orbits with different radii  $r$  and thus different coordinate frequencies, along with an analytic model (line) of that power spectrum. The black hole has mass  $M = 10M_{\odot}$  and spin  $a/M = 0.5$ , while the average hot spot orbit has an eccentricity of 0.1 around a radius of  $r_0 = 4.89M$ , as in Figure 4-1. The peaks have Lorentzian profiles with  $\Delta\nu$  given by equations (4.1) and (4.10) with  $T_l = 100$  ms and  $\Delta r = 0.05M$ .

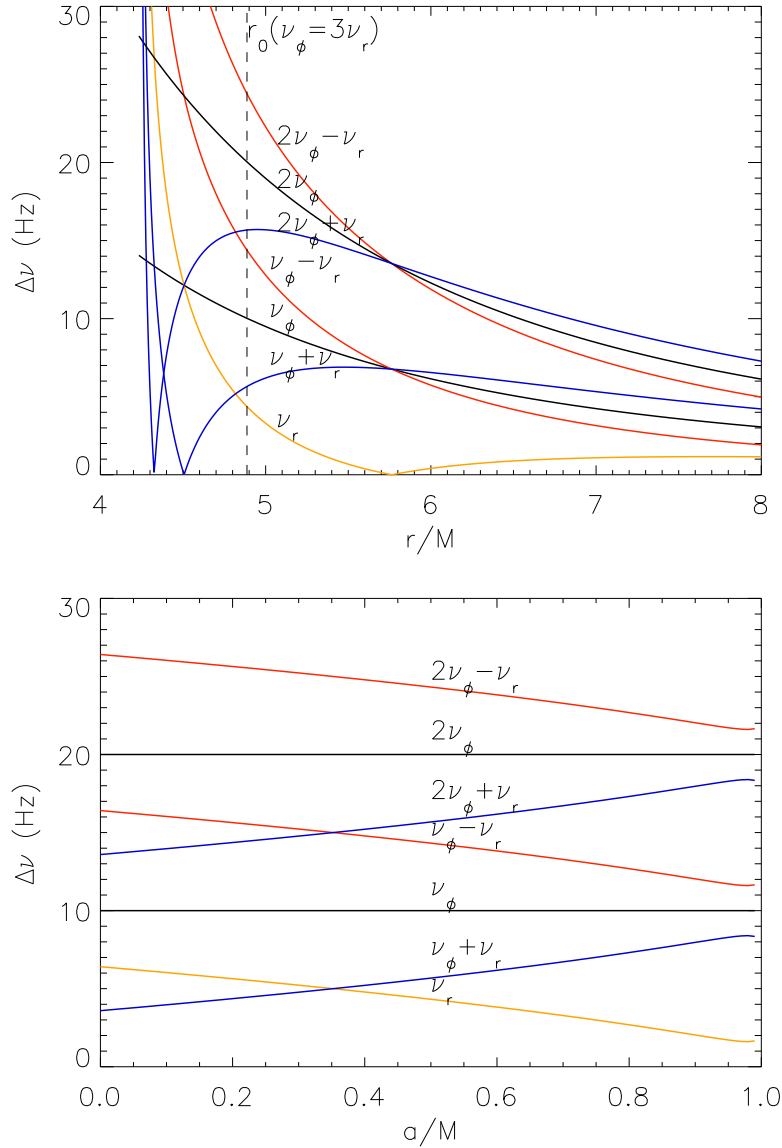


**Figure 4-4:** Widths of QPO peaks  $\Delta\nu_j$  centered at coordinate frequencies  $n\nu_\phi \pm \nu_r$  for a black hole of mass  $10M_\odot$ , as determined by equation (4.10). (top) Peak width as a function of hot spot orbital radius for fixed black hole spin  $a/M = 0.5$ . The vertical dashed line marks the special radius  $r_0$  for which  $\nu_\phi = 3\nu_r$ . (bottom) Peak width as a function of black hole spin, assuming resonant orbits around  $r = r_0$ . To map out the space time around the hot spot orbit, only the relative widths are important, so we have normalized  $\Delta r$  so that  $\Delta\nu_\phi(r_0) = 10$  Hz.

should also be able to map out the spacetime in the region of the hot spot orbit, thus gaining insight into the specific resonance mechanisms that may be causing the QPO frequency commensurability. This technique could conceivably be carried out in one of (at least) two different ways. If we can assume a given value for the black hole spin, perhaps by iron line broadening, then by measuring the QPO peak widths, the specific radius of the preferred hot spot orbit could be identified. An example of this approach is shown in Figure 4-4a, where the various widths at the coordinate frequencies  $n\nu_\phi \pm \nu_r$  are plotted as a function of the orbital radius  $r$ , assuming a black hole spin of  $a/M = 0.5$ . The absolute vertical scale is set by the width of the resonance region, but we are generally only interested in *relative* widths, so here they are normalized to  $\Delta\nu_\phi(r_0) = 10$  Hz without any loss of generality. The dashed vertical line shows the location for the special commensurate orbit at  $\nu_\phi = 3\nu_r$ . Note how the widths become degenerate when  $\partial\nu_r/\partial r = 0$ , around  $r \approx 5.75M$  in this case.

Perhaps the more likely scenario is one in which we do *not* know the spin value *a priori*, but are reasonably sure that the 3:2 commensurability is forced by a resonance at  $r_0$  where  $\nu_\phi = 3\nu_r$ . For different values of  $a/M$ , the shape of the gravitational potential around  $r_0$  changes, thus changing the relative value of the radial epicyclic frequency. In that case, measuring the widths of multiple peaks can directly give an estimate for the black hole spin, as shown in Figure 4-4b. As in Figure 4-4a, the vertical scale is normalized so that  $\Delta\nu_\phi = 10$  Hz, but only the relative widths between multiple peaks are important. With high enough precision, this method might even be used to test the strong-field regime of GR and whether black holes are “bumpy” or indeed “hairless” (Collins & Hughes, 2004).

## 4.5 Electron Scattering in the Corona

Another simplified model we have included is that of scattering photons from the hot spot through a low-density corona of hot electrons around the black hole and accretion disk. This is known to be an important process for just about every observed state of the black hole system (McClintock & Remillard, 2004). Unfortunately, it is also an extremely difficult process to model accurately. Fortunately, for the problem of calculating light curves and power spectra, a detailed description of the scattering processes is probably not necessary. The most important qualitative feature of the coronal scattering is a smearing of the hot spot image: a relativistic emitter surrounded by a cloud of scattering electrons will appear blurred, just like a lighthouse shining its beam through dense fog. The effect is even more pronounced in the black hole case, where the hot spot orbital period is of the same order as the light-crossing time of a small corona, thus spreading out the X-ray signal in time as well as space.

Due to the inverse-Compton effect with hot coronal electrons, the scattered pho-

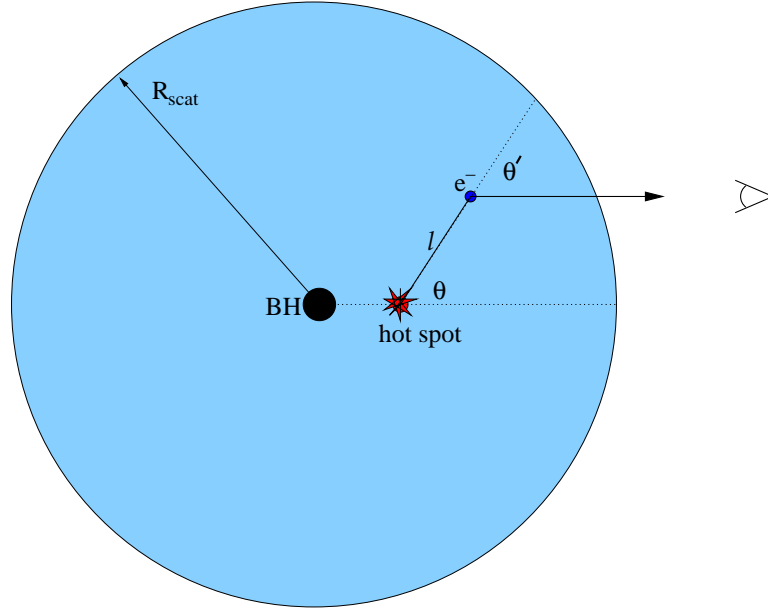


**Figure 4-5:** Schematic diagram of photon scattering geometry for a hot spot emitter orbiting a black hole, surrounded by a corona of hot electrons with length scale  $R_{\text{scat}}$ . The geometry requires  $\theta = \theta'$ . The added photon path length compared to the direct line-of-sight is  $l(1 - \cos \theta)$ .

tons are often boosted to higher energies (see Chapter 6). Since each scattering event also adds a time delay to the photon, a coherent phase lag in the light curves from different energy channels could be used to estimate the overall scale length of the corona. Vaughan et al. (1997) have observed this effect in neutron star QPOs and infer a scattering length of  $\lambda \sim 5 - 15M$  for an optical depth of  $\tau \sim 5$  in the source 4U 1608-52. Ford et al. (1999) perform a similar analysis for black holes, including the possibility for an inhomogeneous corona, and derive a much larger upper limit for the size of the corona ( $\lambda \sim 10^3 M$ ), although Merloni & Fabian (2001) argue for a smaller corona with high energy density. In either case (large or small scattering length), the qualitative effect will be the same: the damping of higher harmonic features in the power spectrum of the X-ray light curve.

The simple model we introduce is based on adding a random time delay to each photon detected from the hot spot. The distribution of this time delay is computed as follows: we fix the optical depth to be unity for scattering through a medium of constant electron density, and for simplicity, each photon is assumed to scatter exactly once between the emitter and the observer, thus determining the length scale of the corona as a function of density. In Chapter 6 below, we will see that this choice

of optical depth is consistent with the observations of the Steep Power Law photon energy spectrum. For this constant density model, the probability of scattering after a distance  $l$  is

$$P(l)dl = \frac{dl}{\lambda} e^{-l/\lambda}, \quad (4.13)$$

where  $\lambda$  is the photon mean free path in the corona.

Next, due to the likely existence of an optically thick disk around the black hole equator, we assume that the photon scattering angle is less than  $\pi/2$  (the scattering angle  $\theta'$  is defined as the angle between the incoming and outgoing wave vectors, so a straight path would correspond to  $\theta' = 0$ ). In other words, only photons emitted in a hemisphere facing the observer can ultimately be scattered in the observer's direction. A schematic view of this geometry is shown in Figure 4-5. For a photon emitted at an angle  $\theta$  to the observer, scattering at a distance  $l$  from the source produces an additional photon path length of  $d = l(1 - \cos \theta)$ , assuming for simplicity a flat spacetime geometry. While the photons are emitted with an isotropic distribution, the scattering distribution is *not* isotropic. Since the scattering geometry requires that  $\theta = \theta'$ , we only detect a subset of the photons emitted with an angular distribution in  $\theta$  that satisfies this relationship. In the limit of low-energy photons ( $h\nu \ll m_e c^2$ ) and elastic scattering, the classical Thomson cross section  $\sigma_T$  for unpolarized radiation is used (Rybicki & Lightman, 1979):

$$\frac{d\sigma}{d\theta'} = \frac{3}{8} \sigma_T \sin \theta' (1 + \cos^2 \theta'). \quad (4.14)$$

Integrating this distribution over all forward-scattered photons ( $\theta' < \pi/2$ ), we find the average additional path length to be  $\langle d \rangle = 7l/16$ . Since the time delay is the path length divided by the speed of light  $c$ , scattering once in the corona adds a time delay  $\Delta t$  to each photon with probability

$$P(\Delta t)d(\Delta t) = \frac{d(\Delta t)}{T_{\text{scat}}} e^{-\Delta t/T_{\text{scat}}}, \quad (4.15)$$

where the average scattering time is given by

$$T_{\text{scat}} = \frac{7}{16} \frac{\lambda}{16c}. \quad (4.16)$$

Applied to the ray-tracing model, this has the effect of smoothing out the light curve with a simple convolution in the time domain of the original signal  $f(t)$  and the time delay probability distribution function  $P(\Delta t)$ . The Fourier transform of the resulting light curve is the product of the two transforms  $F(\nu)$  and  $\tilde{P}(\nu)$ , where for

notational simplicity,  $\tilde{P}(\nu)$  is taken as a dimensionless Fourier transform of  $P(\Delta t)$ :

$$\tilde{P}(\nu) = \frac{1}{1 + 2\pi iT_{\text{scat}}\nu}. \quad (4.17)$$

When we square the product to get the power spectrum  $G^2(\nu) = F^2(\nu)\tilde{P}^2(\nu)$ , the scaling factor is another a Lorentzian:

$$G^2(\nu_j) = \frac{A_j^2}{1 + (\nu_j/\Delta\nu_{\text{scat}})^2}, \quad (4.18)$$

where the scale of frequency damping is given by

$$\Delta\nu_{\text{scat}} \equiv \frac{1}{2\pi T_{\text{scat}}} \quad (4.19)$$

and  $A_j$  are the delta function amplitudes of  $F(\nu_j)$  as defined above in equation (4.3). This analytic result is perhaps a case where the ends justify the means. Our model for electron scattering in the corona is extraordinarily simplified, ignoring the important factors of photon energy, polarization, non-isotropic emission, multiple scattering events in a non-homogeneous medium, and all relativistic effects. However, assuming that almost any analytic model would be equally (in)accurate, at least the treatment we have applied proves to be computationally very convenient.

Equation (4.18) states that the resulting power spectrum of the scattered light curve is a set of delta functions, with the higher harmonics damped out by the effective blurring of the hot spot beam propagating through the coronal electrons. A simulated power spectrum is shown in Figure 4-6a for a scattering length of  $\lambda = 10M$ , comparable to the size of the hot spot orbit. Figure 4-6b shows the effect of a larger, low-density corona with scale length  $\lambda = 100M$ , corresponding to a longer convolution time and thus stronger harmonic damping. The white background noise (Poisson noise with  $\mu = 1$ ) in both cases is due to the statistics of the random scattering of each photon from one time bin to another. The simulated spectra are plotted as dots (asterices at  $\nu_j$  to highlight the peaks) and the analytic model is a solid line.

One significant conclusion from this analysis is that the coronal scattering alone should not contribute to the broadening of the QPO peaks. However, it will have a very significant effect on the overall harmonic structure of the power spectrum, particularly at higher frequencies. In Schnittman & Bertschinger (2004a), we showed a similar result caused by the stretching of the geodesic blob into an arc along its path, also damping out the power at higher harmonics. In this context, it is now clear that the arc damping can be modeled analytically by interpreting the stretching of the blob in space as a convolution of the light curve in time. If the stretched hot spot

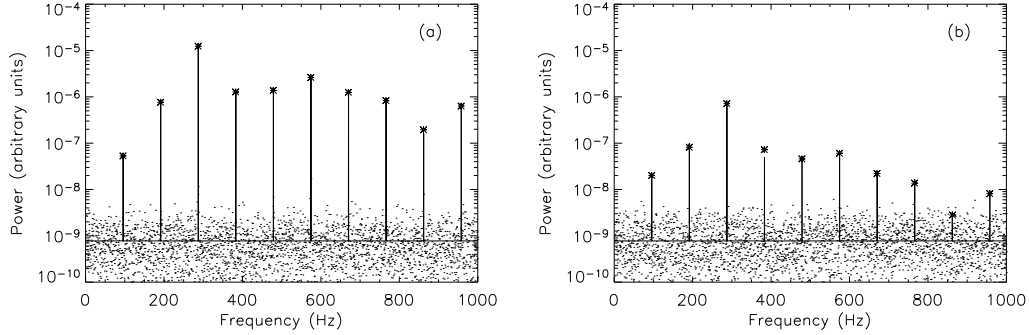


**Figure 4-6:** Simulated power spectrum from a single hot spot light curve where the emitted photons are scattered exactly once each by a uniform corona of electrons. The simulated spectra are plotted as dots and asterices, while the analytic model is a solid line. In (a), the mean free path to scattering is  $\lambda = 10M$ , while (b) represents a much larger, low density corona with  $\lambda = 100M$ .

has a Gaussian distribution in azimuth with length  $\Delta\phi$ , the original X-ray light curve will be convolved with a Gaussian window of characteristic time  $T = \Delta\phi/(\pi\nu\phi)$ . A Gaussian window in time gives a Gaussian profile in frequency space:

$$w(t) = \exp\left(\frac{-t^2}{2T^2}\right) \Leftrightarrow W(\nu) = \sqrt{2\pi}\frac{T}{T_f} \exp\left(\frac{-\nu^2}{2\Delta\nu^2}\right), \quad (4.20)$$

where again the characteristic width is given by  $\Delta\nu = 1/(2\pi T)$ . The exponential damping of the Gaussian  $W(\nu)$  is stronger than the Lorentzian factor [eqn. (4.18)] at higher frequencies, but both effects (coronal scattering and hot spot stretching) are probably important in explaining the lack of significant power in the harmonics above  $\sim 500$  Hz in the *RXTE* observations. From the central limit theorem, in the limit of many scattering events, the time delay distribution should also approach that of a Gaussian, further damping out the higher frequency power. Regardless of the precise shape of the convolution window in time, this simple analytic model shows how the scattering time scale can be understood as another expression of the causality limits on the size of the emission region. For an optically thick corona with length scale  $R_{\text{scat}}$ , all frequency modes above  $\nu \sim c/R_{\text{scat}}$  should be damped out significantly.

## 4.6 Fitting QPO Data from XTE J1550–564

In this Section we combine all the pieces of the model developed above and apply the results to the *RXTE* data from type A and type B QPOs observed in the low-mass X-ray binary XTE J1550–564. To compare directly with the data from Remillard et al. (2002), we need to change slightly our normalization of the power spectrum. Following Leahy et al. (1983) and van der Klis (1997), we define the power spectrum  $Q(\nu)$  (not to be confused with the oscillator quality  $Q$  from Section 4.3) so that the total power integrated over frequency gives the mean square of the discrete light curve  $I_j = I(t_j)$ :

$$\int_{\nu>0}^{\nu_N} Q(\nu)d\nu = \frac{1}{N_s} \sum_{j=0}^{N_s-1} \left( \frac{I_j - \langle I \rangle}{\langle I \rangle} \right)^2, \quad (4.21)$$

where  $I_j$  is sampled over  $j = 0, \dots, N_s - 1$  with average value  $\langle I \rangle$ . In terms of the power spectra used in Sections 4.3 and 4.4,  $Q(\nu)$  is given by

$$Q(\nu) = 2T_f \frac{\tilde{I}^2(\nu)}{\tilde{I}^2(0)}, \quad (4.22)$$

which has units of  $[(\text{rms}/\text{mean})^2 \text{Hz}^{-1}]$ .

As we described in Section 4.1, the hot spot model is constructed in a number of steps. These steps result in a first approximation for the black hole and hot spot model parameters, after which a  $\chi^2$  minimization is performed to give the best values for each data set.

- The black hole mass and the inclination of the disk are given by optical radial velocity measurements. We take  $M = 10.5M_\odot$  and  $i = 72^\circ$  as fixed in this analysis (Orosz et al., 2002). Note this is somewhat higher than the mass used in Chapter 3 to match simultaneously LFQPOs and HFQPOs to coordinate frequencies.
- The black hole spin is determined by matching the frequencies of the HFQPOs to the geodesic coordinate frequencies such that  $\nu_\phi = 3\nu_r$  at the hot spot orbit. This identifies the frequencies of the two major peaks with a 3:2 ratio as the orbital frequency  $\nu_\phi$  and its lower beat at  $\nu_\phi - \nu_r$ . Coupled with the black hole mass of  $10.5M_\odot$ , this assumption gives  $a/M \approx 0.5$  for  $\nu_\phi \approx 276$  Hz and  $\nu_\phi - \nu_r \approx 184$  Hz. The small uncertainties in the measured value of  $\nu_\phi$  can thus be interpreted indirectly as constraints on the mass-spin relationship.
- The orbital eccentricity and hot spot size and overbrightness are chosen to match the total amplitude of the observed fluctuations. We use a moderate eccentricity



of  $e = 0.1$ , consistent with the simple approximation of Section 3.2 and equation (3.11). The question of overbrightness is still an area of much research, since the nature of the background disk is not well known during the “Steep Power Law” state that produces the HFQPOs (McClintock & Remillard, 2004). In practice, we set the hot spot emissivity constant and then fit an additional steady-state background flux  $I_B$  to the variable light curve.

- The hot spot arc length and the coronal scattering time scale are chosen to fit the relative amplitudes of the different QPO peaks.
- The hot spot lifetime and the width of the resonance  $\Delta r$  around  $r_0$  are chosen to fit the widths of the QPO peaks.
- As a final step, we include an additional power law component  $\propto \nu^{-1}$  to account for the contribution due to turbulence and other random processes in the disk [e.g. Press (1978); Mandelbrot (1999); Poutanen & Fabian (1999)] not accounted for by the hot spot model. Instrumental effects such as the detector deadtime and Poisson counting statistics are combined with the turbulent noise to give a simple two-component background spectrum:

$$Q_{\text{noise}}(\nu) = Q_{\text{PL}}\nu^{-1} + Q_{\text{flat}}. \quad (4.23)$$

After using the ray-tracing calculation to determine the Fourier amplitudes  $A_j$  [as in eqns. (4.3, 4.4, and 4.18)] for a single periodic light curve segment, we minimize  $\chi^2$  over the following parameters: orbital frequency  $\nu_\phi$ , hot spot lifetime  $T_l$ , resonance width  $\Delta r$ , scattering length  $\lambda$ , hot spot arc length  $\Delta\phi$ , steady state flux  $I_B$ , and the background noise components  $Q_{\text{PL}}$  and  $Q_{\text{flat}}$ . All these parameters can be combined into a single analytic expression for the power spectrum, making the  $\chi^2$  minimization a computationally simple procedure. The best fit parameters are shown in Table 4.2, along with  $1\sigma$  (68%) confidence limits. These confidence limits are determined by setting  $\Delta\chi^2 < 7.04$ , corresponding to six “interesting” parameters of the hot spot model, holding the noise components constant (Avni, 1976; Press et al., 1992). We find that  $Q_{\text{PL}}$  and  $Q_{\text{flat}}$  are almost identical for both data sets, supporting the presumption that they are indeed a background feature independent of the hot spot model parameters.

In Figure 4-7 we show the observed power spectra for type A and type B QPOs, as reported in Remillard et al. (2002), along with our best fit models. The type A QPOs are characterized by a strong, relatively narrow peak at  $\nu \approx 280$  Hz, corresponding to  $\nu_\phi$  in our model, with a minor peak of comparable width at  $\nu_\phi - \nu_r \approx 187$  Hz. Type B QPOs on the other hand, have a strong, broad peak around 180 Hz with a minor peak at 270 Hz. This implies a longer arc for type B, damping out the higher

**Table 4.2:** Best-fit parameters of the hot spot model for type A and type B QPOs from XTE J1550–564. ( $1\sigma$ ) confidences are shown in parentheses, following the approach of Avni (1976), corresponding to a subset of six “interesting” parameters. In this case, the background noise components  $Q_{\text{PL}}$  and  $Q_{\text{flat}}$  are held constant while varying the model parameters.

Parameter	Type A	Type B
orbital frequency $\nu_\phi$ (Hz)	280.1(2.4)	270.5(12)
mean lifetime $T_l$ (ms)	10(2.0)	5(1.5)
(orbits)	2.8(0.55)	1.4(0.4)
resonance width $\Delta r$ ( $M$ )	0.02(0.05)	0.025(0.12)
scattering length $\lambda$ ( $M$ )	5(10)	10(20)
arc length $\Delta\phi$ ( $^\circ$ )	155(30)	285(20)
flux ratio $\frac{I_{\text{hotspot}}}{I_B + I_{\text{hotspot}}}$	0.085(0.025)	0.38(0.05)
power law noise $Q_{\text{PL}}$	$3.5 \times 10^{-4}$	$3.5 \times 10^{-4}$
flat noise $Q_{\text{flat}}$	$6.5 \times 10^{-7}$	$5.8 \times 10^{-7}$

frequency modes, and a shorter average lifetime, broadening the peaks. Both types of QPO suggest a narrow resonance width  $\Delta r$ , yet the current data does not constrain this parameter very well. Thus we assume the majority of the peak broadening is caused by the addition of multiple hot spots with characteristic lifetimes of  $T_l \sim 3$  orbits for the type A QPOs and about half that for type B.

We performed a covariance analysis of the parameter space near the  $\chi^2$  minimum to identify the best-constrained parameters and their relative (in)dependence. This analysis confirms what the confidence limits suggest: the best-constrained parameters are the orbital frequency  $\nu_\phi$ , the hot spot lifetime  $T_l$ , the arc length  $\Delta\phi$ , and the background flux  $I_B$ . For the type A QPOs, we find  $\nu_\phi$  and  $T_l$  to be independent, while the arc length and background flux are strongly correlated, so that  $\Delta\phi/I_B$  is positive and roughly constant within our quoted confidence region. This is because, for shorter arcs with fixed emissivity, increasing the arc length will increase the amplitude of the light curve modulation, requiring a larger background flux to give the same QPO amplitude. For the type B QPOs on the other hand, a longer arc length does not significantly amplify the modulation, since in the limit  $\Delta\phi \rightarrow 360^\circ$ , the light curve would remain constant, and thus the parameters  $\Delta\phi$  and  $I_B$  are relatively independent. For both type A and type B QPOs, we find that the resonance width and the coronal scattering length are independent, yet not very well constrained. This is because these parameters are most sensitive to the higher frequency peaks, which appear to be damped out by the Gaussian arcs.

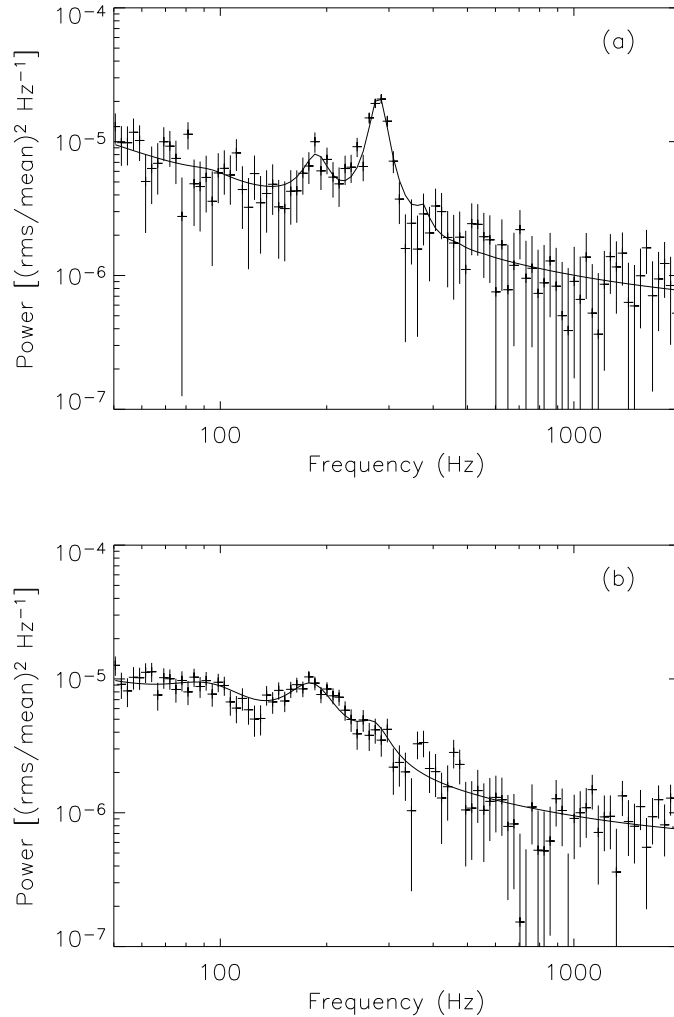


**Figure 4-7:** Comparison of hot spot model power spectrum (line) with data (crosses) from XTE J1550–564 [reproduced with permission from Remillard et al. (2002)]. (a) Type A QPO, dominated by a narrow peak at  $\nu_\phi \approx 280$  Hz. (b) Type B QPO, dominated by a broad peak at  $\nu_\phi - \nu_r \approx 180$  Hz. The best fit model parameters for each data set are shown in Table 4.2 and the resulting QPO amplitudes and widths are shown in Table 4.3.

**Table 4.3:** Amplitudes and widths of type A and type B QPO peaks from XTE J1550–564, as determined by the best fit parameters listed in Table 4.2 and equation (4.24). ( $1\sigma$ ) confidences are shown in parentheses.

Mode	A		B	
	rms (%)	FWHM (Hz)	rms (%)	FWHM (Hz)
$\nu_r$	0.57(0.15)	33.1(6.2)	2.03(0.21)	63.6(16.0)
$\nu_\phi - \nu_r$	1.62(0.26)	35.7(5.9)	2.57(0.14)	67.6(15.5)
$\nu_\phi$	3.35(0.17)	34.6(5.5)	1.48(0.24)	65.9(15.3)
$\nu_\phi + \nu_r$	0.75(0.19)	33.4(5.8)	0.06(0.02)	64.1(15.8)

The resulting amplitudes and widths of the major QPO peaks are shown in Table 4.3, along with  $1\sigma$  confidence limits. These amplitudes are given by the analytic model so that the total rms in the peak centered at  $\nu_j$  is

$$\text{rms}_j = \sqrt{2} \frac{A'_j}{A'_0}, \quad (4.24)$$

where  $A'_0$  is the mean amplitude of the light curve (including the background  $I_B$ ) and  $A'_j$  are the original Fourier amplitudes  $A_j$  given by the ray-tracing code, appropriately scaled according to equation (4.18). This is more instructive than measuring the rms directly from  $Q(\nu)$ , which includes background power and instrumental effects uncorrelated to the actual QPO peaks.

In Schnittman & Bertschinger (2004a), the hot spot light curve was added to a steady-state disk with emissivity that scales as  $r^{-2}$ , which provides an estimate of the size and overbrightness of the hot spots required to produce a given (rms/mean) amplitude in the light curve. Considering that most high frequency QPOs are observed with the greatest significance in the 6-30 keV energy band during the steep power-law spectral state (McClintock & Remillard, 2004), it seems rather unlikely that the background flux *is* coming directly from a thermal, optically thick disk. Even if the flux is originally produced by such a disk, it clearly undergoes significant scattering in a hot corona to give the high temperature power law observed in the photon energy spectrum.

In the context of the model presented here, we can only calculate the fraction of the total flux that is coming from the hot spots, determined by fitting to the QPO data, without presuming an actual model for the background emission. For XTE J1550–564, we find that the type A hot spot/arcs contribute 8.5% of the total

observed flux, while the type B arcs must contribute significantly more (38%) to give a comparable amplitude. This is due to the longer arc length described above: in the limit of an azimuthally symmetric ring, even infinite brightness would produce no variability.

## 4.7 Higher Order Statistics

### 4.7.1 The Bispectrum and Bicoherence

As discussed in Section 1.4, a variety of theoretical models have been proposed to explain the existence and locations of the high frequency QPOs seen by *RXTE*, particularly the ones with multiple peaks at commensurate frequencies. Many of these models require a spinning black hole, but often rather different values of the spin [compare, e.g. Abramowicz & Kluzniak (2004), Rezzolla et al. (2003), and Aschenbach (2004) with  $a/M \approx 0.4$ , 0.94, and 0.996 respectively]. Therefore, there is still much “astrophysics” that must be understood before the fundamental physics can be probed in these systems, but there is strong cause for optimism that these systems really will ultimately tell us something profound about spinning black holes.

A key first step to disentangling the astrophysics is, of course, to develop models which not only match the important frequencies, but also include radiation mechanisms such that the observed X-rays would actually be modulated at that frequency. We believe the hot spot model developed above, motivated physically by the parametric resonance model of Abramowicz & Kluzniak (2001), is a very useful building block for analyzing the observations and understanding the emission properties of the accretion disk. Ideally, any QPO model should not only be able to explain current observations, but should also make predictions for future observations. By doing so, the model can either be further verified or possibly rejected. One of the results of this Chapter is that different sets of model parameters can produce roughly the same Fourier power density spectrum with dramatically different qualitative appearances to the light curves. In this Section, we will show that higher order variability statistics can break this degeneracy.

For now, we will focus on computing the *bispectrum* and the closely related *bicoherence*. The bispectrum computed from a time series broken into  $K$  segments is defined as:

$$B(k, l) = \frac{1}{K} \sum_{i=0}^{K-1} F_i(k) F_i(l) F_i^*(k+l), \quad (4.25)$$

where  $F_i(k)$  is the  $k^{\text{th}}$  frequency component of the discrete Fourier transform of the  $i^{\text{th}}$  time series [see e.g. Mendel (1991); Fackrell (1996) and references within]. It is

a complex quantity that measures the magnitude and the phase of the correlation between the phases of a signal at different Fourier frequencies. Its expected value is unaffected by additive Gaussian noise, although its variance will increase for a noisy signal.

A related quantity, the bicoherence, is the vector magnitude of the bispectrum, normalized to lie between 0 and 1. Defined analogously to the cross-coherence function (Nowak & Vaughan, 1996), it is proportional to the vector sum of a series of bispectrum measurements, appropriately normalized as follows: If the biphas (the phase of the bispectrum) remains constant over time, then the bicoherence will have a value of unity, while if the phase is random, then the bicoherence will approach zero in the limit of an infinite number of measurements. Linear variability is that in which the variability on different timescales is uncorrelated. Thus if the Fourier phases at different frequencies are not random relative to one another, the variability is correlated on these frequencies, and hence it is non-linear. Mathematically, the bicoherence  $b$  is defined as:

$$b^2(k, l) = \frac{|\sum F_i(k)F_i(l)X_i^*(k+l)|^2}{\sum |F_i(k)F_i(l)|^2 \sum |F_i(k+l)|^2}. \quad (4.26)$$

This quantity's value *is* affected by Gaussian noise, but it can be considerably more useful than the bispectrum itself for determining whether two signals are coupled non-linearly. In an astronomical time series analysis context, it has been previously applied to the broad components in the power spectra of Cygnus X-1 and GX 339-4, in both cases finding non-linear variability through the presence of non-zero bicoherences over a wide range of frequencies (Maccarone & Coppi, 2002).

### 4.7.2 The Bicoherence of the Simulated Data

We now apply the bicoherence to the simulated data. We consider two different model calculations from Schnittman (2005) which give similar power spectra (see Figs. 4-1 and 4-3). In each case, the quasi-periodic oscillations are produced by a 3:1 resonance between the orbital frequency and the radial epicyclic frequency. The parameters have been chosen such that the orbital frequency is 285 Hz, and the radial epicyclic frequency is 95 Hz (see Section 4.2). This corresponds to a black hole mass of  $10 M_\odot$  and a spin  $a/M = 0.5$ , with the resonance occurring at a radius of  $4.89M$ ; all these parameters compare reasonably well to those observed in XTE J1550–564 (Miller et al., 2001; Remillard et al., 2002). The disk inclination is also fixed to be 70 degrees; this parameter does not affect the frequencies observed, but can affect the amplitudes of the QPOs in the context of the model we are considering here (Schnittman & Bertschinger, 2004a). In each case we compute 1000 seconds of simulated data with a

binning timescale of the light curve of 0.1 msec. We then compute Fourier transforms by breaking the data into 2441 segments of 4096 data points, making use of 999.84 seconds of the simulated data.

In the first case, the emission comes from short lived hot spots with their orbits all at a single radius, being continually created and destroyed with a characteristic lifetime of four orbits. In the second case, long-lived (lifetimes of 100 msec, or about 30 orbits) hot spots are distributed over a range of radii ( $\Delta r = 0.05M$ ). In both cases, the hot spots are on orbits with eccentricities of  $e = 0.1$ . In this Section, we have not included the extended arcs and coronal scattering that damp out higher frequency modes. For each model, the variability appears quasi-periodic, rather than truly periodic, but for different reasons. In the first case, the creation and destruction of hot spots on short timescales leads to a phase jitter in the light curves. These discontinuous, finite lifetimes broaden the observed periodicity, as described above in Section 4.3. In the second case, the power spectrum is truly showing that there are many periodicities in the system, with coherent phases as in Section 4.4. The bicoherence easily detects this difference, as can be seen from Figure 4-8. In case 1, the bicoherence shows nearly identical elliptical peaks at various combinations of frequencies where there is power at  $\nu_1$ ,  $\nu_2$  and  $\nu_1 + \nu_2$  in the contour plot, essentially delta function peaks convolved with two-dimensional Lorentzians due to the random phase broadening. In case 2, the bicoherence shows thin elongated peaks, oriented in a variety of directions depending on the derivatives of  $\nu_1$  and  $\nu_2$  with respect to  $r$ .

The reason for this difference is straightforward. In the first case, all hot spots have the same geodesic frequencies, so during a hot spot's lifetime, it is phase locked to all the other hot spots, giving a collection of delta function peaks at the coordinate frequencies. The finite lifetimes of the hot spots will broaden the delta functions into QPOs, with a similar Lorentzian width as described in Section 4.3. The hot spots being created and destroyed in the middle of a Fourier transform window will thus create leakage in the power of the QPO to frequencies near the central frequency, but there will be a phase relation between the power in these frequencies and the phase in the central frequency. This effect should thus provide a broadening in the bicoherence similar to that in the power spectrum.

The shape and orientation of the elliptical peaks can be understood by inspecting the shapes of the peaks in the power spectrum. Treating the frequency distribution  $\delta\nu = \nu - \nu_{\text{peak}}$  around each peak as a independent random variable with probability

$$P(\delta\nu) \sim \left[ 1 + \left( \frac{\delta\nu}{\Delta\nu} \right)^2 \right]^{-1}, \quad (4.27)$$

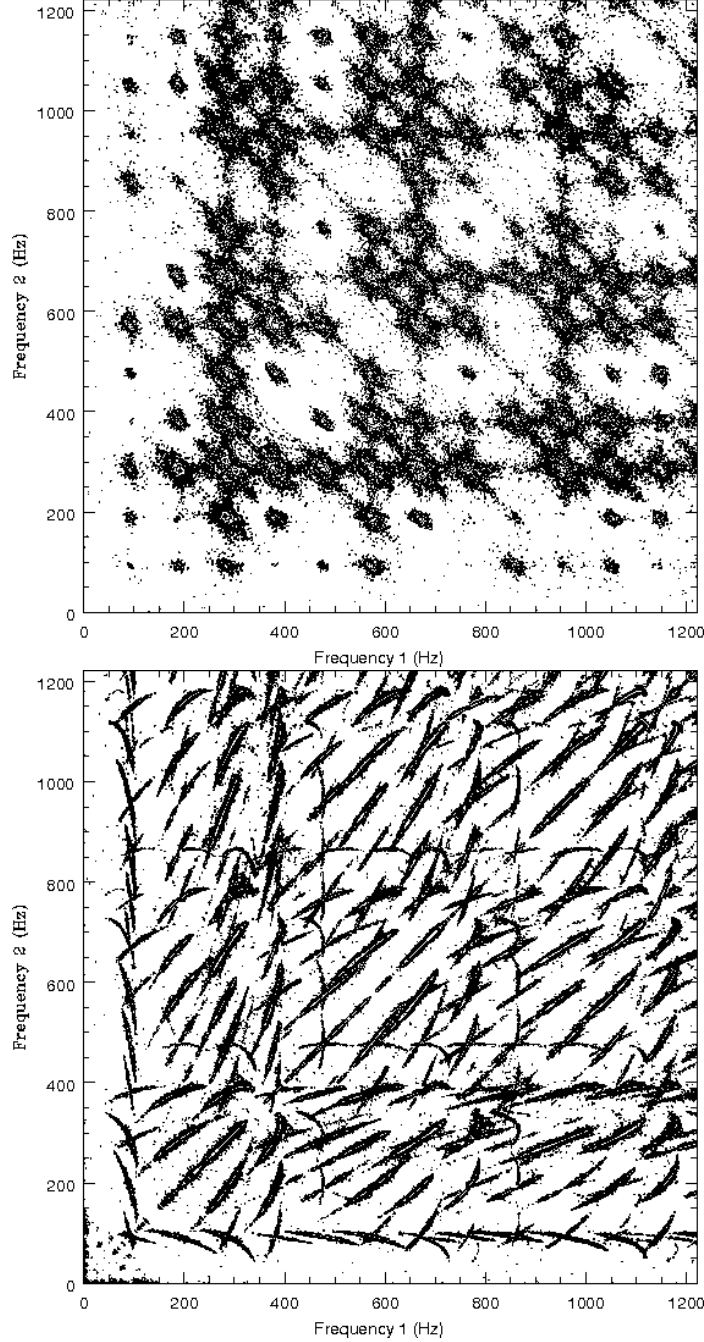


**Figure 4-8:** The bicoherences  $b^2(\nu_1, \nu_2)$  for case 1 (top) and case 2 (bottom) described in the text, with no Poisson statistics corrections made. The contour levels for the squared bicoherence  $b^2$  are  $10^{-0.5}$ ,  $10^{-0.75}$ ,  $10^{-1.0}$ ,  $10^{-1.25}$ ,  $10^{-1.5}$ , and  $10^{-2.0}$ , in the colors black, red, green, dark blue, light blue, and yellow, respectively. The frequencies correspond to a  $10M_\odot$  black hole with spin parameter  $a/M = 0.5$ . Note that the symmetry through the line  $x=y$  is trivial.



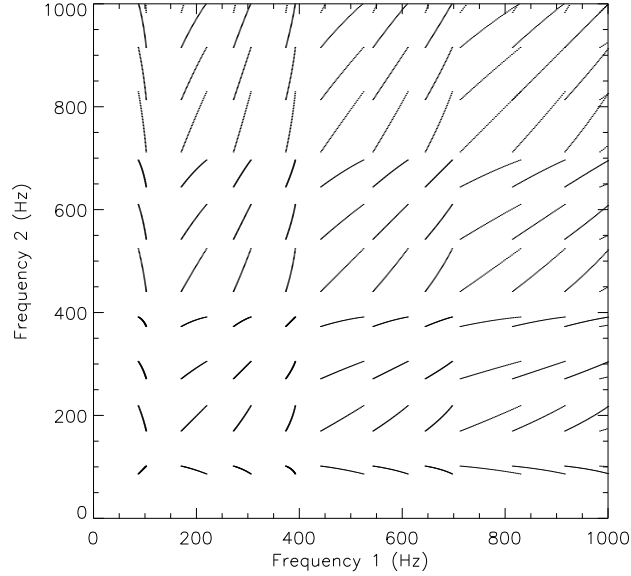


**Figure 4-9:** The tracks showing how different harmonics of the QPO vary with respect to one another when the radius of the hot spot orbit varies around a central value  $r \approx r_0 \pm 0.2M$ . The frequencies correspond to a  $10M_\odot$  black hole with spin parameter  $a/M = 0.5$ .

the distribution of the bicoherence can be written as

$$b^2(\nu_1, \nu_2) \sim P(\delta\nu_1)P(\delta\nu_2)P(\delta\nu_1 + \delta\nu_2). \quad (4.28)$$

Expanding equation (4.28) around the center of each peak and defining  $x \equiv \delta\nu_1/\Delta\nu$  and  $y \equiv \delta\nu_2/\Delta\nu$ , we see that contours of constant bicoherence have the form

$$(1 + x^2 + y^2 + x^2y^2)(1 + x^2 + 2xy + y^2) = \text{const.} \quad (4.29)$$

For small deviations ( $x, y \ll 1$ ), these contours can be written

$$x^2 + y^2 + xy = \text{const}, \quad (4.30)$$

which is the formula for an ellipse with  $a/b = \sqrt{3}$ , oriented with the semimajor axis parallel to the line  $y = -x$ , as can be seen clearly in Figure 4-8a.

In the second case, where there are many frequencies in the power spectrum due to hot spots found over a range of radii, there will be phase coherence between the different harmonics of each individual hot spot, but not with the hot spots at slightly

different frequencies. There will thus be bicoherence between the various harmonic frequencies found at any individual radius, but not between frequencies found at different radii. This second case could be especially interesting. We have calculated analytically the relationships between different coordinate frequencies if the radius at which the hot spot occurs is allowed to vary, and have plotted them in Figure 4-9. If in real data, similar tracks are seen, then, in the context of this model, they would give the relationships between the different relativistic geodesic frequencies. In principle one might expect that, since these tracks trace the coordinate frequencies as a function of radial distance from the black hole, they could be used to make precise measurements of the black hole's mass and spin, plus the central radius of the perturbations, similar to the approach described in Section 4.4. In practice, the range of radii allowed is likely to be quite small, as we saw in Section 4.6, Table 4.2, so this method would probably be of use only with *extremely* high signal-to-noise data.

### 4.7.3 Simulations with Poisson Noise

To consider whether this observational test is really feasible, we have performed simulations with the rms amplitude of the oscillations reduced to realistic levels and with Poisson noise added. We consider two count rate regimes—one similar to that detected by *RXTE* for the typical X-ray transients at about 10 kpc, which is about 10,000 counts per second, and another which would be expected from the same source, but with a 30 m<sup>2</sup> detector. In each case, we allow 6% of the counts to come from the variable component and to have, intrinsically, count rates given by the simulated light curves of Schnittman (2005), and the remaining 94% of the counts to come from a constant component. We then simulate observed numbers of counts in 100 microsecond segments as Poisson deviates (Press et al., 1992) of the model count rates.

For the *RXTE* count rates, we find that the bicoherence plots show only noise and only the strongest peak in the power spectrum is clearly significant in a 1000 second simulated observation, while marginal detections exist for the QPOs at two-thirds of and twice this frequency ( $\nu_\phi - \nu_r$  and  $2\nu_\phi$ ). This is as expected based on real data, which generally requires exposure times much longer than 1000 seconds to detect these QPOs (Strohmayer, 2001a; Miller et al., 2001; Remillard et al., 2002). However, since the signal-to-noise in the bicoherence is generally worse than the signal-to-noise in the power spectrum, bicoherence measurements may be possible only when a peak in the power spectrum is considerably stronger than the Poisson level.

For the count rates expected from a 30 m<sup>2</sup> detector, we find that even within 1000 seconds, several of the higher (i.e.  $n > 4$ ) harmonics are observable in the power spectrum and show the clear elongation in the bicoherence plot for case 2, indicating that proposed next-generation timing missions should be capable of making use of the

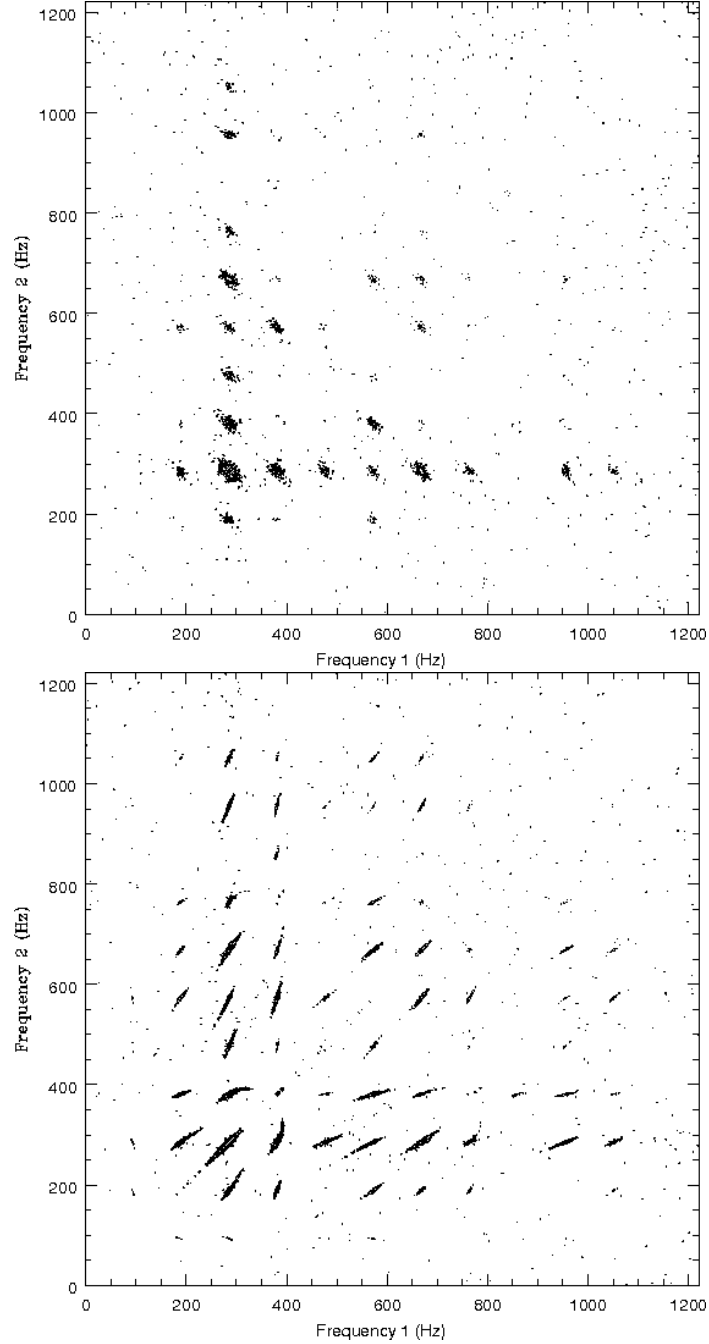


**Figure 4-10:** The bicoherences  $b^2(\nu_1, \nu_2)$  for case 1 (top) and case 2 (bottom) described in the text, assuming  $30 \text{ m}^2$  area for the detector and a 1000 second integration. The color scale is the same as in Figure 4-8. The frequencies correspond to a  $10M_\odot$  black hole with spin parameter  $a/M = 0.5$ .

bicoherence for studying HFQPOs. A few very weak peaks are seen in the bicoherence in case 1 even in 1000 seconds. The simulated bicoherences for a  $30 m^2$  detector are plotted in Figure 4-10. We note that these simulations are a bit over-simplified, in that we have not included the lower frequency QPOs and low frequency band-limited noise that are typically observed in conjunction with the HFQPOs, but that these variability components should not significantly affect the phase coupling of the high frequency QPOs. We also note that it might be possible to make use of the bicoherence even with *RXTE* if a nearby X-ray transient goes into outburst, but that in such a case, the deadtime effects we have neglected here might become important.

## 4.8 Summary

In the context of a geodesic hot spot model, we have developed a few simple analytic methods to interpret the amplitudes and widths of QPO peaks in accreting black holes. The model combines three-dimensional ray tracing calculations in full general relativity with analytic results of basic convolution theory, which are in turn confirmed by simulating the observed light curves of multiple hot spots. Given the Fourier amplitudes of a single hot spot light curve, we have derived a simple formula for the complete QPO power spectrum made up of Lorentzian peaks of varying amplitudes and widths. This power spectrum can then be fit to observed QPO data and used to constrain parameters of the hot spot model, and possibly measure the black hole mass and spin.

For XTE J1550–564, the locations of the HFQPO peaks are well constrained, in turn constraining the spin parameter  $a/M$  when combined with radial velocity measurements of the black hole mass. Based on the presumption that the 3:2 frequency ratio is indeed caused by closed orbits with coordinate frequencies in a 3:1 ratio, an observed mass of  $M = 10.5 \pm 1.0 M_\odot$  and orbital frequency  $\nu_\phi = 276 \pm 5$  Hz would predict a spin of  $a/M = 0.5 \pm 0.1$  (Orosz et al., 2002; Remillard et al., 2002). If reliable, this coordinate frequency method would give one of the best estimates yet for a black hole spin, although it is admittedly very model dependent.

The amplitudes of the QPO peaks can be used to infer the arc length of the sheared hot spot and the relative flux contributions from the hot spot and the background disk/corona. The longer arcs seen in type B QPOs are also consistent with the broader peaks: if the hot spots are continually formed and destroyed along special closed orbits, as the emission region gets stretched into a ring, it is more likely to be dissolved or disrupted, giving a shorter characteristic lifetime  $T_l$  and thus broader peaks.

Some of the power spectrum features discussed in this paper are unique to the geodesic hot spot model, while others could be applied to more general QPO mod-

els. Clearly the harmonic amplitudes  $A_j$  given by the ray-tracing calculation are dependent on the hot spot model, as is the broadening from a finite resonance width, yet both could be generalized and applied to virtually any perturbed disk model. Similarly, the peak broadening and the damping of higher harmonics due to photon scattering will be qualitatively the same for any emission mechanism that produces periodic light curves from black holes.

Unfortunately, the quality of the QPO data is not sufficiently high to confirm or rule out the present hot spot model, leaving a number of questions unanswered. By fitting only two or three peaks, we are not able to tightly constrain all the model parameters, particularly the scattering length scale and the resonance width, both of which are most sensitive to the higher frequency harmonics. Since the high temperature electrons in the corona tend to transfer energy into the scattered photons, measuring the energy spectra of the different QPO peaks would also prove extremely valuable in understanding the emission and scattering mechanisms. For this analysis to be most effective, a more accurate model for the electron scattering will certainly be necessary (see Chapter 6 below). This has been done to some degree with the lower frequency region of the power spectra from black holes and neutron stars (Ford et al., 1999), and may even be observable above  $\sim 100$  Hz with current *RXTE* capabilities, but very well may have to wait for a next generation X-ray timing mission.

In the immediate future, however, there is much more to be done with the *RXTE* data that already exists. Important additional insight might be gained from new analyses of the X-ray light curves in the time domain or by using higher-order statistics like the bicoherence and bispectrum, recovering some of the phase information lost when the power spectrum is computed in frequency space (Maccarone & Schnittman, 2005). There is also an important message in the relationship between the photon energy spectra and the QPO power spectra as well as the connection between the low frequency and high frequency QPOs. Why should the HFQPOs appear in certain spectral states and not others? The answer to these questions may lie in new models of the accretion disk and specifically the radiation physics relating the thermal and power-law emission, as well as broad fluorescent lines like Fe  $K\alpha$ . The fact that the HFQPOs are seen most clearly in the 6-30 keV energy range suggests that standard models of thin, thermal accretion disks are not adequate for this problem. This emphasizes the essential role of radiation transport, particularly through the corona, in any physical model for black hole QPOs.



# Chapter 5

## Steady-state $\alpha$ -disks

*The secret to creativity is knowing how to hide your sources.*

-Albert Einstein

As mentioned in Section 1.2.1 in the Introduction, the standard accretion disk model was developed by Shakura & Sunyaev (1973), followed shortly by Novikov & Thorne (1973) (hereafter “NT”) with a relativistic extension for the Kerr metric. The defining characteristic for both models is the “alpha” prescription for transporting angular momentum via a turbulent viscosity that is proportional to the local pressure in the disk. This shear stress generates heat, which is then radiated from the top and bottom surfaces of the steady-state disk, as the gas loses gravitational energy and spirals in towards the central black hole.

While the original motivation for this Chapter was to develop a disk model which could be used as a test-bed for the 3-D post-processor, the results derived below also give important insights into the structure of  $\alpha$ -disks, particularly at the ISCO boundary. We also learn a good deal about the shape of the continuum energy spectrum for the Thermal-Dominant black hole state.

### 5.1 Steady-state Disks Outside the ISCO

We begin by presenting an outline of the Novikov-Thorne description of a steady-state relativistic accretion disk. In addition to Novikov & Thorne (1973), this model is described in more detail in Page & Thorne (1974) and Thorne (1974), where the famous value of  $a/M = 0.998$  is derived as an upper limit for the spin of an accreting black hole.

First, a few definitions to simplify the subsequent algebra:

$$\mathcal{A} \equiv 1 + \frac{a_\star^2}{r_\star^2} + 2\frac{a_\star^2}{r_\star^3}, \quad (5.1a)$$

$$\mathcal{B} \equiv 1 + \frac{a_\star}{r_\star^{3/2}}, \quad (5.1b)$$

$$\mathcal{C} \equiv 1 - \frac{3}{r_\star} + 2\frac{a_\star}{r_\star^{3/2}}, \quad (5.1c)$$

$$\mathcal{D} \equiv 1 - \frac{2}{r_\star} + \frac{a_\star^2}{r_\star^2}, \quad (5.1d)$$

$$\mathcal{E} \equiv 1 + 4\frac{a_\star^2}{r_\star^2} - 4\frac{a_\star^2}{r_\star^3} + 3\frac{a_\star^4}{r_\star^4}, \quad (5.1e)$$

$$\mathcal{F} \equiv 1 - 2\frac{a_\star}{r_\star^{3/2}} + \frac{a_\star^2}{r_\star^2}, \quad (5.1f)$$

where  $r_\star \equiv r/M$  and  $a_\star \equiv a/M$  are the dimensionless radius and spin, respectively. In the thin disk approximation, the angular coordinate  $\theta$  can be replaced by a vertical coordinate  $z = r \cos \theta \approx r(\pi/2 - \theta)$ .

### 5.1.1 Radial Structure

The radial structure of the disk can be described in terms of the vertically-integrated hydrodynamic variables, as measured in the local rest frame of the gas (denoted by “hat” indices  $\hat{\mu}$ ). This local frame is simply the tetrad for a massive test particle on a stable circular orbit at that radius. The integrated shear stress is given by

$$W(r) \equiv \int T_{\hat{\phi}\hat{r}}(r, z) dz \quad (5.2)$$

and the total radiation flux off either face of the disk is

$$F(r) \equiv T^{\hat{t}\hat{z}}(r, z \rightarrow \infty) = -T^{\hat{t}\hat{z}}(r, z \rightarrow -\infty), \quad (5.3)$$

where  $\mathbf{T}$  is the stress-energy tensor. Local conservation of mass gives the accretion rate

$$\dot{M} = -2\pi r \Sigma v^{\hat{r}} \mathcal{D}^{1/2} \quad (5.4)$$



as a constant everywhere in the disk. Here  $\Sigma(r)$  is the surface density of the disk in the rest frame of the orbiting gas:

$$\Sigma(r) = \int_{-\infty}^{\infty} \rho(r, z) dz = \int_{-\infty}^{\infty} T^{\hat{t}\hat{t}}(r, z) dz, \quad (5.5)$$

and  $v^{\hat{r}} \ll c$  is the average radial velocity of the slowly inspiraling gas (negative for inward-flowing gas, giving a positive value for  $\dot{M}$ ).

Conservation of angular momentum gives a first-order differential equation in  $r$  for the stress  $W(r)$ :

$$\frac{d}{dr} \left( -\frac{\dot{M}L}{2\pi} + r^2 \frac{\mathcal{B}\mathcal{D}}{\mathcal{C}^{1/2}} W \right) + 2rLF = 0, \quad (5.6)$$

where

$$L = \sqrt{\frac{GM}{r}} \mathcal{F} \quad (5.7)$$

is the specific angular momentum of massive particles on circular orbits in the equatorial plane. In equation (5.6), the first term is the rate of angular momentum increase in the gas [when combined with the mass continuity equation (5.4)], the second is the rate at which the stress  $W$  transports angular momentum outward through the disk, and the third is the rate at which radiation removes angular momentum from the two surfaces of the disk.

The flux  $F(r)$  off the face of the disk is given by conservation of energy: in the steady-state disk, all the energy generated by turbulent/magnetic stress in the interior must be radiated off the surface. The energy generated is given by

$$2F = -s_{\alpha\beta} \int T^{\alpha\beta} dz = -2s_{\hat{\phi}\hat{r}} W, \quad (5.8)$$

where  $s_{\alpha\beta}$  is the average shear of the gas. The shear tensor is defined by

$$s_{\alpha\beta} \equiv \frac{1}{2}(v_{\alpha;\mu} P_{\beta}^{\mu} + v_{\beta;\mu} P_{\alpha}^{\mu}) - \frac{1}{3}\theta P_{\alpha\beta}, \quad (5.9)$$

where  $v_{\alpha}$  is the local 4-momentum of the gas,  $\theta$  is the geodesic expansion of the gas defined below in equation (5.52) and  $P_{\alpha\beta}$  is the projection tensor

$$P_{\alpha\beta} \equiv g_{\alpha\beta} + v_{\alpha}v_{\beta}. \quad (5.10)$$

For circular geodesic orbits in the plane, the only non-zero shear terms are

$$s_{\hat{\phi}\hat{r}} = s_{\hat{r}\hat{\phi}} = -\frac{3}{4}\sqrt{\frac{GM}{r^3}}\frac{\mathcal{D}}{\mathcal{C}}. \quad (5.11)$$

The  $\alpha$ -disk model assumes that all the hydrodynamic turbulence, molecular viscosity (typically very small), magnetic stress, and magnetic heating can be combined into a single term for the stress tensor

$$T^{\hat{\phi}\hat{r}} = \alpha p, \quad (5.12)$$

where  $p$  is the sum of the gas and radiation pressure. The dimensionless parameter  $\alpha$  is generally taken to be between 0.01 and 1. A number of papers have attempted to determine  $\alpha$  directly from MHD simulations, and generally find values within this range, but also find that  $\alpha$  can vary significantly between different regions in the disk [see, e.g. Balbus & Hawley (1998); Hawley (2000); Hawley & Krolik (2001)].

Combining equations (5.6, 5.8, and 5.11), and defining the function

$$Z(r) \equiv \frac{2\pi}{\dot{M}} \frac{r^2 \mathcal{B} \mathcal{D}}{M^{1/2} \mathcal{C}^{1/2}} W(r), \quad (5.13)$$

we get the ordinary differential equation

$$\frac{dZ}{dr} = \frac{dL}{dr} - \frac{3}{2} \frac{M^{1/2} L}{r^{5/2} \mathcal{B} \mathcal{C}^{1/2}} Z. \quad (5.14)$$

For a boundary condition, NT set the integrated stress at the ISCO to be zero, so  $Z(R_{\text{ISCO}}) = 0$ . Numerical simulations suggest this is not quite accurate, so we assume some small, non-zero value for the stress across the ISCO, typically  $Z(R_{\text{ISCO}}) \sim 2-3 \times 10^{-2}$ . The exact value is determined self-consistently by matching the turbulent scale length of the disk with the characteristic size of the pressure gradient inside the ISCO, as will be described below in Section 5.2.

Given  $Z(r)$ , the flux radiated from the each point of the disk can be calculated from equation (5.8):

$$F(r) = \frac{3G\dot{M}M}{8\pi} \frac{Z}{r^{7/2} \mathcal{B} \mathcal{C}^{1/2}}. \quad (5.15)$$

This flux is then used as one of the outer boundary conditions for integrating the one-dimensional equations of vertical structure at each radial position in the disk.

### 5.1.2 Vertical Structure

The accretion disk equations of vertical structure are almost identical in form to those of steady-state stellar structure (Hansen & Kawaler, 1994). In the local inertial frame of circular geodesic orbits, the gas can be treated entirely classically. The only relativistic addition necessary is given by the tidal gravitational acceleration, which comes from the Riemann tensor, as calculated in the frame of the gas:

$$g = R_{\hat{t}\hat{z}\hat{t}}^{\hat{z}} z. \quad (5.16)$$

Using the Riemann tensor of the (ZAMO)  $R_{(\alpha)(\beta)(\gamma)(\delta)}$ , as calculated by Bardeen, Press, & Teukolsky (1972), the components in the gas frame come from a simple Lorentz transformation of the velocity  $v^{(\mu)}$  in the ZAMO frame to the local inertial frame  $v^{\hat{\mu}} = \mathbf{e}_{\hat{i}}$ :

$$\begin{aligned} R_{\hat{z}\hat{t}\hat{z}\hat{t}} &= \Lambda_{\hat{z}}^{(\alpha)} \Lambda_{\hat{t}}^{(\beta)} \Lambda_{\hat{z}}^{(\gamma)} \Lambda_{\hat{t}}^{(\delta)} R_{(\alpha)(\beta)(\gamma)(\delta)} \\ &= \Lambda_{\hat{t}}^{(\beta)} \Lambda_{\hat{t}}^{(\delta)} R_{(z)(\beta)(z)(\delta)} \\ &= v^{(\beta)} v^{(\delta)} R_{(z)(\beta)(z)(\delta)} \\ &= (v^{(t)})^2 R_{(z)(t)(z)(t)} + 2v^{(t)} v^{(\phi)} R_{(z)(t)(z)(\phi)} + (v^{(\phi)})^2 R_{(z)(\phi)(z)(\phi)}. \end{aligned} \quad (5.17)$$

This term actually appears to be calculated incorrectly in the NT paper. Riffert & Herold (1995) correctly give it as

$$R_{\hat{t}\hat{z}\hat{t}}^{\hat{z}} = \frac{GM}{r^3} \frac{1 - 4a_{\star} r_{\star}^{-3/2} + 3a_{\star}^2 r_{\star}^{-2}}{1 - 3r_{\star}^{-1} + 2a_{\star} r_{\star}^{-3/2}}, \quad (5.18)$$

which for convenience we will simply call  $\mathcal{R}$ .

The vertical hydrostatic pressure balance is given by

$$\frac{dp}{dz} = -\rho g = -\rho \mathcal{R} z, \quad (5.19)$$

where  $\rho$  is the rest mass density of the gas and the acceleration due to tidal gravity is  $g = \mathcal{R} z$ . The transport of energy in the disk will be dominated by radiation diffusion, so the vertical energy flux  $q^z$  is

$$q^z = -\frac{ac}{3\kappa\rho} \frac{dT}{dz} \quad (5.20)$$

or

$$\frac{dT}{dz} = -\frac{3\kappa\rho}{4acT^3} q^z, \quad (5.21)$$

where we assume local thermodynamic equilibrium with radiation energy density  $aT^4$ . Here the opacity  $\kappa$  is a combination of free-free opacity and electron scattering, but for most of the region of interest it is dominated by electron scattering, so we set

$$\kappa = \kappa_{\text{es}} = 0.40 \text{ cm}^2 \text{g}^{-1}. \quad (5.22)$$

As described above, the energy generation in the  $\alpha$ -disk is given by the product of the shear and stress tensors:

$$\frac{dq^z}{dz} = -2s_{\hat{\phi}\hat{r}}t^{\hat{\phi}\hat{r}} = \frac{3}{2}\sqrt{\frac{GM}{r^3}}\frac{\mathcal{D}}{\mathcal{C}}\alpha p \equiv \bar{\alpha}p, \quad (5.23)$$

where we have compactified a number of terms into the more convenient scaling factor  $\bar{\alpha}(r)$ , which has units of inverse time. Coupled with the equation of state for an ideal gas of ionized hydrogen and radiation

$$p = \frac{2k_B T}{m_p}\rho + \frac{a}{3}T^4, \quad (5.24)$$

we have a complete set of coupled first-order differential equations for the vertical disk structure at each radial position in the disk. In equation (5.24) we have assumed a fully ionized hydrogen gas, where the particle number density is  $n = 2\rho/m_p$ , but any composition could just as easily be used by substituting the relationship (Hansen & Kawaler, 1994)

$$n = \frac{\rho}{\mu m_p}, \quad (5.25)$$

where  $\mu$  is called the “total mean molecular weight.” For a hydrogen mass fraction of  $X$ ,  $\mu$  can be approximated by

$$\mu \approx \frac{4}{3 + 5X}. \quad (5.26)$$

The three equations for  $p$ ,  $T$ , and  $q^z$  require three boundary conditions for a complete solution. As is often done in solving the stellar structure equations (Hansen & Kawaler, 1994), we assume an optically thin, isothermal atmosphere beginning at the photosphere  $z = h$  with surface temperature  $T(h) = T_s$  and density  $\rho(h) = \rho_s$ . All the flux is generated inside of this point, so  $q^z(h) = F$  (given by the radial structure), and plane symmetry ( $z \rightarrow -z$ ) demands that  $q^z(0) = 0$ . To get the third boundary condition, we have to solve for  $T_s$  self-consistently.

The tidal gravitational force on a mass  $m_p$  can be approximated by the effective

potential

$$\Phi_{\text{eff}}(z \approx h) = \frac{\mathcal{R}h}{2}(z - h), \quad (5.27)$$

which produces an isothermal atmosphere with scale height  $H$  and density profile

$$\rho(z > h) = \rho_s \exp \left[ -\frac{m_p \mathcal{R}h(z - h)}{2k_B T_s} \right] \sim e^{-z/H}. \quad (5.28)$$

The density  $\rho_s$  at the “base” of the atmosphere is defined such that the integrated optical depth to electron scattering through the atmosphere is unity (some texts define the photosphere at  $\tau = 2/3$ , but we find the net results to be nearly identical in either case):

$$\int_h^\infty \kappa_{\text{es}} \rho dz = 1, \quad (5.29)$$

which can be solved to give

$$\rho_s = \frac{m_p \mathcal{R}h}{2\kappa_{\text{es}} k_B T_s}. \quad (5.30)$$

Because the opacity is dominated by electron scattering, and not free-free absorption, the resulting radiation will have a modified black-body spectrum, as described in Shakura & Sunyaev (1973). They give two basic models for the scattering atmosphere: a constant density with a sharp cutoff [ $\rho(z < h) = \rho_s$  and  $\rho(z > h) = 0$ ], or the exponential distribution we use here. For the half-plane geometry, the modified spectrum is of the form (Shakura, 1972; Felten & Rees, 1972)

$$F(x) \sim \rho^{1/2} T^{5/4} \frac{x^{3/2} e^{-x}}{(1 - e^{-x})^{1/2}}, \quad (5.31)$$

where  $x$  is defined as a dimensionless scaled frequency  $x \equiv h\nu/k_B T$ . For an exponential density distribution with scale length  $H$ , the modified spectrum has the form (Zeldovich & Shakura, 1969)

$$F(x) \sim H^{-1/3} T^{11/6} \frac{x^2 e^{-x}}{(1 - e^{-x})^{2/3}}, \quad (5.32)$$

which is somewhat more similar to the unmodified blackbody spectrum where

$$F(x) \sim T^3 \frac{x^3 e^{-x}}{1 - e^{-x}}. \quad (5.33)$$

NT use the first model, which gives the total flux integrated over frequency as

$$F = 8.05 \times 10^7 \left( \frac{\rho}{\text{g/cm}^3} \right)^{1/2} \left( \frac{T_s}{\text{°K}} \right)^{9/4} \text{ erg/cm}^2/\text{s}. \quad (5.34)$$

When integrating the stellar structure equations in the diffusion limit, we find the exponential model to more accurately approximate the atmospheric density profile. In that case, the integrated flux is given by

$$F = 1.3 \times 10^4 \left( \frac{H}{\text{cm}} \right)^{-1/3} \left( \frac{T_s}{\text{°K}} \right)^{17/6} \text{ erg/cm}^2/\text{s}. \quad (5.35)$$

Combining equations (5.28) and (5.35) gives the boundary condition for the disk's surface temperature:

$$T_s = 0.28 F^{2/5} \mathcal{R}^{-2/15} h^{-2/15}. \quad (5.36)$$

To simultaneously satisfy all three boundary conditions, the system of differential equations is then solved using a “shooting” method, starting at  $z = h$  and integrating  $p$ ,  $T$ , and  $q^z$  inwards to  $z = 0$ . We iterate this approach for a series of initial values for  $h$ : the solution is given by the value of  $h$  that matches the inner boundary condition of  $q^z(0) = 0$ . Repeating this entire procedure for each value of  $r$  gives the complete structure of the accretion disk outside of the ISCO.

To get a good starting guess for the value of  $h$ , we derive here an approximate solution of the vertical structure equations. The result is somewhat different from that given in NT, as they ignore the (often significant) gas pressure in the inner disk, and also we use different methods of averaging the vertical structure over  $z$ . The difference in disk thickness turns out to be a factor of at least 2 – 3 for typical stellar-mass black holes. Starting with the pressure balance equation (5.19), with the pressure going to zero at the surface of the disk  $p(h) = 0$ , the disk thickness can be approximated in terms of the central pressure  $p_c$  and density  $\rho_c$ :

$$\frac{dp}{dz} \approx \frac{p_c}{h} = \langle \rho z \rangle \mathcal{R}. \quad (5.37)$$

Taking the density profile as roughly linear with  $\rho(h) = 0$ ,

$$\langle \rho z \rangle = \frac{\rho_c}{h} \int_0^h \left( 1 - \frac{z}{h} \right) z dz = \frac{\rho_c h}{6}, \quad (5.38)$$

so our first estimate for  $h$  is

$$h = \left( \frac{6p_c}{\rho_c \mathcal{R}} \right)^{1/2}. \quad (5.39)$$

Taking the average pressure as  $p_c/2$ , the energy generation equation (5.23) gives us an independent expression for  $h$ :

$$h = \frac{F}{\alpha s_{\hat{\phi} \hat{r}} p_c}. \quad (5.40)$$

The third independent estimate for  $h$  comes from the radiation transport equation (5.21):

$$h = \frac{4acT_c^4}{3\kappa_{\text{es}}\rho_c F}. \quad (5.41)$$

Coupled with the equation of state (5.24), we have four (non-linear) equations for the four unknowns  $\rho_c$ ,  $T_c$ ,  $p_c$ , and  $h$  at each radius in the disk. The resulting value of  $h$  gives a remarkably accurate estimate of the disk thickness as determined by directly integrating the structure equations, agreeing within about 10 – 20% for a range of black hole masses, spins, and accretion rates.

In Figure 5-1 we show the comparison of a variety of fluid variables for three versions of the steady-state  $\alpha$ -disk: the numerical integration of the coupled structure equations (solid line), the NT approximation (dotted line), and our revised analytic approximation (dashed line). The basic model parameters used here are  $\alpha = 0.1$ ,  $M = 10M_\odot$ ,  $a/M = 0$ ,  $\dot{M} = 0.05\dot{M}_{\text{Edd}}$  ( $\dot{M}_{\text{Edd}}$  is the mass accretion rate that gives a total disk flux equal to the Eddington luminosity, defined below in Section 5.1.3). Figure 5-2 shows the same disk variables for a black hole with spin  $a/M = 0.9$  but all other parameters identical.

The surface flux  $F(r)$  in our models is determined by integrating equation (5.14) with boundary condition  $Z(R_{\text{ISCO}})$  representing the net torque on the disk at the ISCO, as described below in Section 5.2. Despite the fact that our  $F(r)$  is nearly identical to that of NT, the different methods of solving the vertical structure give very different disk scale heights. Our model predicts a rather thicker disk and much lower density atmosphere [NT assume  $\rho(h) \approx \rho(0)$ ]. The lower-density atmosphere results in a higher surface temperature through equations (5.34) and (5.35). And since the NT disk is cut off at the ISCO [ $h(R_{\text{ISCO}}) \rightarrow 0$ ], the conservation of mass equation (5.4) requires that the density diverges [ $\rho(R_{\text{ISCO}}), \Sigma(R_{\text{ISCO}}) \rightarrow \infty$ ]. However, by slightly modifying the inner torque boundary condition, including gas pressure in the inner disk, and changing the means of averaging the vertical structure equations, a very good analytic approximation can be derived for the disk height, density, and surface temperature. From these fluid variables, we can produce an accurate multi-colored disk spectrum via the ray-tracing post-processor (see Section 5.4 below).

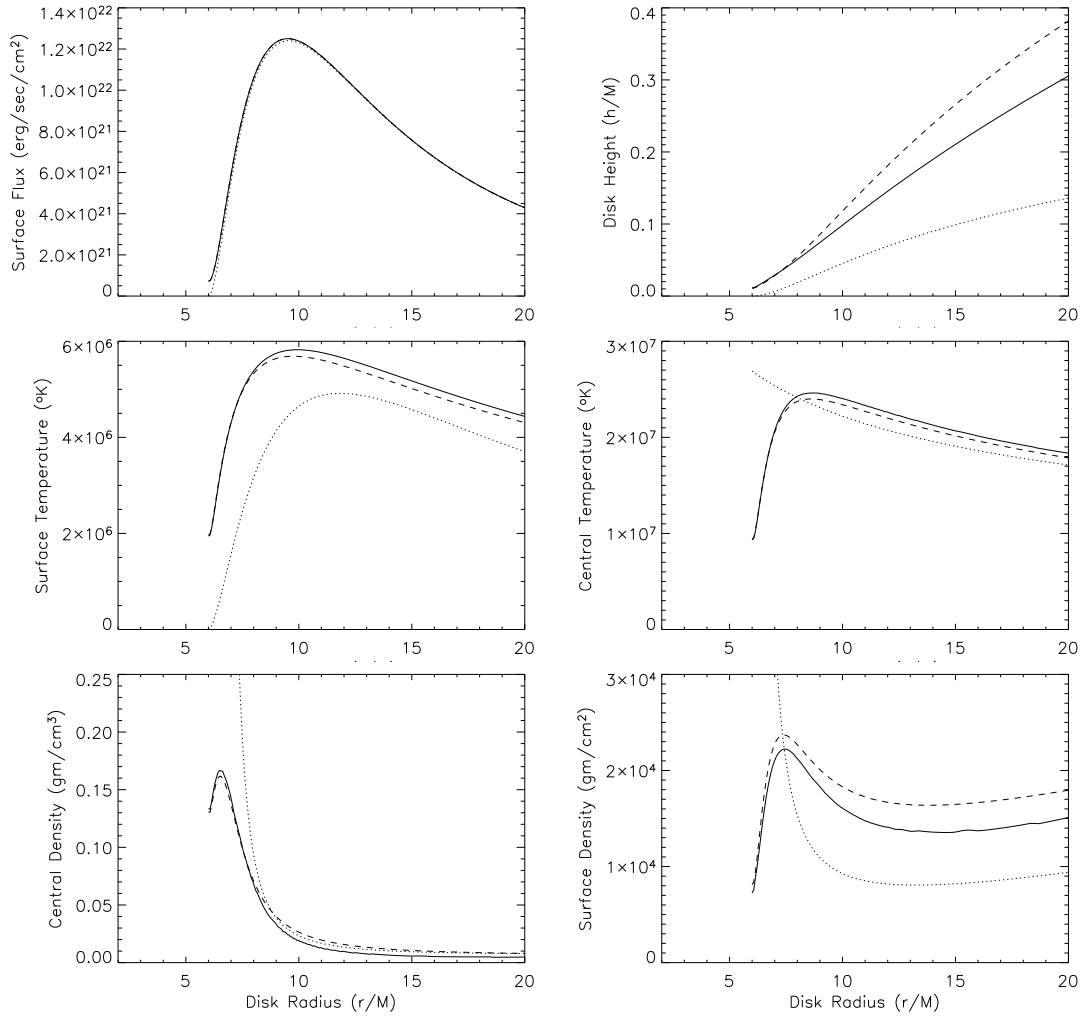


**Figure 5-1:** Comparison of hydrodynamic fluid variables for three versions of the steady-state  $\alpha$ -disk model: Full numerical integration of the vertical structure equations (solid lines); The Novikov-Thorne approximation (dotted line); The revised analytic approximation derived in the text (dashed line). The black hole has mass  $M = 10M_{\odot}$ , spin  $a/M = 0$ , and accretion rate  $\dot{M} = 0.05\dot{M}_{\text{Edd}}$ .



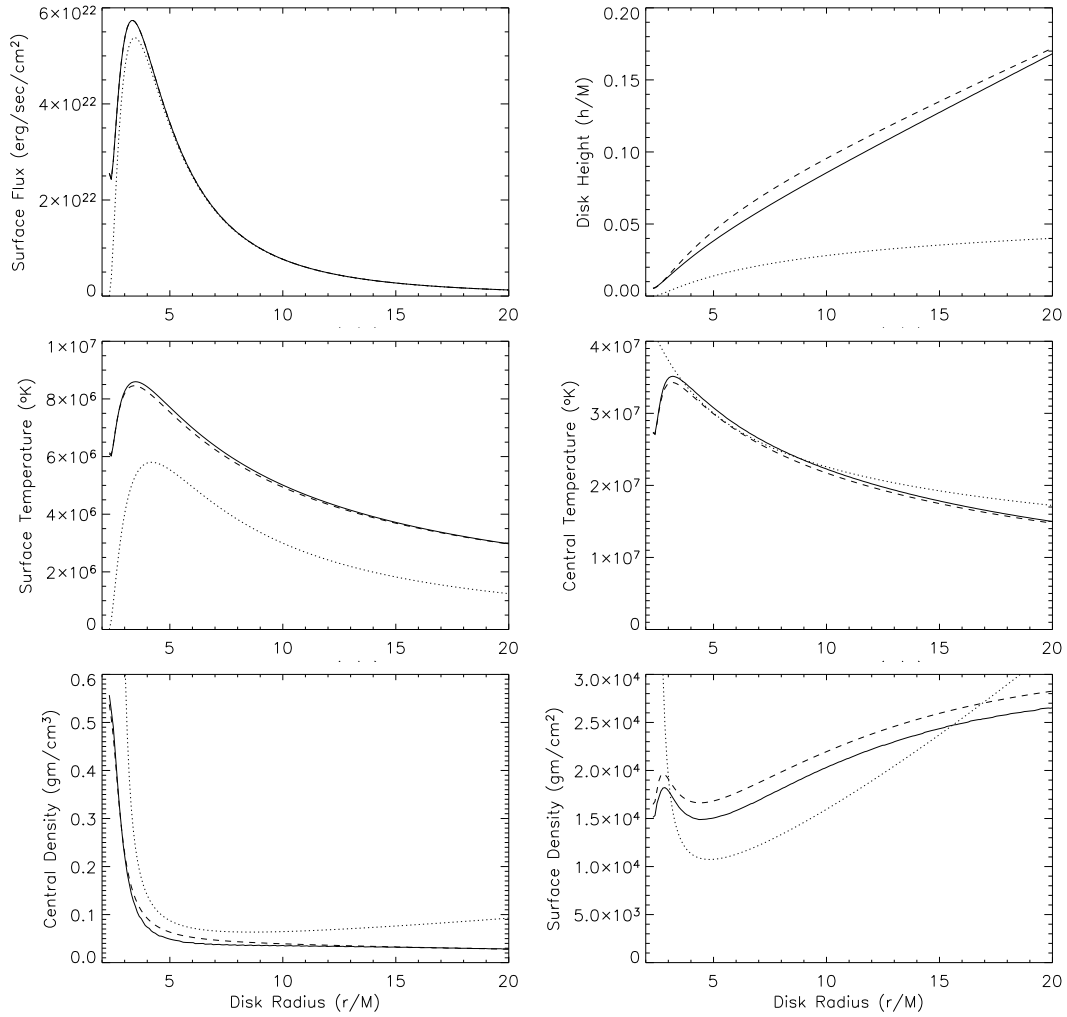


**Figure 5-2:** Comparison of hydrodynamic fluid variables for three versions of the steady-state  $\alpha$ -disk model: Full numerical integration of the vertical structure equations (solid lines); The Novikov-Thorne approximation (dotted line); The revised analytic approximation derived in the text (dashed line). The black hole has mass  $M = 10M_{\odot}$ , spin  $a/M = 0.9$ , and accretion rate  $\dot{M} = 0.05\dot{M}_{\text{Edd}}$ .

### 5.1.3 Revised Eddington Limit

We are now in a position to revisit the traditional Eddington limit on the maximum allowed luminosity for a gravitationally bound, hydrostatic system. The gas can be in hydrostatic equilibrium only if the gravitational force on each proton is greater than the radiation force on each electron. For the traditional derivation of this limit for a spherically symmetric star, the force balance equation can be written (Hansen & Kawaler, 1994)

$$\frac{GMm_p}{r^2} > F \frac{\sigma_T}{c} = \frac{L}{4\pi r^2} \frac{\sigma_T}{c}, \quad (5.42)$$

giving an upper limit on the total luminosity as

$$L_{\text{Edd}} = \frac{4\pi c GM m_p}{\sigma_T} = 3.5 \times 10^4 L_\odot \left( \frac{M}{M_\odot} \right). \quad (5.43)$$

In our case, we must replace the  $1/r^2$  gravitational force with the local tidal gravity at each radius in the disk:

$$m_p \mathcal{R} z > \frac{F \sigma_T}{c}, \quad (5.44)$$

where the classical Thomson cross-section is  $\sigma_T = 6.65 \times 10^{-25} \text{ cm}^2$ . Taking  $z \approx h$ , equations (5.40) and (5.44) give an estimated stability requirement on the central pressure of

$$p_c \lesssim \frac{m_p c \mathcal{R}}{\alpha s_{\hat{\phi}r} \sigma_T}. \quad (5.45)$$

For a given value of  $r_*$ , the Riemann tensor scales as  $\mathcal{R} \sim M^{-2}$  and the shear scales as  $s \sim M^{-1}$ , so the maximum stable pressure is inversely proportional to black hole mass. For  $M = 10M_\odot$  and  $\alpha = 1$ , we find that the maximum stable luminosity is on the order of 5% of Eddington. For supermassive black holes with  $M > 10^6 M_\odot$ , no stable solutions exist with these structure equations, although with a different treatment of the radiation transport (e.g. not diffusion), one might find more success. Presumably this result would also be sensitive to different opacities and boundary conditions more appropriate for the typical AGN disk temperatures of  $T_c \sim 10^4 - 10^5 \text{ K}$ , or the inclusion of important magnetic pressure and stress (Merloni, 2003). It is also quite likely that the slim disk geometry simply does not apply to AGN or to stellar-mass black holes with a high accretion rate. For AGN, a thick, dusty torus may be more appropriate, and the high-luminosity black hole binaries may be better described with a quasi-spherical ADAF geometry (see Section 6.2 below).

## 5.2 Geodesic Plunge Inside the ISCO

The structure of the innermost region of the disk is based on the geodesic trajectories of plunging particles inside of the ISCO. From the mass continuity equation (5.4) and integrating the vertical structure equations to give the surface density  $\Sigma$  at the ISCO, the radial velocity  $v^{\hat{r}}$  can be determined, which in turn gives the momentum of a massive particle at the beginning of its plunge. We assume the gas follows a geodesic trajectory, conserving both the specific energy and angular momentum from the ISCO to the horizon. From the Hamiltonian formulation

$$H(x^\mu, p_\mu) = g^{\mu\nu} p_\mu p_\nu = -1, \quad (5.46)$$

the radial velocity is given by

$$p^r(r) = - \left[ -g^{rr} (1 + g^{tt} E_0^2 - 2g^{t\phi} E_0 l + g^{\phi\phi} l^2) \right]^{1/2}, \quad (5.47)$$

where the integrals of motion are the specific energy  $p_t = -E_0$  and angular momentum  $p_\phi = l$  at the ISCO. Near the plane of the disk, the metric and inverse-metric (for coordinates  $t$ ,  $r$ ,  $z$ , and  $\phi$ ) are given by

$$g_{\mu\nu} = \begin{pmatrix} -\mathcal{D}\mathcal{A}^{-1} + (2Ma/r^2)^2 \mathcal{A}^{-1} & 0 & 0 & -2Ma/r \\ 0 & \mathcal{D}^{-1} & 0 & 0 \\ 0 & 0 & 1 & 0 \\ -2Ma/r & 0 & 0 & r^2 \mathcal{A} \end{pmatrix} \quad (5.48)$$

and

$$g^{\mu\nu} = \begin{pmatrix} -\frac{\mathcal{A}}{\mathcal{D}} & 0 & 0 & -\frac{2Ma}{r^3 \mathcal{D}} \\ 0 & \mathcal{D} & 0 & 0 \\ 0 & 0 & 1 & 0 \\ -\frac{2Ma}{r^3 \mathcal{D}} & 0 & 0 & \frac{1}{r^2 \mathcal{A}} - \left(\frac{2Ma}{r^3}\right)^2 \frac{1}{\mathcal{A}\mathcal{D}} \end{pmatrix}. \quad (5.49)$$

In the coordinate basis, the plunge trajectory 4-velocity inside the ISCO is

$$\begin{aligned} p^t &= -g^{tt} E_0 + g^{t\phi} l, \\ p^r &= - \left[ -g^{rr} (1 + g^{tt} E_0^2 - 2g^{t\phi} E_0 l + g^{\phi\phi} l^2) \right]^{1/2}, \\ p^z &= 0, \\ p^\phi &= -g^{t\phi} E_0 + g^{\phi\phi} l. \end{aligned} \quad (5.50)$$

In the ZAMO basis,

$$\begin{aligned}
p^{(t)} &= \sqrt{\frac{\mathcal{D}}{\mathcal{A}}} p^t, \\
p^{(r)} &= \sqrt{\frac{1}{\mathcal{D}}} p^r, \\
p^{(z)} &= 0, \\
p^{(\phi)} &= -\frac{2Ma}{r^2 \mathcal{A}^{1/2}} p^t + r \mathcal{A}^{1/2} p^\phi.
\end{aligned} \tag{5.51}$$

These components will be necessary for calculating the gravitational tidal force in the local frame of the plunging gas. The result is similar to that derived above for circular orbits in equation (5.17), with one additional term  $(p^{(r)})^2 R_{(z)(r)(z)(r)}$  due to the non-zero radial velocity.

In addition to the modified form of the Riemann tensor, the most significant characteristic of the plunging region is the expansion of the gas due to the divergence of nearby trajectories. For a collection of particles on geodesic orbits in the plane of the disk, an infinitesimal area  $\delta A$  evolves according to the expansion parameter  $\theta$ , defined as

$$\theta \equiv \frac{1}{A} \frac{d}{d\tau} \delta A = p_{;\alpha}^\alpha = \frac{\partial}{\partial x^\alpha} p^\alpha + p^\mu \Gamma_{\mu\alpha}^\alpha, \tag{5.52}$$

where  $\tau$  measures the proper time along the trajectory of the gas. For both Schwarzschild and Kerr black holes, the expansion is given simply by

$$\theta(r) = \frac{\partial p^r}{\partial r} + 2 \frac{p^r}{r}. \tag{5.53}$$

Thus the area evolves according to

$$\delta A = \delta A_0 \exp\left[\int_0^\tau \theta(\tau') d\tau'\right] = \delta A_0 \exp\left[\int_{r_{\text{ISCO}}}^r dr' \theta(r')/p^r\right], \tag{5.54}$$

where  $\delta A_0$  is the (unit) area of a “footprint” of a vertical column of gas at the ISCO. For smaller values of  $p^r(R_{\text{ISCO}})$ , the expansion is greater, as the gas falls sharply out of the disk. For large initial values of  $p^r$ , the expansion is actually negative and the gas is compressed as it flows inward through concentric circles of decreasing  $r$ , then eventually expands as it approaches the horizon and is pulled into the black hole on rapidly plunging trajectories.

As we mentioned above, the specific value for  $p^r(R_{\text{ISCO}})$  is determined by integrating the vertical structure equations and using the constant mass accretion relation. In Section 5.1, when solving the radial structure of the disk outside of the ISCO,

we set the integrated stress at the ISCO to some small non-zero value. Now we can determine what this value should be. As explained in Shakura & Sunyaev (1973), the coefficient of viscosity due to turbulent motion in the gas is

$$\eta \approx \rho v_{\text{turb}} l_{\text{turb}}, \quad (5.55)$$

where  $v_{\text{turb}}$  and  $l_{\text{turb}}$  are the characteristic velocity and size of a turbulent cell. The turbulent velocity is limited by the sound speed or else shocks will develop and dissipate the turbulent energy. MHD simulations suggest these limits are often nearly equalities. Thus let us set  $v_{\text{turb}} \approx c_s \approx \sqrt{p/\rho}$ . The turbulent stress is then (Novikov & Thorne, 1973)

$$\alpha p = t_{\hat{\phi}\hat{r}} = \eta |s_{\hat{\phi}\hat{r}}| \approx \rho c_s l_{\text{turb}} |s_{\hat{\phi}\hat{r}}|, \quad (5.56)$$

which combines with equation (5.39) to give

$$l_{\text{turb}} \approx \frac{\alpha h}{-s_{\hat{\phi}\hat{r}}} \sqrt{\mathcal{R}/6} \sim \alpha h. \quad (5.57)$$

This turbulent length scale determines the region over which viscous torques can act on the gas. Inside of the ISCO, the gas expands rapidly, thus decreasing the pressure, which in turn is responsible for creating the viscosity in the gas. Therefore the scale length for the turbulent cells should be the same as the scale length of the pressure drop inside of the ISCO. In the NT model, since no stresses act across the ISCO, there is no means for transporting away angular momentum and allowing the gas to cross the ISCO. Thus the matter should start to “pile up” at the ISCO, increasing the disk thickness until the turbulence scale length extends far enough inside the ISCO to get pulled in by the plunging geodesics.

A non-zero torque on the disk at the ISCO increases the overall radiative efficiency of the disk by effectively removing energy from the accreting matter even after it has crossed the ISCO. Much of this energy is then transported outward and radiated at a greater value of  $r$ , increasing the temperature of the entire disk (Agol & Krolik, 1999). Table 5.1 shows the efficiency of the torqued  $\alpha$ -disk as a function of spin, compared to the zero-torque NT disk. Also listed are the respective Eddington accretion rates  $\dot{M}_{\text{Edd}}$  for a black hole with mass  $10M_{\odot}$ . These accretion rates decrease for increased efficiency, as it takes less mass to produce the same luminosity.

To estimate the scale length of the pressure drop inside the ISCO, consider an ideal gas dominated by radiation pressure

$$p = \frac{a}{3} T^4 \quad (5.58)$$

**Table 5.1:** Accretion efficiency  $\eta = L/\dot{M}c^2$  for torqued and non-torqued (NT) disks. For a given efficiency,  $L_{\text{Edd}} = \eta\dot{M}_{\text{Edd}}c^2$

BH Spin ( $a/M$ )	$\eta_{\text{torqued}}$	$\eta_{\text{NT}}$	$\dot{M}_{\text{Edd}}(\text{torqued})$ $\times 10^{19}$ gm/s	$\dot{M}_{\text{Edd}}(\text{NT})$ $\times 10^{19}$ gm/s
0	0.058	0.056	2.29	2.37
0.25	0.069	0.067	1.92	1.98
0.5	0.088	0.084	1.52	1.58
0.75	0.128	0.118	1.04	1.12
0.9	0.186	0.170	0.71	0.78
0.998	0.453	0.379	0.29	0.35

with energy density

$$u = aT^4. \quad (5.59)$$

From the first law of thermodynamics,

$$d \ln T = -\frac{1}{3} d \ln V \quad (5.60)$$

so

$$p \sim V^{-4/3}, \quad (5.61)$$

where  $V$  is the volume of the gas, and in our case  $V = h\delta A$ . Conservation of mass gives  $\rho \sim V^{-1}$ , so equation (5.39) gives

$$h^2 \sim \frac{p}{\rho\mathcal{R}} \sim V^{-1/3}\mathcal{R}^{-1} \sim \delta A^{-1/3}h^{-1/3}\mathcal{R}^{-1} \Rightarrow h \sim \left(\frac{1}{\delta A\mathcal{R}^3}\right)^{1/7}. \quad (5.62)$$

Thus the pressure scaling inside of the ISCO can be approximated by

$$p(r < r_{\text{ISCO}}) \sim \frac{\mathcal{R}^{4/7}}{\delta A^{8/7}}, \quad (5.63)$$

where  $\mathcal{R}$  and  $\delta A$  are given by the geodesic plunge trajectories. Of course, those trajectories are defined by the initial inward radial velocity, which is in turn determined by the disk thickness and density at the ISCO. The consistent disk solution is that in which the pressure falls off at a length scale of  $l_{\text{turb}}$ :

$$p(r_{\text{ISCO}} - l_{\text{turb}}) \approx \frac{1}{2}p(r_{\text{ISCO}}). \quad (5.64)$$

For solar-mass black holes with a given stress parameter  $\alpha$ , we are able to find solutions to equation (5.64) for a range of accretion rates  $\dot{M}$  by varying the boundary condition for the integrated stress at the ISCO  $W(R_{\text{ISCO}})$ . Consider the two limits: for a small  $W$ , the flux off the disk surface is small, the disk is thin, and the surface density  $\Sigma$  is small, giving a large inward velocity  $p^r$ ; however, for a large value of  $W(R_{\text{ISCO}})$ , the high flux demands a large surface density and thus a small velocity  $p^r$ . From the geodesic plunge trajectories, we find that a small initial inward velocity gives a small scale length for the plunge (matter falls out over a small range of  $r$ ), while a large initial velocity gives a longer scale length as the matter “coasts” for a while before plunging. These competing factors ensure a solution to equation (5.64): small  $W$  with small  $h \Rightarrow$  coasting plunge with large  $l_{\text{plunge}}$ ; large  $W$  with large  $h \Rightarrow$  sharp plunge with small  $l_{\text{plunge}}$ . Thus somewhere between the two limits a solution for  $l_{\text{plunge}} = l_{\text{turb}}$  exists.

### 5.3 Numerical Implementation

As we described in Section 5.1, the equations of vertical structure outside of the ISCO can be integrated in a fashion very similar to that of the standard stellar structure equations. We have three coupled first-order differential equations for  $p$ ,  $T$ , and  $q^z$  as a function of  $z$ , the vertical height above the accretion disk midplane. The physical solution is determined by the boundary conditions on these three equations, setting  $q^z(0) = 0$ ,  $q^z(h) = F$ , and  $T(h) = T_s$ , with the surface temperature  $T_s$  defined by equation (5.36).

The actual solution of these structure equations is relatively straightforward, using a standard fourth-order Runge-Kutta algorithm with constant step size  $dz$ . From a Lagrangian mass viewpoint, this results in finer zone resolution in the outer layers of the disk, allowing an accurate solution of the atmospheric structure. The resolution  $dz$  is different for each radius in the disk, so that the thinner inner disk can be divided into roughly the same number of zones as the thick outer disk. The appropriate step size can be estimated *a priori* from the analytic result (5.39) and  $dz \approx h/N_z$  for  $N_z$  zones in the disk.

Inside the ISCO, the one-dimensional solution to the vertical structure equations evolves dynamically in time (proper time of local free-falling tetrad), so we must replace the coupled ODEs with a set of hydrodynamic partial differential equations. Following Bowers & Wilson (1991), we adopt an implicit Lagrangian scheme for our numerical solution to these equations. The Lagrangian approach is preferred for the one-dimensional problem due to its simplicity and accuracy in monitoring conserved quantities.

An implicit scheme is necessary because of the high sound speed of the radiation

pressure-dominated gas in the inner disk, requiring a very small time step to satisfy the explicit Courant condition. For typical resolutions of  $N_z \sim 200$ , the Courant time step would be prohibitively small at  $dt \sim 10^{-8}$  sec, while the plunge from the ISCO to the horizon of a  $10M_\odot$  black hole could take  $\sim 2 - 3 \times 10^{-2}$  sec. During this plunge, the gas is quite “well-behaved,” i.e. no shock waves or discontinuities in the state variables, so in the absence of numerical instability, much larger time steps are appropriate (we typically use  $dt \approx 100 \times \Delta t_{\text{Courant}}$ ).

In the discussion below, we shall use subscripts for spatial indices and superscripts for temporal indices. The position, velocity, acceleration, and flux will be defined at the zone boundaries  $k = 0, \dots, N_z$ , while the state variables of mass, density, temperature, pressure, and internal energy will be defined at the zone interiors  $k = 1/2, \dots, N_z - 1/2$ . A second-order accurate scheme defines the positions at the whole time steps  $n = 0, 1, \dots$  and the velocities at the half-time steps  $n = 1/2, 3/2, \dots$ :

$$v_k^{n+1/2} = \frac{z_k^{n+1} - z_k^n}{\Delta t^{n+1/2}}. \quad (5.65)$$

The acceleration of each zone is caused by the tidal gravity and any pressure gradients in the gas:

$$a_k^n = \frac{v_k^{n+1/2} - v_k^{n-1/2}}{\Delta t^n} = \frac{p_{k+1/2}^{n+1} - p_{k-1/2}^{n+1}}{\Delta m_k} - R_{i\hat{z}i}^{\hat{z}}(r) z_k^{n+1}, \quad (5.66)$$

where the mass in each zone is given by

$$\Delta m_{k+1/2} = \rho_{k+1/2}^n (z_{k+1}^n - z_k^n) \delta A, \quad (5.67)$$

where we take the footprint of the gas column to have unit area  $\delta A = 1$ . The masses on the boundaries are just the averages of neighboring zones:

$$\Delta m_k = \frac{1}{2} (\Delta m_{k-1/2} + \Delta m_{k+1/2}). \quad (5.68)$$

Note that in equation (5.66) the pressure and gravitational acceleration are defined at the next time step  $t^{n+1}$ , thus making this an implicit scheme.

For our mixture of ionized hydrogen gas and radiation, the internal specific energy  $\varepsilon$  and pressure  $p$  are given explicitly as functions of the fluid density and temperature:

$$\varepsilon(\rho, T) = \frac{3k_B T}{m_p} + \frac{aT^4}{\rho} \quad (5.69)$$



and the equation of state given above in equation (5.24):

$$p(\rho, T) = \frac{2k_B T}{m_p} \rho + \frac{a}{3} T^4.$$

The first law of thermodynamics can be written in the form (Bowers & Wilson, 1991)

$$\left( \frac{\partial \varepsilon}{\partial T} \right)_\rho dT = dQ + T \left( \frac{\partial p}{\partial T} \right)_\rho \frac{d\rho}{\rho^2}, \quad (5.70)$$

where all non-adiabatic contributions (shocks, radiation, etc.) to the internal energy is included in the term  $dQ$ . These effects are included in a separate implicit treatment using the technique of “operator splitting,” described below. Thus the purely adiabatic expansion and compression of the fluid can be described in finite difference form:

$$T_{k+1/2}^{n+1} - T_{k+1/2}^n = - \frac{T_{k+1/2}^{n+1} (p, T)_{k+1/2}^n}{(\varepsilon, T)_{k+1/2}^n} \left( \frac{1}{\rho_{k+1/2}^{n+1}} - \frac{1}{\rho_{k+1/2}^n} \right). \quad (5.71)$$

Here  $\varepsilon, T$  and  $p, T$  are the partial derivatives of energy and pressure with respect to temperature. Note that the temperature on the right hand side of equation (5.71) is also given implicitly at time  $t^{n+1}$ . Defining the dimensionless parameter

$$\Gamma_{k+1/2}^n \equiv - \frac{(p, T)_{k+1/2}^n}{(\varepsilon, T)_{k+1/2}^n} \left( \frac{1}{\rho_{k+1/2}^{n+1}} - \frac{1}{\rho_{k+1/2}^n} \right), \quad (5.72)$$

the temperature at time  $t^{n+1}$  is given by

$$T_{k+1/2}^{n+1} = T_{k+1/2}^n (1 + \Gamma_{k+1/2}^n)^{-1}. \quad (5.73)$$

On the right hand side of equation (5.72), the density  $\rho_{k+1/2}^{n+1}$  can be estimated *explicitly* to first order from  $v_k^{n-1/2}$  and  $v_{k+1}^{n-1/2}$ .

The Lagrangian hydrodynamics conserves the mass in each zone  $\Delta m_{k+1/2}$  between time steps, so the density is given by

$$\rho_{k+1/2}^{n+1} = \frac{\Delta m_{k+1/2}}{z_{k+1}^{n+1} - z_k^{n+1}}. \quad (5.74)$$

Equations (5.73) and (5.74) and the equation of state give the pressure at time  $t^{n+1}$ . This pressure is then used in equation (5.66), which can be combined with (5.65) to give a set of relations defined on the zone boundaries, expressible as a set of coupled

nonlinear equations

$$f_k(z_{k+1}^{n+1}, z_k^{n+1}, z_{k-1}^{n+1}) = -\frac{1}{\Delta t^n} \left( \frac{z_k^{n+1} - z_k^n}{\Delta t^{n+1/2}} - \frac{z_k^n - z_k^{n-1}}{\Delta t^{n-1/2}} \right) + \frac{p_{k+1/2}^{n+1} - p_{k-1/2}^{n+1}}{\Delta m_k} - R_{\hat{t}\hat{z}\hat{t}}(r) z_k^{n+1} = 0. \quad (5.75)$$

On the right hand side, the pressure terms  $p^{n+1}$  are functions of the positions  $z_{k+1}^{n+1}$  and  $z_{k-1}^{n+1}$ . The function  $f_k$  is well-defined by the equations above for the interior zones ( $1 \leq k \leq N_z - 1$ ) and we use linear extrapolation to give  $f_{N_z}$ , while planar symmetry requires  $z_{-1}^{n+1} = -z_1^{n+1}$ , thus defining  $f_0$ . The solution to equation (5.75) gives the positions of the zone boundaries  $z_k^{n+1}$ , from which all the other hydrodynamic variables can be determined.

Bowers & Wilson (1991) outline the standard approach to solving this set of equations using Newton-Raphson iteration and a tridiagonal solver. Denoting the first order solution to  $f_k(z_k^{n+1}) = 0$  by the vector  $z_k^i$ , equation (5.75) can be written as

$$f_k(z_{k+1}^i, z_k^i, z_{k-1}^i) = f_k(z_{k+1}^n, z_k^n, z_{k-1}^n) + \left( \frac{\partial f_k}{\partial z_{k+1}^n} \right)^n \Delta z_{k+1}^n + \left( \frac{\partial f_k}{\partial z_k^n} \right)^n \Delta z_k^n + \left( \frac{\partial f_k}{\partial z_{k-1}^n} \right)^n \Delta z_{k-1}^n + \mathcal{O}(\Delta z^2). \quad (5.76)$$

Then an approximate solution to (5.75) is

$$z_k^{n+1} = z_k^n + \Delta z_k^n. \quad (5.77)$$

We solve for these  $\Delta z_k^n$  iteratively by setting  $f_k(z_{k+1}^i, z_k^i, z_{k-1}^i) = 0$  and solving the tridiagonal system

$$-\left( \frac{\partial f_k}{\partial z_{k+1}^n} \right)^n \Delta z_{k+1}^n - \left( \frac{\partial f_k}{\partial z_k^n} \right)^n \Delta z_k^n - \left( \frac{\partial f_k}{\partial z_{k-1}^n} \right)^n \Delta z_{k-1}^n = f_k(z_{k+1}^n, z_k^n, z_{k-1}^n) \quad (5.78)$$

and then re-evaluating  $f_k(z_{k+1}^i, z_k^i, z_{k-1}^i)$  until an acceptable accuracy is reached for  $z_k^{n+1}$  in equation (5.75). This typically take only about seven or eight iterations to reach machine accuracy, due to the rapid convergence of the Newton-Raphson root finding algorithm. This accuracy far exceeds the limiting first-order accuracy of the finite difference equation for energy (5.71), so we generally use only four or five iterations in the implicit scheme.

As mentioned above, the technique of operator splitting is employed to model the energy transfer in the gas via radiation diffusion. Since the change in heat in a fluid element is given by  $dQ$ , the rate of energy flow due to radiation and viscous heating

(really turbulent magnetic stress) can be written:

$$\frac{dQ}{dt} = \frac{\partial \varepsilon}{\partial T} \frac{dT}{dt} = -\frac{1}{\rho} \frac{dq^z}{dz} + \frac{\bar{\alpha} p}{\rho}, \quad (5.79)$$

where  $\bar{\alpha}$  is the compact form of the  $\alpha$  parameter defined in equation (5.23), and in general we use  $\alpha = 0.1$ . Converting to the Lagrangian mass coordinate  $dm = \rho dz$  and linearizing  $T$ , equations (5.79) and (5.20) give a single, second-order diffusion equation (with a turbulent heating source) for the temperature:

$$\frac{dT}{dt} = \left( \frac{\partial \varepsilon}{\partial T} \right)^{-1} \left[ \frac{4ac}{3\kappa} \frac{d^2 T}{dm^2} + \frac{\bar{\alpha} p}{\rho} \right]. \quad (5.80)$$

In finite difference form, we have

$$T_{k+1/2}^{n+1} = T_{k+1/2}^n + \frac{\Delta t}{(\varepsilon_T)_{k+1/2}^n} \left[ \frac{4ac}{3\kappa} \frac{(T_{k+1/2}^n)^3}{\Delta m_{k+1/2}^2} (T_{k+3/2}^{n+1} - 2T_{k+1/2}^{n+1} + T_{k-1/2}^{n+1}) + \bar{\alpha} \frac{p_{k+1/2}^n}{\rho_{k+1/2}^n} \right] \quad (5.81)$$

where again the implicit scheme uses the temperatures at the future time step  $t^{n+1}$  on the right hand side. Equation (5.81) gives another tridiagonal set of linear equations that solve for  $T_{k+1/2}^{n+1}$ . In practice, for each time step, we solve this system first, then set  $T^n = T^{n+1}$  and solve for the new positions  $z_k^{n+1}$  with the adiabatic implicit hydrodynamics described above.

So far, we have followed a standard one-dimensional approach to the problem of radiation hydrodynamics. For the relativistic accretion disk inside the ISCO, we need to include a couple additional GR effects. First, the gravitational force given by the Riemann tensor in equation (5.66) must be determined in the local frame of a plunging geodesic particle, as in equation (5.17). The time coordinate  $t^n$  used throughout this Section is then the proper time as measured in this local tetrad.

Furthermore, due to the geodesic expansion of the gas inside the ISCO, the integrated surface density of the disk will fall off rapidly during the plunge. In other words, the ‘‘footprint’’ of a vertical column of gas at the ISCO will expand in area, while maintaining a constant mass. We model this expansion by varying the size of the mass element  $\Delta m_{k+1/2}$  for a column of unit area. From equation (5.54), we get

$$\Delta m_{k+1/2}(r) = \Delta m_{k+1/2}(r_{\text{ISCO}}) \exp\left[-\int_{r_{\text{ISCO}}}^r dr' \theta(r')/p^r\right], \quad (5.82)$$

thus modifying equation (5.67) to give the density

$$\rho_{k+1/2}^n = \frac{\Delta m_{k+1/2}(r^n)}{z_{k+1}^n - z_k^n}, \quad (5.83)$$

with  $r^n$  being the radial coordinate of the geodesic trajectory at proper time  $t^n$ . This “expanded” density is that which is actually used in equations (5.66) and (5.71).

Lastly, the viscous stress parameter  $\bar{\alpha}$  in equations (5.23, 5.79, and 5.80) should be modified to account for the geodesic shear  $s_{\hat{\phi}\hat{r}}$  inside the ISCO. However, we find that inside the ISCO, the rapid expansion of the gas and corresponding drop in the disk’s surface density and optical depth causes radiation diffusion to completely dominate over viscous heating in the plunge region. Thus we simply set  $\bar{\alpha}$  constant at the value it has at the ISCO. Numerically, we typically use a few hundred zones in the vertical direction, and achieve reasonable convergence for time steps of  $\Delta t \sim 100\Delta t_{\text{Courant}}$ , thus requiring  $\sim 10^3 - 10^4$  steps to plunge from the ISCO to the horizon.

Combining all the above results for the disk structure inside and outside the ISCO, we can now produce a full three-dimensional (axisymmetric) density and temperature profile for the relativistic  $\alpha$ -disk. Figure 5-3 shows the inner disk structure for a Schwarzschild black hole of mass  $10M_{\odot}$  and accretion rate  $0.02\dot{M}_{\text{Edd}}$ . Even with a significant stress at the ISCO, the gas plunges so rapidly inside the ISCO that the density and temperature fall off quickly in that region. However, while there is not significant thermal radiation emitted from inside the ISCO, the total optical depth to electron scattering is still greater than unity, suggesting that this inner region may still be quite important as an emitter of fluorescent iron lines (see Section 2.4.1).

Figure 5-4 shows the same density and temperature profiles, now for a Kerr black hole with spin  $a/M = 0.9$ . For the same Eddington-normalized accretion rate, the higher spin value leads to a denser, hotter disk. As the ISCO moves in to  $R_{\text{ISCO}} \approx 2.3M$ , the tidal gravity in the inner disk becomes stronger, maintaining hydrostatic equilibrium even for the higher radiation flux.

## 5.4 Observed Spectrum of the Disk

The net result of the previous three Sections is a complete three-dimensional description of the density, temperature, and velocity of the accretion disk everywhere outside the event horizon. From this tabulated set of data, we can then calculate the predicted spectral appearance of the accretion system with our ray-tracing post-processor. For a first approximation, we will again assume that electron scattering dominates the opacity for most of the disk and then consider a two-dimensional “photosphere” one optical depth below the surface of the disk. Given the temperature and density of the

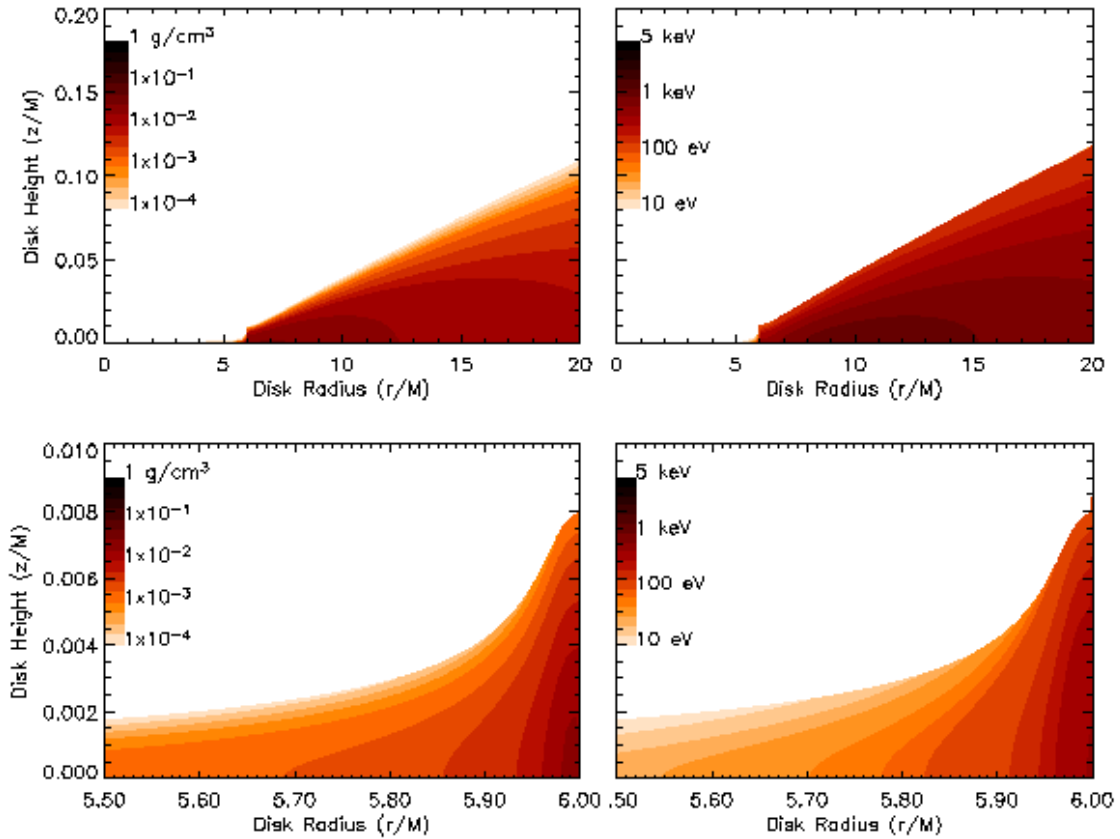


**Figure 5-3:** Top panels: density (left) and temperature (right) contours in the  $r - z$  plane for an axisymmetric  $\alpha$ -disk around a Schwarzschild black hole. Bottom panels: plunge region of the disk immediately inside the ISCO, matching  $l_{\text{plunge}} \approx l_{\text{turb}} \approx h$ . The black hole has mass  $10M_{\odot}$  and accretion rate  $0.02\dot{M}_{\text{Edd}}$ .

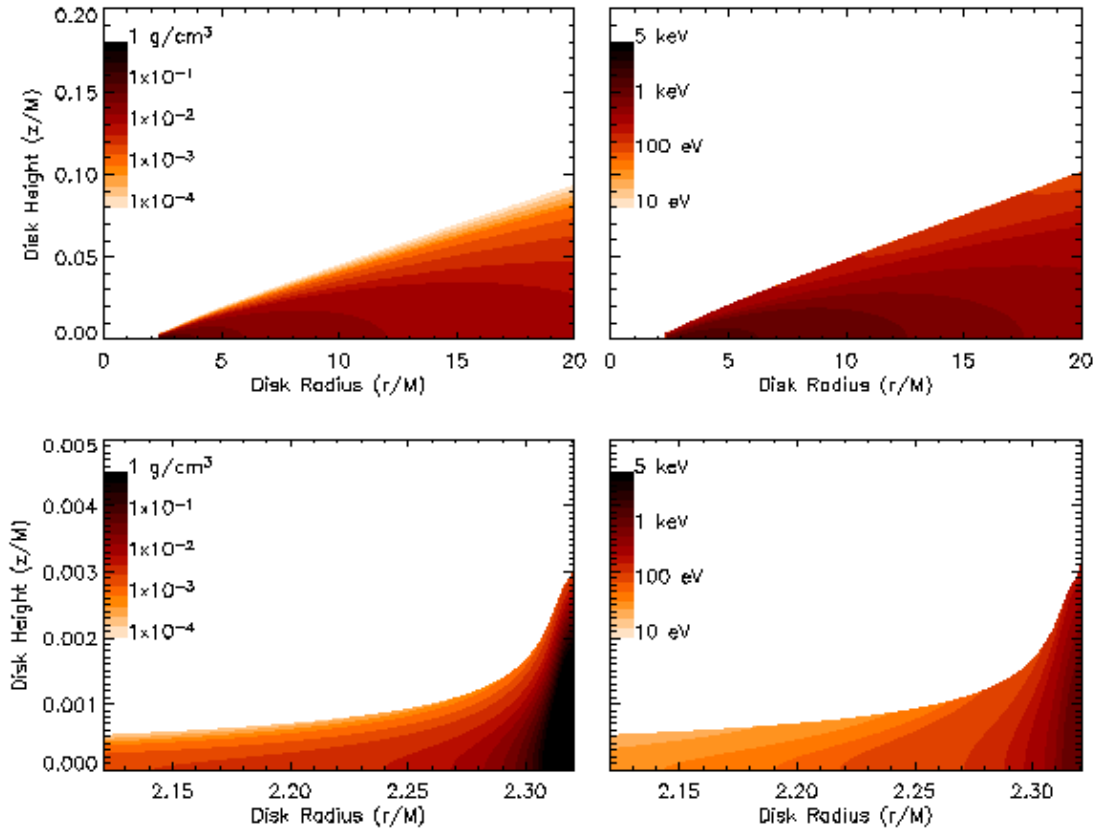


**Figure 5-4:** Top panels: density (left) and temperature (right) contours in the  $r - z$  plane for an axisymmetric  $\alpha$ -disk around a Kerr black hole with  $a/M = 0.9$ . Bottom panels: plunge region of the disk immediately inside the ISCO, matching  $l_{\text{plunge}} \approx l_{\text{turb}} \approx h$ . The black hole has mass  $10M_{\odot}$  and accretion rate  $0.02\dot{M}_{\text{Edd}}$ .

disk at the photosphere, a modified blackbody spectrum for the radiation is derived by Zeldovich & Shakura (1969) for an exponential atmosphere and Shakura (1972) and Felten & Rees (1972) for a constant density atmosphere.

While the forms of these modified spectra were presented above in Section 5.1.2, we repeat them here in more detail. In the approximation of a homogeneous, isothermal atmosphere with density  $\rho_s$  and temperature  $T_s$ , the emitted flux is given by

$$F_\nu = \pi B_\nu \left( \frac{\kappa_\nu^{\text{ff}}}{\kappa_{\text{es}}} \right)^{1/2}. \quad (5.84)$$

The term  $(\kappa_\nu^{\text{rff}}/\kappa_{\text{es}})^{1/2}$  is due to the modified path length of a photon that takes a random walk through a medium dominated by electron scattering [for a detailed derivation, see e.g. Shapiro & Teukolsky (1983)]. Here  $B_\nu$  is the blackbody brightness with units of  $[\text{erg sec}^{-1} \text{ cm}^{-2} \text{ Hz}^{-1} \text{ ster}^{-1}]$ :

$$B_\nu(T) \equiv \frac{2h\nu^3/c^2}{\exp(h\nu/k_B T) - 1} = \frac{2k_B^3 T^3}{h^2 c^2} \frac{x^3}{e^x - 1} \quad (5.85)$$

and  $\kappa_\nu^{\text{ff}}$  is the opacity for free-free absorption, for which we use Kramer's law with (Shapiro & Teukolsky, 1983)

$$\kappa_\nu^{\text{ff}} = 1.5 \times 10^{25} \rho_s T_s^{-7/2} x^{-3} (1 - e^{-x}) \text{ cm}^2/\text{g}, \quad (5.86)$$

where we have defined the dimensionless parameter  $x \equiv h\nu/kT$ . Now equation (5.84) becomes

$$F_\nu = 2.56 \times 10^{-3} \rho_s^{1/2} T_s^{5/4} \frac{x^{3/2} e^{-x/2}}{(e^x - 1)^{1/2}}. \quad (5.87)$$

For the exponential atmosphere with scale height  $H$ , we have a slightly different form:

$$F_\nu = \pi B_\nu \left( \frac{\kappa_\nu^{\text{ff}}}{\kappa_{\text{es}}^2 \rho H} \right)^{1/3}. \quad (5.88)$$

The scale height can be determined from equation (5.28) as

$$H = \frac{2k_B T_s}{m_p \mathcal{R} h_{\text{disk}}}, \quad (5.89)$$

giving the modified spectrum

$$F_\nu = 3.5 \times 10^{-10} (\mathcal{R} h_{\text{disk}})^{1/3} T_s^{3/2} \frac{x^2 e^{-x/3}}{(e^x - 1)^{2/3}}. \quad (5.90)$$

Given the emitted spectrum from each surface element of the disk, we use the ray-tracing code of Chapter 2 to calculate the effects of redshift and gravitational lensing to a distant observer (Schnittman & Bertschinger, 2004a). As described there, the photon trajectories are traced backwards in time from the observer with initial energy  $E_{\text{obs}} = -p_t$ . The redshift from the point of the emitter to the observer is calculated by

$$\frac{E_{\text{obs}}}{E_{\text{em}}} = \frac{p_\mu(\mathbf{x}_{\text{obs}})v^\mu(\mathbf{x}_{\text{obs}})}{p_\mu(\mathbf{x}_{\text{em}})v^\mu(\mathbf{x}_{\text{em}})},$$

where for a distant observer at  $r \rightarrow \infty$ , we take  $v^\mu(\mathbf{x}_{\text{obs}}) = [1, 0, 0, 0]$ . Lorentz invariance of  $I_\nu/\nu^3$  along a photon bundle gives the observed spectral intensity:

$$I_\nu(\text{obs}) = I_\nu(\text{em}) \frac{\nu_{\text{obs}}^3}{\nu_{\text{em}}^3}.$$

Taking  $v^\mu(\mathbf{x}_{\text{em}})$  as the velocity of a planar geodesic trajectory and assuming an isotropic emitter  $I_\nu(\text{em}) = F_\nu/\pi$ , the observed spectrum is the sum of the redshifted spectra from each individual path (pixel) ray-traced from the observer. As we see from Figures 5-1 to 5-4, the steady-state  $\alpha$ -disks for  $M = 10M_\odot$  are quite thin, with  $h/r \lesssim 0.02$  in the inner disk. This allows us to use the simple transfer function of Section 2.4.1 to calculate the total disk spectrum. Our job is made even easier because the spectrum at each radius in the disk is a function only of the atmospheric temperature and scale height at that point in the disk. The observed temperature is simply scaled by the transfer function redshift (much like the cosmological redshift scales the apparent blackbody temperature of receding stars and background radiation), allowing us to integrate over the image plane quite easily. This follows the approach of Hubeny et al. (2000, 2001), who also include non-LTE transfer in the atmosphere to model the Lyman- $\alpha$  line in AGN.

The resulting modified blackbody spectra are shown in Figure 5-5 for a variety of black hole parameters, with  $M = [5, 10, 15]M_\odot$ ,  $a/M = [0, 0.5, 0.9]$ , and  $i = [0^\circ, 45^\circ, 80^\circ]$ . The disk-integrated spectra are characterized by a low energy rise with  $I_\nu \propto \nu$ , followed by a broad thermal peak around  $0.5 - 2$  keV, and a steep cutoff around 10 keV, consistent with many of the ‘‘Thermal-Dominant’’ state spectra observed with *RXTE* (McClintock & Remillard, 2004). The specific location of the peak  $E_{\text{max}}$  is most sensitive to the black hole’s mass and accretion rate, scaling roughly like the surface temperature given in NT:

$$E_{\text{max}} \sim \alpha^{2/9} \left( \frac{M}{M_\odot} \right)^{-2/9} \left( \frac{\dot{M}}{\dot{M}_{\text{Edd}}} \right)^{8/9}. \quad (5.91)$$



**Table 5.2:** Ratio of  $E_{\text{cut}}/E_{\text{max}}$  for relativistic  $\alpha$ -disks for a range of black hole masses  $5 \leq (M/M_{\odot}) \leq 20$  and luminosities  $0.01 \leq (L/L_{\text{Edd}}) \leq 0.2$ . The “errors” quoted are the typical variation of this ratio over the sample of masses and luminosities.

Inclination ( $^{\circ}$ )	BH Spin ( $a/M$ )		
	0	0.5	0.9
0	$12.3 \pm 0.1$	$13.6 \pm 0.3$	$16.4 \pm 0.8$
45	$14.5 \pm 0.1$	$16.9 \pm 0.3$	$22.7 \pm 1.0$
80	$15.8 \pm 0.1$	$18.9 \pm 0.2$	$27.9 \pm 0.8$

This relationship may prove very useful in identifying ultra-luminous X-ray sources as intermediate-mass black holes (Terashima & Wilson, 2004; Miller, Fabian, & Miller, 2004), but for a given black hole mass and Eddington accretion rate, there appears to be relatively little dependence on spin for this peak energy.

However, if we are able to measure both the peak location and the cutoff energy, then it is possible the ratio may be used to determine the black hole spin. Defining  $E_{\text{cut}}$  as the point where the intensity  $I_{\nu}(E_{\text{cut}})$  is a factor of  $10^5$  smaller than  $I_{\nu}(E_{\text{max}})$ , we find that  $E_{\text{cut}}/E_{\text{max}}$  is relatively insensitive to the black hole mass and accretion rate. Over a range of masses  $5 \leq (M/M_{\odot}) \leq 20$  and luminosity  $0.01 \leq (L/L_{\text{Edd}}) \leq 0.2$ , this ratio appears to be a function primarily of black hole spin and disk inclination. Table 5.2 shows the mean values for this ratio for a few different spins and inclination angles, along with the typical scatter over the mass/luminosity sample. If the inclination is known from optical radial velocity curves or broadened iron emission lines, then by measuring the ratio  $E_{\text{cut}}/E_{\text{max}}$ , the spin may be inferred from Table 5.2. However, there may be significant observational challenges to this technique: as we will see in Chapter 6, even in the Thermal-Dominant spectral state, there is typically still a small power-law component to the high-energy part of the photon spectrum. This power-law tail will make it more difficult to accurately measure the cut off energy  $E_{\text{cut}}$ , but even this tail may be modeled by the scattering calculations described there, and possibly might even make this approach more feasible.

Despite the apparent promise of this technique, there are also a number of systematic errors involved in arriving at these predicted spectra, not the least of which is the entire premise of an  $\alpha$ -based stress/viscosity. Even with our self-consistent treatment of the ISCO boundary conditions to apply a non-zero torque to the inner disk, the density and temperature profiles still do not agree qualitatively with global MHD simulations. Thus we may be seriously “under-weighting” the emission inside the ISCO. Future work on this subject should attempt to incorporate the magneto-

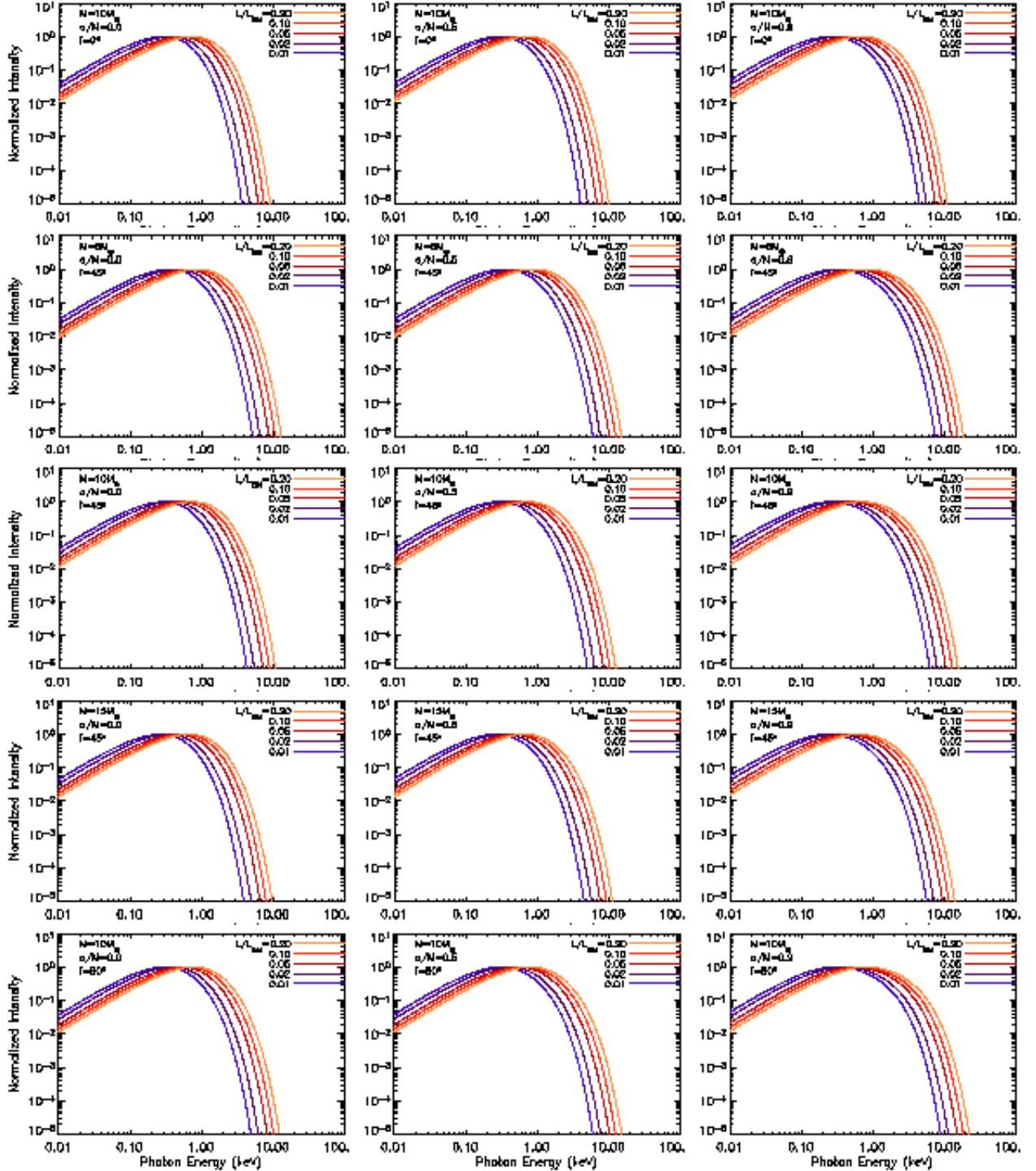


**Figure 5-5:** Sample of normalized photon energy spectra produced by steady-state  $\alpha$ -disks for a variety of black hole masses, spins, and inclinations. For each case, a range of Eddington-scaled luminosities are shown. The peak energy  $E_{\max}$  scales as in equation (5.91) while the ratio  $E_{\text{cut}}/E_{\max}$  is sensitive to the spin and inclination angle.

rotational instability as the driving force behind angular momentum transport in the disk, especially the inner regions where the majority of energy is released.

Furthermore, to completely match the X-ray spectra from black holes in the Thermal-Dominant state, one must also include a small high-energy power-law component (McClintock & Remillard, 2004). It is likely that this high-energy tail is caused by the Compton upscattering of thermal photons through a hot, low-density electron corona above the disk. In the next Chapter, we introduce a Monte-Carlo code to calculate the effect of this scattering on the continuum photon spectra.



# Chapter 6

## Electron Scattering

*If we knew what it was we were doing, it would not be called research, would it?*

*I am convinced that God does not play dice with the universe.*

-Albert Einstein

As we saw in a simplified model in Chapter 4, the scattering of hot spot photons off of coronal electrons will have a significant effect on the shape of the observed light curves. As mentioned in the discussion there, many of the important aspects of the scattering physics were ignored in the basic model in the interest of deriving an analytic solution. In this Chapter we develop a more sophisticated Monte Carlo model that reproduces many of the same qualitative features of the simple model, while also introducing a number of new physics predictions.

### 6.1 Physics of Scattering

#### 6.1.1 Classical Electron Scattering

To begin with, we present here a review of the classical scattering of a plane electromagnetic wave incident on an electron at rest, as derived in Rybicki & Lightman (1979). In the low-energy limit with  $h\nu \ll m_e c^2$ , the electric field of the incoming photon will cause the electron to oscillate with a velocity  $v \ll c$  in the direction of the polarization axis of the EM wave. The force on the electron will be

$$\mathbf{F} = e\epsilon E_0 \sin \omega_0 t, \tag{6.1}$$

where  $\epsilon$  is the direction of the electric field  $E_0$  for a plane-polarized wave oscillating at angular frequency  $\omega_0 = 2\pi\nu$ . In response to this incident wave, the electron will produce a time-varying dipole moment  $\mathbf{d}$ :

$$\mathbf{d} = e\mathbf{r} = - \left( \frac{e^2 E_0}{m_e \omega_0^2} \right) \epsilon \sin \omega_0 t. \quad (6.2)$$

Such a dipole will produce a radiation field with time-averaged power

$$\frac{dP}{d\Omega} = \frac{e^4 E_0^2}{8\pi m_e^2 c^3} \sin^2 \Theta, \quad (6.3)$$

where  $\Theta$  is the polar angle measured with respect to the polarization (dipole) vector, as shown in Figure 6-1. Assuming that the incident flux  $\langle S \rangle = E_0^2(c/8\pi)$  is entirely re-radiated by the dipole, we can define the differential cross section for polarized radiation:

$$\frac{dP}{d\Omega} = \frac{cE_0^2}{8\pi} \left( \frac{d\sigma}{d\Omega} \right)_{\text{pol}}, \quad (6.4)$$

or

$$\left( \frac{d\sigma}{d\Omega} \right)_{\text{pol}} = r_0^2 \sin^2 \Theta. \quad (6.5)$$

Here the classical electron radius  $r_0$  is given by

$$r_0 = \frac{e^2}{m_e c^2} = 2.82 \times 10^{-13} \text{ cm}. \quad (6.6)$$

While equation (6.5) gives the cross section for radiation polarized in the plane of the page in Figure 6-1, we can also use it to calculate the average cross section for unpolarized radiation. Since unpolarized radiation is really just the linear combination of two oppositely polarized waves, we can calculate the unpolarized cross section by averaging the cross sections for perpendicular polarization vectors. The geometry for such a system is shown in Figure 6-2: an incident wave  $\mathbf{k}_i$  is scattered into  $\mathbf{k}_f$ , with final polarization in the same plane as  $\mathbf{k}_f$  and the initial polarization  $\epsilon_i$ . The initial polarization is either in the same plane as the two wave vectors ( $\epsilon_1$ ) or perpendicular to that plane ( $\epsilon_2$ ).

The probability of scattering into  $\mathbf{k}_f$  from an initial polarization of  $\epsilon_1$  is the same as in equation (6.5), since that is the same geometry as in Figure 6-1. If the initial polarization is  $\epsilon_2$ , then we can again use equation (6.5), evaluated at the perpendicular scattering angle  $\Theta = \pi/2$ . The cross section for unpolarized radiation is then given

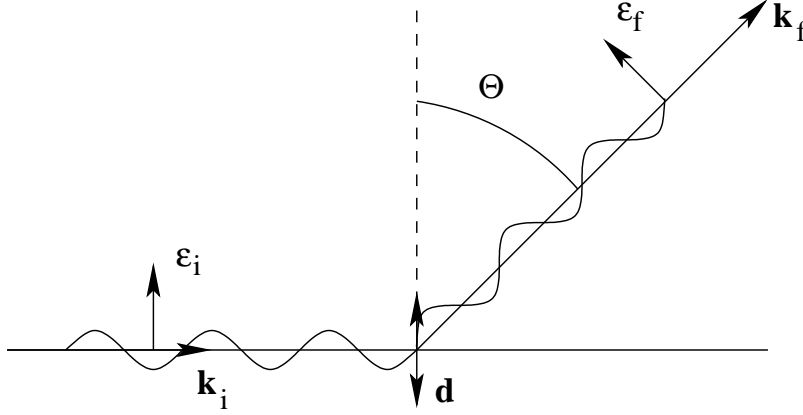


**Figure 6-1:** Planar geometry of a plane-parallel wave of electromagnetic radiation  $\mathbf{k}_i$  incident on an electron at rest at the origin. The incident wave has (vertical) linear polarization in the plane of the page, denoted by  $\epsilon_i$ . The wave scatters at an angle  $\Theta$  with respect to the dipole  $\mathbf{d}$ , which is parallel to  $\epsilon_i$ . The scattered wave vector  $\mathbf{k}_f$  is not necessarily in the plane of the page, but must be in the same plane as the final polarization  $\epsilon_f$  and  $\mathbf{d}$ .

by the average of the two polarized cross sections:

$$\begin{aligned}
 \left(\frac{d\sigma}{d\Omega}\right)_{\text{unpol}} &= \frac{1}{2} \left[ \left(\frac{d\sigma(\Theta)}{d\Omega}\right)_{\text{pol}} + \left(\frac{d\sigma(\pi/2)}{d\Omega}\right)_{\text{pol}} \right] \\
 &= \frac{1}{2} r_0^2 (1 + \sin^2 \Theta) \\
 &= \frac{1}{2} r_0^2 (1 + \cos^2 \theta)
 \end{aligned} \tag{6.7}$$

For the rest of the results in this chapter, we will restrict ourselves to this cross section for nonrelativistic, unpolarized scattering. In future work, we hope to include a more formal treatment of the covariant scattering of polarized light (Portsmouth & Bertschinger, 2004a,b).

It is important to note that when we say “nonrelativistic,” this is a reference to the *photon* energy, not the electron energy. In the electron rest frame, we require  $h\nu \ll m_e c^2$  in order for the above cross sections to be valid, in which case the scattering is nearly elastic or *coherent*. For higher energy photons, the scattering involves quantum effects and requires the “Klein-Nishina” cross section [see e.g. Heitler (1954)]. Since we are primarily interested in the scattering of photons from a relatively cool thermal accretion disk ( $h\nu \sim 1 - 5$  keV), the classical treatment should suffice.

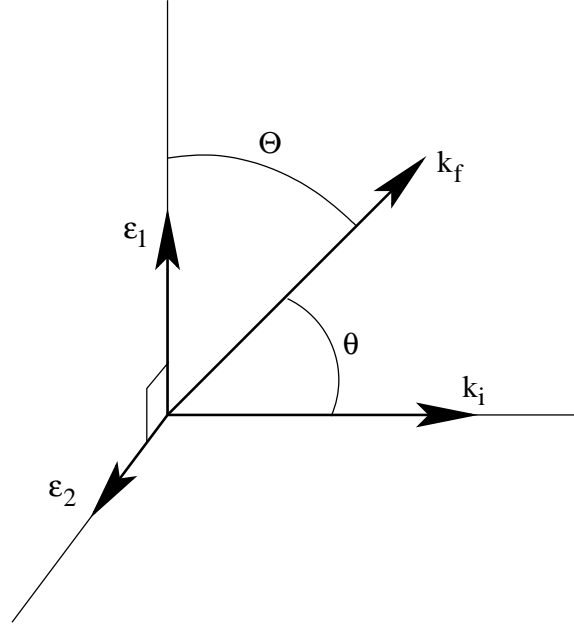


**Figure 6-2:** Scattering geometry for unpolarized radiation incident on an electron at rest. The incoming radiation is made up of a combination of two different linear polarizations  $\epsilon_1$  and  $\epsilon_2$ . The scattered radiation  $\mathbf{k}_f$  is in the plane of  $\mathbf{k}_i$  and  $\epsilon_1$ , with  $\Theta + \theta = 90^\circ$ .

Even though we treat the scattering as coherent in the electron frame, in the lab frame energy can be (and often is) transferred from the electron to the photon. To see this boosting effect, consider a photon with initial energy  $\varepsilon_i$  scattering off an electron with velocity  $\beta$  in the  $x$ -direction in the “lab frame”  $K$ . In this frame, the angle between the incoming photon and electron velocity is  $\theta$ . In the electron rest frame  $K'$ , the photon is scattered at an angle  $\theta'$  with respect to the  $x'$ -axis. The Doppler shift formula gives (Rybicki & Lightman, 1979):

$$\begin{aligned}\varepsilon'_i &= \varepsilon_i \gamma (1 - \beta \cos \theta) \\ \varepsilon_f &= \varepsilon'_f \gamma (1 + \beta \cos \theta'),\end{aligned}\tag{6.8}$$

where  $\gamma = 1/\sqrt{1 - \beta^2}$  and  $\varepsilon_f$  is the post-scattering energy in the lab frame. In the electron frame, we assume elastic scattering with  $\varepsilon'_i = \varepsilon'_f$ , which should be the case for the typical seed photons from a thermal emitter at  $T_{\text{em}} \sim 1$  keV.

Averaging over all angles  $\theta$  (isotropic) and  $\theta'$  (weighted by eqn. 6.7), we find that



the typical scattering event boosts the photon energy by

$$\frac{\varepsilon_f}{\varepsilon_i} \approx \gamma^2. \quad (6.9)$$

For scattering electrons with a thermal velocity distribution around  $T_e$ , this factor can be written

$$\gamma^2 \approx \left(1 - \frac{2kT_e}{m_e c^2}\right)^{-1} \approx 1.6 \quad \text{for } T_e \approx 100 \text{ keV}. \quad (6.10)$$

To be more precise, we consider a Maxwell-Boltzmann distribution function in electron momentum  $p = \gamma m v$ :

$$f(p) d^3 \mathbf{p} \propto 4\pi p^2 \exp\left(-\frac{\sqrt{p^2 c^2 + m_e^2 c^4}}{kT_e}\right). \quad (6.11)$$

For highly relativistic velocities ( $\gamma \gg 1$ ), the distribution is replaced by the *Juttner distribution*, which involves more complicated terms including a modified Bessel function of the second kind (Melrose & Gedalin, 1999). For the moderate velocities corresponding to  $T_e \lesssim 100$  keV, equation (6.11) is accurate enough for our purposes.

### 6.1.2 General Relativistic Implementation

As was emphasized in Chapter 2, many of the classical results of radiation transport physics can be easily applied to general relativistic fluids when considered in the appropriate reference frame. Here too, we can split the problem into two basic pieces: the ray-tracing of photons in curved space, an inherently general relativistic process, and the scattering of these low-energy photons off of hot electrons, a purely classical process in the electron frame. However, unlike the approach taken in Chapter 2, where the photons were traced backwards in time from a distant observer to the emitting region, here it is conceptually easier to trace the photons *forward* in time from the emitter to the observer, then use Monte Carlo methods to determine the distribution of scattered photons.

This Monte Carlo approach has its trade-offs: a vastly larger number of photons must be traced in order to “observe” enough at the detector to produce a reasonable image or spectrum. But all those photons that do not reach the detector need not be wasted. Consider an enormous spherical shell detector at large  $r$  covering the entire sky surrounding the black hole. For hot spots on circular orbits, any emitted photon can be mapped in azimuth from its intersection with the theoretical detector to the “real” observer by rotating the photon back in time. Let the ray-traced photon

emitted at spacetime coordinates  $(t_0, \phi_0)$  hit the sphere at  $(t_1, \phi_1)$ , while the observer is located at  $\phi_{\text{obs}}$ . If the emitter has an orbital period of  $T_{\text{orb}}$  as measured in coordinate time, then the same identical photon could have come from the emitter at  $(t'_0, \phi'_0)$ , with

$$\begin{aligned} t_0 - t'_0 &= t_1 - t_{\text{obs}}, \\ \phi_0 - \phi'_0 &= \phi_1 - \phi_{\text{obs}} \end{aligned} \quad (6.12)$$

and

$$t_{\text{obs}} = t_1 - \frac{\phi_1 - \phi_{\text{obs}}}{\Omega_\phi} = t_1 - \frac{T_{\text{orb}}}{2\pi}(\phi_1 - \phi_{\text{obs}}). \quad (6.13)$$

In this way, every photon is essentially detected at the same location in azimuth with the appropriate time delay, which in turn can be used for calculating the light curve and dynamic spectrum of the emitter. Since the orbital geometry lacks rotational symmetry in the  $\mathbf{e}_\theta$  direction, we cannot produce a similar mapping in latitude. But all is not lost—by dividing the detector into equally spaced slices in  $\cos\theta$ , a single Monte Carlo computation produces simulated data at all viewer inclinations simultaneously. So in the end, every ray-traced photon contributes equally to the light curve and spectrum (except of course those photons that get captured by the black hole, but even they contribute indirectly by their absence).

Unlike the approach in Chapter 2, where the Lorentz invariant  $I_\nu/\nu^3$  was used to appropriately handle relativistic beaming, when we begin in the emitter's rest frame, the beaming is introduced automatically by the reference frame transformations. The photons here should be thought of primarily as particles, and not the continuous beams we envisioned for the radiative transfer equation in Section 2.2.2. However, because of the coherent scattering assumption, the ray-traced path of each photon is energy-independent, so the photon's final observed energy can be thought of as a fiducial redshift  $E_{\text{obs}}/E_{\text{em}}$  that can be convolved with the spectrum in the local emitter frame to produce the total spectrum seen by the observer [see caveats below following equation (6.31)].

To get the initial coordinate momentum of each photon, we construct a tetrad centered on the emitter's rest frame, denoted by tilde indices  $\tilde{\mu}$ . Then  $\mathbf{e}_{\tilde{t}}$  is parallel to the emitter's 4-velocity  $p^\mu(\text{em})$ ,  $\mathbf{e}_{\tilde{r}}$  and  $\mathbf{e}_{\tilde{\phi}}$  are in the coordinate directions  $\mathbf{e}_r$  and  $\mathbf{e}_\theta$ , and  $\mathbf{e}_{\tilde{\phi}}$  is given by orthogonality. Recall from Section 2.4.1 the expressions for the energy and angular momentum of a particle on a stable circular orbit around a Kerr black hole:

$$-p_t = \frac{r^2 - 2Mr \pm a\sqrt{Mr}}{r(r^2 - 3Mr \pm 2a\sqrt{Mr})^{1/2}} \quad (6.14)$$

and

$$p_\phi = \pm \frac{\sqrt{Mr}(r^2 \mp 2a\sqrt{Mr} + a^2)}{r(r^2 - 3Mr \pm 2a\sqrt{Mr})^{1/2}}. \quad (6.15)$$

From these we construct the 4-velocity via the inverse metric  $p^\mu(\text{em}) = g^{\mu\nu}p_\nu(\text{em})$ , which gives  $\mathbf{e}_{\tilde{t}}$ . In Boyer-Lindquist coordinates,  $\mathbf{e}_{\tilde{r}}$  and  $\mathbf{e}_{\tilde{\theta}}$  are trivially normalized as in the ZAMO basis [eqns. (2.48b) and (2.48c)]. Writing

$$\mathbf{e}_{\tilde{\phi}} = A\mathbf{e}_t + B\mathbf{e}_\phi, \quad (6.16)$$

the orthonormality conditions are

$$\mathbf{e}_{\tilde{t}} \cdot \mathbf{e}_{\tilde{t}} = (p^t)^2 g_{tt} + 2p^t p^\phi g_{t\phi} + (p^\phi)^2 g_{\phi\phi} = -1, \quad (6.17a)$$

$$\mathbf{e}_{\tilde{t}} \cdot \mathbf{e}_{\tilde{\phi}} = Ap^t g_{tt} + (Ap^\phi + Bp^t)g_{t\phi} + Bp^\phi g_{\phi\phi} = 0, \quad (6.17b)$$

$$\mathbf{e}_{\tilde{\phi}} \cdot \mathbf{e}_{\tilde{\phi}} = A^2 g_{tt} + 2ABg_{t\phi} + B^2 g_{\phi\phi} = 1. \quad (6.17c)$$

Novikov & Thorne (1973) give analytic expressions for the emitter's tetrad basis in terms of the functions defined in Section 5.1:

$$\mathbf{e}_{\tilde{t}} = \frac{\mathcal{B}}{\mathcal{C}^{1/2}}\mathbf{e}_t + \frac{M^{1/2}}{r^{3/2}\mathcal{C}^{1/2}}\mathbf{e}_\phi, \quad (6.18a)$$

$$\mathbf{e}_{\tilde{r}} = \sqrt{\frac{\Delta}{\rho^2}}\mathbf{e}_r, \quad (6.18b)$$

$$\mathbf{e}_{\tilde{\theta}} = \sqrt{\frac{1}{\rho^2}}\mathbf{e}_\theta, \quad (6.18c)$$

$$\mathbf{e}_{\tilde{\phi}} = \frac{\mathcal{F}M^{1/2}}{(r\mathcal{C}\mathcal{D})^{1/2}}\mathbf{e}_t + \frac{\mathcal{B}\mathcal{D} + r^{1/2}\mathcal{A}\mathcal{F}M^{1/2}}{r\mathcal{A}\mathcal{D}\mathcal{C}^{1/2}}\mathbf{e}_\phi. \quad (6.18d)$$

In this basis, the initial photon direction is picked randomly from an isotropic distribution, uniform in spherical coordinates  $\cos\tilde{\theta} = [-1, 1]$  and  $\tilde{\phi} = [0, 2\pi)$ . All photons are given the same initial energy in the emitter frame  $p_{\tilde{t}} = -E_0$ , which is used as a reference energy for calculating the final redshift with respect to a stationary observer at infinity. From the basis vectors  $\mathbf{e}_{\tilde{\mu}}$  we construct a transformation matrix  $E_{\tilde{\mu}}^\mu$  as in Section 2.2.1 to get the initial conditions for ray-tracing in the coordinate basis  $p^\mu = E_{\tilde{\mu}}^\mu p^{\tilde{\mu}}$ .

Given  $p_\mu = g_{\mu\nu}p^\nu$ , the photon's geodesic trajectory is simply integrated using the Hamiltonian formulation according to equations (2.4a) and (2.4b). Figure 6-3 shows an “overhead view” of photon trajectories in the plane of the disk, emitted isotropically by a massive test particle on a circular orbit at the ISCO. Figure 6-3a shows a black hole with  $a/M = 0.5$  and Figure 6-3b has  $a/M = 0.99$ . The photons are

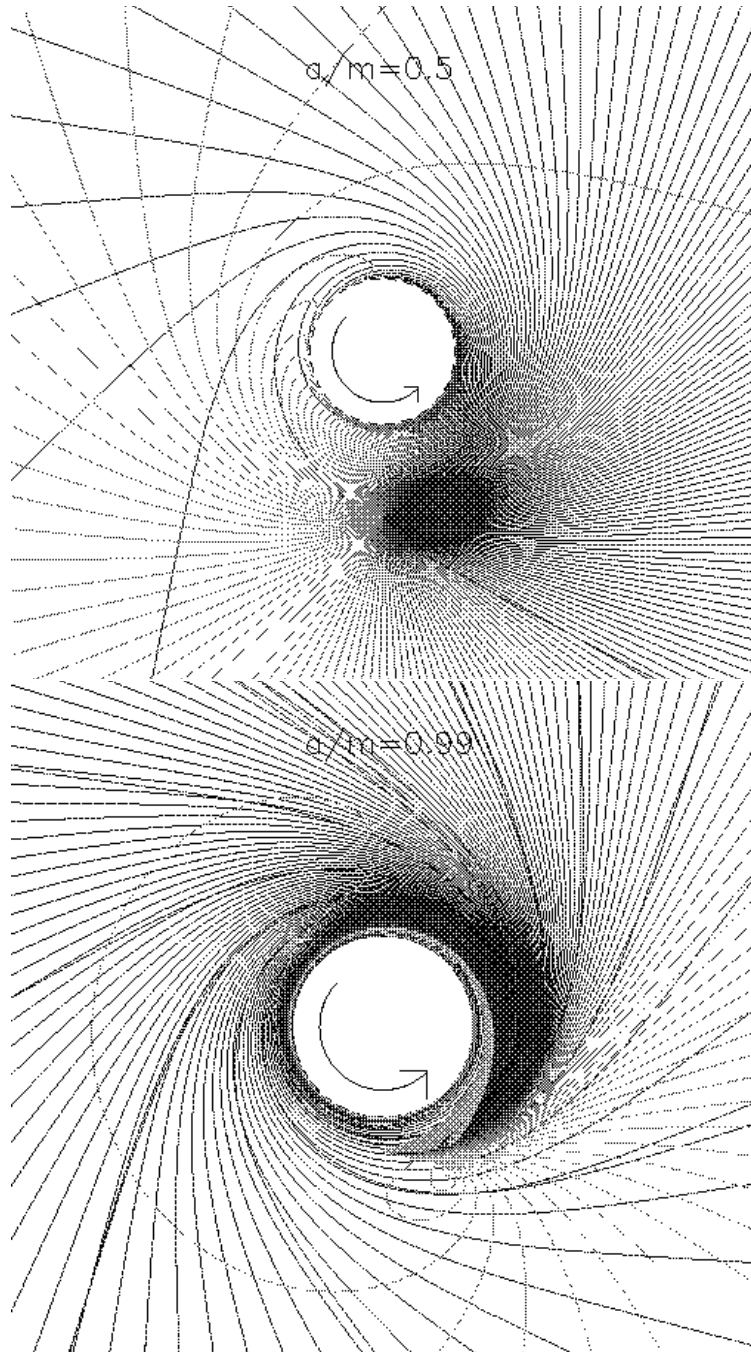


**Figure 6-3:** Planar photons emitted isotropically in the rest frame of a massive particle on a circular orbit at the ISCO. The black hole has spin  $a/M = 0.5$  (top) and  $a/M = 0.99$  (bottom). The photon paths are colored according to their red- or blue-shift in energy with respect to  $E_0$  measured in the emitter's frame. For the black hole with  $a/M = 0.99$ , the ISCO is located inside the ergosphere, so all photons are forced to move forward in  $\phi$ , and some are even created with negative energies ( $p_t > 0$ ).

colored according to their energy-at-infinity  $E_\infty = -p_t$ , either blue- or redshifted with respect to their energy in the emitter frame  $E_0$ . For the black hole with  $a/M = 0.99$ , the ISCO is located inside the ergosphere, so all photons are forced to move forward in  $\phi$ , and some are even created with negative energies ( $p_t > 0$ ). As mentioned above, the relativistic beaming is done automatically by the Lorentz boost from the emitter to the coordinate (or ZAMO) frame, so the blue photons are clearly bunched more tightly together, as required by the invariance of  $I_\nu/\nu^3$ .

As in Chapter 2, the photon's position and momentum are tabulated at each step along its path. However, now we have to check at each interval to see if the photon scatters off an electron. Conveniently, the Runge-Kutta algorithm takes shorter steps as smaller  $r$ , where the electron density tends to be highest, so we can reliably use the differential formula for the optical depth to electron scattering:

$$d\tau_{\text{es}} = \kappa_{\text{es}} \rho ds. \quad (6.19)$$

The density  $\rho$  is defined in the ZAMO frame and the opacity  $\kappa_{\text{es}}$  is given by the classical cross section derived above in equation (6.7)

$$\kappa_{\text{es}} = \frac{\sigma_T}{m_p} = \frac{8\pi}{3} \frac{r_0^2}{m_p} = 0.4 \text{ cm}^2/\text{g}. \quad (6.20)$$

The proper distance  $ds$  in equation (6.19) is calculated from the path segment  $dx_i^{\hat{\mu}}$  as in equation (2.67). For relatively small steps, the probability of scattering after each step is given by  $d\tau_{\text{es}} \lesssim 0.1$ .

If the photon does in fact experience a scattering event, we first transform into the ZAMO basis, where the electron temperature is defined. Given the electron temperature, we assume an isotropic distribution of velocities as defined in equation (6.11), and pick an electron 4-velocity with random direction in that basis. Next we must transform to the electron rest frame, in which the photon scatters according to the Thomson cross section from equation (6.7), reducing a difficult problem in curved spacetime to a simple classical problem with a single variable—the scattering angle  $\theta$ . This set of transformations from coordinate basis to ZAMO basis to electron rest frame is shown schematically in Figure 6-4 (again the ZAMO basis is denoted by  $\hat{\mu}$  subscripts, and the electron frame by  $\tilde{\mu}$ , not to be confused with the emitter frame defined earlier).

The transformation from the ZAMO basis to the electron frame is defined by a Lorentz boost in the direction of the electron 4-velocity  $u^{\hat{\mu}} \rightarrow \mathbf{e}_{\tilde{x}}$ . Since the scattering probability is symmetric around this axis, the rotational degree of freedom that fixes the other spatial axes  $\mathbf{e}_{\tilde{y}}$  and  $\mathbf{e}_{\tilde{z}}$  is completely arbitrary. One convenient form of the

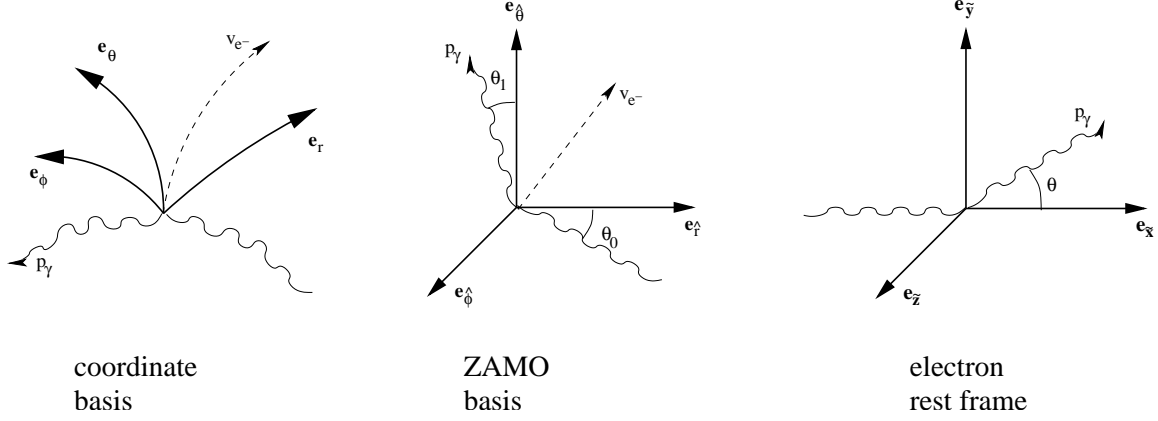


**Figure 6-4:** Schematic picture of coordinate transformations from the coordinate basis  $e_\mu$  in which the geodesic trajectories are integrated, to the ZAMO basis  $e_{\hat{\mu}}$  in which the electron density and temperature are defined, to the electron rest frame basis  $e_{\tilde{\mu}}$  in which the electron scattering angle  $\theta$  is given simply by the Thomson cross section for unpolarized radiation.

generalized Lorentz boost is given by Misner, Thorne, & Wheeler (1973):

$$\begin{aligned}
 u^\mu &= [\gamma, \beta n^j] \quad (|n| = 1), \\
 \Lambda_t^{t'} &= \gamma, \\
 \Lambda_j^{t'} &= \Lambda_t^{j'} = -\beta\gamma n^j, \\
 \Lambda_k^{j'} &= \Lambda_j^{k'} = (\gamma - 1)n^j n^k + \delta^{jk}.
 \end{aligned} \tag{6.21}$$

The photon momentum in the electron frame is thus given by  $p^{\tilde{\mu}} = \Lambda_{\hat{\mu}}^{\tilde{\mu}} p^{\hat{\mu}}$ .

All that is left to do is calculate the scattering angle  $\theta$ . Most portable random number generators produce a random variable  $X$  uniformly distributed in the range  $[0, 1]$ , and from this we must produce a random variable  $\theta$  with distribution according to equation (6.7). The cross section can be re-written in terms of the normalized probability distribution function

$$f(\theta)d\theta = \frac{3}{2} \sin\theta(1 + \cos^2\theta)d\theta \tag{6.22a}$$

or defining  $z \equiv \cos\theta$ ,

$$f(z)dz = \frac{3}{8}(1 + z^2)dz. \tag{6.22b}$$

Let  $g(z)$  be the cumulative distribution function

$$g(z) = \int_{-1}^z f(z') dz' \quad (6.23)$$

so that  $g(-1) = 0$  and  $g(1) = 1$ . Then given a uniformly distributed  $X$ , we can solve for  $z = g^{-1}(X)$ . Unfortunately, this involves finding the roots to the cubic equation

$$z^3 + 3z + 4 - 8X = 0. \quad (6.24)$$

While not trivial, the solution to (6.24) is at least unique [ $g(z)$  has no turning points] and can be written in closed form (Zwillinger et al., 1996). After picking a random 3-vector  $\tilde{p}_\perp^j$  perpendicular to  $\tilde{p}^j$  (with the same magnitude  $|\tilde{p}_\perp^j| = |\tilde{p}^j| = -\tilde{p}^0$ ), we construct the 4-vector of the scattered photon:

$$p_f^\mu = [p^0, \cos \theta \tilde{p}^j + \sin \theta \tilde{p}_\perp^j]. \quad (6.25)$$

$p_f^\mu$  is then transformed back to the ZAMO basis with a boost by  $-u^\mu$ , then to the coordinate basis, and then we continue with integrating the new geodesic trajectory until the next scattering event or detection by a distant observer.

## 6.2 Effect on Spectra

As we showed at the end of the Section 6.1.1, the net effect of this whole procedure is generally a transfer of energy from the electron to the photon. One way to quantify this energy transfer is through the Compton  $y$  parameter, defined as the average fractional energy change per scattering, times the number of scatterings through a finite medium. For nonrelativistic electrons, Rybicki & Lightman (1979) show that the average energy transfer per scattering event is

$$\frac{\varepsilon_f - \varepsilon_i}{\varepsilon_i} = \frac{4kT_e}{m_e c^2}. \quad (6.26)$$

This is actually slightly higher than the estimate we gave in equation (6.10). The reason for this is that the average energy of a photon in thermal equilibrium with an electron gas is not  $kT_e$ , but rather  $3kT_e$ .

The mean number of scatterings for an optically thin medium is simply  $\tau_{\text{es}}$ , the total optical depth through the medium. For optically thick systems, the photons must take a random walk to escape, so the number of scatterings becomes  $\tau_{\text{es}}^2$ . Thus

the Compton  $y$  parameter for a finite medium of nonrelativistic electrons is

$$y = \frac{4kT_e}{m_e c^2} \text{Max}(\tau_{\text{es}}, \tau_{\text{es}}^2). \quad (6.27)$$

For a low-energy soft photon source with multiple scattering events, the final spectrum due to inverse-Compton scattering can be calculated using the *Kompaneets equation*, which is a form of the Fokker-Plank diffusion equation (Kompaneets, 1957). For  $h\nu \lesssim kT_e$ , the resulting spectrum takes the power-law form

$$I_\nu \sim \nu^{-\alpha}, \quad (6.28)$$

with

$$\alpha = \frac{3}{2} + \sqrt{\frac{9}{4} + \frac{4}{y}}. \quad (6.29)$$

At energies above  $kT_e$ , the electrons no longer efficiently transfer energy to the photons, so the spectrum shows a cutoff for  $h\nu \gtrsim kT_e$ :

$$I_\nu \sim \nu^3 \exp(-h\nu/kT_e). \quad (6.30)$$

With the assumption of purely elastic scattering, we cannot actually reproduce this cutoff effect; all photons are scattered equally, and thus the ratio  $\varepsilon_f/\varepsilon_i$  is independent of energy. Thus equation (6.26) would predict infinite energy boosts until  $h\nu \gg m_e c^2$ . In reality, higher energy photons tend to lose energy in scattering, due to the recoil of the electron. This effect is relatively easy to calculate from conservation of energy and momentum in the electron rest frame:

$$\varepsilon_f = \frac{\varepsilon_i}{1 + \frac{\varepsilon_i}{m_e c^2} (1 - \cos \theta)} \quad (6.31)$$

To accurately include this effect, we would have to keep track of the real “physical” energy of each photon, instead of the fiducial redshift method that we currently use to reconstruct the total spectrum afterwards. Ultimately, this is just a matter of computational intensity and no real conceptual difficulty. To first-order, we can treat the thermal photon source as a monochromatic emitter at  $E_0 = 3kT_{\text{em}}$ , which should give a reasonable approximation to the true solution.

Before we can actually produce such a spectrum, we must first define the electron temperature and density profile through which the photons will scatter. Like relativistic jets, there is still no real consensus in the literature as to what exactly produces the electron corona surrounding the black hole and accretion disk. By measuring the power-law part of the continuum spectrum [see e.g. Sunyaev & Truemper



(1979); Makishima et al. (1986)], it seems clear that the corona is quite hot ( $T_e \gtrsim 50$  keV) and diffuse ( $\tau_{\text{es}} \lesssim 5$ ). Many of the early works on this subject treated the corona as an isothermal and uniform density sphere with a sharp cutoff at some radius  $R_c$ , using the Kompaneets equation to propagate the seed photons through the corona (Shapiro, Lightman, & Eardley, 1976; Sunyaev & Titarchuk, 1980; Titarchuk, 1994). Nobili et al. (2000) basically follow this approach, but also allow for two layers in the corona at different temperatures: an inner hot sphere surrounded by a “warm” layer at slightly lower temperature. More recent Monte Carlo methods (Stern et al., 1995a; Poutanen & Svensson, 1996; Yao et al., 2003; Wang et al., 2004) allow for arbitrary distributions, but in practice usually only consider similar isothermal, uniform density profiles.

We have investigated a number of different models, including the uniform distributions mentioned above as well as isothermal and polytropic gases in hydrostatic equilibrium (constructed by integrating the Oppenheimer-Volkoff equation). Both cases require some arbitrary cut-off radius for the corona in order to have a low enough optical depth to agree with the observations. Future work will include a more comprehensive exploration of hydrostatic corona models with various polytropic equations of state. Perhaps a more physical option is that of the Advection Dominated Accretion Flow (ADAF) model proposed by Narayan & Yi (1994), where the self-similar density and temperature profiles scale as

$$\rho \propto r^{-3/2}, \quad (6.32a)$$

$$T \propto r^{-1} \quad (6.32b)$$

outside of the ISCO. We have ignored the bulk velocity of the inwardly flowing gas, which will typically have  $v_{\text{bulk}} \ll v_{\text{therm}}$  in the ADAF model. For larger inflow velocities of  $v_{\text{bulk}} \gtrsim 0.1c$ , the effect of “bulk Comptonization” has been studied in detail by Psaltis (2001b).

For such a profile, most of the scattering events happen at small  $r$  and relatively high  $T$ . Figure 6-5 shows roughly what the electron distribution would look like and where the scattering takes place. As in Figure 6-3, the photons are color-coded according to their blue/redshifted energy  $E_\infty = -p_t$ . Upon close inspection, it is clear that this energy changes slightly during each scattering event via the inverse-Compton process.

To create a simulated spectrum for a thermal hot spot or disk, we follow the steps described above, starting with isotropic, monochromatic emission in the emitter’s rest frame. To approximate the high-energy cutoff at  $h\nu \approx kT_e$ , the initial photon energy is set as  $E_0 = 3kT_{\text{em}}$  and equation (6.31) is used to limit the runaway energy boosting from the hot electrons. For decent spectral and timing resolution, we typically ray-trace  $10^7 - 10^8$  photons, which are either captured by the horizon or detected

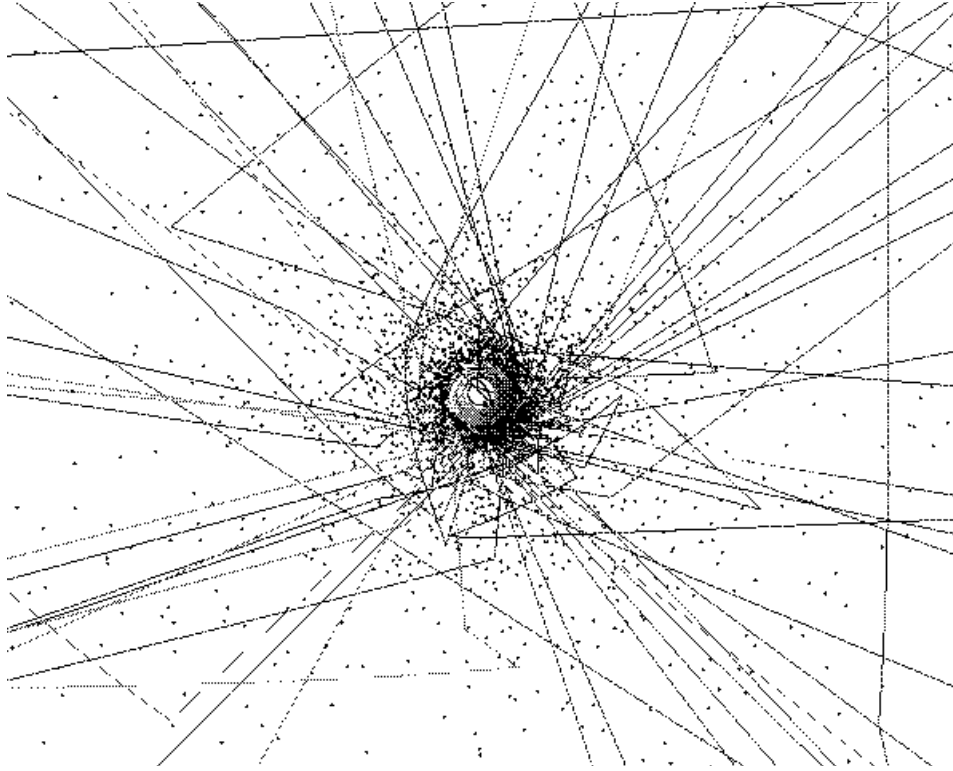


**Figure 6-5:** Electron distribution (black dots) for ADAF corona model with  $\tau_{\text{es}} \approx 1$ . As in Figure 6-3a, the photons are emitted isotropically by a massive particle in a circular orbit at the ISCO of a black hole with  $a/M = 0.5$ . The photons are colored according to their blue/redshift with respect to that of the emitter’s rest frame. Many of the photons clearly change color during scattering events, as they are boosted to higher energies by the hot electrons.

by a distant observer with a time and energy label, much like a real astronomical instrument. For example, if there was no scattering, the time-averaged “numerical” spectrum could be described by the relativistic transfer function discussed in Section 2.4.1, defined over an infinitesimal band in radius  $R_{\text{in}} \approx R_{\text{out}} = r_{\text{em}}$ . The inverse-Compton processes in the corona serve to further broaden this transfer function, as shown by the curves in Sunyaev & Titarchuk (1980) and Titarchuk (1994). This transfer function is then normalized to the rest energy  $E_0$  and convolved with the actual emission spectrum (e.g. a thermal blackbody at  $kT_{\text{em}}$ ) to give the simulated observed spectrum.

Figure 6-6 shows a set of these simulated spectra from a hot spot emitter around a black hole with  $a/M = 0.5$ , as in Figure 6-5. The emission spectrum is thermal

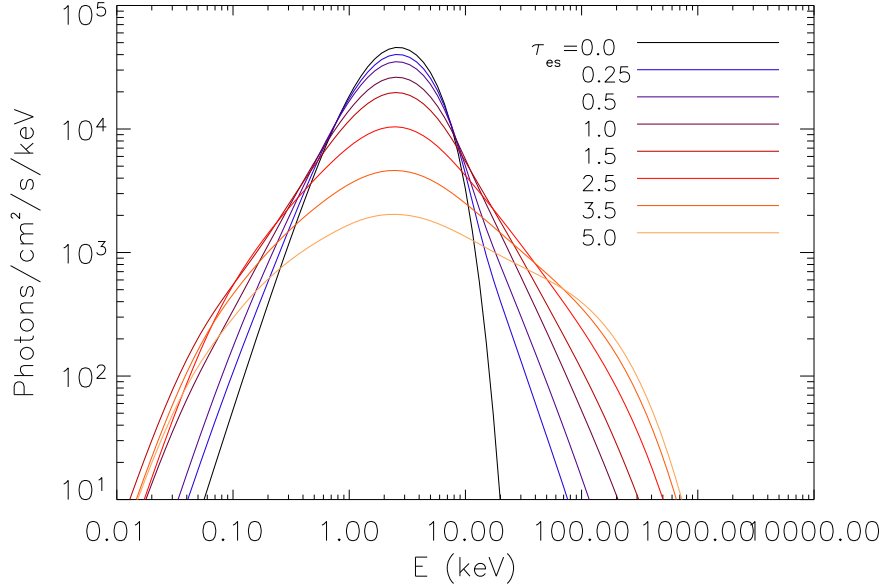


**Figure 6-6:** Simulated observed spectra of a thermal hot spot emitter with  $T_{\text{em}} = 1$  keV, on a circular orbit at the ISCO as in Figure 6-5. The thermal spectrum is modified by relativistic effects and Compton scattering off a hot corona with  $T_e = (r_{\text{ISCO}}/r)100$  keV. The resulting spectrum is composed of a power-law component with a high-energy cut-off at  $h\nu \approx kT_e$ . These two features can be used to infer the corona temperature and optical depth. Note that the magnitude scale of the  $y$ -axis is arbitrary and in general would depend on the luminosity and distance to the source.

in the hot spot rest frame with  $T_{\text{em}} = 1$  keV. The coronal ADAF model has  $T_e = (r_{\text{ISCO}}/r)100$  keV, and electron density  $n_e \sim r^{-3/2}$  for a variety of optical depths  $\tau_{\text{es}}$ . The spectra are plotted in units of [ $\#\text{Photons/s/cm}^2/\text{keV}$ ], as is the convention by many observers, but the actual magnitude of the  $y$ -axis is arbitrary, and would normally depend on the distance to the source. With these units, the power-law section of the spectrum scales as

$$N_\nu \sim I_\nu/\nu \sim \nu^{-1-\alpha} \quad (6.33)$$

and the high energy cut-off as

$$N_\nu \sim \nu^2 \exp(-h\nu/kt_e). \quad (6.34)$$

From the slope of the power-law and the location of the cut-off, the corona temperature and optical depth can be inferred from observations (Pozdniakov, Sobol, & Sunyaev, 1977; Sunyaev & Truemper, 1979; Gilfanov et al., 1994; Gierlinsky et al., 1997; Zdziarski, 2000).

While the spectra in Figure 6-6 come from a single hot spot at a single temperature, the total spectrum from a steady-state disk could be calculated easily by superimposing the results from many such calculations at different radii. The seed photon spectrum at each radius would be determined by the results in Chapter 5 [e.g. equation (5.35)]. Currently, many X-ray observations of black hole binaries fit the spectrum as a simple superposition of a thermal blackbody peak (either at a single temperature, or the popular “multi-color disk”) and a separate power-law component [see e.g. Gierlinsky et al. (1999); McClintock & Remillard (2004)]. Our full ray-tracing and Monte Carlo scattering approach, while somewhat more computationally intensive, would give more accurate and physically motivated spectra with which to compare observations.

### 6.3 Effect on Light Curves

The spectra in Figure 6-6 were created by integrating over the complete hot spot orbital period and over all observer inclination angles. However, during the Monte Carlo calculation, it is just as simple to bin all the photons according to their final values of  $\theta$ ,  $t_{\text{obs}}$ , and energy  $-p_t$ . With  $10^8$  photons, we achieve decent resolution for  $N_\theta = 20$ ,  $N_t = 100$ , and  $N_E = 200$ . The latitude bins are evenly spaced in  $\cos\theta$  so that a comparable number of photons land in each zone. The energy bins are spaced logarithmically to include the high energy tail and also maintain high enough spectral resolution at lower energies. As described above, the photons at any azimuthal position can be mapped into the appropriate bin in  $t_{\text{obs}}$  by equation (6.13), assuming a hot spot on a circular periodic orbit.

An excellent way to see the effects of scattering on the hot spot light curves is by plotting the same type of time-dependent spectrograms we used in the original hot spot model in Chapter 3. However, the spectrograms of unscattered hot spots will appear slightly different than those produced in Chapter 3, which traced the photons backwards from the observer to an opaque disk (only passing through each latitude zone once, thus not producing multiple images — this is a feature inherent to the code, not the physical model). The number of rays required to resolve the image was then proportional to the solid angle subtended by the hot spot. When starting at the emitter, the hot spot can be infinitesimally small and also the photons can orbit the black hole multiple times, forming the multiple images inherent in strong gravitational lensing.

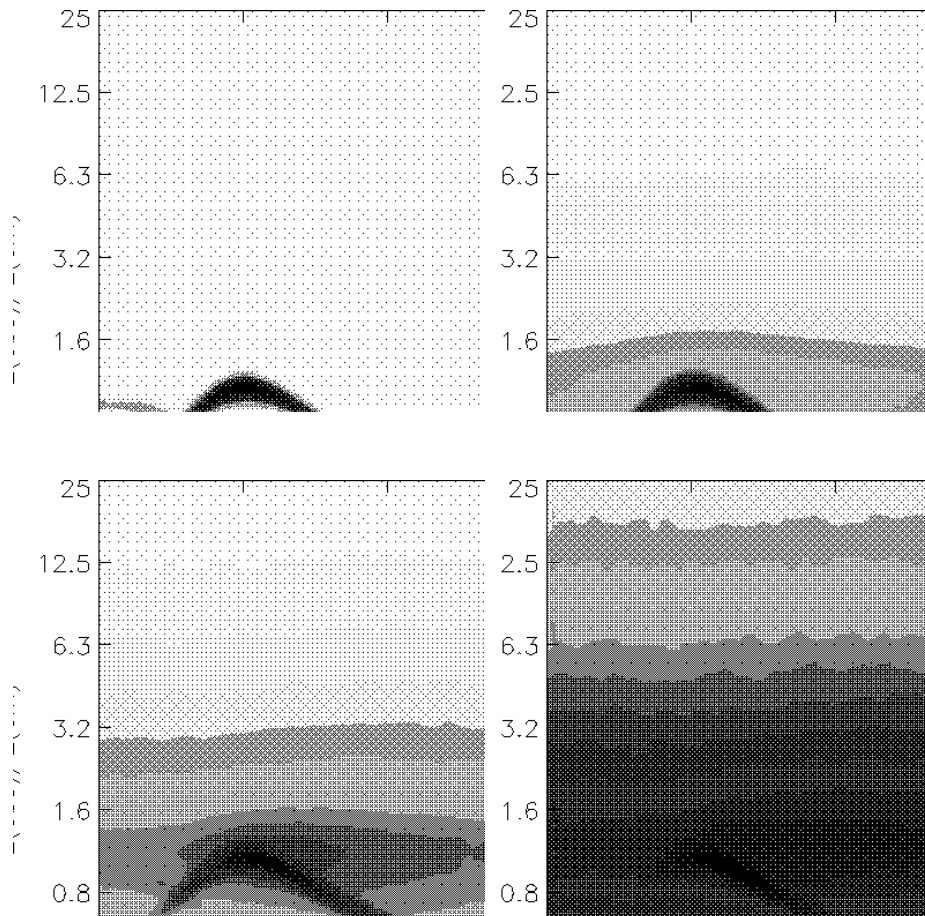


**Figure 6-7:** Time-dependent spectra of a monochromatic, isotropic hot spot emitter on an ISCO orbit with  $a/M = 0.5$  and inclination angle  $i = 45^\circ$ . The four panels show spectrograms for systems of increasing optical depth  $\tau_{\text{es}} = [0, 1, 2, 4]$ . The scattering clearly spreads out the light curve in phase and photon energy, with a trend towards greater time delays for higher optical depth, and thus more scattering events. The logarithmic color scale shows the number of photons in each time/energy bin, normalized to the peak value for each panel.

These effects are clearly visible in the first panel of Figure 6-7, which shows the time-dependent spectrum of a monochromatic emitter, as viewed by an observer at  $45^\circ$ . The logarithmic color scale shows [#photons/s/cm<sup>2</sup>/keV/period], normalized to the peak intensity in each panel. At “0” phase, when the emitter is moving away from the observer, the spectrum shows two distinct lines, one blueshifted in the forward direction of hot spot motion, and one redshifted in the backward direction. As the hot spot comes around towards the observer, the directly beamed blueshifted line dominates, and then when the phase is  $\sim 0.5$  and the hot spot is on the near side of the black hole, a single line dominates. This is due to the gravitational demagnification of the secondary images formed by photons that have to complete a full circle around the black hole to reach the observer. While these features would most likely be unresolvable for black hole binaries, they may well be observable in X-ray flares from Sgr A\* as well as other supermassive black holes [e.g. see Baganoff et al. (2001)].

In the subsequent panels, the spectrum is modified by the scattering of the hot spot photons in the surrounding corona. As in Section 6.2, the temperature and density profile of the corona is given by an ADAF model with  $T_e(r_{\text{ISCO}}) = 100$  keV. The four panels of Figure 6-7 show increasing values of  $\tau_{\text{es}} = [0, 1, 2, 4]$ . The effects of scattering on the spectra are really quite profound. As we described qualitatively in Chapter 4, the electron corona is like a cloud of fog surrounding a lighthouse, spreading out the delta-function beam in time and frequency. Unlike the simple model there, where each photon was assigned some positive time delay, the Monte Carlo scattering code shows that some photons actually arrive *earlier* in time by taking a “shortcut” to the observer instead of waiting for the hot spot to come around and move towards the observer. And of course, the photons are also spread out in frequency due to the inverse-Compton effects. As the optical depth increases, the well-defined curve in Figure 6-7a is smeared out into a nearly constant blur at  $\tau_{\text{es}} = 4$ , with a broad spectral peak as in Figure 6-6. Only a slight trace of the original coherent light curve remains, composed of roughly 1% of the emitted photons that do not scatter before reaching the observer or get captured by the event horizon. When  $\tau_{\text{es}} > 1$ , multiple scattering become more common, so photon shortcuts become rarer, tending to spread the light curve preferentially to the right (delay in observer time), as seen in Figures 6-7c,d.

We show a similar set of spectrograms in Figure 6-8, now with orbital inclination  $i = 75^\circ$ . The qualitative effects are the same, but the higher inclination gives stronger relativistic effects and more powerful beaming. The strongly peaked light curve maintains a somewhat sharper contrast even for high optical depth. While the detailed spectral and timing features of Figures 6-7 and 6-8 promise to reveal much about the underlying physical processes at work, we are still a very long way from achieving such observational resolution in black hole binary sources, where the relevant time

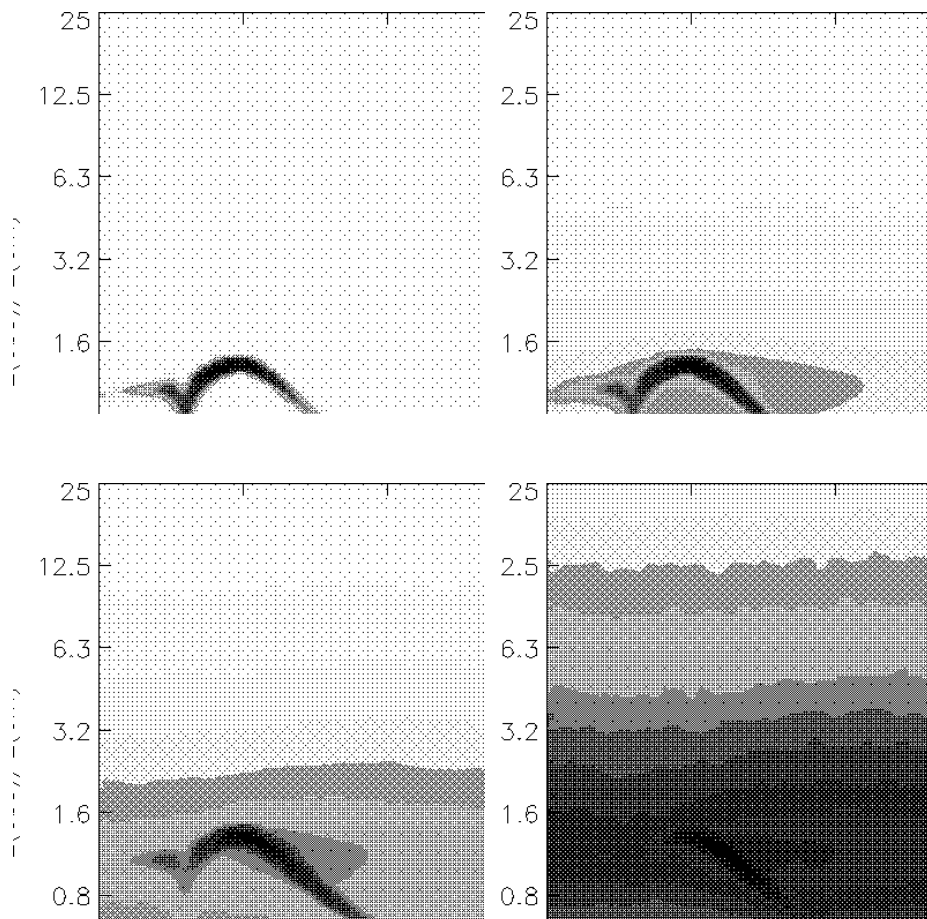


**Figure 6-8:** Spectrograms of a monochromatic, isotropic hot spot emitter, as in Figure 6-7, but now with inclination  $i = 75^\circ$ .

scales are on the order of milliseconds. More promising is the application to hot spots from AGN sources or the X-ray flares around Sgr A\* (Baganoff et al., 2001).

By integrating over broad energy bands such as those typically used in *RXTE* observations, we can increase our “signal” strength while sacrificing spectral resolution. For millisecond periods, there will still not be nearly enough photons to provide phase resolution, but these features may show up statistically in the power spectrum or bispectrum, as explained in Chapter 4. Figure 6-9 shows a set of integrated light curves for a variety of optical depths. The black hole and hot spot parameters are as in Figure 6-7, here assuming a thermal emission with hot spot temperature  $T_{\text{hs}} = 1$  keV. The photons are integrated over the energy range 0.5-30 keV.

As the optical depth to electron scattering increases, the rms amplitude of each light curve decreases as the photons get smoothed out in time. Similarly, due to the average time delay added to each photon by the increased path length, the relative location of each peak is shifted later in time. These amplitudes and phase shifts are listed in Table 6.1 for inclinations of  $i = 45^\circ$  and  $75^\circ$ . At even higher optical depths, the average light curve intensity begins to decrease, as more photons end up getting captured by the black hole and never reaching the observer.

**Table 6.1:** Amplitudes and phase shifts of light curve peaks for hot spot inclinations of  $i = 45^\circ$  and  $75^\circ$  for a range of optical depths  $\tau_{\text{es}}$ . The amplitude quoted is the standard deviation  $\sigma(I)$  normalized by the mean intensity  $\mu(I)$ . The phase shift is where the peak intensity is located in time, relative to that of the unscattered light curve.

$\tau_{\text{es}}$	$45^\circ$		$75^\circ$	
	$\sigma/\mu$	phase shift (periods)	$\sigma/\mu$	phase shift (periods)
0	1.14	0	1.51	0
0.5	0.53	0.01	0.88	0.01
1.0	0.27	0.02	0.46	0.03
2.0	0.086	0.06	0.12	0.06
3.5	0.021	0.29	0.035	0.31
5.0	0.018	0.35	0.021	0.40

In all likelihood, the relative phase shifts would be nearly impossible to detect, regardless of the instrument sensitivity, since to do so would require measuring the light curve from a single coherent hot spot at two different optical depths. It is difficult to imagine a scenario where the coronal properties could change on such short time scales [yet it is possible that a fixed hot spot on the surface of an X-ray



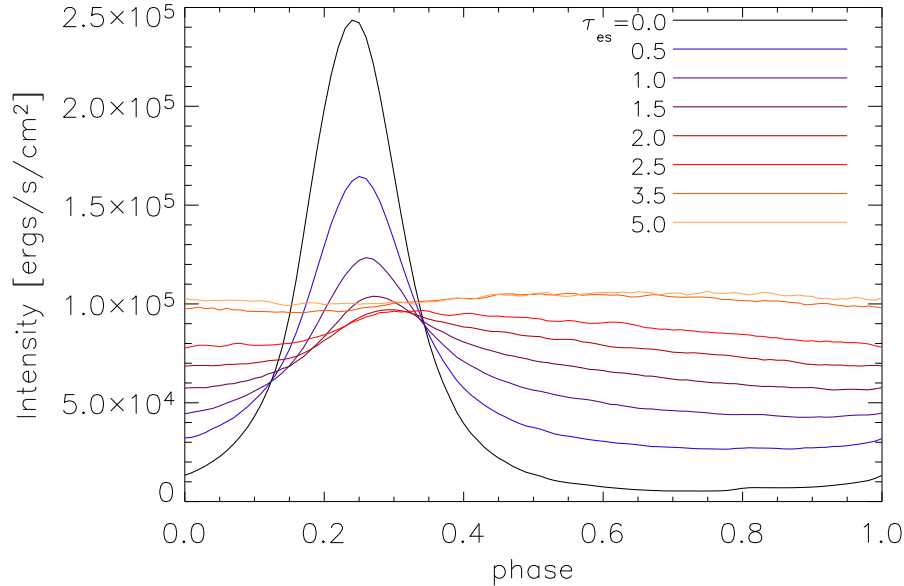


**Figure 6-9:** Energy-integrated light curves for a hot spot with orbital parameters as in Figure 6-7. The emitted spectrum is assumed to be thermal with a hot spot temperature  $T_{\text{hs}} = 1$  keV, integrated over 0.5 – 30 keV in the observer’s frame. With increasing optical depth to scattering, the rms amplitudes decrease significantly, and their peaks move slightly to the right, due to the time delay from repeated scattering events.

pulsar might actually be used for this technique; see Ford (2000) and Gierlinsky, Done, & Barret (2002)]. However, the higher harmonic peaks of the different light curves may in fact be measurable with the next-generation X-ray timing mission, or under extremely favorable conditions, even with *RXTE*. In Figure 6-10 we show the damping of the Fourier modes  $A_n/A_0$  with increasing optical depth. Not only does the overall amplitude of modulation decrease with increased scattering, but also the relative amplitudes of the higher harmonics ( $n > 1$ ) decreases relative to the fundamental ( $n = 1$ ).

While the absolute peak shifts for hot spot light curves at different optical depths would probably not be detectable, the relative shifts of simultaneous light curves in different energy bands may be observable, at least on a statistical level with a cross-correlation analysis. Since the average scattering event boosts photons to higher energy bands and also causes a net time delay due to the added geometric path, the light curves in higher energy bands should be delayed with respect to the lower energy

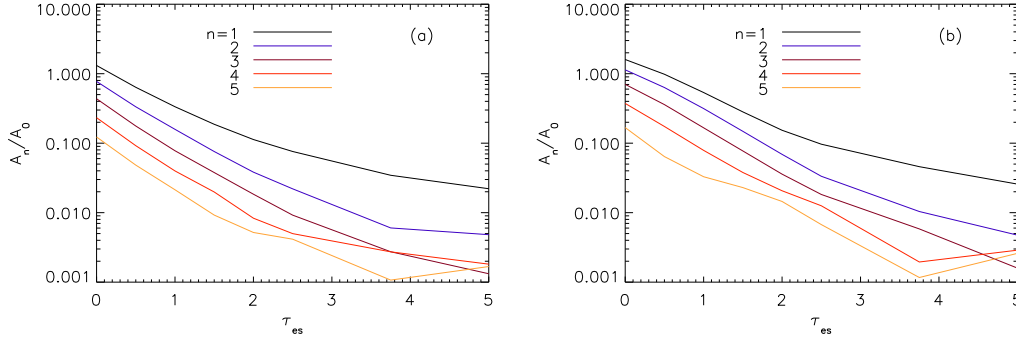


**Figure 6-10:** Normalized Fourier amplitudes  $A_n/A_0$  for hot spot light curves as in Figure 6-9, for inclinations of (a)  $45^\circ$  and (b)  $75^\circ$ . As the optical depth to electron scattering increases, the modulation amplitudes of the light curves decrease. The higher-order harmonics  $n > 1$  are damped even more with respect to the fundamental mode at  $n = 1$ .

light curves. A few of the typical energy bands used for *RXTE* observations are 2–6, 6–15, and 15–30 keV. To fully cover the peak emission from a thermal hot spot at 1 keV, we expand the lowest energy band in our calculations to cover 0.5–6 keV. The light curves in these three bands are plotted in Figure 6-11 for  $i = 75^\circ$ . The low energy band resembles the unscattered light curve plus a roughly flat background, while the higher energy light curves show a much smaller modulation with a significant phase shift ( $\sim 0.3$  periods) due to the additional photon path lengths.

## 6.4 Implications for QPO Models

The original motivation for the application of scattering to the hot spot model was to answer a few important questions raised by *RXTE* observations:

- The distinct lack of power in higher harmonics at integer multiples of the peak frequencies.
- The larger significance of high frequency QPO detections in the higher energy bands (6-30 keV) relative to the signal in the lower energy band (2-6 keV).
- The trend for these HFQPOs to exist predominantly in the “Steep Power Law” (SPL) spectral state of the black hole.

Beginning with the final point, it appears to be quite reasonable that the physical mechanism causing the power law spectra is the inverse-Compton scattering of cool,

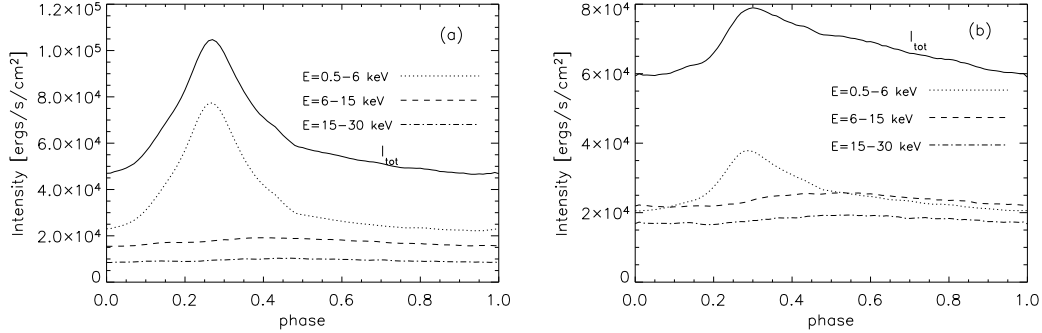


**Figure 6-11:** Hot spot light curves in a few different *RXTE* energy bands (we have expanded the lowest energy band down to 0.5 keV to include the thermal emission of a hot spot at  $T_{hs} = 1$  keV). The hot spot inclination is  $75^\circ$  and the coronal properties are as in Figure 6-8. The optical depth to scattering is  $\tau_{es} = 1.5$  in (a) and 2.5 in (b). The higher energy light curves are made from photons that have experienced more scattering events, boosting their energy and delaying their arrival time.

thermal photons off of hot coronal electrons. The *steep* power law suggests a small-to-moderate value for the Compton  $y$  parameter, inferred from equation (6.29), in the range  $0.5 \lesssim y \lesssim 10$ . From equation (6.27), this suggests either a small optical depth or a small electron temperature. To gain insight into which of these two options is more likely, we need to address the other two observational clues.

In Chapter 4, we first proposed the scattering model as an explanation for harmonic damping. There, the model simply assigned a random time delay to each photon detected by the observer, but the photons still followed their unobstructed geodesic paths. Thus, photons beamed towards the observer at the peak of the light curve were still beamed towards the observer, but delayed slightly in phase. With the more careful treatment in this chapter, we include not only the temporal, but also the spatial effects of electron scattering. The photons originally beamed toward the observer are now scattered in the opposite direction, while the photons emitted away from the observer can now be scattered back to him. This smoothes out the light curve in time more effectively than the localized convolution functions used in Chapter 4. At the same time, the scattering is not completely isotropic [see eqn. 6.7], so some modulation remains. This modulation is probably also supported in the Kerr geometry because of the bulk rotation of the corona gas (treated “at rest” in the ZAMO frame): photons emitted with angular momentum parallel to the black hole spin get swept along by the electrons moving in the same direction, maintaining

a slight level of beamed modulation. Thus, to maintain a significant modulation in the light curve, we require a relatively small optical depth, reducing the smoothing effects of the scattering.

The fact that most HFQPOs appear more significantly in higher energy bands also points towards Compton scattering off hot electrons. However, as the calculations above show (see Fig. 6-11), with the basic thermal disk/hot spot model, the light curves actually have *smaller* amplitude fluctuations in the higher energy bands, as these scattered photons get smoothed out more in time. Furthermore, while the higher harmonic modes are successfully damped in the scattering geometry, so is the fundamental peak. Thus, in order to agree with observations, the hot spot over-brightness would need to be much higher than the values quoted in Chapters 3 and 4.

Based on these arguments alone, we find it unlikely that the HFQPOs are coming from a cool, thermal hot spot getting upscattered by a hot corona. From the photon continuum spectra of the SPL state, there appears to be a hot corona with Compton  $y \sim 1$ , but as Figure 6-11a shows, the lowest energy ( $< 6$  keV) band has by far the greatest amplitude modulations. It is possible that the relative modulation would appear smaller due to the added flux from the rest of the cool, thermal disk, but much of this steady-state emission should also get scattered to higher energies, further damping the modulations in the 6-30 keV bands.

The high luminosity of the SPL state (also called the Very High state) suggests that the thermal, slim disk geometry may not be appropriate here. Perhaps it is more likely that these cases correspond to an ADAF model, traditionally associated with very low or very high accretion rates. Since the ADAF model cannot radiate energy efficiently, the gas in the innermost regions (where causality arguments focus our attention) will be much hotter than in the  $\alpha$ -disk paradigm. Thus *hot* hot spots with  $T_{\text{hs}} \gtrsim 5$  keV could be forming inside a small ADAF coronal region, providing seed photons that are already in the higher energy bands, and are only moderately upscattered by the surrounding corona. In this model, the harmonic damping would be primarily caused by the formation of arc hot spots as in Chapter 4.

Of course, this schematic description still leaves many of the original QPO questions unanswered, like why should the hot spots form at special radii with commensurate frequencies. If a global oscillation [such as the pressure-dominated torus of Rezzolla et al. (2003)] is producing the seed photons, scattering will also damp out the light curve modulations, although probably not as much, since relativistic beaming plays a smaller role in that axisymmetric geometry. Ultimately, the aim of this research is to construct a formalism in which these different models can be accurately evaluated and compared directly to the observed data.

# Chapter 7

## Conclusions and Future Work

*Science is a wonderful thing if one does not have to earn one's living at it.*

*I never think of the future. It comes soon enough.*

-Albert Einstein

### 7.1 Summary of Results

In this concluding Chapter, we will briefly summarize the results of the Thesis, their relevance to X-ray observations, and directions for future work.

#### 7.1.1 Ray-tracing

In Chapter 2, we developed the foundation of a fully relativistic ray-tracing code that can be used as a “post-processor” to analyze the output data from three-dimensional hydrodynamics simulations. This code is based on a Hamiltonian formulation of the equations of motion in Boyer-Lindquist coordinates. In Section 2.1 we showed how certain symmetries in  $t$  and  $\phi$  can be used to reduce the dimensionality of the ray-tracing problem. This results in a system of five coupled first-order differential equations for  $[r, \theta, \phi, p_r, p_\theta]$ , which are solved numerically using an adaptive step fifth-order Runge-Kutta integrator (Section 2.3). The fourth integral of motion, Carter's constant  $\mathcal{Q}$ , is used as an independent check of the accuracy of the numerics.

While our code uses Boyer-Lindquist coordinates to perform the global ray-tracing calculation, we also discuss the advantages of the Doran coordinate system in Section 2.1.2, which is particularly useful for modeling processes inside and near the horizon.

These coordinates are based on observers free-falling from infinity, so they experience no coordinate singularity at the horizon, and are thus especially convenient for producing movies of exotic black hole processes such as passing through inner and outer horizons into parallel universes.

After the geodesic ray-tracing is performed, we have a tabulated set of positions and momenta along each photon path. Coupled with the density and temperature profiles from some dynamic disk model, we can integrate the radiative transfer equation along the path length to produce time-varying images and spectra of the disk. To successfully merge the ray-tracing and radiative transfer pieces of the code, in Section 2.2.1 we introduced a tetrad formalism that defines a locally flat, orthonormal basis at each point on the photon path.

In Section 2.4.1 we applied the ray-tracing code to a simple disk model composed of test particles on planar circular orbits normal to the black hole rotation axis. Assuming each particle is emitting monochromatic, isotropic radiation in its rest frame, we calculated the *transfer function* that maps redshifts from the plane of the disk to the observer's image plane. This transfer function can be used to model the broad iron emission lines observed in black hole binaries and AGN. For disks that extend inside the ISCO, we showed that the emission line profile is not sensitive to the black hole spin, and thus at this point is not an especially promising method for measuring  $a/M$ .

### 7.1.2 The Hot Spot Model

In order to apply the post-processor code developed in Chapter 2 to *RXTE* timing observations, we introduced a simple geodesic hot spot model in Chapter 3, and then expanded it in Chapter 4 to fit data from XTE J1550–564. The basic hot spot model is composed of a small region of overbrightness moving on a geodesic orbit around the black hole, which in turn produces a periodic modulation in the X-ray light curve. In Section 3.1.1 we showed how this modulated emission can be added to a steady-state disk flux and used to infer the size and overbrightness of the hot spot.

While the actual light curve is not resolvable over such short periods as 3 – 10 msec, the harmonic structure of the Fourier modes can be used to infer the orbital inclination and hot spot arc length, and to a lesser degree, the eccentricity and black hole spin (Sections 3.1.2 and 3.2). We showed how the radial coordinate frequency can form beat modes with the fundamental orbital frequency, giving Fourier power at  $\nu_\phi \pm \nu_r$ . For closed orbits with  $\nu_\phi = 3\nu_r$ , these modes have commensurate frequencies 2 : 3 : 4, as observed in a growing number of black hole binaries (with the  $\nu_\phi + \nu_r$  mode damped due to the shearing of the hot spot into an arc).

In Section 3.3, we described the effects of Lense-Thirring precession on non-planar orbits and examined the possibility that this precession is responsible for producing

the low frequency QPOs often seen concurrently with the HFQPOs. If these three QPO peaks (one LF and two HF) are in fact linked, then the black hole mass *and* spin could be determined independently by matching the peak frequencies to the geodesic frequencies  $\nu_{LT}$ ,  $\nu_\phi - \nu_r$ , and  $\nu_\phi$ . If the LFQPO is in fact not related to the hot spot emitter, then the location of the two HFQPOs alone could be used to determine the spin for a given black hole mass.

In Chapter 4, we expanded the hot spot model to account for the peak broadening in the QPO power spectrum, deriving two analytic models for the superposition of multiple hot spots with finite lifetimes and a range of coordinate frequencies. For a collection of hot spots with random phases, the finite lifetime of each hot spot causes every delta-function peak of the periodic power spectrum to be broadened into a Lorentzian with exactly the same width. Assuming the hot spots are formed on commensurate orbits with some finite resonance width in radius (and thus a range of coordinate frequencies), the different QPO peaks will all be broadened by a different amount. In Section 4.4 we showed how this differential peak broadening is sensitive to the black hole spin and may be used to map out the spacetime in the innermost regions of the accretion disk.

In Section 4.5, we derived a simple electron scattering model for a low-density corona surrounding the hot spot emitter. The primary effect of this coronal scattering was to assign each photon a randomized time delay due to the added path length to the detector, smoothing out the light curve in time. While this does not affect the width of the QPO peaks, it does cause a significant damping of the higher harmonic modes. This scattering model and the formulae for the peak widths can be combined into a single analytic expression for the power spectrum, allowing us to fit the data by minimizing  $\chi^2$  over some small set of model parameters. In Section 4.6 we applied these models to the *RXTE* data for XTE J1550–564, and were able to explain the power spectra of type A and type B QPOs with different hot spot arc lengths and lifetimes.

Finally, in Section 4.7, we introduced the use of higher order statistics such as the bispectrum and bicoherence as a means for distinguishing between various QPO models. In particular, we showed how the random phase broadening and the coordinate frequency broadening would have distinctly different signatures in the bispectrum contours. For a next-generation X-ray timing mission, these signatures could be used to map out the spacetime around accreting black holes and serve to further constrain or rule out the hot spot model.

### 7.1.3 Steady-state Disks

As a test-bed for the ray-tracing post-processor and to gain more insight into the X-ray spectrum of the steady-state disk, in Chapter 5 we developed a relativistic  $\alpha$ -

disk model, based on the work of Shakura & Sunyaev (1973) and Novikov & Thorne (1973). While their treatment can be thought of as a one- or two-zone model (uniform density; temperature defined at disk mid-plane and surface), we actually integrate the complete set of vertical structure equations for density, temperature, pressure, and energy flux. Coupled with the Novikov-Thorne equations for radial structure, with the appropriate selection of boundary conditions for the disk atmosphere, the vertical structure equations have a unique solution at each radius.

To self-consistently model the torque on the inner edge of the disk, in Section 5.2 we showed how the accreting gas expands and plunges along geodesic trajectories inside of the ISCO. Following a one-dimensional column of gas in the frame of the plunging particle, we can model the time-dependent vertical structure of the innermost disk with a Lagrangian approach to the partial differential equations of hydrodynamics. We found that the plunging disk pressure falls off at a scale length of  $l_{\text{plunge}}$  inside the ISCO. Since the angular momentum transport (torque) acts over a turbulent length scale of  $l_{\text{turb}} \approx h$ , we can solve for the integrated stress (and thus the surface density  $\Sigma$  and radial velocity  $p^r$ ) at the ISCO by setting  $l_{\text{plunge}} = l_{\text{turb}}$ .

In Section 5.3 we outlined the numerical methods used to solve for the disk structure inside and outside of the ISCO. The Lagrangian hydrodynamics is based on an implicit scheme described in Bowers & Wilson (1991). We found that the density and temperature profiles of the disk fall off rapidly inside the ISCO, but that even a small torque can significantly affect the temperature and total efficiency of the  $\alpha$ -disk outside of the ISCO. Given the temperature and scale height of the disk atmosphere, in Section 5.4 we used the relativistic ray-tracing code (see Chapter 2) to calculate the modified “multi-colored” spectrum of the disk. The peak of the spectrum occurs at  $E_{\text{max}}$ , which is a function of the black hole mass and Eddington-scaled accretion rate. Defining a high-energy cutoff such that  $I(E_{\text{cut}}) = 10^{-5}I(E_{\text{max}})$ , we showed that the ratio  $E_{\text{cut}}/E_{\text{max}}$  may be used to determine the inclination and/or spin of the black hole system.

### 7.1.4 Electron Scattering

Motivated by the fact that most black hole HFQPOs are seen in the “Very High” or “Steep Power-Law” spectral state (McClintock & Remillard, 2004), we replaced the simple coronal scattering model from Section 4.5 with a more detailed Monte Carlo treatment, including angular dependence and energy transfer via the inverse-Compton effect. Reversing the ray-tracing paradigm of Chapter 2, in Chapter 6 we explained how thermal photons are traced from isotropic hot spot emitters through an ADAF-type corona, and then detected by a distant observer. Like the radiative transfer equation in Section 2.2.2, the electron scattering can be treated classically in the appropriate reference frame, and then the post-scattered photon is transformed



back to the coordinate basis and proceeds along its new geodesic trajectory.

The electron scattering has two major observable effects: it modifies the photon spectrum, adding a power-law tail at high energies (Section 6.2), and it smoothes out the light curve in time as the photons get re-directed into new time bins (Section 6.3). We showed how the slope of this power-law component can be used to determine the density (optical depth) and temperature of the corona, assuming a self-similar ADAF profile. We also predicted significant phase shifts in the light curves observed in different *RXTE* energy channels, since photons that experience more scattering events tend to get a larger energy boost and longer time delay before reaching the detector. This effect may ultimately be observable with a next-generation timing mission and the careful application of higher order statistical analysis.

In Section 6.4 we summarized some of the major results of QPO observations and compared them to the predictions of the Monte Carlo hot spot scattering calculations. We concluded that the seed photons causing the QPO modulations in higher energy channels most likely are coming from an intrinsically hot source, and *not* getting up-scattered by coronal electrons. For an ADAF corona, the steep power law component of the X-ray spectrum suggests an optical depth of  $\tau_{\text{es}} \approx 1$  and electron temperature  $T_e \approx 100$  keV. The arc shearing described in Chapters 3 and 4 is still a likely candidate for damping higher harmonic modes in the power spectrum. It is also quite possible that a more “global” oscillation in the inner disk (e.g. one that does not rely on hot spot beaming) is producing the seed photons, which then propagate like sound waves through an optically thick corona, boosting them in energy while damping out the higher harmonics.

## 7.2 Caveats

In the interest of full disclosure, we include here a number of caveats and qualifications for the models and methods used throughout the Thesis. Some are more significant than others, but all should be kept in mind when evaluating the results presented above.

First and foremost, the geodesic hot spot model still lacks convincing physical explanations for the following questions:

- (1) How are the hot spots formed?
  - (2) How long should the hot spots survive and what causes their destruction?
  - (3) What is a reasonable size and overbrightness for the typical hot spot?
- and perhaps most importantly,
- (4) *Why should the hot spots have special orbits with commensurate coordinate frequencies?*

The first three questions may eventually be answered empirically by global MHD simulations, but even the most sophisticated 3-D global GR codes still lack important radiation physics, an essential ingredient in any accretion disk model. As far as the fourth question, an answer may lie in the heuristic resonance models of Abramowicz & Kluzniak, but these still have a long ways to go before producing a convincing argument for the formation of hot spots along special commensurate orbits.

When fitting the relative amplitudes of the QPO peaks in Section 4.6, we found that the hot spot arc length was a well-constrained parameter of the model for both type A and type B QPOs (although the two types gave two different values for  $\Delta\phi$ ). For the type B power spectrum in particular, it was especially important to have a very long arc to damp out the higher frequency peaks at  $\nu_\phi$  and  $\nu_\phi + \nu_r$ , while amplifying the power at  $\nu_\phi - \nu_r$ . Is it reasonable to think that over observations of thousands of seconds, the random hot spot arc lengths could be so consistent and well constrained? Ideally, any model that is proposed to explain commensurate QPOs should be quite robust and applicable to a range of black hole masses and spins. At this point, the geodesic hot spot model still requires a little too much “fine tuning” to satisfy this robustness criterion, but is nonetheless a powerful tool as a building block for more physical models.

As mentioned in Chapter 5, the steady-state  $\alpha$ -disks can be quite useful for estimating accretion efficiency and temperatures for multi-color disk models, but do not necessarily give an accurate treatment of the innermost regions of the disk, particularly inside the ISCO. While our solution for the turbulence length gives a reasonable first-order estimate for the torque at the inner edge, the geodesic plunge still does not agree well with MHD simulations, which show little if any change in the local temperature and density of the disk at the ISCO. Furthermore, to quote Novikov & Thorne (1973), “Almost all of the uncertainties and complications of the model are lumped into the vertical structure. Ten years hence one will have a much improved theory of the vertical structure, whereas the equations of (averaged, steady-state) radial structure will presumably be unchanged.” Well, more than thirty years later, we still do not have a complete understanding of the vertical structure. And as we saw in Section 5.1.2, the vertical structure (particularly that of the atmosphere) will have a significant effect on the emitted spectrum. There is growing consensus that the  $\alpha$  viscosity/turbulence model is not correct (certainly for a constant  $\alpha$ ), and the most likely candidate for angular momentum transfer seems to be the magneto-rotational instability of Balbus & Hawley (1991). Despite the progress made with MHD simulations, there is not yet an elegant way of incorporating this process into an analytic steady-state model like the  $\alpha$ -disk.

One of the important assumptions of Chapter 5 was that the accretion disks are

thin, with  $h/r \ll 1$ . While this appears to be reasonable for low accretion rates, the hydrostatic structure equations will break down in the limit of high luminosity (an important limit for the Very High state associated with HFQPOs). Our revised derivation of the Eddington luminosity may help quantify these limits, but is still in a very early stage of development and has not yet been studied rigorously for a broad range of black hole masses and accretion rates. Similarly, while we argued in Section 5.2 that a self-consistent solution for the torque exists at the ISCO, this line of reasoning was based on the assumption that with increasing mass accretion rates, the disk just gets thicker and thicker until  $l_{\text{plunge}} \approx l_{\text{turb}}$ . It is now clear that this limit may not exist for equilibrium slim disks solutions without violating the modified Eddington limit of Section 5.1.3.

Lastly, in Chapter 6 we assumed a static ADAF model for the corona geometry. While the photon energy spectrum seems to be dependent only on the Compton  $y$  parameter, and not the detailed density and temperature profiles of the corona, the dependence of the light curves on these parameters has not been examined comprehensively. Also, while the corona is treated as static in the ZAMO frame, the underlying hot spot is moving relativistically through this medium on circular planar orbits. A consistent model is needed to explain how these two very different pieces of the accretion flow could exist simultaneously. This ultimately brings us back to a fundamental question raised throughout the Thesis: What exactly does the accretion geometry look like in the Very High/SPL state? Until we can arrive at a decent answer to this question, none of the various theoretical models will be acceptable as providing an unambiguous explanation for the source of high frequency QPOs.

## 7.3 New Applications of Current Code

The methods and results presented in this Thesis provide a number of different directions for proceeding with future work. They can be roughly divided into three categories, in order of increasing labor requirements and potential scientific reward: (1) Applications of the current ray-tracing code to answer new questions and analyze new simulations and observations; (2) Adding new physics modules to the basic structure of the existing code; and (3) Developing entirely new models to explain black hole QPOs and observations of X-ray spectra. In the next three Sections we will outline a few ideas for each of these categories and try to evaluate their relative promise for producing important astrophysical results.

The first obvious application of the current code is simply to apply it to a much wider range of model parameters in order to carry out a comprehensive study of the features of the QPO power spectrum. In particular, we would like to understand better the harmonic dependence on orbital eccentricity and hot spot shape (not just

the Gaussian arcs considered in Chapters 3 and 4), as well as exploring the upper limits to the allowable eccentricity. The results in Chapter 5 also only scratch the surface of what might be learned from the thermal disk model. The ISCO boundary condition should be studied more carefully to see if a self-consistent solution really exists for a wider range of black hole and accretion parameters. The scattering model in Chapter 6 must also be examined to better understand the dependence (if any) on black hole mass and spin, as well as the corona parameters.

The results of Chapters 5 and 6 may easily be combined to produce a complete integrated spectrum of the multi-colored disk, modified by scattering both in the disk atmosphere and surrounding hot corona. With this integrated approach we hope to explain the observed spectra over a broad range of luminosity states such as those enumerated by Esin, McClintock, & Narayan (1997). This approach could also lead to a more detailed understanding of radiation transport from one radius of the disk to another. In particular, by modeling the photons that get inverse-Compton scattered from the corona back to the disk, we should be able to produce a more accurate model for the fluorescent iron emission profile.

As was mentioned in Section 1.2.2, Miller & Homan (2005) have recently discovered a correlation between the phase of the low frequency QPO and the instantaneous shape of the iron emission line in the black hole source GRS 1915+105. Our ray-tracing code is ideally suited for investigating the possibility of whether the emission may be coming from an inclined ring or torus precessing at the Lense-Thirring frequency. As this ring precesses around the black hole spin axis, the solid angle seen by the distant observer should oscillate periodically, thus modulating the X-ray light curve. At the same time, the transfer function from the ring to the image plane will also vary periodically, changing the shape of any relativistic emission lines. Our code should be able to fit the data with a small number of model parameters, which may even be used to constrain the black hole spin. Furthermore, the higher-order statistical methods of Section 4.7 might be applied to these LFQPOs to further constrain the emission model.

The ultimate purpose of the ray-tracing code has always been to use it as a totally general post-processor analysis tool for any 3-D (magneto)hydrodynamic accretion simulation. We believe that we are now in a position to begin applying it as such and producing quantitative predictions with which to compare observations. It has recently been used to produce preliminary light curves from the oscillating torus model of Rezzolla & Zanotti. These light curves are found to be nearly sinusoidal and almost entirely limited to a single fundamental frequency mode. We plan on investigating other initial conditions and emission mechanisms to see whether the torus may in fact be able to produce commensurate QPOs with 3:2 ratios. Another exciting collaboration that should develop in the near future is with John Hawley's

group at the University of Virginia. Even if we cannot identify clear QPOs, by post-processing their global MHD simulations, we hope to understand more about the continuum photon energy distribution and power spectra for turbulent disks.

## 7.4 New Features for Code

In addition to applying the existing code to new problems, we also plan to add new physics capabilities to the code to make it more accurate and useful for a larger number of applications. For the hot spot model, we would like to be able to include more complicated temporal evolution for the hot spot emissivity. Instead of simply turning “on” and “off” instantaneously, the emission should be able to evolve continuously like turbulent modes that grow, saturate, and eventually decay. While the analytic methods derived in Chapter 4 can model this type of evolution reasonably well, it is always nice to be able to simulate it directly with actual hot spots being viewed by the ray-tracing code.

The Monte Carlo calculations of Chapter 6 could be expanded significantly to include a more careful treatment of the relativistic scattering (i.e. the Klein-Nishina cross section), the geometry and dynamics of the electron corona [bulk velocity and angular momentum; see Psaltis (2001b)], and the addition of photon polarization. For increased computational efficiency, the Monte Carlo scattering may be replaced by a more elegant density matrix formalism for the radiation field (Portsmouth & Bertschinger, 2004a,b). While we expect the revised cross sections for polarized light to have only a small effect on the integrated light curves (multiply-scattered photons will be preferentially scattered at different angles than for unpolarized light), it is possible that the detailed calculations may give interesting predictions for a next-generation observatory that is sensitive to X-ray polarization (Sunyaev & Titarchuk, 1985; Laor, 1991; Dovciak, 2004). Also, new models for the corona should be investigated, e.g. “clumpy” coronae made up of optically thick clouds that might affect the light curves and spectra of the scattered photons (Fuerst & Wu, 2004).

After integrating the electron scattering calculations with the  $\alpha$ -disk modified thermal emission, we hope to “streamline” the process in order to produce many different disk spectra in an efficient manner. In this way, one could fit spectral data with an accurate model consisting of only a few key parameters such as the black hole mass, spin, accretion rate, inclination, and the coronal density/temperature profile. Ultimately, we would like to make the code publicly available, much like the popular CMBFAST code (Seljak & Zaldarriaga, 1996), so that many different users can analyze stellar-mass, intermediate-mass, and supermassive black hole spectra,

Finally, it is possible that with slight modifications, the ray-tracing code could be used to model even more exotic physical processes around black holes. In recent

years, there have been a number of very exciting observations of Sgr A\*, home to the supermassive black hole at the center of our galaxy [see, e.g. Baganoff et al. (2001); Genzel et al. (2003)]. Tsuchiya et al. (2004) and Aharonian et al. (2004) have both reported significant detection of extremely high energy  $\gamma$ -ray emission from the vicinity of Sgr A\*. One speculative but extremely exciting possible explanation for this TeV emission could be the annihilation of dark matter particles in the central cusp of the galactic halo [Bergstrom et al. (2004) and references therein]. The very same code used to trace hot spot photons could also calculate the redshift and energy distribution of the annihilation  $\gamma$ -rays, assuming a simple model for their production. Eventually, with the proper theoretical foundation, these observations may also be used to map out the spacetime around black holes, and even understand the fundamental particle physics of dark matter.

## 7.5 Development of New Models

While it is definitely a useful achievement to develop a post-processor ray-tracing code capable of analyzing any general accretion disk model, what would be really exciting is to develop a new physical model that could predict the existence of HFQPOs from first principles. The very fact that there are currently so many alternative (and certainly not completely convincing) models in the literature was what motivated us to focus on the post-processor approach in the first place. But as they often say, “the more the merrier,” so we propose to add a couple more possibilities to this growing list.

Perhaps the simplest to analyze would be a set of spiral density waves forming in a relatively cold, thin disk of test particles on geodesic orbits. Much like the sweeping spiral arms that make up many galaxies (Toomre, 1964; Toomre & Toomre, 1972), these accretion disk density waves would be produced around regions in phase space where the epicyclic orbits overlap and form caustic sheets (Gottlieb, 2002). While the individual particles in the disk will be orbiting at the same geodesic frequencies as the hot spot model, the spiral density arms may appear to be moving at quite a different velocity, perhaps even explaining the low frequency QPOs. Also, the formation of these waves may be closely related to the resonant interaction between azimuthal and radial coordinate frequencies, just as in the forced resonance model for hot spot formation.

As we mentioned at the end of Section 6.4, the QPOs may be coming from a more global oscillation in the inner regions of the corona. We have recently begun to investigate the possibility of forming radiation “eigenmodes” that can grow in a type of resonance cavity around the black hole. For example, consider a ring of hot gas in a planar circular orbit, with a non-axisymmetric  $m = 2$  temperature perturbation

in  $\phi$ . The two opposite points of maximum temperature, and thus emission, will “see” each other greatly magnified by the gravitational lensing of the central black hole. These points will thus absorb more radiation than the rest of the ring, growing even hotter, thus amplifying any small initial perturbations. A global ray-tracing calculation could be used to find any special radii where such radiation eigenmodes would form and evolve. This model seems particularly appropriate for the hot, low-density, quasi-spherical ADAF geometries that might form at high luminosities.

Despite the optimistic language of Novikov & Thorne (1973) quoted above in Section 7.2, we still do not have a real physical model for the transport of angular momentum and energy for a thin accretion disk, particularly inside the ISCO. Such a model would be critical for understanding the shapes of broad iron emission lines, which almost certainly originate in the inner disk, and thus for measuring black hole spin. A successful model would most likely incorporate the magneto-rotational instability as the primary source for turbulent viscosity and angular momentum transport, which may possibly be done analytically with the heuristic treatment of Gammie (2004). At the same time, the model must also include a means for treating the radiation diffusion through the disk, which will likely result in thinner, cooler disks than those predicted by the current generation of global MHD simulations. If we could derive such an elegant, analytic model, it could also be used to form the basis for detailed perturbation analysis, returning us to the central problem of giving an explanation for high frequency QPO emission.





# Appendix A

## Formulae for Hamiltonian Equations of Motion

The equations of motion for the reduced Hamiltonian  $H_1$  in Boyer-Lindquist coordinates, as given in Chapter 2, are repeated here:

$$H_1(r, \theta, \phi, p_r, p_\theta, p_\phi; t) = -p_t = \omega p_\phi + \alpha \left( \frac{\Delta}{\rho^2} p_r^2 + \frac{1}{\rho^2} p_\theta^2 + \frac{1}{\varpi^2} p_\phi^2 + m^2 \right)^{1/2},$$

and according to classical theory:

$$\frac{dx^i}{dt} = \frac{\partial H_1}{\partial p_i} \tag{A.1a}$$

$$\frac{dp_i}{dt} = -\frac{\partial H_1}{\partial x^i}. \tag{A.1b}$$

For convenience of notation, we define the quantity  $D^2$  as

$$D^2(r, \theta, \phi, p_r, p_\theta, p_\phi) = \frac{\Delta}{\rho^2} p_r^2 + \frac{1}{\rho^2} p_\theta^2 + \frac{1}{\varpi^2} p_\phi^2 + m^2. \tag{A.2}$$

Then for an arbitrary variable  $y \in (x^i, p_i)$ , the partial derivative of  $H_1$  can be written

$$\frac{\partial H_1}{\partial y} = \frac{\partial}{\partial y}(\omega p_\phi) + \frac{\partial \alpha}{\partial y} D - \frac{1}{2} \frac{\alpha^2}{p_t + \omega p_\phi} \frac{\partial D^2}{\partial y}. \tag{A.3}$$

The first set of Hamiltonian's equations are straightforward to produce:

$$\frac{dr}{dt} = \frac{\partial H_1}{\partial p_r} = -\frac{p_r}{p_t + \omega p_\phi} \frac{\alpha^2 \Delta}{\rho^2}, \quad (\text{A.4a})$$

$$\frac{d\theta}{dt} = \frac{\partial H_1}{\partial p_\theta} = -\frac{p_\theta}{p_t + \omega p_\phi} \frac{\alpha^2}{\rho^2}, \quad (\text{A.4b})$$

$$\frac{d\phi}{dt} = \frac{\partial H_1}{\partial p_\phi} = \omega - \frac{p_\phi}{p_t + \omega p_\phi} \frac{\alpha^2}{\varpi^2}. \quad (\text{A.4c})$$

The momentum equations are a bit more involved, but there are only two of them (for  $p_r$  and  $p_\theta$ ;  $p_\phi$  is conserved):

$$\begin{aligned} \frac{dp_i}{dt} = -\frac{\partial H_1}{\partial x^i} &= -\frac{\partial \omega}{\partial x^i} p_\phi + \frac{p_t + \omega p_\phi}{\alpha} \frac{\partial \alpha}{\partial x^i} + \\ &\frac{\alpha^2}{2(p_t + \omega p_\phi)} \left[ \frac{\partial}{\partial x^i} \left( \frac{\Delta}{\rho^2} p_r^2 + \frac{1}{\rho^2} p_\theta^2 + \frac{1}{\varpi^2} p_\phi^2 \right) \right]. \end{aligned} \quad (\text{A.5})$$

The relevant spatial derivatives are as follows:

$$\frac{\partial \omega}{\partial r} = -\frac{\omega^2}{2Ma} \left[ 3r^2 + a^2(1 + \cos^2 \theta) - \frac{a^4}{r^2} \cos^2 \theta \right] \quad (\text{A.6a})$$

$$\frac{\partial \omega}{\partial \theta} = -\frac{\omega^2}{2Ma} \left[ \left( 2Ma^2 - a^2r - \frac{a^4}{r} \right) \sin \theta \cos \theta \right] \quad (\text{A.6b})$$

$$\frac{\partial \alpha^2}{\partial r} = -\alpha^4 \left( \frac{2M}{\Delta \rho^2} \right) \left( \frac{a^4 - r^4}{\Delta} - \frac{2r^2 a^2 \sin^2 \theta}{\rho^2} \right) \quad (\text{A.6c})$$

$$\frac{\partial \alpha^2}{\partial \theta} = -\alpha^4 \left[ \frac{4Ma^2 r \sin \theta \cos \theta (a^2 + r^2)}{\Delta \rho^2} \right] \quad (\text{A.6d})$$

$$\frac{\partial}{\partial r} \left( \frac{1}{\varpi^2} \right) = -\frac{2}{\varpi^4} \left[ \sin^2 \theta \left( r + \frac{2Ma^2 \sin^2 \theta (a^2 \cos^2 \theta - r^2)}{\rho^4} \right) \right] \quad (\text{A.6e})$$

$$\frac{\partial}{\partial \theta} \left( \frac{1}{\varpi^2} \right) = -\frac{4 \sin \theta \cos \theta}{\varpi^4} \left[ 2Ma^2 \sin^2 \theta \left( \frac{r^2 + a^2}{\rho^4} + \frac{1}{\rho^2} \right) + (r^2 + a^2) \right] \quad (\text{A.6f})$$

$$\frac{\partial}{\partial r} \left( \frac{\Delta}{\rho^2} \right) = \frac{2}{\rho^2} \left( r - M - \frac{r\Delta}{\rho^2} \right) \quad (\text{A.6g})$$

$$\frac{\partial}{\partial \theta} \left( \frac{\Delta}{\rho^2} \right) = \frac{2}{\rho^4} a^2 \Delta \sin \theta \cos \theta \quad (\text{A.6h})$$

$$\frac{\partial}{\partial r} \left( \frac{1}{\rho^2} \right) = -\frac{2r}{\rho^4} \quad (\text{A.6i})$$

$$\frac{\partial}{\partial \theta} \left( \frac{1}{\rho^2} \right) = \frac{2}{\rho^4} a^2 \sin \theta \cos \theta. \quad (\text{A.6j})$$



# Appendix B

## Summing Periodic Functions with Random Phases

In this Appendix we derive the shape of a QPO peak in Fourier space broadened by the summation of multiple periodic functions combined with random phases. There are many different accepted conventions for discrete and continuous Fourier transforms (Press et al., 1992), so we begin by defining the forward- and reverse-transforms between the time and frequency domains ( $t$  and  $\nu$ ). For a Fourier pair  $f(t)$  and  $F(\nu)$ ,

$$F_j = \frac{1}{N_s} \sum_{k=0}^{N_s-1} f_k e^{-2\pi i j k / N_s} \rightarrow F(\nu) = \frac{1}{T_f} \int_0^{T_f} f(t) e^{-2\pi i \nu t} dt \quad (\text{B.1})$$

and

$$f_k = \sum_{j=0}^{N_s-1} F_j e^{2\pi i j k / N_s} \rightarrow f(t) = T_f \int_{-\nu_N}^{\nu_N} F(\nu) e^{2\pi i \nu t} d\nu, \quad (\text{B.2})$$

where  $f(t)$  is defined on the time interval  $[0, T_f]$  and  $\nu_N = 1/(2\Delta t)$  is the Nyquist frequency for a sampling rate  $\Delta t = T_f/N_s$ . With this convention,  $f(t)$  and  $F(\nu)$  conveniently have the same units and Parseval's theorem takes the form

$$\int_0^{T_f} f^2(t) dt = T_f^2 \int_{-\nu_N}^{\nu_N} F^2(\nu) d\nu. \quad (\text{B.3})$$

For such a time series  $f(t)$ , the power spectrum is defined as  $F^2(\nu)$ , the squared amplitude of the Fourier transform.

Consider a purely sinusoidal function

$$f(t) = A \sin(2\pi\nu_0 t + \phi), \quad (\text{B.4})$$

where  $\phi$  is some constant phase. If there are an integer number of complete oscillations within the time  $T_f$ , or in the limit of  $T_f \rightarrow \infty$ , the Fourier transform of  $f(t)$  will be

$$F(\nu) = \begin{cases} \frac{A}{2} e^{i(\phi-\pi/2)} & \nu = \nu_0 \\ \frac{A}{2} e^{-i(\phi-\pi/2)} & \nu = -\nu_0 \\ 0 & \text{otherwise} \end{cases} . \quad (\text{B.5})$$

If we then truncate the function  $f(t)$  by multiplying it with a boxcar window function  $w(t)$  of length  $\Delta T$ , the convolution theorem gives the transform of the resulting function  $g(t)$ :

$$g(t) = f(t)w(t) \Leftrightarrow G(\nu) = (F \star W)(\nu). \quad (\text{B.6})$$

In the case where the window function is longer than a single period and short compared to the total sampling time ( $1/\nu_0 < \Delta T \ll T_f$ ), the convolved power  $G^2(\nu)$  can be well approximated by

$$G^2(\nu) \approx \frac{A^2}{4T_f^2} \frac{\sin^2[\pi(\nu \pm \nu_0)\Delta T]}{\pi^2(\nu \pm \nu_0)^2}. \quad (\text{B.7})$$

For  $f(t)$  real,  $F(-\nu) = F^*(\nu)$  and since we are primarily concerned with the power spectrum  $F^2(-\nu) = F^2(\nu)$ , we will generally consider only positive frequencies (unless explicitly stated otherwise). Of course, when calculating the actual observable power in a signal, both positive and negative frequencies must be included.

All the information about the phase  $\phi$  of  $f(t)$  and the location in time of the window function is contained in the complex phase of the function  $G(\nu)$ . This phase information is important when considering the total power contributed by a collection of signals, each with a different time window and random phase. When summing a series of complex functions with random phase, the total amplitude adds in quadrature as in a two-dimensional random walk. Therefore combining  $N$  different segments of  $f(t)$ , each of length  $\Delta T$  and random  $\phi$ , gives a Fourier transform with amplitude  $\sqrt{N}|G(\nu)|$ , and thus the net power spectrum is  $NG^2(\nu)$ .

The result in equation (B.7) is valid only if every segment of  $f(t)$  has the exact same sampling length  $\Delta T$  and frequency  $\nu_0$ . Motivated by the physical processes of radioactive decay, we assume here an exponential distribution for the lifetime of each segment. For a characteristic lifetime of  $T_l$ , the differential probability distribution of lifetimes  $T$  for coherent segments is

$$P(T)dT = \frac{dT}{T_l} e^{-T/T_l}. \quad (\text{B.8})$$

Over a sample time  $T_f \gg T_l$ , the number of segments with a lifetime between  $T$  and  $T + dT$  is given by

$$dN(T) = \frac{T_f}{T_l^2} e^{-T/T_l} dT. \quad (\text{B.9})$$

Assuming for the time being that each coherent section of the signal is given by the sinusoidal function  $f(t)$  used above, we can sum all the individual segments to give the total light curve  $I(t)$  with corresponding power spectrum

$$\begin{aligned} \tilde{I}^2(\nu) &= \int_0^\infty G^2(\nu, T) dN(T) \\ &= \left( \frac{A}{2\pi T_f} \right)^2 \int_0^\infty \frac{\sin^2[\pi(\nu - \nu_0)T]}{\pi^2(\nu - \nu_0)^2} \frac{T_f}{T_l^2} e^{-T/T_l} dT \\ &= 2A^2 \frac{T_l}{T_f} \frac{1}{1 + 4\pi^2 T_l^2 (\nu - \nu_0)^2}. \end{aligned} \quad (\text{B.10})$$

Hence we find the shape of the resulting power spectrum is a Lorentzian peaked around  $\nu_0$  with characteristic width

$$\Delta\nu = \frac{1}{2\pi T_l}. \quad (\text{B.11})$$

Since the boxcar window represents an instantaneous formation and subsequent destruction mechanism, the resulting power spectrum contains significant power at high frequencies, a general property of discontinuous functions. A smoother, Gaussian window function in time gives a Gaussian profile in frequency space:

$$w(t) = \exp\left(\frac{-t^2}{2T^2}\right) \Leftrightarrow W(\nu) = \sqrt{2\pi} \frac{T}{T_f} \exp\left(\frac{-\nu^2}{2\Delta\nu^2}\right) \quad (\text{B.12})$$

where again the characteristic width is given by  $\Delta\nu = 1/(2\pi T)$ . After integrating over the same distribution of lifetimes  $dN(T)$  as above, we get the power spectrum

$$\tilde{I}^2(\nu) = 4\pi N_{\text{spot}} A^2 \frac{T_l}{T_f} z^3 \left[ \sqrt{\pi} (1 + 2z^2) \text{erfc}(z) e^{z^2} - 2z \right], \quad (\text{B.13})$$

where we have defined

$$z \equiv \frac{1}{4\pi T_l (\nu - \nu_0)}. \quad (\text{B.14})$$

For large  $z$  (near the peak at  $\nu = \nu_0$ ), equation (B.13) can be approximated by the

narrow Lorentzian

$$\tilde{I}^2(\nu) \approx 4\pi N_{\text{spot}} A^2 \frac{T_l}{T_f} \frac{1}{1 + 48\pi^2 T_l^2 (\nu - \nu_0)^2}. \quad (\text{B.15})$$

As with the boxcar window, the exponential lifetime distribution has the effect of narrowing the peak of the net power spectrum compared with that of a single Gaussian segment of the light curve with length  $T_l$ . These results are in fact easily generalized. For any set of localized, self-similar window functions  $w(t, T) = w(t/T)$ , the corresponding power spectra  $W^2(\nu; T)$  can be approximated near  $\nu = 0$  as a Lorentzian:

$$W^2(\nu; T) \approx \frac{T^2}{T_f^2} \frac{1}{1 + \beta^2 T^2 \nu^2}, \quad (\text{B.16})$$

with  $\beta$  a dimensionless constant over the set of  $w(t, T)$ . The characteristic width of  $W^2(\nu, T)$  is thus defined as  $1/(\beta T)$ . Integrating over the lifetime distribution  $dN(T)$  from equation (B.9), the net power function is given by

$$\tilde{I}^2(\nu) \approx \tilde{I}^2(\nu_0) \frac{1}{1 + 12\beta^2 T_l^2 (\nu - \nu_0)^2}. \quad (\text{B.17})$$

We see now that the general effect of an exponential distribution of sampling lifetimes is to decrease the peak width, and thus increase the coherency, by a factor of  $\sqrt{12}$ .



# Bibliography

- Abramowicz, M. A., Lanza, A., Spiegel, E., & Szuszkiewicz, E. 1992, *Nature*, 356, 41
- Abramowicz, M. A., & Kluzniak, W. 2001, *A&A*, 374, L19
- Abramowicz, M. A., et al. 2003, *PASJ*, 55, 467
- Abramowicz, M. A., & Kluzniak, W. 2003, *Gen. Relativ. Gravitation*, 35, 69
- Abramowicz, M. A., et al. 2004, *ApJ*, 609, L63
- Abramowicz, M. A., & Kluzniak, W. 2004, in *X-Ray Timing 2003: Rossi and Beyond*, ed. P. Kaaret, F. K. Lamb, & J. H. Swank (Melville, NY: American Institute of Physics)
- Agol, E., & Krolik, J. H. 1999, *ApJ*, 528, 161
- Aharonian, F., et al. 2004, submitted to *A&A*, preprint (astro-ph/0408145)
- Armitage, P. J., Reynolds, C. S., & Chiang, J. 2001, *ApJ*, 548, 868
- Aschenbach, B., Grosso, N., Porquet, D., & Predehl, P. 2004, *A&A*, 417, 71
- Aschenbach, B. 2004, *A&A*, 425, 1075
- Avni, Y. 1976, *ApJ*, 210, 642
- Baganoff, F. K., et al. 2001, *Nature*, 413, 45
- Balbus, S. A., & Hawley, J. F. 1991, *ApJ*, 376, 214
- Balbus, S. A., & Hawley, J. F. 1998, *Rev. Mod. Phys.*, 70, 1
- Bao, G. 1992, *A&A* 257, 594
- Bardeen, J. M., Press, W. H., Teukolsky, S. A. 1972, *ApJ*, 178, 347

- Barr, P., White, N. E., & Page, C. G. 1985, MNRAS, 312, 65
- Bekenstein, J. D. 1973, Phys. Rev. D, 7, 2333
- Bekenstein, J. D. 1975, Phys. Rev. D, 12, 3077
- Belloni, T., et al. 2002, ApJ, 572, 392
- Beloborodov, A. M. 1999, ApJ, 510, L123
- Bergstrom, L., Bringmann, T., Eriksson, M., & Gustafsson, M. 2004, submitted to PRL, preprint (astro-ph/0410359)
- Bertschinger, E. 1999, "Hamiltonian Dynamics of Particle Motion," Class notes from MIT physics course 8.962
- Bertschinger, E. 2001, "Geodesics in Kerr Spacetime," Class notes from MIT physics course 8.962
- Blandford, R. D., & Znajek, R. L. 1977, MNRAS, 179, 433
- Blandford, R. D., & Begelman, M. C. 1999, MNRAS, 303, L1
- Bolton, C. T. 1972, Nature, 240, 124
- Bondi, H., & Hoyle, F. 1944, MNRAS, 104, 273
- Bowers, R. L., & Wilson, J. R. 1991, *Numerical Modeling in Applied Physics and Astrophysics* (Boston: Jones and Bartlett)
- Bowyer, S., et al. 1965, Science, 147, 394
- Boyer, R. H., & Lindquist, R. W. 1967, J. Math. Physics, 8, 265
- Bromley, B. C., Chen, K., & Miller, W. A. 1997, ApJ, 475, 57
- Carter, B. 1966, Phys. Rev., 141, 1242
- Carter, B. 1968a, Phys. Rev. Lett. 26, 331
- Carter, B. 1968b, Phys. Rev., 174, 1559
- Collins, N. A., & Hughes, S. A. 2004, Phys. Rev. D, 69, 124022
- Damour, T., & Esposito-Farese, G. 1993, Phys. Rev. Letters, 70, 2220

- Damour, T., & Esposito-Farese, G. 1996, *Phys. Rev. D*, 54, 1474
- Davis, S. W., Blaes, O. M., Hubeny, I., & Turner, N. J. 2004, submitted to *ApJ*, preprint (astro-ph/0408590)
- De Deo, S., & Psaltis, D. 2004, submitted to *Phys. Rev. Lett.*, preprint (astro-ph/0405067)
- De Villiers, J.-P., & Hawley, J. F. 2003, *ApJ*, 592, 1060
- De Villiers, J.-P., Hawley, J. F., & Krolik, J. H. 2003, *ApJ*, 599, 1238
- Di Matteo, T. 1998, *MNRAS*, 299, L15
- Doran, C. J. L. 2000, *Phys. Rev. D*, 61, 067503
- Dovciak, M., Karas, V., & Yaqoob, T. 2004, *ApJS*, 153, 205
- Dovciak, M. 2004, PhD Thesis, Astronomical Institute, Academy of Sciences of the Czech Republic, Prague (astro-ph/0411605)
- Esin, A. A., McClintock, J. E., & Narayan, R. 1997, *ApJ*, 489, 865
- Fabbiano, G. 1989, *ARA&A*, 27, 87
- Fabbiano, G., Zezas, A., & Murray, S. S. 2001, *ApJ* 554, 1035
- Fackrell, J. 1996, PhD Thesis, University of Edinburgh
- Felten, J. E., & Rees, M. J. 1972, *A&A*, 17, 226
- Fiorito, R., & Titarchuk, L. 2004, *ApJ*, 614, L113
- Ford, E. C. et al. 1999, *ApJ*, 512, L31
- Ford, E. C. 2000, *ApJ* 535, L119
- Fuerst, S. V., & Wu, K. 2004, *A&A*, 424, 733
- Gammie, C. F., McKinney, J. C., & Toth, G. 2003, *ApJ*, 589, 444
- Gammie, C. F. 2004, accepted to *ApJ*, preprint (astro-ph/0406532)
- Galeev, A. A., Rosner, R., & Vaiana, G. S. 1979, *ApJ*, 229, 318
- Genzel, R., et al. 2003, *ApJ*, 594, 812

- George, I. M., & Fabian, A. C. 1991, MNRAS, 249, 352
- Ghez, A. M., et al. 2003, accepted to ApJ, preprint (0306130)
- Ghosh, P., & Lamb, F. K. 1978, ApJ, 223, L83
- Giacconi, R., Gursky, H., Paolini, F. R., & Rossi, B. B. 1962, Phys. Rev. Letters, 9, 439
- Giacconi, R., et al. 1971, ApJ, 167, L67
- Gierlinsky, M., et al. 1997, MNRAS, 288, 958
- Gierlinsky, M., et al. 1999, MNRAS, 309, 496
- Gierlinsky, M., Done, C., Barret, D. 2002, MNRAS 331, 141
- Gilfanov, M., et al. 1994, ApJS, 92, 411
- Ginzburg, V. L. 1964, Sov. Phys. Doklady, 9, 329
- Gottlieb, J. D. 2002, MIT Research Science Institute Summer Project
- Greenstein, J. L., & Matthews, T. A. 1963, Nature, 197, 1041
- Haardt, F., & Maraschi, L. 1993, ApJ, 413, 507
- Haardt, F., Maraschi, L., & Ghisellini, G. 1994, ApJ, 432, L95
- Hamilton, A. J. S. 2004, American Astronomical Society Meeting, 204, 78.06, URL <http://casa.colorado.edu/~ajsh/schw.shtml>
- Hamilton, A. J. S., & Lisle, J. P. 2004, submitted to Phys. Rev. D, preprint (gr-qc/0411060)
- Hansen, C. J., & Kawaler, S. D. 1994, *Stellar Interiors: Physical Principles, Structure, and Evolution*, (New York: Springer-Verlag)
- Hawking, S. W., & Ellis, G. F. R. 1973, *The Large Scale Structure of Space-time* (Cambridge: Cambridge University Press)
- Hawking, S. W. 1974, Nature, 248, 30
- Hawking, S. W. 1975, Commun. Math. Phys., 43, 199
- Hawler, J. F., & Gammie, C. F., & Balbus, S. A. 1995, ApJ, 440, 742

- Hawler, J. F., & Gammie, C. F., & Balbus, S. A. 1996, ApJ, 464, 690
- Hawley, J. F. 2000, ApJ, 528, 462
- Hawley, J. F., & Krolik, J. H. 2001, ApJ, 548, 348
- Heitler, W. 1954, *The Quantum Theory of Radiation*, (London: Oxford University Press)
- Hewitt, J. N., et al. 1988, Nature, 333, 537
- Homan, J., et al. 2001, ApJS, 132, 377
- Homan, J., et al. 2004, accepted to ApJ, preprint (astro-ph/0406334)
- Horak, J. 2004, in Proc. of Workshop *Processes in the Vicinity of Black Holes and Neutron Stars*, Silesian Univ., Opava, October 2003, preprint (astro-ph/0408092)
- Hubeny, I., & Hubeny, V. 1997, ApJ, 484, L37
- Hubeny, I., & Hubeny, V. 1998, ApJ, 505, 558
- Hubeny, I., Agol, E., Blaes, O., & Krolik, J. H. 2000, ApJ, 533, 710
- Hubeny, I., Blaes, O., Krolik, J. H., & Agol, E. 2001, ApJ, 559, 680
- Humphrey, P. J., et al. 2003, MNRAS, 344, 134
- Israel, W. 1967, Phys. Rev., 164, 1776
- Jimenez-Garate, M. A., Raymond, J. C., Liedahl, D. A., & Hailey, C. J. 2001, ApJ, 558, 448
- Jimenez-Garate, M. A., et al. 2002, ApJ, 578, 391
- Karas, V., Vokrouhlicky, D., & Polnarev, A. G. 1992, MNRAS, 259, 569
- Karas, V. 1999, PASJ, 51, 317
- Kato, S., Fukue, J., & Mineshige, S. 1998, *Black Hole Accretion Disks* (Kyoto University Press: Kyoto)
- Kato, S. 2001, PASJ, 53, 1
- Kerr, R. P. 1963, Phys. Rev. Letters, 11, 237

- Kojima, Y. 1991, MNRAS 250, 629
- Kompaneets, A. S. 1957, Sov. Phys. JETP, 4, 730
- Kluzniak, W., & Abramowicz, M. A. 2001, preprint (astro-ph/0105057)
- Kluzniak, W., Michelson, P., & Wagoner, R. V. 1990, ApJ, 358, 538
- Lamb, F. K. 2003, in *X-ray Binaries and Gamma-Ray Bursts*, ASP, 308, ed. E. P. J. van den Heuvel (San Francisco: Astronomy Society of the Pacific)
- Lanzafame, G., Molteni, D., & Chakrabarti, S. K. 1998, MNRAS, 299, 799
- Laor, A. 1991, ApJ, 376, 90
- Leahy, D. A., et al. 1983, ApJ, 266, 160
- Lee, J. C., et al. 2002, ApJ, 570, L47
- Lee, W. H., Abramowicz, M. A., & Kluzniak, W. 2004, ApJ, 603, L93
- Lee, W. H., & Ramirez-Ruiz, E. 2002, ApJ, 577, 893
- Li, L.-X., & Narayan, R., 2004, ApJ, 601, L414
- Lynden-Bell, D. 1969, Nature, 223, 690
- Maccarone, T. J., & Coppi, P. S. 2002, MNRAS, 336, 817
- Maccarone, T. J., & Schnittman, J. D. 2005, accepted to MNRAS, preprint (astro-ph/0411266)
- Makishima, K., et al. 1986, ApJ, 308, 635
- Makishima, K., et al. 2000, ApJ, 535, 632
- Mandelbrot, B. B. 1999, *Multifractals and 1/f Noise: Wild Self-Affinity in Physics* (Heidelberg: Springer-Verlag)
- Markovic, D., & Lamb, F. K. 1998, ApJ, 507, 316
- Markovic, D., & Lamb, F. K. 2000, preprint (astro-ph/0009169)
- Markwardt, C. B., Swank, J. H., & Taam, R. E. 1999, ApJ, 513, L37
- Matthews, T. A., & Sandage, A. R. 1963, ApJ, 138, 30

- McClintock, J. E., & Remillard, R. A. 2004, in *Compact X-ray Sources*, ed. W. H. G. Lewin & M. van del Klis (New York: Cambridge Univ. Press), in press, preprint (astro-ph/0306213)
- Melrose, D. B., & Gedalin, M. E. 1999, *ApJ*, 521, 351
- Mendel, J. 1991, *Proc. IEEE*, 79, 278
- Merloni, A., Vietri, M., Stella, L., & Bini, D. 1999, *MNRAS*, 304, 155
- Merloni, A., & Fabian, A. C. 2001, *MNRAS*, 321, 549
- Merloni, A. 2003, *MNRAS*, 341, 1051
- Michell, J. 1784, *Phil. Trans. Royal Soc. of London*, 74, 35
- Miller, J. M., et al. 2001, *ApJ*, 563, 928
- Miller, J. M. et al. 2002a, *ApJ*, 570, L69
- Miller, J. M. et al. 2002b, *ApJ*, 577, L15
- Miller, J. M., Fabian, A. C., & Miller, M. C. 2004, *ApJ*, 614, L117
- Miller, J. M., & Homan, J. 2005, *ApJ*, 618, L107
- Misner, C. W., Thorne, K. S., & Wheeler, J. A. 1973, *Gravitation* (New York: W. H. Freeman)
- Mitsuda, K. et al. 1984, *PASJ*, 36, 741
- Narayan, R., & Yi, I. 1994, *ApJ*, 428, L13
- Narayan, R., Igumenshchev, I. V., & Abramowicz, M. A. 2000, *ApJ*, 539, 798
- Nobili, L., Turolla, R., Zampieri, L., & Belloni, T. 2000, *ApJ*, 538, L137
- Novikov, I. D., & Thorne, K. S. 1973, in *Black Holes*, ed. C. DeWitt & B. S. DeWitt (New York: Gordon and Breach)
- Nowak, M. A., & Vaughan, B. A. 1996, *MNRAS*, 280, 227
- Nowak, M. A., Wagoner, R. V., Begelman, M. C., & Lehr, D. E. 1997, *ApJ*, 477, L91
- Nowak, M. A., 2000, *MNRAS*, 318, 361

- Okazaki, A.T., Kato, S. & Fukue, J., 1987, PASJ, 39, 457
- Olive, J. F., et al. 1998, A&A, 333, 942
- Orosz, J. A., et al. 2002, ApJ, 568, 845
- Orosz, J. A., et al. 2004, ApJ, 616, 376
- Paczynski, B. 1978, Acta Astronomica, 28, 241
- Paczynski, B., & Wiita, P. J. 1980, A&A, 88, 23
- Page, D. N., & Thorne, K. S. 1974, ApJ, 191, 499
- Papaloizou, J. C. B., & Pringle, J. E. 1984, MNRAS, 208, 721
- Papaloizou, J. C. B., & Pringle, J. E. 1985, MNRAS, 213, 799
- Pariev, V. I., Bromley, B. C., Miller, W. A. 2001, ApJ, 547, 649
- Penrose, R. 1969, Riv. Nuovo Cim., 1, 252
- Perez, C. A., et al. 1997, ApJ, 476, 589
- Portsmouth, J., & Bertschinger, E. 2004a, preprint (astro-ph/0412094)
- Portsmouth, J., & Bertschinger, E. 2004b, preprint (astro-ph/0412095)
- Poutanen, J., & Svensson, R. 1996, 470, 249
- Poutanen, J., & Fabian, A. C. 1999, MNRAS, 306, L31
- Pozdniakov, L. A., Sobol, I. M., & Sunyaev, R. A. 1977, Sov. Astron., 21, 708
- Press, W. H. 1978, Comm. Astrophys., 7, 103
- Press, W. H., et al. 1992, *Numerical Recipes in C: The Art of Scientific Computing* (Cambridge: Cambridge University Press)
- Price, W. H. 1972, Phys. Rev. D, 5, 2149 and 2439
- Pringle, J. E., & Rees, M. J. 1972, A&A, 21, 1
- Psaltis, D., & Norman, C. 2000, submitted to ApJ, preprint (astro-ph/0001391)
- Psaltis, D. 2001a, Advances in Space Research, 28, 481



- Psaltis, D. 2001b, ApJ, 555, 786
- Psaltis, D. 2004a, in *X-Ray Timing 2003: Rossi and Beyond*, ed. P. Kaaret, F. K. Lamb, & J. H. Swank (Melville, NY: American Institute of Physics)
- Psaltis, D. 2004b, in *Compact X-ray Sources*, ed. W. H. G. Lewin & M. van del Klis (New York: Cambridge Univ. Press), in press, preprint (astro-ph/0410536)
- Rappaport, S., & Joss, P. C. 1983, in *Accretion Driven Stellar X-Ray Sources*, ed. W. H. G. Lewin and E. P. J. van den Heuvel (Cambridge: Cambridge University Press)
- Rappaport, S. A., Podsiadlowski, P., & Pfahl, E. 2004, submitted to MNRAS, preprint (astro-ph/0408032)
- Rauch, K. P., & Blandford, R. D. 1994, ApJ, 421, 46
- Rebusco, P. 2004, PASJ, 56, 553
- Remillard, R. A. et al. 1996, ApJ, 522, 397
- Remillard, R. A., & Morgan, E. H. 1998, in *The Active X-Ray Sky*, ed. L. Scarsi, H. Bradt, P. Giommi, & F. Fiore (Amsterdam: Elsevier)
- Remillard, R. A. et al. 1999, IAU Circ., 7123, 2
- Remillard, R. A. et al. 2002, ApJ, 580, 1030
- Remillard, R. A. 2004, in *X-Ray Timing 2003: Rossi and Beyond*, ed. P. Kaaret, F. K. Lamb, & J. H. Swank (Melville, NY: American Institute of Physics)
- Remillard, R. A., et al. 2004, submitted to ApJ, preprint (astro-ph/0407025)
- Reynolds, C. S., & Begelman, M. C. 1997, ApJ, 488, 109
- Reynolds, C. S., & Nowak, M. A. 2003, Phys. Rep., 377, 389
- Reynolds, C. S., et al. 2004, MNRAS, 349, 1153
- Reynolds, C. S., Brenneman, L. W., & Garofalo, D. 2004, in *From X-ray Binaries to Quasars: Black Hole Accretion on All Mass Scales*, ed. T. Maccarone, R. Fender, & L. Ho (Amsterdam: Kluwer Academic Publishers)
- Rezzolla, L., Yoshida, S'i., Maccarone, T. J., & Zanotti, O. 2003, MNRAS, 344, L37
- Rezzolla, L., Yoshida, S'i., & Zanotti, O. 2003, MNRAS, 344, 978

- Riffert H., & Herold, H. 1995, ApJ, 450, 508
- Rybicki, G. B., & Lightman, A. P. 1979, *Radiative Processes in Astrophysics* (New York: Wiley-Interscience)
- Schmidt, M. 1963, Nature, 197, 1040
- Schnittman, J. D., & Bertschinger, E. 2004a, ApJ, 606, 1098
- Schnittman, J. D., & Bertschinger, E. 2004b, in *X-Ray Timing 2003: Rossi and Beyond*, ed. P. Kaaret, F. K. Lamb, & J. H. Swank (Melville, NY: American Institute of Physics)
- Schnittman, J. D. 2005, ApJ in press, preprint (astro-ph/0407179)
- Schodel, R., et al. 2003, ApJ, 596, 1015
- Schwarzschild, K. 1916a, Proc. Prussian Acad. Sciences, 1916, 189
- Schwarzschild, K. 1916b, Proc. Prussian Acad. Sciences, 1916, 424
- Seaquist, E. R., et al. 1982, ApJ, 260, 220
- Seljak, U., & Zaldarriaga, M. 1996, ApJ, 437
- Shahbaz, T., et al. 1999, MNRAS, 306, 89
- Shakura, N. I. 1972, Astron. Zhurn., 49, 652
- Shakura, N. I., & Sunyaev, R. A. 1973, A&A, 24, 337
- Shapiro, S. L., Lightman, A. P., & Eardley, D. M. 1976, ApJ, 204, 187
- Shapiro, S. L., & Teukolsky, S. A. 1983, *Black Holes, White Dwarfs, and Neutron Stars: The Physics of Compact Objects* (New York: Wiley-Interscience)
- Silbergleit, A. S., Wagoner, R. V., & Ortega-Rodriguez, M. 2001, ApJ, 548, 335
- Stella, L., & Vietri, M. 1998, ApJ, 492, L59
- Stella, L., & Vietri, M. 1999, Phys. Rev. Lett., 82, 17
- Stella, L., Vietri, M., & Morsink, S. M. 1999, ApJ, 524, L63
- Stern, B., Begelman, M. C., Sikora, M., & Svensson, R. 1995a, MNRAS, 272, 291

- Stern, B., et al. 1995b, ApJ, 449, L13
- Stone, J. M., et al. 1996, ApJ, 463, 656
- Strohmayer, T. E. et al. 1996, ApJ, 469, L9
- Strohmayer, T. E. 2001a, ApJ, 552, L49
- Strohmayer, T. E. 2001b, ApJ, 554, L169
- Sunyaev, R. A. 1972 Astron. Zhurn., 49, 1153. English translation in Sov. Astron. AJ, 16, 941
- Sunyaev, R. A., & Truemper, J. 1979, Nature, 279, 506
- Sunyaev, R. A., & Titarchuk, L. G. 1980, A&A, 86, 121
- Sunyaev, R. A., & Titarchuk, L. G. 1985, A&A, 143, 374
- Tagger, M., & Pellat, R. 1999, A&A, 109, 301
- Tagger, M., Varniere, P., Rodriguez, J., & Pellat, R. 2004, ApJ, 607, 410
- Tanaka, Y. et al. 1995, Nature, 375, 659
- Terashima, Y., & Wilson, A. S. 2004, ApJ, 601, 735
- Teukolsky, S. A. 1972, Phys. Rev. Letters, 29, 1115
- Thorne, K. S. 1974, ApJ, 191, 507
- Thorne, K. S. 1994, *Black Holes and Time Warps: Einstein's Outrageous Legacy* (Norton: New York)
- Titarchuk, L. G. 1994, ApJ, 434, 570
- Titarchuk, L. G., & Osherovich, V. 2000, ApJ, 542, L111
- Titarchuk, L. G. 2002, ApJ, 578, L71
- Titarchuk, L. G. 2003, ApJ, 591, 354
- Toomre, A. 1964, ApJ, 139, 1217
- Toomre, A., & Toomre, J. 1972, ApJ, 178, 623
- Torok, G. 2004, submitted to A&A, preprint (astro-ph/0412500)

- Tsuchiya, K., et al. 2004, ApJ, 606, L115
- van der Klis, M. 1989, ARA&A, 27, 517
- van der Klis, M. et al. 1996, ApJ, 469, L1
- van der Klis, M. 1997, in *Statistical Challenges in Modern Astronomy II*, ed. G. J. Babu and E. D. Feigelson (Berlin: Springer-Verlag)
- Vaughan, B. A. et al. 1997, ApJ, 483, L115
- Wagoner, R. V. 1999, Phys. Rep., 311, 259
- Wagoner, R. V., Silbergleit, A. S., & Ortega-Rodriguez, M. 2001, ApJ, 559, L25
- Wang, D. X., et al. 2003, MNRAS, 344, 473
- Wang, Q. D., et al. 2004, ApJ, 609, 113
- Watson, M. G., et al. 1983, ApJ, 273, 688
- Webster, B. L., & Murdin, P. 1972, Nature, 235, 37
- Wheeler, J. A. 1968, American Scientist, 56, 1
- Will, C. M. 2001, Living Reviews in Relativity, 4, 4
- Wilms, J. et al. 2001, MNRAS, 328, L27
- Yao, Y. et al. 2003, submitted to ApJ, preprint (astro-ph/0303535)
- Zanotti, O., Rezzolla, L., & Font, J. A. 2003, MNRAS, 341, 832
- Zdziarski, A. A. 2000, in IAU Symp., 195, *Highly Energetic Physical Processes and Mechanisms for Emission from Astrophysical Plasmas*, ed. P. C. H. Martens, S. Tsuruta, & M. A. Weber (San Francisco: ASP), 153
- Zeldovich, Ya. B., & Shakura, N. I. 1969, Astron. Zhurn., 46, 225
- Zwillinger et al. 1996, *CRC Standard Mathematical Tables and Formulae*, ed. D. Zwillinger, S. G. Krantz, & K. H. Rosen, (Boca Raton, FL: CRC Press)
- Zycki, P. T., Done, C., & Smith, D. A. 1999a, MNRAS, 305, 231
- Zycki, P. T., Done, C., & Smith, D. A. 1999b, MNRAS, 309, 561
- Zycki, P. T. 2002, MNRAS, 333, 800